Low-energy atomic phenomena: probing fundamental physics and searching for dark matter

Author:
Roberts, Benjamin

Publication Date:
2016

DOI:
https://doi.org/10.26190/unsworks/18778

UNIVERSITY OF NEW SOUTH WALES
DEPARTMENT OF THEORETICAL PHYSICS

SYDNEY · AUSTRALIA

Low-energy atomic phenomena:
probing fundamental physics and searching for dark matter

Benjamin M. ROBERTS

Supervisors:
Prof. Victor FLAMBAUM
Dr. Vladimir DZUBA

This thesis is submitted in requirement for the degree of Doctor of Philosophy in physics.

4 March 2016

THE UNIVERSITY OF NEW SOUTH WALES
Thesis/Dissertation Sheet

Surname or Family name: **Roberts**

First name: **Benjamin**
Other name/s: **Matthew**

Abbreviation for degree as given in the University calendar: **PhD**

School: **Physics**
Faculty: **Science**

Title: **Low-energy atomic phenomena: probing fundamental physics and searching for dark matter**

Abstract 350 words maximum: (PLEASE TYPE)

A huge effort from scientists all around the world has pushed tests of physics to ever higher energy scales (e.g. at CERN), though no trace of non-standard model physics has yet been found. In this thesis, I explore another avenue: the use of high precision atomic physics to study fundamental interactions at low energy.

I present new calculations of parity-violating effects in atoms. I consider several approaches, including exploiting the very high accuracy that is possible in simple systems, the very large effects that can be found in more complex systems, and studying processes that are sensitive to hadronic parity violation.

Then, I consider the interaction of atoms with various background ``cosmic" fields. Candidates for such fields include dark matter (e.g. axions) and physics described by extensions to the standard model. By combining my calculations with existing experimental results, new limits on several parameters of physics beyond the standard model are set.

I then consider the specific case of axion dark matter in detail. I calculate several new effects that an axion field would induce in atoms. Crucially, these effects are linear in the axion interaction strength; most current search techniques are based on effects that are at least quadratic in this (extremely small) parameter.

Finally, I consider the interaction of WIMPs with electrons in regard to dark matter detection experiments. A very promising claim of a positive detection of WIMPs was made by the DAMA Collaboration. This result is the only long-standing claim for a positive WIMP detection, and electron-interacting WIMPs are the lead candidate. I demonstrate that relativistic effects give the dominant contribution to such processes, meaning that non-relativistic calculations may underestimate the cross section by many orders of magnitude; all previous calculations were performed using non-relativistic wavefunctions. I employ accurate relativistic methods to calculate model-independent cross sections and event rates. By assuming the DAMA signal is due to WIMPs, I calculate the signal that would be expected in another experiment, XENON. By comparing this to the observations of the XENON Collaboration, I entirely rule out electron-interacting WIMPs as the source of the DAMA signal.

Declaration relating to disposition of project thesis/dissertation

I hereby grant to the University of New South Wales or its agents the right to archive and to make available my thesis or dissertation in whole or in part in the University libraries in all forms of media, now or here after known, subject to the provisions of the Copyright Act 1968. I retain all property rights, such as patent rights. I also retain the right to use in future works (such as articles or books) all or part of this thesis or dissertation.

I also authorise University Microfilms to use the 350 word abstract of my thesis in Dissertation Abstracts International (this is applicable to doctoral theses only).

…………………………	…………………………	4/3/2016
Signature	Witness	Date

The University recognises that there may be exceptional circumstances requiring restrictions on copying or conditions on use. Requests for restriction for a period of up to 2 years must be made in writing. Requests for a longer period of restriction may be considered in exceptional circumstances and require the approval of the Dean of Graduate Research.

FOR OFFICE USE ONLY
Date of completion of requirements for Award:

THIS SHEET IS TO BE GLUED TO THE INSIDE FRONT COVER OF THE THESIS

Originality Statement

I hereby declare that this submission is my own work and to the best of my knowledge it contains no materials previously published or written by another person, or substantial proportions of material which have been accepted for the award of any other degree or diploma at UNSW or any other educational institution, except where due acknowledgement is made in the thesis. Any contribution made to the research by others, with whom I have worked at UNSW or elsewhere, is explicitly acknowledged in the thesis. I also declare that the intellectual content of this thesis is the product of my own work, except to the extent that assistance from others in the project's design and conception or in style, presentation and linguistic expression is acknowledged.

Signed

Date 4/3/2016

Copyright Statement

Signed

Date 4/3/2016

Authenticity Statement

Signed

Date 4/3/2016

Contents

Abstract

A huge effort from scientists all around the world has pushed tests of physics to ever higher energy scales (e.g. at CERN), though no trace of non-standard model physics has yet been found. In this thesis, I explore another avenue: the use of high precision atomic physics to study fundamental interactions at low energy.

I present new calculations of parity-violating effects in atoms. I consider several approaches, including exploiting the very high accuracy that is possible in simple systems, the very large effects that can be found in more complex systems, and studying processes that are sensitive to hadronic parity violation.

Then, I consider the interaction of atoms with various background "cosmic" fields. Candidates for such fields include dark matter (e.g. axions) and physics described by extensions to the standard model. By combining my calculations with existing experimental results, new limits on several parameters of physics beyond the standard model are set.

I then consider the specific case of axion dark matter in detail. I calculate several new effects that an axion field would induce in atoms. Crucially, these effects are linear in the axion interaction strength; most current search techniques are based on effects that are at least quadratic in this (extremely small) parameter.

Finally, I consider the interaction of WIMPs with electrons in regard to to dark matter detection experiments. A very promising claim of a positive detection of WIMPs was made by the DAMA Collaboration. This result is the only long-standing claim for a positive WIMP detection, and electron-interacting WIMPs are the lead candidate. I demonstrate that relativistic effects give the dominant contribution to such processes, meaning that non-relativistic calculations may underestimate the cross section by many orders of magnitude; all previous calculations were performed using non-relativistic wavefunctions. I employ accurate relativistic methods to calculate model-independent cross sections and event rates. By assuming the DAMA signal is due to WIMPs, I calculate the signal that would be expected in another experiment, XENON. By comparing this to the observations of the XENON Collaboration, I entirely rule out electron-interacting WIMPs as the source of the DAMA signal.

Acknowledgements

First and foremost, I would like to thank my supervisors, Prof. Victor Flambaum and Dr. Vladimir Dzuba, for providing such an interesting and fruitful project for me to work on, and for their unwavering help, guidance, and support over my years here at UNSW. Victor was always available to offer his valuable insights, to help me understand my mistakes, and to provide me with the knowledge and tools to succeed with the given task. Vladimir always made the time to listen to my (many) questions and to patiently explain all aspects of the various problems. I am also grateful to Vladimir for providing me with, and teaching me to use, his codes for the atomic structure calculations.

I express a huge gratitude to my co-authors, including Dmitry Budker, Gleb Gribakin, Nathan Leefer, Maxim Pospelov, and fellow UNSW student Yevgeny Stadnik. It has been an honour and a great privilege to have had the opportunity to work alongside such fine scientists; I am exceedingly grateful for the knowledge and experience this has gifted me, and for the guidance, encouragement, and support they all so willingly offered me.

I thank Maxim Pospelov for inviting me to visit the Perimeter Institute for Theoretical Physics, Waterloo, Canada, to collaborate; it was an invaluable experience for which I am most grateful. I also express my gratitude to Maxim, the Perimeter Institute, and the University of Victoria, Canada, for the funding and support I received during my stay.

I would also like to thank TRIμMF, the University of Manitoba, and the UNSW Graduate Research School for the generous financial support that allowed me to attend the *6th International Symposium on Symmetries in Subatomic Physics*, in Victoria BC, Canada; Dmitry Budker, Surjeet Rajendran, and the Mainz Institute for Theoretical Physics for their kind invitation, hospitality, and financial support during my stay for the *Ultra-Light Frontier* meeting and workshop at the Johannes Gutenburg University, in Mainz, Germany; the University of Zaragoza and the Patras workshop committee for their generous financial support that helped me attend the *11th Patras Workshop on Axions, WIMPs and WISPs*, at the University of Zaragoza, Spain; and my supervisor Victor Flambaum for making funds available for me to attend the *2014 Australian Institute of Physics Congress* at the Australian National University, Canberra, and the *10th Conference in the Symposium on Cosmology and Particle Astrophysics Series*, at the University of Auckland, New Zealand.

Of course, I also thank past and present fellow students from the theory office: Amy, Dima, Graham, Greg, Harley, Sam, Sasha, Yaroslav, and Yevgeny, as well as Celal, Jacinda, and Julian for all the many discussions, of both physics and non-physics, and for making the past few years both enjoyable and memorable.

Lastly, I express a special gratitude to my friends, my family, and of course Lisa, for their always present support.

Publications

Work from this thesis has been published in:

1) B. M. Roberts, V. A. Dzuba, V. V. Flambaum, M. Pospelov, and Y. V. Stadnik, *Dark matter scattering on electrons: Accurate calculations of atomic excitations and implications for the DAMA signal* (In preparation).

2) B. M. Roberts, V. V. Flambaum, and G. F. Gribakin, *Ionization of atoms by slow heavy particles, including dark matter*
Phys. Rev. Lett. **116**, 023201 (2016) — [arXiv:1509.09044]

3) B. M. Roberts, V. A. Dzuba, and V. V. Flambaum, *Parity and Time-Reversal Violation in Atomic Systems*,
Annu. Rev. Nucl. Part. Sci. **65**, 63–86 (2015) — [arXiv:1412.6644]

4) B. M. Roberts, Y. V. Stadnik, V. A. Dzuba, V. V. Flambaum, N. Leefer, and D. Budker, *Parity-violating interactions of cosmic fields with atoms, molecules, and nuclei: Concepts and calculations for laboratory searches and extracting limits*,
Phys. Rev. D **90**, 096005 (2014) *Editors' Suggestion* — [arXiv:1409.2564]

5) B. M. Roberts, Y. V. Stadnik, V. A. Dzuba, V. V. Flambaum, N. Leefer, and D. Budker, *Limiting P-Odd Interactions of Cosmic Fields with Electrons, Protons, and Neutrons*,
Phys. Rev. Lett. **113**, 081601 (2014) — [arXiv:1404.2723]

6) B. M. Roberts, V. A. Dzuba, and V. V. Flambaum, *Strongly enhanced atomic parity violation due to close levels of opposite parity*,
Phys. Rev. A **89**, 042509 (2014) — [arXiv:1401.6262]

7) B. M. Roberts, V. A. Dzuba, and V. V. Flambaum, *Nuclear-spin-dependent parity nonconservation in* s-$d_{5/2}$ *and* s-$d_{3/2}$ *transitions*,
Phys. Rev. A **89**, 012502 (2014) — [arXiv:1311.2373]

8) B. M. Roberts, V. A. Dzuba, and V. V. Flambaum, *Double-core-polarization contribution to atomic parity-nonconservation and electric-dipole-moment calculations*,
Phys. Rev. A **88**, 042507 (2013) — [arXiv:1309.3371]

9) B. M. Roberts, V. A. Dzuba, and V. V. Flambaum, *Parity nonconservation in Fr-like actinide and Cs-like rare-earth-metal ions*,
Phys. Rev. A **88**, 012510 (2013) — [arXiv:1304.7591]

Other publications (not included in this thesis):

10) V. A. Dzuba, J. C. Berengut, V. V. Flambaum, and B. M. Roberts, *Revisiting Parity Nonconservation in Cesium*
Phys. Rev. Lett. **109**, 203003 (2012) — [arXiv:1207.5864]

11) V. A. Dzuba, V. V. Flambaum, and B. M. Roberts, *Calculation of the parity-violating 5s-6s* $E1$ *amplitude in the rubidium atom*,
Phys. Rev. A **86**, 062512 (2012) — [arXiv:1211.0075]

12) B. M. Roberts, V. A. Dzuba, and V. V. Flambaum, *Quantum electrodynamics corrections to energies, transition amplitudes, and parity nonconservation in Rb, Cs, Ba$^+$, Tl, Fr, and Ra$^+$*,
Phys. Rev. A **87**, 054502 (2013) — [arXiv:1302.0593]

13) Y. V. Stadnik, B. M. Roberts, and V. V. Flambaum, *Tests of CPT and Lorentz symmetry from muon anomalous magnetic dipole moment*,
Phys. Rev. D **90**, 045035 (2014) — [arXiv:1407.5728]

14) V. V. Flambaum, B. M. Roberts, and Y. V. Stadnik, *Comment on "Axion induced oscillating electric dipole moments"*, Phys. Rev. D (In Press, 2015) — [arXiv:1507.05265]

15) V. A. Dzuba, V. V. Flambaum, and B. M. Roberts, *Calculations of energy levels, transition amplitudes, and lifetimes of low-lying states of actinium* (In preparation).

Conference proceedings:

16) B. M. Roberts, Y. V. Stadnik, V. A. Dzuba, V. V. Flambaum, N. Leefer, and D. Budker, *New Atomic Methods for Dark Matter Detection*,
J. Phys. Conf. Ser. **635**, 022033 (2015)

17) V. V. Flambaum, V. A. Dzuba, M. Pospelov, A. Derevianko, and B. M. Roberts, *Atomic Ionization by Dark Matter Particles*,
J. Phys. Conf. Ser. **635**, 022012 (2015)

18) B. M. Roberts, Y. V. Stadnik, V. V. Flambaum, and V. A. Dzuba, *Searching for Axion Dark Matter in Atoms: Oscillating Electric Dipole Moments and Spin-Precession Effects*,
Proceedings of the 11th PATRAS Workshop on Axions, WIMPs and WISPs (2015) — [arXiv:1511.04098]

19) Y. V. Stadnik, B. M. Roberts, V. V. Flambaum, and V. A. Dzuba, *Searching for Scalar Dark Matter in Atoms and Astrophysical Phenomena: Variation of Fundamental Constants*,
Proceedings of the 11th PATRAS Workshop on Axions, WIMPs and WISPs (2015) — [arXiv:1511.04100]

I have presented the results from this thesis at several international conferences:

- Patras 2015: The 11th Patras Workshop on Axions, WIMPs and WISPs, University of Zaragoza, Spain, 2015.
  Talk: *Axion and WIMP phenomena in atomic systems*
  [doi:10.13140/RG.2.1.4458.8963]
  Talk: *Manifestations of Dark Matter and Variations of Fundamental Constants in Atoms and Astrophysical Phenomena*
  [doi:10.13140/RG.2.1.2130.5448]
  Poster: *Axion Dark Matter: New atomic detection schemes*

- The Ultra-Light Frontier, Mainz Institute for Theoretical Physics, Johannes Gutenberg University, Mainz, Germany, 2015.
  Talk: *Axion-induced EDMs in paramagnetic systems*
  [doi:10.13140/RG.2.1.3410.3204]

- SSP2015: The 6th International Symposium on Symmetries in Subatomic Physics, Victoria, BC, Canada, 2015.
  Talk: *New Atomic Methods for Dark Matter Detection*
  [doi:10.13140/RG.2.1.2623.8880]
  Poster: *Atomic Symmetry Violation: New applications for tests of fundamental physics*

- CosPA2014: The 10th Conference in the Symposium on Cosmology and Particle Astrophysics Series, University of Auckland, New Zealand, 2014.
  Talk: *Manifestations of dark matter and cosmic fields in atomic phenomena*
  [doi:10.13140/2.1.1158.8167]

- AIP2014: Australian Institute of Physics Congress, Australian National University, Canberra, 2014.
  Talk: *Violations of fundamental symmetries in atoms and tests of unification theories* [doi:10.13140/2.1.3829.4083]
  Poster: *Limits on P-odd interactions of cosmic fields with electrons, protons and neutrons*

Units and Notation

Units— Except for where explicitly stated, I use Hartree atomic units throughout this thesis, in which $\hbar = m_e = a_{\rm B} = e = 1$, $c = 1/\alpha \approx 137.036$, where m_e is the electron mass, $a_{\rm B}$ is the Bohr radius, $e = |e|$ is the fundamental charge, c is the speed of light, and α is the fine-structure constant. Some useful conversions between atomic units, natural relativistic ($\hbar = c = 1$) units, and SI are given:

- Energy: $1\,{\rm au} \equiv 2\,{\rm Ry} \approx 27.211\,{\rm eV} \approx 4.3598 \times 10^{-18}\,{\rm J}$,
- Momentum: $1\,{\rm au} \equiv 2\,{\rm Ry}/c \approx 3.7289\,{\rm keV}/c \approx 1.9928 \times 10^{-24}\,{\rm kg\,m\,s^{-1}}$,
- Mass: $1\,{\rm au} \equiv 1\,m_e \approx 0.51100\,{\rm MeV}/c^2 \approx 9.1095 \times 10^{-31}\,{\rm kg}$,
- Length: $1\,{\rm au} \equiv 1\,a_{\rm B} \approx 268.17\,{\rm MeV}^{-1}\,\hbar c \approx 5.2918 \times 10^{-11}\,{\rm m}$,
- Time: $1\,{\rm au} \equiv \hbar/2\,{\rm Ry} \approx 36.749\,{\rm keV}^{-1}\,\hbar \approx 2.4189 \times 10^{-17}\,{\rm s}$.

Note that to aid with comparison with other works, I adopt (in places) the common spectroscopic convention and typically present our calculated energy levels in units ${\rm cm}^{-1}$; $1\,{\rm au} \approx 219475\,{\rm cm}^{-1}$.

Energies and wavefunctions— I employ different notations for the exact and calculated energies:

- $\mathcal{E}_n$ denotes the "exact"[1] many-body energy corresponding to the "exact" atomic or molecular state Ψ_n,
- E_n denotes the calculated energy-level for an atomic state with approximate wavefunction ψ_n,
- ε_n denotes the single particle energy corresponding to orbital ϕ_n.

In which approximation the calculations were performed will be made clear in-text; where confusion could arise I use superscripts, e.g., energies calculated in the Hartree-Fock approximation may be denoted as $E^{\rm HF}$. Note that the calculated values E_n do not include the core energy, so that for a single-valence atom in the state n, $E_n = \varepsilon_n$. For convenience with comparison to non-relativistic calculations, none of the above energies include the electron rest energy.

Operators— For operators, I typically use capital letters to represent many-electron operators, and lower-case letters to represent the corresponding single-particle operators,

$$\hat{\boldsymbol{D}} = \sum_{i=1}^{N} \hat{\boldsymbol{d}}_i. \tag{1}$$

I use a tilde to mean that the operator has been modified to include the core-polarisation correction (see Sec. A.6)

$$\widetilde{\boldsymbol{d}} = \hat{\boldsymbol{d}} + \delta V_d \tag{2}$$

---

[1] Here, and throughout, I use the word "exact" to refer either to the real/experimental value, or to hypothetical exact solutions to the Dirac equation for a given Hamiltonian.

Dirac and Lorentz conventions— I employ the standard $(+---)$ form of the metric and use the Einstein summation convention, with Greek indices running 0 through 3, and reserve Latin indices for the spatial components running 1 through 3; $A_\mu \equiv g_{\mu\nu}A^\nu = (A^0, -\boldsymbol{A})$. I use the Dirac representation, in which the Dirac matrices take the form:

$$\begin{aligned} \gamma^0 = \gamma_0 = \beta = \begin{pmatrix} 1 & 0 \\ 0 & -1 \end{pmatrix} , \qquad \gamma^i = -\gamma_i = \begin{pmatrix} 0 & \sigma_i \\ -\sigma_i & 0 \end{pmatrix} , \\ \boldsymbol{\gamma} = \gamma^0\boldsymbol{\alpha} = (\gamma^1, \gamma^2, \gamma^3)^{\rm T} , \qquad \gamma^5 = -\gamma_5 = i\gamma^0\gamma^1\gamma^2\gamma^3 = \begin{pmatrix} 0 & 1 \\ 1 & 0 \end{pmatrix} , \end{aligned} \tag{3}$$

where σ_i are the usual 2×2 Pauli spin matrices, and '1' is understood to be the 2×2 identity matrix. Then, the four-component Dirac functions, which correspond to the single-electron orbitals, can be expressed as

$$\phi_{n\kappa m}(\boldsymbol{r}) = \frac{1}{r}\begin{pmatrix} f_{n\kappa}(r)\Omega_{\kappa m}(\boldsymbol{n}) \\ i\alpha g_{n\kappa}(r)\Omega_{-\kappa,m}(\boldsymbol{n}) \end{pmatrix}, \tag{4}$$

where $f_{n\kappa}$ and $g_{n\kappa}$ are known as the "large" and "small" radial components, respectively, and

$$\Omega_{\kappa m}(\boldsymbol{n}) = \begin{pmatrix} (-1)^{j-l-1/2}\sqrt{\frac{\kappa+1/2-m}{2\kappa+1}}Y_{l,m-1/2}(\theta,\phi) \\ \sqrt{\frac{\kappa+1/2+m}{2\kappa+1}}Y_{l,m+1/2}(\theta,\phi) \end{pmatrix} \tag{5}$$

are the two-component spherical spinors. Here, $\kappa = (l-j)(2j+1)$ is the Dirac quantum number that specifies the values of both the orbital (l) and total ($j = l \pm s$) angular momentum, $m = j_z$ is the projection of the total angular momentum $\boldsymbol{j} = \boldsymbol{l} + \boldsymbol{s}$ on the (z-)axis of quantisation, $l = |\kappa + 1/2| - 1/2$ is the value of the orbital angular momentum, $\boldsymbol{n} = \boldsymbol{r}/r$, and Y_{lm} are the spherical harmonics.

Uncertainties— Uncertainties (1σ by default) in values are represented by digits in parenthesis directly following the value, where the uncertainty is in the last digits of the value. For example, $x = 1.234(56) \equiv 1.234 \pm 0.056$. Unless otherwise stated, limits (e.g., $x < 1.29$) are given to 1σ significance.

Abbreviations— The following abbreviations, which are also defined upon their first use in each chapter, are used frequently throughout this thesis:

- **ALP** Axion-like particle,
- **AM** Anapole moment,
- **CPSCI** Correlation potential in the screened coulomb interaction,
- **DM** Dark matter,
- **EDM** Electric dipole moment,
- **NSI/NSD** Nuclear spin independent/Nuclear spin dependent,
- **PNC** Parity nonconservation,
- **QCD/QED** Quantum chromodynamics/Quantum electrodynamics,
- **SM** Standard Model.

CHAPTER 1:
Introduction

Despite its extraordinary success, the standard model is known to be incomplete. For example, the allowed charge-parity violation in the standard model cannot account for the observed matter–antimatter asymmetry in the universe, there is no explanation for dark matter or dark energy, and there is no working quantum theory of gravitation. It is widely believed that the standard model is a low-energy manifestation of a more complete theory. So-called Grand Unified Theories attempt to unify the electroweak theory with quantum chromodynamics. There exist several candidate theories, such as various supersymmetry models, which make predictions that differ between each other and from the standard model; experiments must be performed to determine which, if any, is the more correct description of nature.

A huge concerted effort from scientists all around the world has pushed tests of physics ever further on the high-energy frontier. The success of this considerable investment is embodied in the triumphant discovery of the Higgs boson at CERN just a few years ago. Other notable large-scale searches include astrophysics experiments, such as the Planck and BICEP space telescopes, which provide insight into the conditions of the early universe. Such grand expeditions have, in a certain light, been ultimately disappointing in the sense that any physics beyond the standard model remains as elusive as ever.

In this thesis, I explore another avenue: the use of high precision atomic and molecular physics to study fundamental interactions at low energy. In particular, I investigate processes that involve the violation of fundamental symmetries, including time-reversal (T), parity (P), charge-conjugation (C), and Lorentz-invariance. Such effects are typically highly suppressed in the standard model, and are thus especially sensitive to new physics beyond it.

The benefits of exploiting low-energy atomic phenomena as probes of physics beyond the standard model are threefold. Firstly, atomic and molecular experiments are considerably cheaper than their high-energy counterparts, allowing for a broader area of exploration. Secondly, low-energy atomic experiments probe a very different sector of physics than the high-energy colliders and astrophysics telescopes, which means they can investigate otherwise inaccessible phenomena. Thirdly, new advances in experimental methods (such as molecular cooling and trapping, and spectroscopy with highly charged ions) and in atomic theory have led to the ability to make extremely precise theoretical calculations and experimental measurements of small effects that are particularly sensitive to new physics.

In Chapter 2, I provide a brief review of the relevant background theory and current status of the literature for investigations of parity and time-reversal violations in atomic systems. Then, in Chapter 3, I present our new calculations of parity-violating effects in atoms. I consider several approaches, including exploiting the very high theoretical accuracy that is possible in simple systems, the very large effects (and therefore experimental sensitivity) that can be found in more complex systems, and studying processes that are sensitive to hadronic parity violation. These calculations can be expected to motivate and direct future experimental work in this important area. In Chapter 4, I present a detailed study of one particular atomic many-body effect that has received little attention in the literature. This effect, the so-called "double core polarisation", provides a significant contribution to calculations of parity and time-reversal violating effects in atoms, and may have been missed in some previous calculations. It is shown that this effect is larger than may have been expected, and our calculations may help to alleviate some disagreement in the literature. This effect is particularly large in parity-violating electronic transitions involving d-states, which is especially important as new measurements based on these transitions are currently under way.

Chapter 5 considers the interaction of atomic systems with various background "cosmic" fields. Candidates for such fields include dark matter (e.g. axions), dark energy, and even more exotic physics described by extensions to the standard model. The interactions of such fields with atomic electrons and nuclei can induce parity and time-reversal violating effects in atoms and molecules. The study of such effects can in turn shed light on fundamental physics that gave rise to them. I derive several important and general results regarding the interaction of atoms with such background fields, and perform accurate atomic calculations of the induced observable effects. By combining our calculations with existing experimental results, new limits on several parameters of Lorentz and CPT violation are set.

Building on the results of the previous chapter, I consider the specific case of axions in more detail in Chapter 6. Axions are pseudoscalar particles that were first introduced as an elegant solution to one of the most important problems from quantum chromodynamics, the strong-CP problem (the observed lack of CP-violation in the strong interactions). Since then, it has been noted that axions (and other axion-like particles) well satisfy the conditions for cold dark matter, and are currently one of the leading dark matter candidates. I calculate several new observable effects that an axion field would induce in atoms (including oscillating electric dipole moments). The effects considered here are greatly enhanced in certain systems, and are sensitive to a different region of the parameter space than the effects utilised in most existing axion searches. As a consequence, our results may lead to new experiments which are complementary to existing ones.

In Chapter 7, I consider the interaction of WIMPs (weakly interaction massive particles) with atomic electrons. WIMPs are one of the simplest models for dark matter, and are generally considered to be one of the best dark matter candidates. The interaction of WIMPs with electrons is particularly important for the interpretation of the results of the European DAMA collaboration. The DAMA experiment is a dark matter direct-detection experiment that aims to detect the scintillation light emitted when dark matter particles scatter off the NaI detector. Due to the relative motion of the earth around the sun, one of the major experimental signatures sought for in direct detection experiments is an annual modulation in the event rate; and this is precisely what the DAMA collaboration have observed. The DAMA result is currently the only long-standing claim for a positive dark matter detection. Null results from many other more precise experiments, however, all but rule out the possibility that the DAMA result is due to a WIMP–nucleus interaction, which was thought to be the most likely explanation. Despite this, it has been noted that dark matter particles that interact favourably with electrons could potentially explain the DAMA modulation, without being ruled out by the other null results. In that case, the DAMA signal would be caused by atomic ionisation that is induced by the scattering of dark matter particles off the atomic electrons. This has been investigated previously, however, until now a rigorous *ab initio* relativistic treatment of the atomic structure has not been implemented.

First, general results are derived for the ionisation of atomic systems due to the scattering of slow, heavy particles (such as WIMPs). Conventional wisdom has it that the ionisation probability for such a process should be exponentially small. It is shown, however, that due to non-analytic, cusp-like behaviour of Coulomb functions close to the nucleus this suppression is removed, leading to an effective atomic structure enhancement. Further, I demonstrate that relativistic effects actually give the dominant contribution to such a process, meaning that non-relativistic calculations may underestimate the cross section by many orders of magnitude. This is a particularly significant finding, since all previous calculations relating to this problem were done using non-relativistic wavefunctions. I then employ the relativistic Hartree-Fock method to calculate model-independent cross sections and event rates for the atomic ionisation induced by the interaction with dark matter for several atoms of experimental interest.

By assuming the DAMA modulation is a positive detection, I calculate the event rates that would be expected in two other direct detection experiments, XENON and CoGeNT, which are also sensitive to WIMP–electron interactions. The CoGeNT results are more-or-less consistent with DAMA, however, the XENON results are not. From this I am able to set extremely tight constraints, and completely rule out electron-interacting WIMPs as the source of the DAMA modulation.

I note here that this thesis is primarily concerned with the application of atomic calculations to tests of fundamental physics, and not the atomic calculations themselves. Therefore, except for when directly relevant, most details on how the calculations were done are presented only in Appendix A.

CHAPTER 2:
Parity and Time-Reversal Violation in Atomic Systems

In this chapter, I outline the relevant background theory for studies of atomic parity and time-reversal violation, and give a brief overview of the current status of the literature.

2.1 Introduction

Parity violation was first observed by Wu *et al.* [1] in 1957, not long after Lee and Yang made their Nobel prize winning suggestion that parity may not be conserved in weak interactions [2]; see Fig. 2.1. Atomic parity nonconservation (PNC) is caused by the weak interaction—either by Z^0-boson exchange between the electrons and the nucleus or by P-violating inter-nuclear forces. It is manifested in P-violating atomic observables, the measurement of which provide a unique and effective channel for probing the Standard Model (SM) and searching for physics beyond it.

Experiments using Cs have been the focus of much of the attention over the past few decades (see, e.g., the review in Ref. [3]). The most precise measurement of atomic PNC is a measurement of the Cs $6s$–$7s$ PNC amplitude, made by the group lead by Nobel laureate C. Wiemen [4]. In conjunction with the highly-accurate calculations that are required for the interpretation (see Refs. [5–11] and references therein), this led to a determination of the ^{133}Cs nuclear weak charge (Q_W), an electron–nucleus weak coupling constant, that stands as the most precise low-energy test of the SM to date. The result of this analysis differers from the SM prediction by 1.5σ [11]. Though this should be considered reasonable agreement, it does indicate that further investigations may yield important new results.

Much of the interest in the area of atomic PNC has been focused on several other important areas: measuring PNC in a chain of isotopes [12]; nuclear anapole moments (AMs) [13, 14] (see also [15]); and PNC in molecules [16]. Accurate atomic calculations are not required for interpreting the measurements of PNC in a chain of isotopes of the same atom, since the atomic structure remains largely unchanged and cancels in the ratio. The nuclear AM, first introduced

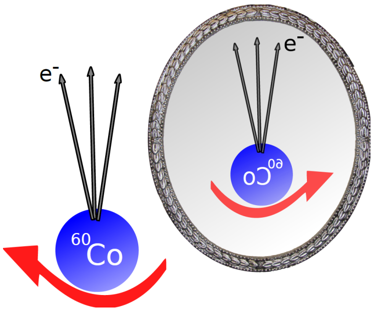

Figure 2.1 The distribution of electrons emitted in the β-decay of polarised ^{60}Co nuclei was observed to be anisotropic, providing unequivocal proof of parity violation [1].

by Zel'dovich [17], is a P-violating, T-conserving nuclear moment borne of P-violating forces inside the nucleus. The experiment [4] of the Wieman group provides the only observation of a nuclear AM so far; further measurements of AMs would provide especially valuable information for the study of hadronic parity violation.

I also note that it is possible to search for the parity and time-reversal violating effects that are induced in atoms and molecules via their interaction with dark matter, including axions. Crucially, these effects are linear in the small parameter that quantifies the interaction strength between dark matter and ordinary matter particles; most current search techniques are based on effects that are at least quadratic in this parameter. This will be discussed in more detail in later sections.

2.2 Sources of atomic parity violation

The Hamiltonian describing the electron–nucleus weak interaction due to Z^0-boson exchange can be expressed

$$\hat{h}_{\rm PNC} = \frac{-G_F}{\sqrt{2}} \sum_N \left(C_{1N} \bar{N}\gamma_\mu N \bar{e}\gamma^\mu\gamma_5 e + C_{2N} \bar{N}\gamma_\mu\gamma_5 N \bar{e}\gamma^\mu e \right), \tag{2.1}$$

where the sum runs over all nucleons, e and N are the electron and nucleon wavefunctions, respectively, $G_F \simeq 2.223 \times 10^{-14}$ au ($= 1.166 \times 10^{-5}$ GeV^{-2}) is the Fermi weak constant, γ_μ and γ_5 are Dirac matrices, and to lowest order in the SM, $C_{1n} = -1/2$, $C_{1p} = (1 - 4\sin^2\theta_W)/2 \approx 0.04$ (where n and p denote neutrons and protons), and $C_{2p} = -C_{2n} = (1 - 4\sin^2\theta_W)\lambda/2 \approx 0.05$, where $\lambda \approx 1.26$, and θ_W is the Weinberg angle, $\sin^2\theta_W \approx 0.24$. This Hamiltonian is P-violating, but T-conserving.

Treating the nucleons non-relativistically, the temporal component ($\mu = 0$) of the pseudovector electron (vector nucleon) part of the interaction (2.1) leads to the nuclear-spin-independent (NSI) Hamiltonian,

$$\hat{h}_{\rm NSI} = \frac{-G_F}{2\sqrt{2}} \Big(Q_W \tilde{\rho}(\boldsymbol{r}) + [N C_{1n} - Z C_{1p}]\, \Delta\rho(\boldsymbol{r}) \Big) \gamma_5,$$

where N and Z are the number of neutrons and protons, respectively, $Q_W = 2ZC_{1p} + 2NC_{1n} \approx -N$, and $\tilde{\rho} = (\rho_n + \rho_p)/2$ and $\Delta\rho = (\rho_n - \rho_p)$ with $\rho_{n,p}$ the normalised nucleon density. In the calculations, it is assumed that $\rho_n = \rho_p = \rho$, and the second term above drops out:

$$\hat{h}_{\rm NSI} = \frac{-G_F}{2\sqrt{2}} Q_W \rho(\boldsymbol{r}) \gamma_5. \tag{2.2}$$

In reality, there is a small difference between average radii of protons and neutrons, the so-called neutron skin; though small, this gives important corrections (see, e.g., Refs. [18–20]).

The spatial components of the vector electron part of (2.1) lead to the nuclear-spin-dependent (NSD) Hamiltonian

$$\hat{h}^Z_{\rm NSD} = \frac{-G_F}{\sqrt{2}} \kappa_Z \frac{K - 1/2}{I(I+1)} \boldsymbol{\alpha} \cdot \boldsymbol{I} \rho(\boldsymbol{r}), \tag{2.3}$$

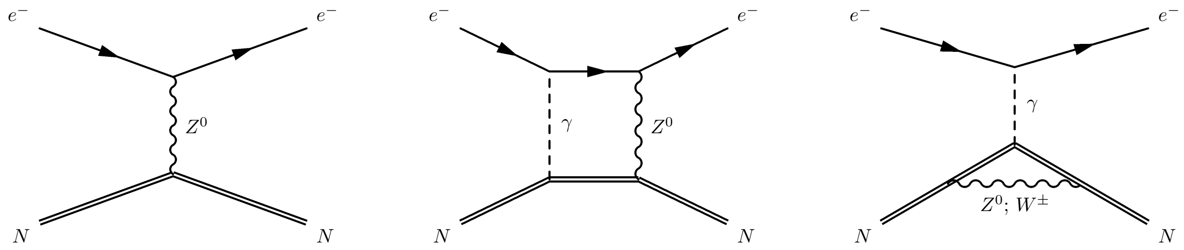

Figure 2.2 Example diagrams representing the interaction of atomic electrons with Q_W (2.2) and (2.3), Q_W perturbed by the hyperfine interaction (2.4), and the nuclear AM (2.5), respectively.

where $\boldsymbol{\alpha} = \gamma_0\boldsymbol{\gamma}$, $\kappa_Z = -C_{2n,p}$, and $K = (I+1/2)(-1)^{I+1/2-l}$ with l the orbital momentum of the unpaired nucleon. This contribution is suppressed due to a number of factors; the coefficient $|C_{2N}| \ll |Q_W|$, and also (unlike in the NSI case) the nucleons do not contribute coherently. In the shell model only the unpaired (valence) nucleons contribute. There is also a NSD contribution that comes from the interaction with Q_W perturbed by the hyperfine interaction [21, 22],

$$\hat{h}^Q_{\rm NSD} = \frac{G_F}{\sqrt{2}}\kappa_Q\frac{\boldsymbol{\alpha}\cdot\boldsymbol{I}}{I}\rho(\boldsymbol{r}), \tag{2.4}$$

which is suppressed by the ratio of hyperfine to fine-structure coefficients: $\kappa_Q = -\frac{1}{3}Q_W\frac{\alpha\mu_N}{m_pR_N} \simeq 2.5\times10^{-4}A^{2/3}\mu_N$ ($A = N+Z$, m_p is the nucleon mass, α is the fine-structure constant, R_N is the nuclear radius, and μ_N is the nuclear magnetic moment).

For heavy atoms, however, it is the contribution from the AM of the nucleus that dominates the NSD effects. The Hamiltonian describing the interaction of atomic electrons with the nuclear AM is

$$\hat{h}^a_{\rm NSD} = \frac{G_F}{\sqrt{2}}\kappa_a\frac{K}{I(I+1)}\boldsymbol{\alpha}\cdot\boldsymbol{I}\rho(\boldsymbol{r}), \tag{2.5}$$

where $\kappa_a \sim \alpha A^{2/3}$ for heavy atoms. The investigation of AMs will be discussed further in Sec. 2.4.1.

Example diagrams for the contributions to atomic PNC are represented in Fig. 2.2. Overall, the PNC Hamiltonian can be written as the sum the the NSI and NSD parts,

$$\hat{h}_{\rm PNC} = \hat{h}_{\rm NSI} + \hat{h}_{\rm NSD} = \frac{G_F}{\sqrt{2}}\left(\frac{-Q_W}{2}\gamma_5 + \varkappa\frac{\boldsymbol{\alpha}\cdot\boldsymbol{I}}{I}\right)\rho(\boldsymbol{r}), \tag{2.6}$$

where $\varkappa = \frac{K}{I+1}\kappa_a - \frac{K-1/2}{I+1}\kappa_Z + \kappa_Q$. The contributions from the NSI and NSD parts have different experimental signatures, and can thus be treated separately in the analysis. It should also be noted that the NSI part is a scalar interaction, and therefore cannot mix atomic states of different angular momentum J, whereas the vector NSD interaction can ($\Delta J \leq 1$, $J_i + J_f > 0$).

2.3 Measurements and calculations of atomic PNC

The prospect of measuring PNC in atoms was first considered for hydrogen in 1959 by Zel'dovich [23], who concluded that the effect was too small to be measurable. More than a decade later, however, the Bouchiats demonstrated that the magnitude of atomic PNC scales a little faster than Z^3 [24–26], where Z is the nuclear charge, meaning that there was a real possibility for non-zero measurements in heavier systems. For more detail, see also the book [27] and the reviews [3, 28].

From quantum electrodynamics (QED), an electric dipole ($E1$) transition between atomic states of the same parity cannot arise without external fields due to the conservation of parity. However, the weak interaction, which violates parity, leads to the mixing of opposite-parity states and therefore gives rise to small P-violating $E1$ amplitudes between states ($a \to b$) of the same (nominal) parity, known as PNC amplitudes:

$$\boldsymbol{E}_{\rm PNC}^{a\to b} = \sum_n \left[\frac{\langle\Psi_b|\hat{\boldsymbol{D}}|\Psi_n\rangle\langle\Psi_n|\hat{h}_{\rm PNC}|\Psi_a\rangle}{\mathcal{E}_a - \mathcal{E}_n} + \frac{\langle\Psi_b|\hat{h}_{\rm PNC}|\Psi_n\rangle\langle\Psi_n|\hat{\boldsymbol{D}}|\Psi_a\rangle}{\mathcal{E}_b - \mathcal{E}_n} \right], \tag{2.7}$$

where $\hat{\boldsymbol{D}} = -e\sum_i \boldsymbol{r}_i$ is the many-body operator of the electric-dipole ($E1$) interaction (in the length-form). Formulas linking equation (2.7) to the reduced matrix elements of the relevant operators are given in Appendix B.1. In experiments, it is typically the interference of this amplitude with a P-conserving effect that is directly measured. In the case of Stark-interference experiments, such as that used for Cs [4], the P-conserving effect is induced by an applied static electric field. The electric field gives rise to the Stark-induced $E1$ amplitude, $E_{\rm Stark}$, which is proportional to the electric field strength and the vector transition polarisability, β. In the PNC experiment, it is the ratio ${\rm Im}(E_{\rm PNC})/\beta$ is measured; as such, in order to extract the amplitude $E_{\rm PNC}$, a determination of β is also required.

Stark interference is not the only method that has been successfully utilised. The first observation of atomic PNC was made in 1978 at Novosibirsk using the "optical rotation" technique with Bismuth [29]. Such experiments aim to measure the interference between the P-violating $E_{\rm PNC}$ and P-conserving $M1$ transitions between the same states. This relies on the fact that PNC in atoms produces a "spin helix" (see, e.g., [27]), which interacts differently with left- and right-polarised light. The plane of polarisation of light is rotated as the light passes through an atomic vapour [23]. The angle of rotation for light that is tuned to a highly forbidden transition ($a \to b$) is proportional to ${\rm Im}(E_{\rm PNC})/\langle b|M1|a\rangle$, and it is this quantity that measured.

Since then, PNC has also been successfully observed in Pb, Tl, Yb, and Cs. Table 2.1 presents a brief summary of some of the more accurate non-zero measurements of atomic PNC and Table 2.2 presents the corresponding most accurate calculations. The calculations are presented in units of $10^{-11}i(-Q_W/N)$ au, where N is the number of neutrons; this factor is chosen since $Q_W \approx -N$. Theoretical and experimental work has been carried out for many other systems, see Sec. 2.4.

The Z^3 scaling of atomic PNC means that heavier atoms are favoured for the measurements, since it is natural to expect a higher experimental sensitivity with a larger effect. However, in order to extract the relevant electroweak parameters, highly accurate atomic calculations are required, which work best for simpler atoms. Cesium, with high nuclear charge, $Z = 55$, and relatively simple electron structure (single $6s$ valence electron above tight Xe-like $5p^6$ core) is an ideal compromise between a large effect and simplicity in the calculations. The

Table 2.1 Summary of the more recent/accurate measurements of atomic PNC.

System		$-\mathrm{Im}(E_{\mathrm{PNC}})/M1_{ab}$ (10^{-8})	Year	Source	
^{209}Bi	$^4S_{3/2}$–$^2D_{3/2}$	10.12(20)	1991	Oxford	[30]
	$^4S_{3/2}$–$^2D_{5/2}$	9.8(9)	1993	Oxford	[31]
^{208}Pb	$^3P_0$–$^3P_1$	9.86(12)	1993	Seattle	[32]
		9.80(33)	1996	Oxford	[33]
^{205}Tl	$^2P_{1/2}$–$^2P_{3/2}$	14.68(17)	1995	Seattle	[34]
		15.68(45)	1995	Oxford	[35]
System		$-\mathrm{Im}(E_{\mathrm{PNC}})/\beta$ (mV/cm)	**Year**	**Source**	
^{174}Yb	$^1S_0$–$^3D_1$	39(6)	2009	Berkeley	[36]
^{133}Cs	$6s_{1/2}$–$7s_{1/2}$	1.5935(56)	1997	Boulder	[4]

Table 2.2 Most accurate calculations of E_{PNC} $[-10^{-11}i(-Q_W/N)$ a.u.] for transitions listed in Table 2.1. Cs is excluded here, since it is discussed in more detail in the next section.

System		E_{PNC}	Year	Source	
^{209}Bi	$^4S_{3/2}$–$^2D_{3/2}$	26(3)	1989	Dzuba *et al.*	[5]
	$^4S_{3/2}$–$^2D_{5/2}$	4(3)	1989	Dzuba *et al.*	[5]
^{208}Pb	$^3P_0$–$^3P_1$	28(2)	1988	Dzuba *et al.*	[37]
^{205}Tl	$^2P_{1/2}$–$^2P_{3/2}$	27.0(8)	1987	Dzuba *et al.*	[38]
		27.2(7)	2001	Kozlov *et al.*	[39]
^{174}Yb	$^1S_0$–$^3D_1$	195(25)	2011	Dzuba *et al.*	[40]

incredible precision that has been attained in both the theoretical and experimental determinations of PNC in Cs have made it the focus of much of the research in this area, and has made PNC in Cs one of the most sensitive tests for new physics beyond the standard model.

2.3.1 Parity nonconservation in cesium

The possibility of measuring PNC in cesium was first considered in 1974 by the Bouchiats [24], who also made the first observation in 1982 [41]. Since then, several independent measurements have been performed by the Paris and Boulder groups, led by M.-A. Bouchiat and C. Wieman, respectively. A summary of the main results is presented in Table 2.3.

The measurements culminated in 1997 when the Boulder group performed

Table 2.3 Measurements of the $6s$–$7s$ NSI-PNC amplitude in ^{133}Cs (mV/cm).

$-\mathrm{Im}(E_{\mathrm{PNC}})/\beta$	Year	Source	
1.52(18)	1982–6	Paris	[41, 42]
1.576(34)	1985–8	Boulder	[43–45]
1.5935(56)	1997	Boulder	[4]
1.538(40)	2003–5	Paris	[46, 47]

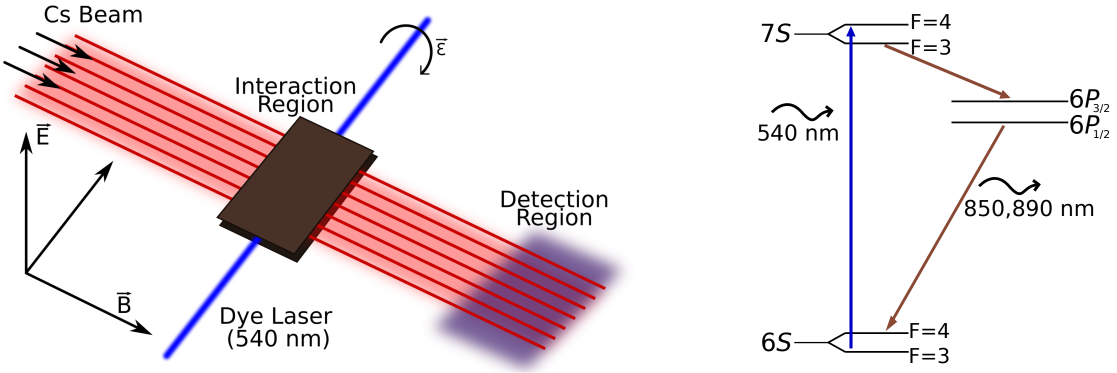

Figure 2.3 As the beam of Cs passes through the region of perpendicular magnetic and electric fields, the $6s$–$7s$ transition is excited by the 540 nm dye laser [4]. The transition rate is determined from the intensity of 850 and 890 nm $6p_{1/2,3/2} \to 6s$ fluorescence. All relevant directions (electric, $\vec{E}$, and magnetic, $\vec{B}$, fields, and the laser polarisation, $\vec{\mathcal{E}}$) are reversed to change the "handedness" of the experiment, and to control systematics.

an extraordinarily precise measurement with an uncertainty of just 0.35% [4], a relative precision unmatched by any other atomic PNC measurement to date. They used a Stark-interference technique in which a beam of atomic cesium passes through a region of perpendicular electric, magnetic, and laser fields, as shown in Fig. 2.3. This process excites the highly forbidden $6s$–$7s$ transition, which contains a small part that is due to the mixing of opposite-parity states by the electron–nucleus weak interaction (2.6). The transition rate is obtained by measuring the amount of 850- and 890-nm light emitted in the $6p_{1/2,3/2} \to 6s$ step of the $7s \to 6s$ decay sequence. The P-violating part of the amplitude manifests itself in small modulations to the transition rate as the "handedness" of the experiment is changed by reversing the direction of all fields; see [4] and references therein for details. Their final result was

$$-\,\mathrm{Im}\frac{E_{\mathrm{PNC}}}{\beta} = \begin{cases} 1.6349(80)\,\mathrm{mV/cm} & (6s_{F=4} \to 7s_{F=3}) \\ 1.5576(77)\,\mathrm{mV/cm} & (6s_{F=3} \to 7s_{F=4}). \end{cases} \tag{2.8}$$

Since the interaction with the weak charge is independent of nuclear spin, it contributes the same amplitude to each hyperfine component. Thus, by averaging over the hyperfine components, one can determine the contribution due to Q_W: $-\mathrm{Im}(E_{\mathrm{PNC}}/\beta) = 1.5935(56)\,\mathrm{mV/cm}$. The precision of the Boulder measurement for the first (and so far only) time also allowed for the detection of NSD-PNC effects, which led to a determination of the ^{133}Cs nuclear AM [4, 48].

The more recent measurements of the Paris group [46, 47] (see also [49]) used a different method—chiral optical gain—to detect the PNC signal. The results using this method are not at the same level of accuracy as the Boulder measurements [4], however, promising progress has been made. These new results may prove particularly significant as an independent verification of the important Boulder results. Even more recently, work on developing new methods has been under way; in 2014 an experimental group from Indiana successfully utilised a "two-pathway coherent control interference" technique to measure an $M1$ transition amplitude in Cs [50], which may be applied to measuring PNC in Cs with reduced errors from systematics and unwanted interference [51].

In order to determine a value of Q_W for ^{133}Cs from the measurement [4],

Table 2.4 Calculations of the ^{133}Cs $6s$–$7s$ PNC amplitude $[-10^{-11}i(-Q_W/N)$ a.u.]. Breit, QED, and neutron skin corrections are not included[a].

$E_{\rm PNC}$	Year	Source		$E_{\rm PNC}$	Year	Source	
0.88(3)	1984	Dzuba *et al.*	[70]	0.905(9)	2001	Kozlov *et al.*	[7]
0.90(2)	1987	Dzuba *et al.*	[71]	0.9078(45)	2002	Dzuba *et al.*	[8]
0.95(5)	1988	Blundell *et al.*	[72]	0.8998(24)	2009	Porsev *et al.*	[9, 10]
0.908(9)	1989	Dzuba *et al.*	[5]	0.9079(40)	2012		[9–11][b]
0.909(9)	1990	Blundell *et al.*	[6]				

[a] Accurate calculations require inclusion of Breit [20, 55, 56, 58] and QED [59–67] effects.

[b] "Main" term from Ref. [9, 10], with corrected core and tail contributions from Ref. [11]

both a value for the vector transition polarisability, β, and a calculation of the atomic structure (2.7) are required. The most accurate value, $\beta = 26.957(51)\,a_B^3$ (a_B the Bohr radius), comes from an analysis [52] of the Bennett and Wieman measurements [53]. This is not the only determination of β, and less than perfect agreement exists between methods, see, e.g., Refs. [8, 52, 54]. At the moment, however, this is not a major problem since the uncertainty in the extraction of Q_W is dominated by the calculations. Combined with the most accurate calculations available at the time [5, 6], the measurements indicated good agreement with the standard model. However, the declared theoretical uncertainty of these early calculations (1%) was not at the same level as the measurements.

An analysis of the accuracy of the calculations was performed in light of new experimental tests concerning $E1$ amplitudes and hyperfine constants in Ref. [53]. The authors noted that many of the previous discrepancies between theory and experiment were resolved in favor of theory, which led them to conclude that the accuracy of the calculations for Cs [5, 6] was actually as good as 0.4% [53]. The new analysis indicated that the observed value for the weak charge of the ^{133}Cs nucleus differed from the SM prediction by 2.5σ—signaling the possibility that new physics had been observed. The excitement was short-lived, however, when the inclusion of the Breit (magnetic and retardation) [20] (see also [55–58]) and radiative QED corrections [59–67] (see also [68, 69]) into the calculations led to a triumphant restoration of the Cs results with the standard model. Concurrently, several new calculations [7, 8, 69] agreed well with the previous results [5, 6] and confirmed the suggestion made in Ref. [53] that the theoretical accuracy was high. At this point, all recent calculations were in excellent agreement, and the new value of Q_W was consistent with the SM, being about 1σ smaller than predicted.

More recently, a new calculation was reported by Porsev *et al.* [9, 10]. They used a very sophisticated approach, applying the coupled-cluster method with single, double, and valence triple excitations (CCSDvT)—for details, see [9, 10] and references therein. (A brief overview of the coupled cluster method is presented in Appendix A.5.) Determining just 0.27% uncertainty of the calculations, their "correlated" PNC amplitude (that is, not including Breit, QED or neutron-skin corrections) was about 0.9% smaller than the results of previous calculations; see Table 2.4. This led to perfect agreement with the SM; the central points for the weak nuclear charge extracted from the measurements coincided exactly with that predicted by the SM: $Q_W = -73.16(29)_{\rm exp}(20)_{\rm th}$, $Q_W^{\rm SM} = -73.16(3)$[1] [9, 10]. The variation from the previous calculations was attributed to the role of a few higher-order correlations.

In Refs. [9, 10], the "main" ($n = 6, 7, 8, 9$) terms in the summation (2.7) were treated very accurately with the CCSDvT method; however, a simpler method was used to calculate the remaining core ($n \leq 5$) and highly excited "tail" ($n > 9$) terms. The main terms contribute about 97% to the total amplitude, though at this level of precision accuracy of the remaining terms is important also. From an analysis of the variation of these terms in different approximations, a 10% uncertainty for the core and tail was adopted. In Ref. [11], however, it was shown the inclusion of many-body effects (correlations and core polarisation) that were neglected in Ref. [9, 10] for these terms has a larger than expected impact on the calculations. With a change in sign, the core contribution shifts by about 200%; beyond the assumed 10% uncertainty. The tail contribution also becomes significantly larger. With the core and tail contributions of Ref. [9, 10] substituted by those calculated in Ref. [11], the excellent agreement with previous calculations is restored.

The final result from Ref. [11] (last row in Table 2.4) leads to a value of $Q_W = -72.58(29)_{\rm exp}(32)_{\rm th}$, which is in reasonable agreement with the SM prediction. Adding theoretical and experimental errors in quadrature, the Cs PNC result deviates from the SM value by 1.5σ: $\Delta Q_W \equiv Q_W - Q_W^{\rm SM} = 0.65(43)$. This can be related to the deviation in $\sin^2\theta_W$, giving $\sin^2\theta_W = 0.2356(20)$, 1.5σ from the SM value of 0.2386(1) [73] at near zero momentum transfer.

Though the results of Refs. [9, 10] and [11] both indicate reasonable agreement with the SM, the constraints on new physics beyond it are different. New physics originating from vacuum polarisation can be described by the weak isospin-conserving S and -breaking T parameters: $\Delta Q_W = -0.800\,S - 0.007\,T$ [74, 75]. At the 1σ level, the result of Ref. [11] leads to $S = -0.81(54)$, whereas in Refs. [9, 10] it was constrained at $|S| < 0.45$. Additionally, a positive ΔQ_W can be interpreted as evidence for an extra neutral boson, Z_χ, in the weak interaction [76]. The result of Ref. [11] leads to a constraint on its mass of $M_{Z_\chi} > 650$ GeV/c^2 (85% confidence level), a significantly less stringent bound than the 1.4 TeV/c^2 set in Refs. [9, 10].

Furthermore, recent measurements made by the $Q_{\rm weak}$ Collaboration in 2013 at the Jefferson Lab have led to the first determination of the weak charge of the proton, $Q_W^p = 0.064(12)$ [77]. Combining this with the weak charge obtained via Cs PNC leads to a value for the weak charge of the neutron, $Q_W^n = -0.975(10)$.

2.4 New directions

Though it remains the case that the Cs results are the most precise atomic PNC measurements, there are promising signs for successful parity violation determinations in several other atomic systems. Heavy analogues of Cs, such as Fr, have the advantage that the PNC effects can be largely enhanced [78, 79]. Preparations for PNC experiments in Fr are currently under way at the TRIUMF facility in Vancouver [80–84].

The largest PNC signal to date was observed in Yb at Berkeley [36]. The effect was about two orders of magnitude larger than that of Cs, and significant

---

[1] Note that the SM prediction has since been updated: $Q_W^{\rm SM}(^{133}{\rm Cs}) = -73.23(2)$ [73].

improvements in the sensitivity are expected in the near future [85, 86]. Though the accuracy of the interpretation for Yb is only around 10% [40, 87, 88], it may prove especially fruitful for measurements of the AM and PNC in a chain of isotopes. Also at Berkeley are ongoing measurements to search for PNC in Dy [89, 90]. Dy possesses two nearly degenerate states (A and B) of opposite parity and the same angular momentum, $J = 10$, at $E = 19797.96$ cm^{-1}. By observing time-resolved quantum beats between these levels caused by interference between the Stark and PNC mixing, the weak-interaction matrix element was found to be $\langle A|\hat{h}_{\rm PNC}|B\rangle = 2.3(29)_{\rm stat.}(07)_{\rm sys.}$ a.u. [89], consistent with theory [91]. The unfortunate smallness of the relevant matrix element is due to the fact that the PNC interaction cannot mix the dominant configurations of the A and B states. Experimental work is continuing, however, with an expected improvement in the statistical sensitivity of a few orders of magnitude [90]; this would provide an important test of the SM and potentially lead to a measurement of the Dy AM.

There have also been suggestions put forward to measure PNC in s–$d_{3/2}$ transitions of single-trapped ions, such as Ba$^+$ and Ra$^+$ [92] (see also [93–95]). Experimental work is currently in progress for Ba$^+$ at Seattle [96], and for Ra$^+$ at the KVI institute in Groningen [94, 97–100]. In Chapter 3 of this thesis, I also consider PNC in the heavier Cs- and Fr-like ions, which have electron structure similar to Cs. By exploiting PNC effects in heavy alkali-like ions, very high experimental sensitivity can be achieved while not impacting too heavily the accuracy of the calculations.

Another possibility is to move towards the lighter elements. Rb, a lighter analogue of Cs, is a promising option to search for both Q_W and the AM [101]. A similar proposal has been put forward for Sr$^+$ [102]. The atomic physics calculations for Rb can surpass the accuracy of those for Cs, due to the simpler electron structure and smaller relativistic corrections. This is important, since currently (in Cs) it is the theoretical uncertainty that outweighs the experimental error.

As the theoretical accuracy for the calculations approaches the level already attained in Cs, smaller, sub-1% corrections become important. As discussed above, QED effects have already proven to be crucial for the interpretation of the results in Cs. Radiative QED corrections to the $\hat{h}_{\rm NSI}$ matrix elements were calculated in Refs. [59–67]. In Ref. [68], the "radiative potential" method was developed as a simple yet accurate way of including these effects into the atomic calculations for many-electron systems. This allows the inclusion of QED effects into the $E1$ matrix elements and energy denominators [see (2.7)]. Along with the calculations for the $\hat{h}_{\rm NSI}$ matrix elements from Refs. [59–67], this method was used to determine QED corrections to several PNC amplitudes in Ref. [103]. It is crucial that high theoretical accuracy can be confirmed through independent calculations by several different groups. At the moment, however, for certain systems there exists small, but significant, disagreement. In Chapter 4 of this thesis, one particular many-body effect, the so-called double core polarisation, is studied in detail. This effect may have been missed in some calculations, which suggests that it has the potential to resolve some of the disagreement in the literature [104].

Recent developments in experimental techniques are also showing a great promise for highly precise new measurement of atomic PNC in the near future.

For example, in Ref. [105], an optical cavity was developed that can enhance optical rotation signals by as much as four orders of magnitude. This advantage can be made more significant by combining this signal enhancement with further PNC enhancements in diatomic molecules, which have nearby opposite parity states [106].

2.4.1 Nuclear anapole moments

It was first shown by Zel'dovich in 1957 that P-violation inside a charge distribution could give rise to an AM [17]. It was subsequently pointed out that an AM in the nucleus would contribute to NSD PNC in atoms and molecules [13] (see also [14, 107, 108]); in fact it was demonstrated that the effect of the AM was enhanced in heavy nuclei as $A^{2/3}$, and that it dominates the NSD contribution to PNC in atoms and molecules. This meant that, with sufficiently precise measurements, atomic experiments could be used to study P-violation in the hadron sector. This "tabletop" nuclear physics provides a unique low-energy probe for physics that is relatively inaccessible by other means; see, e.g., Refs. [15, 109].

P-violating forces acting between nucleons create a spin helix structure inside the nucleus. A part of the vector potential created in this configuration is of a contact nature, $\boldsymbol{A}^{\rm AM} = \boldsymbol{a}\delta^3(\boldsymbol{r})$, where $\boldsymbol{a} = -\pi\int r^2\boldsymbol{j}(\boldsymbol{r})\,{\rm d}^3r$ is the AM with $\boldsymbol{j}(\boldsymbol{r})$ the electromagnetic current density; see, e.g., Refs. [27, 110]. A diagram of a current distribution that gives rise to an AM is shown in Fig. 2.4. Note that such a moment must violate parity; the AM contains the current vector $\boldsymbol{j}$, which is P-odd, but it's also directed along the nuclear spin $\boldsymbol{I}$, which is P-even: $\langle\boldsymbol{a}\rangle = -\pi\langle r^2\boldsymbol{j}\rangle = |\boldsymbol{a}|\boldsymbol{I}/I$.

The AM is quantified by the dimensionless parameter κ_a,

$$\boldsymbol{a} = \frac{1}{e}\frac{G_F}{\sqrt{2}}\frac{K\boldsymbol{I}}{I(I+1)}\kappa_a, \tag{2.9}$$

where e is the proton charge, and K is defined in (2.3). The interaction of atomic electrons with the AM, which has the form $\hat{h}^a = e\boldsymbol{\alpha}\cdot\boldsymbol{a}\rho(\boldsymbol{r})$ [see (2.5)], leads to NSD-PNC effects in atoms. The interaction with the AM is the dominant NSD contribution to PNC in heavy atoms, however its effect is indistinguishable from that of κ_Z and κ_Q (see Sec. 2.2), and these must be calculated and subtracted in order to extract κ_a from the measurements.

The Cs experiment [4] of the Boulder group provides the only definitive observation of a nuclear AM to date (there are limits on the ^{203,205}Tl AM from experiment [34]). The NSD contribution to the $6s$–$7s$ PNC amplitude was found to be ${\rm Im}(E_{\rm PNC})/\beta = 0.077(11)$ (2.8). In Ref. [48], a value for the NSD-PNC constant $\varkappa(^{133}{\rm Cs}) = 0.393(56)$ was extracted from the measurements by taking the ratio of the calculated NSD-PNC amplitude from Ref. [111] to the NSI amplitude, calculated in Ref. [38]. These works were chosen since they were performed using an identical technique, and the theoretical uncertainties would cancel in the ratio [48]. This value was confirmed in Ref. [112].

In the (nuclear) single-particle approximation, κ_Z for ^{133}Cs is given by $\kappa_Z = -C_{2p} \simeq -0.05$. Taking many-body effects into account, a value of $\kappa_Z = -0.063$ was calculated in Ref. [113]. Atomic calculations performed in Ref. [112] (see also [21, 22, 114]) found $\kappa_Q = 0.017$. Taking these into account leads to a value for the AM constant [28]

$$\kappa_a(^{133}\mathrm{Cs}) = 0.362(62) \tag{2.10}$$

(see [48] for a discussion of finite-nuclear-size effects).

The SM prediction of κ_a is highly dependent on nuclear physics calculations. For ^{133}Cs, it ranges from as high as $\kappa_a = 0.36$ in the single-particle approximation down to $\kappa_a = 0.11$ depending on how the many-body effects are included, see, e.g., [22, 110, 113, 115, 116] (see also [28] for a discussion). It must, therefore, be concluded that the Cs results are in reasonable agreement with the standard model.

There are, however, discrepancies between weak meson-nucleon coupling constants extracted from the Cs AM and those extracted from hadron scattering experiments; see, e.g., [28, 117]. There is also a problem from the measurements in Tl. The AM of ^{203,205}Tl has been constrained as $\kappa_a = -0.22(30)$ [34, 118], which is inconsistent both with that predicted by nuclear theory (between $\kappa_a = 0.10$ and 0.48, see, e.g., [22, 110, 113, 116]) and with the Cs results. It is clear that there is much to be gained from further investigation into this field.

The current status of nuclear physics means that even modestly accurate measurements of the AM can shed light on important physics. Therefore, the extreme precision that is required of the atomic calculations for extracting Q_W is not necessary. This frees the possibility of exploiting favorable conditions in more complicated atoms and molecules where the effect is larger. Also, it would be extremely beneficial to measure AMs for nuclei with an unpaired neutron (Cs and Tl have unpaired protons). In Sec. 3.4 of Chapter 3 of this thesis, I present calculations for AM (due both to unpaired protons and neutrons) and Q_W induced PNC amplitudes for several heavy rare-earth and actinide atoms in which the effect is enhanced by the presence of pairs of close opposite-parity levels (see also Refs. [119, 120]). Experimental work to measure AMs is in progress at Berkeley for Dy [89, 90] and Yb [36, 85], at Heraklion for Xe and Hg [105], and at TRIUMF for Fr [80–84].

In Refs. [16, 108] it was noted that the effect of the AM is strongly enhanced in diatomic molecules due to the mixing of close rotational states of opposite parity, including the mixing of Λ or Ω doublets (see also [121]). The PNC effects

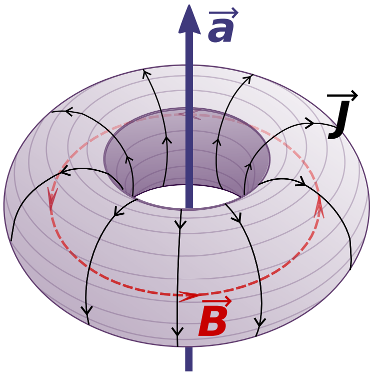

Figure 2.4 Diagram showing the toroidal current, $\boldsymbol{J}$, the magnetic field it produces, $\boldsymbol{B}$, and the resulting anapole moment, $\boldsymbol{a}$.

produced by Q_W are not enhanced, meaning it is the AM effect that dominates PNC in molecules. For a review of P- and T-violation in diatomic molecules, I direct the reader to Ref. [122].

The enhancement of the AM effects in molecules is due to the ability of the AM to mix very closely spaced rotational levels of opposite parity. The intervals between these levels are around five orders of magnitude smaller than those between opposite-parity states in atoms, meaning the PNC effects can be around five orders of magnitude larger. Further enhancement may be achieved by a reduction of the intervals by an external magnetic field [108]. Note that very close levels of opposite parity can also be found in heavy atomic systems, such as the actinide and rare-earth metals [12]; however, this is often at the loss of single-particle s-$p_{1/2}$ mixing [91, 123], which suppresses the overall effect.

Molecules and molecular ions with $\Sigma_{1/2}$ or $\Pi_{1/2}$ electronic ground states are good candidates for the measurements [16, 108]. Molecular PNC experiments are currently in progress for BaF at Yale [124] and RaF at KVI [125]. Measurements of the AM in molecules also require electron structure calculations for their interpretation. A number of calculations have been performed for diatomic molecules of experimental interest; see, e.g., Refs. [125–129] and references within.

Recent progress in molecular cooling and trapping techniques have made this area particularly exciting for breakthroughs in the very near future; see, e.g., [130] and references therein. Laser cooling of molecules was first demonstrated experimentally with polar SrF molecules in 2010, where temperatures of a few milli-Kelvin were achieved [131]. In mid-2014, magneto-optical trapping of SrF was demonstrated at a temperature of about 2.5 mK [132]. Other schemes, such as those employed recently to cool polyatomic CH_3F molecules [133], are also making promising leeway. Such techniques will prove exceptionally useful not only in searching for PNC, but also increasingly in the search for permanent EDMs of molecules.

2.4.2 Electric dipole moments

It should be noted that any "new physics" involved in atomic PNC would constitute a relatively small correction to an already very small effect. The case of electric dipole moments (EDMs), however, is somewhat different. Permanent EDMs of fundamental particles—which are necessarily P- and T-violating—are highly suppressed in the SM, and those predicted by new theories are often many orders of magnitude larger. Atomic and molecular EDMs are therefore particularly sensitive probes for theories beyond the standard model. Recent advances in both theoretical and experimental techniques makes this a very exciting area for potential discovery in the near future, e.g., in constraining the electron EDM. Furthermore, if CPT is a good symmetry (as it is in gauge theories), T-violation would be accompanied by CP-violation, which was first observed in 1964 in the decay of K^0 particles [134]. It is well known that the CP-violation allowed by the SM is insufficient to explain the matter-antimatter asymmetry of the universe; the search for new sources of T- and CP-violation is therefore a crucial front for fundamental physics.

A permanent EDM of a stable particle (e.g., a nucleon, atom, or molecule) would violate both P and T invariance, see Fig. 2.5. The SM allows only extremely small EDMs of fundamental particles. Conversely, most extensions to the SM predict much larger EDMs, which are within experimental reach—making EDMs an extraordinarily sensitive probe for new physics [135]. The parameter space for CP-violation allowed in supersymmetric theories is already very strongly limited by EDM measurements [135–137].

The EDM, $\boldsymbol{D}^{(a)}$, of an atom or molecule in state a can arise either from the sum of the intrinsic EDMs of the constituent particles, or from the mixing of opposite-parity states due to a P- and T-violating interaction, $\hat{h}_{PT}$:

$$\boldsymbol{D}^{(a)} = 2\sum_n \frac{\langle\Psi_a|\hat{\boldsymbol{D}}|\Psi_n\rangle\langle\Psi_n|\hat{h}_{PT}|\Psi_a\rangle}{\mathcal{E}_a - \mathcal{E}_n}. \tag{2.11}$$

An atomic or molecular EDM can be generated via several (P,T)-violating mechanisms, e.g., the interaction with the electron EDM, and (P,T)-violating electron–nucleon and nucleon–nucleon interactions [138, 139]. Different systems have different sensitivities to the various sources, depending on electronic and nuclear structure. For example, in paramagnetic systems (with non-zero J), the EDM is due almost entirely to the electron EDM and (P,T)-violating electron–nucleon interactions. For diamagnetic systems ($J = 0$), however, EDMs are mostly due to the (P,T)-odd inter-nuclear forces and the NSD electron–nucleon interaction.

The existence of (P,T)-odd nuclear forces gives rise to (P,T)-violating nuclear moments in the multipole expansion of the nuclear potential. The lowest-order term in the expansion, the nuclear EDM, is unobservable in neutral atoms due to total screening of the external electric field by the atomic electrons (the Schiff theorem) [140]. I note, however, that it may be possible to observe the nuclear EDM in ions (see, e.g., Ref. [141]). The first non-vanishing terms that survive the screening in neutral systems are the so-called Schiff moment and the electric octopole moment. After the nuclear magnetic dipole moment, the lowest magnetic term in the expansion is the magnetic quadrupole moment.

From theoretical calculations, the atomic and molecular EDMs can be linked to the hadronic and leptonic mechanisms that gave rise to them, leading to limits—and potentially values—for important fundamental physics parameters. A summary of some of the more recent atomic and moleculer EDM measurements are presented in Table 2.5. Experiments have also been performed using Rb [142], the excited $5p^5 6s\ ^3D_2$ state of Xe [143], and the YbF [144], PbO [145], and ThO [146] molecules. No non-zero EDM has been observed for atoms or molecules (or indeed any fundamental particle) so far; the most stringent limit $D(^{199}\text{Hg}) < 3.1 \times 10^{-29}$ (2σ) comes from the measurements in Hg [147, 148].

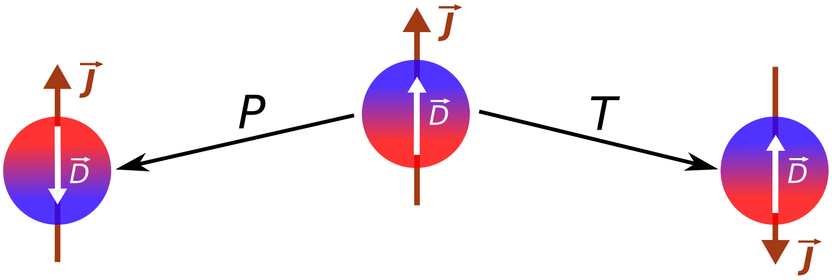

Figure 2.5 The expectation value of the electric dipole operator, $\boldsymbol{d}$, lies in the direction of the total angular momentum, $\boldsymbol{J}$; however, $\boldsymbol{d}$ is P-odd and T-even while $\boldsymbol{J}$ is P-even and T-odd.

Table 2.5 Summary of the more recent atomic and molecular EDM measurements.

System		EDM ($e \cdot \mathrm{cm}$)	Year	Source	
Paramagnetic	^{133}Cs	$-0.18(69) \times 10^{-23}$	1989	Massachusetts	[149]
	^{205}Tl	$-0.40(43) \times 10^{-24}$	2002	Berkeley	[150]
	^{225}Ra	$-0.05(25) \times 10^{-21}$	2015	Argonne Nat. Lab.	[151]
Diamagnetic	^{129}Xe	$0.07(33) \times 10^{-26}$	2001	Michigan	[152]
	^{199}Hg	$0.049(150) \times 10^{-28}$	2009	Seattle	[147]
Molecular	TlF	$-0.17(29) \times 10^{-22}$	1991	Yale	[153]

Much experimental work is currently under way that promises significant improvements in the measurements in the near future, e.g., in Xe [154], YbF [155, 156], TlF [157] and ThO [158–161]. New experiments are also in preparation designed to measure the EDM of Xe [162] and Fr [163] at CYRIC in Tohoku, and Rn at TRIUMF [164] (see also [165]). Very recently, the SrF molecule was successfully trapped and cooled, demonstrating the the ability of this technique, which can be applied to molecular EDM and PNC experiments [131, 132].

EDM measurements have recently been perfomed for Ra at the Argonne national laboratory [151] (see also [166, 167]). Though not at the same level of precision as the Hg or Tl measurements, this result represents a great step forward and is very promising in terms of future measurements in heavy systems. Measurements using Ra are also currently underway at the KVI institute [168].

A proposal to use mixtures of ^{3}He and ^{129}Xe gas offers the possibility of up to four orders of magnitude improvement compared to the ^{199}Hg EDM result [169]. A recent proposal to use an atomic fountain experiment to measure the EDMs of alkali atoms is presented in Ref. [170]. Experiments to search for EDMs in condensed matter systems have been proposed [171–173], and recently performed using $\mathrm{Eu_{0.5}Ba_{0.5}TiO_3}$ [174].

Electron EDM The EDM of an electron, should it exist, can induce an EDM in an atom or molecule by interacting with the atomic field leading to the mixing of opposite-parity states (2.11). The magnitude of such an EDM can be expressed in the form $D = Kd_e$, where d_e is the electron EDM magnitude, and K is an electron structure factor that comes from atomic calculations [138, 175]. Roughly, for heavy atoms with an external s or $p_{1/2}$ electron, it can be estimated as $K \sim 3Z^3\alpha^2 R \sim 10^2$–$10^3$ [138, 176] (R is a relativistic factor). The factor K is referred to as the electron EDM enhancement factor for obvious reasons—the EDM of an atom can be many orders of magnitude larger than the electron EDM that caused it. In molecules, much larger enhancement $K \sim 10^7$–10^{11} can be realised due to the mixing of the close opposite-parity rotational levels [16].

Polar molecules have an exceptionally high sensitivity to an electron EDM. The effective electric fields inside polar molecules can exceed several GV/cm—orders of magnitude larger than any laboratory field. The energy shift of a particle due its EDM is proportional to the external field strength, and as such an electron passing through this region would experience a significantly enhanced shift. The effective electric field in ThO has been calculated to be 84 GV/cm, one of the largest known [177]. In early 2014, the ACME Collaboration [146] exploited this technique and used ThO to place the most stringent limit on the electron EDM to date. They found

$$d_e = -2.1(37)_{\rm stat}(25)_{\rm sys} \times 10^{-29}\ e\cdot{\rm cm}, \tag{2.12}$$

which, at the 90% confidence level, leads to a limit of $|d_e| < 8.7 \times 10^{-29}\ e \cdot {\rm cm}$ [146], an order of magnitude improvement over the previous best limits, which came from experiments using YbF [144] and Tl [150]. Note that newer calculations suggest a slightly larger limit of $|d_e| < 9.8 \times 10^{-29}\ e \cdot {\rm cm}$ [178].

The Tl result is the best limit on the electron EDM coming from a paramagnetic atom [150]. Using the calculated value for the enhancement factor $K = -585$ from Ref. [179], this led to the value $d_e = 6.9(74) \times 10^{-28}\ e \cdot {\rm cm}$. The value of K for Tl is very sensitive to atomic many-body effects, but there is excellent agreement between the most complete calculations [179–181] (see also [182] which gives a smaller result). The diamagnetic (closed shell) atoms are much less sensitive to the electron EDM; e.g. the enhancement factor for Hg is $K \sim 10^{-2}$ [108]. Despite this, the strong constraint on the Hg EDM [147, 148] means the limit on electron EDM extracted from these measurements is competitive with the Tl result.

I also note that the interaction of various background cosmic fields may also induce EDMs in atomic systems. One case of particular interest is that of axions, which are a promising dark-matter candidate. This idea is the focus of Chapters 5 and 6.

CHAPTER 3:
New Directions for Atomic Parity Violation

In this chapter, I explore possible future directions for investigations of atomic parity violation. With the aim of motivating future experiments, I present here calculations of energy levels, matrix elements, lifetimes, hyperfine structure constants, and parity nonconservation amplitudes of several heavy atoms and ions. I consider parity-violating effects that are induced both by the nuclear weak charge and the nuclear anapole moment, which are relevant to tests of the electroweak theory at low energy, and to tests of parity violation in the hadron sector, respectively.

3.1 Introduction

Measurements and calculations of the $6s$–$7s$ parity nonconservation (PNC) amplitude in cesium have lead to a determination of the nuclear weak charge, a parameter of the electroweak theory quantifying the coupling of electrons to the nucleus via Z^0-boson exchange. This result stands as the most precise low-energy test of the standard model to date. This precision is a result of highly accurate measurements [4, 53] and the almost equally accurate atomic calculations used for their interpretation [5–11, 183] (see Sec. 2.3.1 for a more detailed discussion). The interpretation shows that the value of the weak nuclear charge for ^{133}Cs, coming from the PNC measurements, differs from the prediction of the standard model by 1.6σ [4, 9, 11]. Although this cannot be regarded as disagreement, it indicates that further improvements to the accuracy of the measurements and interpretation may lead to new important results.

These measurements have also lead to the only determination of a nuclear anapole moment, a nuclear moment created by parity-violating forces inside the nucleus (see Sec. 2.4.1). Further measurements of anapole moments would be invaluable tools to investigate low-energy quantum chromodynamics and parity-violation in nuclear physics.

It is imperative that the cesium results are verified using another system, even if the accuracy is not improved. Moreover, I present arguments here that in fact it may be possible to improve the accuracy using optimal conditions found in heavy ions and more complex systems.

One way to proceed would be to try to improve the accuracy in both the measurements and calculations in Cs. This pathway is being actively pursued from both the theoretical [184, 185] and experimental [46, 47, 49] sides. While this is an important endeavour, it is unlikely that a significant increase in the accuracy for Cs can be achieved in the near future. Another possibility is to look to other systems; several proposals have been put forward to search for PNC in heavier atoms, where the PNC signal is expected to be larger (e.g. [78, 119, 186]), and in systems such as Rb [101], where the theoretical accuracy could be higher. A promising alternative is to perform measurements of PNC in a chain of isotopes [12], where the accuracy is limited only by the knowledge of the (poorly understood) neutron distribution.

In Sec. 3.2, I present calculations of nuclear-spin-independent (NSI) PNC amplitudes that are induced by the nuclear weak charge for the s-s and s-$d_{3/2}$

transitions in several Fr-like actinide and Cs-like rare-earth-metal ions. Parity-violating effects in these ions are significantly larger than the effects in cesium, while they maintain the simple single-valence electron structure. This means that these systems may prove to be an excellent compromise between the size of the effect and the simplicity of the calculations. In particular, it is demonstrated that isotopes of La^{2+}, Ac^{2+}, and Th^{3+} ions have strong potential in the search for new physics beyond the standard model: the PNC amplitudes are large, the calculations are accurate, and the nuclei are practically stable. In addition, $^{232}\mathrm{Th}^{3+}$ ions have recently been trapped and cooled [187].

Then, in Sec. 3.3, I present my calculations of s-$d_{5/2}$ nuclear-spin-dependent (NSD) PNC amplitudes for Rb, Cs, Ba^+, Yb^+, Fr, Ra^+, and Ac^{2+}. These systems prove to be good candidates for use in atomic experiments to extract the nuclear anapole moment. When considering s-s, or s-$d_{3/2}$ PNC amplitudes, both the NSI and NSD parts of the parity-violating interaction contribute. This means that if one is to extract the anapole moment, the NSI part of the amplitude must be subtracted. However, due to the large change in angular momentum in the s-$d_{5/2}$ transitions, the (scalar) NSI interaction cannot contribute, meaning that the only large contribution will come from the nuclear AM, which would lead to a cleaner extraction.

Finally, in Sec. 3.4, I present my calculations of NSI and NSD parity violating amplitudes in Ba, Ra, Ac^+, Th, and Pa. Parity nonconservation in these systems is greatly enhanced due to the presence of very close electronic energy levels of opposite parity, large nuclear charge, and strong nuclear enhancement of parity-violating effects. The presented amplitudes constitute several of the largest atomic parity-violating signals predicted so far. Experiments using these systems may be performed to determine values for the nuclear AM. The considered NSI transitions could also be used to measure the ratio of weak charges for different isotopes of the same atom, the results of which would serve as a test of the standard model and also of neutron distributions. Barium, with seven stable isotopes, is particularly promising in this regard.

3.2 Parity violation in Fr-like actinide and Cs-like rare-earth-metal ions

3.2.1 A better balance between theory and experiment?

It is natural to expect a higher accuracy in measurements of systems where the PNC effect is larger. On the other hand, for achieving high accuracy in the calculations it is important to have systems with a simple electron structure. In this chapter, the s-d transitions in the Fr-like ions are shown to be very promising in this respect. The PNC amplitude is larger for atoms or ions with higher nuclear charge Z [24]. It is also larger for the s-d transitions than for the s-s transitions like the one used in Cs [93]. The accuracy for the here considered calculations is also demonstrated to be high. This is because these ions have a simple electron structure with one valence electron above closed shells—similar to that of Cs.

There are several additional factors which promise potentially better theoretical accuracy for these ions than for Cs:

(i) The main source of theoretical uncertainty comes from inclusion of electron correlations (see Apendix A). The relative value of the correlation correction is smaller for ions than for neutral atoms (since the core is more tightly bound).

(ii) There are no strong cancellations between different correlation corrections for *s*-*d* PNC amplitudes [93] in contrast to very strong cancellation for the $6s$–$7s$ PNC amplitude in Cs.

(iii) The *s*-*d* PNC amplitude is strongly dominated by a single term in the summation that has the $d_{3/2}$–$p_{1/2}$ $E1$ and s–$p_{1/2}$ PNC matrix elements. This term can be checked and/or corrected if an accurate experimental value for the *d*-*p* $E1$ amplitude is known. A similar approach in Cs works with only a limited accuracy due to strong cancellation between $6s$–np and $7s$–np contributions.

PNC measurements have been considered for Ba^{+} [92] and are in progress for Ra^{+} at the KVI institute in the Netherlands [94, 97–100]. The FrPNC Collaboration, based at the TRIUMF laboratory in Canada, has begun the construction of a laser cooling and trapping apparatus with the purpose of measuring atomic PNC in microwave and optical transitions of Fr [80–84]. With a PNC amplitude in the $7s$–$8s$ optical transition expected to be around 15 times larger than that of Cs, and its relatively simple electronic configuration, Fr is a very good candidate atom for precision measurements and calculations of PNC [78, 79, 93].

With the aim of motivating experiment in this important area, I present calculations of *s*-*s* and *s*-*d* PNC amplitudes for several Cs- and Fr-like ions. Simple estimates show that the size of the PNC effect should scale as $E_{PNC} \sim Z^3 R(Z\alpha) \,/\, Z_a$, where R is a relativistic factor and Z_a is the effective charge defined via $E_n = -Z_a^2/2n^2$ au (see, e.g., Ref. [27]). Here, E_n is the binding energy of the valence electron, with n the principal quantum number ($n = 7$ for Fr-like ions). Therefore, PNC effects in these ions are only slightly smaller than in neutral atoms.

Of particular interest are the optical *s*-*d* PNC transitions of ^{232}Th^{3+} and ^{139}La^{2+}, and the IR transition in ^{227}Ac^{2+}. ^{232}Th has a half-life of 1.5×10^{10} yr and ^{227}Ac of 21.8 yr, much more stable than Fr, for which the most stable isotope (^{223}Fr) has a half-life of just 22 min. ^{139}La^{2+} is stable. Importantly, the ^{232}Th^{3+} ion has recently been trapped and cooled by Campbell *et al.* [187], in what was the first reported laser cooling of a multiply charged ion.

The experiment needed to measure the $7s$–$6d_{3/2}$ PNC amplitude in Th^{3+} is somewhat different to the conventional PNC experiments. Neither of the states of interest are the ground state and the PNC amplitude must be reached by first populating the metastable $7s$ state. This is explored in more detail in Sec. 3.2.4. Ac^{2+} maintains a $7s$ ground state, and has a very long lived $6d_{3/2}$ state, which is highly beneficial for PNC measurements [92].

^{227}Ac and the odd-nucleon isotope ^{229}Th (with a half-life of 7340 yr) will also be of interest for measurements of nuclear-spin-dependent PNC in optical or hyperfine transitions, including the extraction of the nuclear anapole moment and the strength of the PNC nuclear forces, as discussed in Sec. 2.4.1. I investigate the applicability of these ions (as well as Cs and Fr) to this scenario in Sec. 3.3.

Table 3.1 Comparison of calculated energy levels and experimental values (Ref. [188]) for Cs, Ba^+, Fr and Ra^+. (cm^{-1})

	Cs			Ba^+			Fr			Ra^+	
Level	Calc.	Exp.		Calc.	Exp.		Calc.	Exp.		Calc.	Exp.
$6s_{1/2}$	0	0	$6s_{1/2}$	0	0	$7s_{1/2}$	0	0	$7s_{1/2}$	0	0
$6p_{1/2}$	11168	11178	$5d_{3/2}$	4280	4874	$7p_{1/2}$	12218	12237	$6d_{3/2}$	11741	12084
$6p_{3/2}$	11736	11732	$5d_{5/2}$	5128	5675	$7p_{3/2}$	13954	13924	$6d_{5/2}$	13471	13743
$5d_{3/2}$	14310	14499	$6p_{1/2}$	20234	20262	$6d_{3/2}$	16200	16230	$7p_{1/2}$	21291	21351
$5d_{5/2}$	14426	14597	$6p_{3/2}$	21960	21952	$6d_{5/2}$	16412	16430	$7p_{3/2}$	26259	26209
$7s_{1/2}$	18631	18536	$7s_{1/2}$	42647	42355	$8s_{1/2}$	19862	19740	$8s_{1/2}$	43757	43405
$7p_{1/2}$	21818	21765	$6d_{3/2}$	46234	45949	$8p_{1/2}$	23190	23113	$7d_{3/2}$	49082	48744
$7p_{3/2}$	22000	21946	$6d_{5/2}$	46438	46155	$8p_{3/2}$	23737	23658	$5f_{5/2}$	49254	48988
$6d_{3/2}$	22611	22589	$4f_{5/2}$	47829	48259	$7d_{3/2}$	24311	24244	$7d_{5/2}$	49485	49240
$6d_{5/2}$	22656	22632	$4f_{7/2}$	48219	48483	$7d_{5/2}$	24402	24333	$5f_{7/2}$	49569	49272
$8s_{1/2}$	24391	24317	$7p_{1/2}$	49595	49390	$9s_{1/2}$	25773	25671	$8p_{1/2}$	50864	50606
$4f_{7/2}$	24528	24472	$7p_{3/2}$	50213	50011	$5f_{7/2}$	25970	—	$8p_{3/2}$	52635	52392
$4f_{5/2}$	24528	24472	$8s_{1/2}$	58258	58025	$5f_{5/2}$	25971	—	$9s_{1/2}$	59448	59165
Lim.:[a]	31458	31406		80838	80686		32925	32849		82035	81842

[a] Single-electron (valence) ionisation energy of the ground state

3.2.2 Atomic-structure calculations and accuracy

To perform the calculations I use the all-order *correlation potential in the screened Coulomb interaction* (CPSCI) method, as described in section A.4.2. To calculate the PNC amplitudes I use the so-called mixed-states method, outlined in Appendix A.8, including double core polarisation.

Table 3.1 compares my calculated energy levels for Cs, Ba^+, Fr and Ra^+ with experimental values. My calculations are accurate to around 0.1–0.5% for most levels, which is typical for this type of calculation. Table 3.2 presents my calculated energy levels for the Fr-like actinide ions, and Table 3.3 shows the percentage difference between my calculations and experimental values for the most important energy intervals for PNC in Fr, Ra^+, Ac^{2+} and Th^{3+}. These intervals are important since they show up in the expression for the PNC amplitude [see Eq. (2.7) on page 7], and are quite sensitive to correlation effects due to the inherent cancellation. (Note, though, that by employing the mixed-states approach, I do not include these intervals directly in the calculations; see Appendix A.8.)

In order to get a handle on the accuracy of the atomic calculations, as well as the all-order method, I also perform the calculations using the second-order correlation potential (where the correlation effects are only included to second-order in perturbation theory). I also employ a simple scaling mechanism, where the correlation potential is scaled to reproduce the exact experimental energies of the lowest-lying valence states, i.e. $\Sigma \to \lambda\Sigma$ in Eq. (A.19) of Appendix A.4.2, where λ are constants of order 1 (a different λ is used for each orbital angular momentum value). This procedure is a rough way of accounting for missed correlation effects, and gives a good estimate for the size of missing correlation diagrams. As an example, in Table 3.4, I present the calculated binding energies for Cs in the second-order ($\Sigma^{(2)}$) and all-order ($\Sigma^{(\infty)}$) approximations, both with

Table 3.2 Calculated energy levels (cm^{-1}) including all-order correlations for the Fr-like actinide ions and comparison with available experimental data [189].

	Ac^{2+}			Th^{3+}			Pa^{4+}		U^{5+}			Np^{6+}
Level	Calc.	Exp.		Calc.	Exp.		Calc.		Calc.	Exp.		Calc.
$7s_{1/2}$	0	0	$5f_{5/2}$	0	0	$5f_{5/2}$	0	$5f_{5/2}$	0	0	$5f_{5/2}$	0
$6d_{3/2}$	435	801	$5f_{7/2}$	4393	4325	$5f_{7/2}$	6061	$5f_{7/2}$	7784	7609	$5f_{7/2}$	9470
$6d_{5/2}$	3926	4204	$6d_{3/2}$	8681	9193	$6d_{3/2}$	48302	$6d_{3/2}$	90713	91000	$6d_{3/2}$	139415
$5f_{5/2}$	23467	23455	$6d_{5/2}$	14084	14486	$6d_{5/2}$	55753	$6d_{5/2}$	100369	100511	$6d_{5/2}$	151486
$5f_{7/2}$	26112	26080	$7s_{1/2}$	22948	23131	$7s_{1/2}$	79208	$7s_{1/2}$	141157	141448	$7s_{1/2}$	211402
$7p_{1/2}$	29375	29466	$7p_{1/2}$	59957	60239	$7p_{1/2}$	123396	$7p_{1/2}$	193744	193340	$7p_{1/2}$	273437
$7p_{3/2}$	38136	38063	$7p_{3/2}$	72995	73056	$7p_{3/2}$	141201	$7p_{3/2}$	216937	215886	$7p_{3/2}$	301680
$8s_{1/2}$	69660		$8s_{1/2}$	120357	119622	$7d_{3/2}$	201271	$6f_{5/2}$	283289		$6f_{5/2}$	365542
$7d_{3/2}$	73543		$7d_{3/2}$	120907	119685	$7d_{5/2}$	203789	$6f_{7/2}$	284244		$6f_{7/2}$	366832
$7d_{5/2}$	74579		$7d_{5/2}$	122622	121427	$6f_{5/2}$	203997	$7d_{3/2}$	288691		$7d_{3/2}$	382067
$8p_{1/2}$	80612		$8p_{1/2}$	135196	134517	$6f_{7/2}$	204665	$7d_{5/2}$	292124		$7d_{5/2}$	386532
$6f_{5/2}$	83166		$8p_{3/2}$	140536	139871	$8s_{1/2}$	205653	$8s_{1/2}$	299566		$8s_{1/2}$	400640
$6f_{7/2}$	83513		$9s_{1/2}$	161461	160728	$8p_{1/2}$	224369	$8p_{1/2}$	322245		$8p_{1/2}$	428393
Lim.:	141221	140590[a]		232015	231065[a]		363394		509109	500000[a]		667359

[a] Theoretical values: 140590(160), 231065(200), 500000(13000) [188]

Table 3.3 Percentage difference between calculations and experiment [188, 189] for the important energy intervals.

Energy Interval	Fr	Ra^{+}	Ac^{2+}	Th^{3+}
$7s_{1/2} - 7p_{1/2}$	−0.2%	−0.3%	−0.3%	−0.3%
$7s_{1/2} - 8p_{1/2}$	0.3%	0.5%	—	0.8%

Table 3.4 Calculated binding energies (cm^{-1}) for Cs in various approximations and comparison with experiment (Ref. [188]). Blank means calculated value matches exactly with experiment by construction.

Level	$\Sigma^{(2)}$	$\lambda\Sigma^{(2)}$	$\Sigma^{(\infty)}$	$\lambda\Sigma^{(\infty)}$	Exp.
$6s_{1/2}$	−32416		−31457		−31406
$6p_{1/2}$	−20539		−20290		−20228
$6p_{3/2}$	−19940		−19722		−19674
$5d_{3/2}$	−17567		−17146		−16907
$5d_{5/2}$	−17407		−17030		−16810
$7s_{1/2}$	−13024	−12832	−12827	−12817	−12871
$7p_{1/2}$	−9710	−9628	−9640	−9624	−9641
$7p_{3/2}$	−9521	−9448	−9458	−9445	−9460
$8p_{1/2}$	−5724	−5689	−5694	−5687	−5698
$8p_{3/2}$	−5639	−5607	−5611	−5606	−5615

Table 3.5 Calculated binding energies (cm^{-1}) including ladder diagrams for La^{2+} and comparison with experiment.

Level	$\Sigma^{(\infty)}$	δ Ladder[a]	Total	Exp. [188]	% Diff.
$6s_{1/2}$	−141301	204	−141097	−141084	0.01%
$6p_{1/2}$	−112930	189	−112741	−112660	0.07%
$6p_{3/2}$	−109780	174	−109606	−109564	0.04%
$5d_{3/2}$	−155565	1005	−154561	−154675	−0.07%
$5d_{5/2}$	−153902	1025	−152877	−153072	−0.13%

[a] Calculations of the ladder diagrams provided by V. Dzuba [191].

and without scaling.

Note that the accuracy can be further improved by including the contributions of the so-called *ladder diagrams* [190]. This is illustrated this using La^{2+} as an example. Table 3.5 presents calculations of La^{2+} ionisation energies including ladder diagrams. The experimental energies are reproduced to an extraordinary accuracy, even for the notoriously difficult d levels. A full inclusion of the ladder diagrams for all ions is beyond the scope of this thesis; currently, the method I employ only allows inclusion of ladder diagrams perturbatively in the energy levels, but not PNC. Here, it is demonstrate that by including the ladder diagrams the accuracy is significantly improved, and that the accuracy in all of these ions is very good.

I also calculate several reduced $E1$ matrix elements that are of interest to PNC transitions, which are presented in Table 3.6. When matrix elements are calculated with the intention of determining the PNC amplitude by insertion into Eq. (2.7) (i.e. the “direct summation” method, see Sec. A.8), the time-dependent Hartree-Fock (TDHF) equations [Eqs. (A.39) – (A.41) in Sec. A.6.1] should be solved at the frequency of the PNC transition, *not* at the frequency of the individual $E1$ transitions. Therefore, the values in Table 3.6 should not be compared with experiment, rather they are presented so future PNC calculations can be easily compared with ours. In Table 3.7, I present calculations of several of the reduced matrix elements of the considered Fr-like actinide ions for which

Table 3.6 Calculated $E1$ reduced matrix elements (au) of transitions of interest to s-d PNC calculations. Here, the TDHF equations were solved at the energy of the relevant PNC transition, and should not be compared with experiment (see discussion in text).

Transition	Ra^{+}	Ac^{2+}	Th^{3+}
$7s_{1/2}-7p_{3/2}$	4.485	3.775	3.326
$7s_{1/2}-8p_{3/2}$	0.3729	0.1755	0.0770
$6d_{3/2}-7p_{1/2}$	3.533	2.569	2.100
$6d_{3/2}-8p_{1/2}$	0.0440	0.2047	0.2275

the TDHF equations were solved at the energy of each $E1$ or $E2$ transition, and can be compared with experiment. I employ that the notation that the tilde over an operator implies that it has been modified to include core polarisation, e.g., $\tilde{d}_{E1} = d_{E1} + \delta V_{E1}$; see Appendix A.6.1. To demonstrate the accuracy of the matrix elements, Table 3.8 presents my calculations of the reduced matrix elements for several $E1$ transitions in Cs using varying approximations, and comparison with experiment. The transitions involving the s and lowest $p_{1/2,3/2}$ states are reproduced exceptionally well, all to better than 0.5%. Also, for these transitions, the rescaling procedure ($\Sigma \to \lambda\Sigma$, discussed above) makes no practical difference. For the transitions involving higher p and d states the accuracy is lower, but still reasonable, and the scaling procedure has a larger (but still quite small) impact.

3.2.3 Parity-violating amplitudes

In Fr, the $7s$ state is the ground state. However, in charged ions this is not necessarily the case. For the ions after Ac the $5f$ state is pushed below $7s$, forming a new ground state (see Table 3.2). Also, after Ac the $6d_{3/2}$ state is pushed below the $7s$ state. The ions after Np^{6+} no longer have closed p-shells and are not considered in this thesis. A similar crossing of configurations also occurs in the Cs isoelectronic sequence; Cs and Ba^{+} have $6s$ ground-states, La^{2+} has $5d_{3/2}$, and Ce^{3+} and Pr^{4+} have $4f$ ground-states (see Tables 3.1 and 3.5).

For a $7s$–$6d_{3/2}$ interval to be a viable transition for the measurement of PNC, one of these states ($7s$ or $6d_{3/2}$) should be either the ground state or a metastable state that can first be populated and then the PNC transition observed. Also, it was shown it the pivotal work of N Fortson [92] that to ensure accurate PNC measurements of a single trapped ion both the upper and lower levels of the transition should be long lived. In Table 3.9 I present calculations of the lifetimes of the relevant levels for Ba^{+}, La^{2+}, Ra^{+}, Ac^{2+} and Th^{3+}. I show that this condition is met in all of these ions except for Th^{3+}, which has a long-lived upper level but a lower level that quickly decays via $E1$ transitions.

Note in particular the very long-lived upper ($6d_{3/2}$) state of Ac^{2+}. This state is practically stable, the $E2$ transition back to the $7s$ ground state (the only lower state—see Table 3.2) is highly suppressed due to the very small energy interval of this state, 801 cm^{-1}. This is very beneficial for the measurement of PNC in single-trapped ions [92].

Final Results The final calculations of the s-d and (near) optical s-s PNC amplitudes for the Fr-like ions are presented in Table 3.10, along with some

Table 3.7 Calculations of reduced $E1$ and $E2$ matrix elements for the Fr-like actinide ions, including all-order correlation corrections and core polarisation. Note that the reduced matrix elements observe the symmetry property $\langle a||\hat{d}||b\rangle = (-1)^{J_a - J_b}\langle b||\hat{d}||a\rangle$. The absence of a value means the TDHF equations did not converge to the desired accuracy. THDF equations solved at energy of each transition, i.e. $\omega = E_f - E_i$ in Eq. (A.40), so these values can be compared with experiment.

i	f	Fr	Ra$^+$	Ac^{2+}	Th^{3+}	Pa^{4+}	U^{5+}	Np^{6+}
$E1$		$\langle\psi_f\|\|\tilde{d}_{E1}\|\|\psi_i\rangle$ (a.u.)						
$7s_{1/2}$	$7p_{1/2}$	4.287	3.228	2.707	2.377	2.147	1.969	1.830
	$7p_{3/2}$	5.906	4.482	3.771	3.316	2.995	2.745	2.546
	$8p_{1/2}$	0.287	−0.071	−0.196	−0.261	−0.306	−0.342	−0.370
	$8p_{3/2}$	0.890	0.360	0.148	0.026	−0.060	−0.131	—
$8s_{1/2}$	$7p_{1/2}$	−4.195	−2.497	−1.887	−1.554	−1.340	−1.188	−1.101
	$7p_{3/2}$	−7.425	−4.621	−3.563	−2.974	−2.595	−2.329	−2.162
	$8p_{1/2}$	10.150	7.006	5.599	4.758	4.186	3.762	3.426
	$8p_{3/2}$	13.442	9.386	7.547	6.437	5.676	5.107	4.643
$6d_{3/2}$	$7p_{1/2}$	7.174	3.533	2.571	2.096	1.803	1.587	1.433
	$7p_{3/2}$	−3.301	−1.496	−1.050	−0.837	−0.708	−0.614	−0.549
	$8p_{1/2}$	−2.489	0.041	0.189	0.185	0.13	—	—
	$8p_{3/2}$	0.764	−0.137	−0.156	−0.138	—	—	—
$6d_{5/2}$	$5f_{7/2}$	−9.117	−5.666	−2.819	−1.930	−1.498	−1.217	−0.996
	$7p_{3/2}$	10.156	4.795	3.417	2.749	2.344	2.044	1.835
	$8p_{3/2}$	−2.499	0.379	0.487	0.453	0.366	—	—
$5f_{5/2}$	$6d_{3/2}$	7.318	4.441	2.173	1.510	1.184	0.968	0.795
	$6d_{5/2}$	−2.037	−1.257	−0.604	−0.417	−0.327	−0.271	−0.229
$E2$		$\langle\psi_f\|\|\tilde{d}_{E2}\|\|\psi_i\rangle$ (a.u.)						
$7s_{1/2}$	$6d_{3/2}$	−33.367	−14.676	−9.529	−7.065	−5.612	−4.591	—
	$6d_{5/2}$	−41.568	−18.868	−12.373	−9.225	−7.359	−6.049	−3.9
$5f_{5/2}$	$7p_{1/2}$	69.761	33.569	6.711	3.086	1.97	1.35	—
	$7p_{3/2}$	−47.191	−20.289	−3.408	−1.438	—	—	—

Table 3.8 Calculations of reduced matrix elements (au) of electric dipole transitions of interest to PNC studies in Cs and comparison with experiment. The last column shows the percentage difference between final calculations (using the rescaled all-order correlation potential, $\lambda\Sigma^{(\infty)}$) and the experimental value.

	This work				Experiment		
Transition	$\Sigma^{(2)}$	$\lambda\Sigma^{(2)}$	$\Sigma^{(\infty)}$	$\lambda\Sigma^{(\infty)}$	Value	Ref.	% Diff.
$6s_{1/2} - 6p_{1/2}$	4.387	4.503	4.506	4.512	4.4890(65)	[192]	0.45
					4.5097(74)	[193]	0.04
$6s_{1/2} - 6p_{3/2}$	6.170	6.337	6.343	6.351	6.3238(73)	[192]	0.43
					6.3403(64)	[193]	0.17
$6s_{1/2} - 7p_{1/2}$	0.2995	0.2744	0.2645	0.2724	0.2757(20)	[194]	−1.2
					0.2825(20)	[194, 195]	−3.6
$6s_{1/2} - 7p_{3/2}$	0.6050	0.5686	0.5581	0.5659	0.580(10)	[194]	−1.7
					0.5856(50)	[194]	−3.4
$5d_{3/2} - 6p_{1/2}$	6.744	7.039	6.927	7.032	7.33(6)	[196]	−4.1
$5d_{3/2} - 6p_{3/2}$	3.037	3.173	3.121	3.170	3.28(3)	[196]	−3.0
$5d_{5/2} - 6p_{3/2}$	9.254	9.629	9.481	9.616	9.91(3)	[196]	−2.9

Table 3.9 Lifetimes (s) of upper and lower states of the *s*-*d* PNC transitions for main ions of interest. Here, n is the principal quantum number: $n = 6$ for Ba$^+$ and La^{2+}, $n = 7$ for Ra$^+$, Ac^{2+} and Th^{3+}.

Level	Ba$^+$	La^{2+}	Ra$^+$	Ac^{2+}	Th^{3+}
$(n-1)d_{3/2}$	84.5	∞	0.642	1.19×10^6	0.58
$ns_{1/2}$	∞[a]	0.347	∞	∞	1.12×10^{-6}

[a] Here, "∞" means ground state.

Table 3.10 Calculated $7s$–$6d_{3/2}$ and $7s$–$8s$ PNC amplitudes for the Fr-like actinide ions. Also shown are the ground-state levels, experimental wavelengths of the transitions (λ), and several existing PNC calculations for comparison.

Ion	ground -state		λ (nm)	$\lvert E_{PNC}\rvert$ ($i(-Q_W/N)\times10^{-11}$ au) This work	Others	
^{223}Fr	$7s_{1/2}$	*sd*	616	57.99	57.1(23)	[93]
		ss	507	15.38	15.56(17)[a]	[79]
					15.69(16)[b]	[197]
^{226}Ra$^+$	$7s_{1/2}$	*sd*	827	44.35	43.9(17)[c]	[93]
					46.4	[94]
					46.47[a]	[95]
		ss	230	10.89		
^{227}Ac^{2+}	$7s_{1/2}$	*sd*	12484	42.81		
^{232}Th^{3+}	$5f_{5/2}$	*sd*	717	43.59		
^{231}Pa^{4+}	$5f_{5/2}$	*sd*	324[d]	43.49		
^{238}U^{5+}	$5f_{5/2}$	*sd*	198	45.94		
^{237}Np^{6+}	$5f_{5/2}$	*sd*	139[d]	44.07		

[a] Breit interaction is removed for comparison. The final result of Ref. [79] is 15.41, and of Ref. [95] is 45.89

[b] Breit and QED corrections removed for comparison. The final result of [197] is 15.49

[c] Rescaled from ^{223}Ra

[d] Calculated ($\Sigma^{(\infty)}$) wavelength (no experimental data available)

previous calculations for comparison. The final amplitudes are calculated using the mixed-states method with the all-order correlation potential and core polarisation (including double core polarisation).

For comparison and completeness, these calculations were also performed for Cs, Ba$^+$, and the first few Cs-like lanthanide ions. These much lighter ions have correspondingly smaller PNC amplitudes. The results are presented in Table 3.11. I have not presented a result for the $6s$–$7s$ transition in Cs since this has been investigated by thoroughly in the recent work [11] (also see Sec. 2.3.1, and the review [3]).

The PNC amplitudes calculated in this thesis agree very well with previous determinations for Cs, Ba$^+$, Fr and Ra$^+$. For Ra$^+$ my result is within 1% of the result calculated in Ref. [93] using the same 'mixed states' method used here[1]. My Ra$^+$ value is also, however, 4–5% smaller than the amplitudes calculated in

---

[1] The information about isotope numbers is not presented Ref. [93]. It is most likely ^{223}Ra in the mixed states calculations and ^{226}Ra in the direct-summation calculations.

Table 3.11 Calculations of the PNC amplitudes for the Cs-like actinide ions and comparison with existing calculations.

Ion	ground -state		λ (nm)	$\lvert E_{PNC}\rvert$ $(i(-Q_W/N)\times 10^{-11}$ au) This work	Others	
^{133}Cs	$6s_{1/2}$	sd	690	3.703	3.62(14)	[93]
^{137}Ba$^+$	$6s_{1/2}$	sd	2051	2.197	2.17(9)	[93]
					2.46(2)	[198]
		ss	236	0.6582		
^{139}La^{2+}	$5d_{3/2}$	sd	736	2.135		
^{140}Ce^{3+}	$4f_{5/2}$	sd	721	2.076		
^{141}Pr^{4+}	$4f_{5/2}$	sd	156	2.102		

that same work as well as in Ref. [95], which used a different 'direct summation' approach. (See Appendix A.8 for an explanation of these two methods.) The difference is most likely due to the *double core polarisation* contribution, which I calculate to contribute -4.7% to this amplitude, and is not included in the direct-summation calculations. Double core polarisation is discussed in more depth in Ch. 4.

The s-d PNC transitions tend to have a single dominating term which contributes $\sim 90\%$ to the total amplitude [93]. In Th^{3+}, for example, the term with the $7s$–$7p_{1/2}$ energy interval (i.e. $7s$–$7p_{1/2}$ weak-mixing) contributes approximately 96% to the total amplitude. The energy interval for this term agrees with experiment to 0.3% (see Table 3.3). Based on comparison with experimental energies and previous calculations, I expect these amplitudes to be accurate to around 1%. This accuracy can be improved by including the Breit [58], neutron-skin [55] and QED [103] corrections, missed high-order correlations such as ladder diagrams [190] (see Table 3.5) and structural radiation [5, 199], and with the use of experimental p-d $E1$ amplitudes. With these corrections the theoretical accuracy can reasonably be expected to surpass that of Cs.

The experimental accuracy can be expected to be high due to stable nuclei and large PNC signals. Additionally, in the case of Ac^{2+} where both upper and lower levels are extremely long-lived, the experimental accuracy has the potential to be very high.

3.2.4 Experimental accessibility of the parity-violating amplitudes

In order to observe the $7s$–$6d_{3/2}$ PNC transitions in the actinide ions with the $5f_{5/2}$ ground states, the $7s$ state must first be populated. In these ions the $5d_{3/2}$ state lies below the $7s$ state, however it is unstable as it will decay very quickly via an $E1$ transition to the $5f_{5/2}$ ground state. Population of the $7s$ state can be achieved via optical excitation to the $7p_{1/2}$ or $7p_{3/2}$ levels by a series of $E1$ transitions (e.g. $5f$–$6d$–$7p$), a 2γ transition, or an $E2$ transition, then $7p_{1/2,3/2}$ will spontaneously decay to the $7s$ state via an $E1$ transition (see Fig. 3.1).

For this method to be viable, several criteria must be met. First, the $7s$ state must be metastable and have an appropriate lifetime. Second, the pumping transition frequencies (to populate $7s$) must be in the range of laser spectroscopy. Also, it is necessary that the de-excitation from the p to s-level is relatively

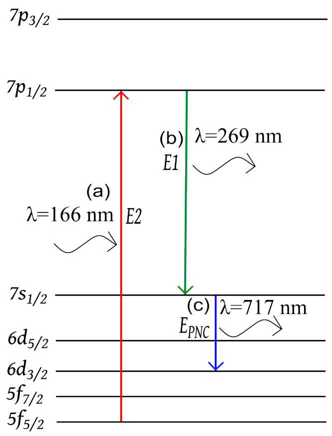

Figure 3.1 Level scheme for Th^{3+} showing one possible pathway to access the relevant PNC transition.

Table 3.12 Energies (ω), transition probabilities (Γ), and spontaneous-emission transition rates (A_r) for several $E1$ and $E2$ transitions for the Th^{3+} ion.

Transition		ω (a.u.)	Γ (a.u.)	A_r (s^{-1})
$5f_{5/2} - 6d_{3/2}$	$E1$	0.042	1.46×10^{-11}	6.07×10^{5}
$6d_{3/2} - 7p_{1/2}$	$E1$	0.233	7.21×10^{-9}	2.99×10^{8}
$5f_{5/2} - 7p_{1/2}$	$E2$	0.274	3.41×10^{-15}	142
$7p_{1/2} - 7s_{1/2}$	$E1$	0.169	7.07×10^{-9}	2.92×10^{8}
$7p_{1/2} - 6d_{3/2}$	$E1$	0.233	1.45×10^{-8}	5.97×10^{8}
$5f_{5/2} - 7p_{3/2}$	$E2$	0.333	1.96×10^{-15}	81.4
$7p_{3/2} - 7s_{1/2}$	$E1$	0.227	1.66×10^{-8}	6.90×10^{8}
$7p_{3/2} - 6d_{3/2}$	$E1$	0.291	2.24×10^{-9}	9.28×10^{7}
$7p_{3/2} - 6d_{5/2}$	$E1$	0.267	1.87×10^{-8}	7.30×10^{8}
$7s_{1/2} - 6d_{3/2}$	$E2$	0.064	3.57×10^{-17}	1.48
$7s_{1/2} - 6d_{5/2}$	$E2$	0.039	5.57×10^{-18}	0.23

probable compared to transitions to other levels. If this last condition is not met it is possible to enforce it using stimulated emission, which should not be a problem since these transitions are optical. All of these criteria should be easily possible in Th^{3+} and La^{2+}.

Table 3.12 shows the probabilities and per-second transition rates for these transitions in Th^{3+}. My calculations are in very good agreement with existing calculations of Safronova *et al.* [200, 201]. The $7s$ state should be relatively stable, since there are no allowed $E1$ transitions to lower states. The only significant contributions to its decay are from $E2$ transitions to the $6d_{3/2}$ and $6d_{5/2}$ states. I calculate a long lifetime of 0.58 s, in excellent agreement with the recent calculation of M. S. and U. I. Safronova of 0.570(8) s [201].

3.3 Spin-dependent parity violation in s-d transitions

3.3.1 Anapole measurement with a clean extraction?

In the preceding section, I investigated the possibility of using the combination of the high nuclear charge and simple electron structure that is available in alkali-like ions to achieve a highly accurate extraction of the nuclear weak charge (Q_W) that could complement, and potentially rival, that derived from Cs. In this section, however, I focus on another area; the measurement the P-odd T-even nuclear moment that arises due to parity violation in the nucleus, the so-called nuclear anapole moment (AM) [13, 14]. As discussed in Sec. 2.4.1, the experiment [4] of Wieman *et al.* provides the only measurement of a nuclear AM to-date. Any new measurements of an AM would prove to be an invaluable tool in the study of parity violation in the hadron sector, particularly if the measurement is from a system where the AM is caused by an unpaired neutron (the AM of ^{133}Cs is due to an unpaired proton).

There is interest in measuring PNC in the $6s$–$5d_{5/2}$ transition in Cs [203], and the possibility of measuring PNC in this transition in Ba$^+$ and in the $7s$–$6d_{5/2}$ transition of Ra$^+$ has been discussed [204, 205]. In this section, I perform calculations of this and similar amplitudes for several isotopes of Rb, Cs, Ba$^+$, Yb$^+$, Fr, Ra$^+$, and Ac^{2+} with the hope of motivating experiment in this important area. The s–$d_{5/2}$ transitions have practically no contribution from the nuclear weak charge, and thus provide good systems for the clean extraction of the AM. In Cs, for example, the AM induced contribution to the $6s$–$7s$ transition was only a small percentage of the NSI (Q_W-induced) contribution. PNC in s-d transitions of moderately charged ions could potentially be measured using techniques first put forward by N. Fortson in Ref. [92].

I present order-of-magnitude calculations of NSD PNC amplitudes for the s–$d_{5/2}$ transitions of several heavy atoms and ions. These amplitudes, given by the formula

$$E_{\rm PNC} = \frac{\langle d_{5/2}|\boldsymbol{d}_{E1}|np_{3/2}\rangle\langle np_{3/2}|\hat{h}_{\rm NSD}|s\rangle}{E_s - E_{np_{3/2}}} + \frac{\langle d_{5/2}|\hat{h}_{\rm NSD}|np_{3/2}\rangle\langle np_{3/2}|\boldsymbol{d}_{E1}|s\rangle}{E_{d_{5/2}} - E_{np_{3/2}}}, \tag{3.1}$$

[the $h_{\rm NSD}$ operator is defined in Eq. (2.5)] are different from the other amplitudes since they only contain intermediate $p_{3/2}$ states. Also presented are NSD PNC amplitudes of the s–$d_{3/2}$ transitions of the same ions (where not presented previously) that are accurate to the $\sim 10\%$ level.

3.3.2 Calculations and accuracy

In this section, I do not take into account the effect of core polarisation due to simultaneous action of the weak and $E1$ fields. This 'double-core-polarisation' (DCP) effect is explored in more detail in Ch. 4. Accurate calculations would require the use of the mixed-states method to calculate the PNC amplitude (see Appendix A.8), a more numerically stable method based on solving differential equations, which includes the DCP contribution. However, since high accuracy is not needed for the NSD PNC, I use simpler approach which is based on a direct summation over states. Where they exist, I present NSI-PNC amplitudes alongside the NSD amplitudes. The NSI amplitudes, calculated in the previous chapter, do include the DCP effect.

Table 3.13 Percentage variation between the experimental energy intervals (from Ref. [188]) of relevance to PNC in Cs and calculations in various approximations. Blank means calculated value matches exactly with experiment by construction.

Interval	$\Sigma^{(2)}$	$\lambda\Sigma^{(2)}$	$\Sigma^{(\infty)}$	$\lambda\Sigma^{(\infty)}$
$6s_{1/2}-6p_{1/2}$	6.35		−0.10	
$6s_{1/2}-6p_{3/2}$	6.31		0.02	
$6s_{1/2}-7p_{1/2}$	4.08	−0.02	0.24	0.08
$6s_{1/2}-7p_{3/2}$	4.08	−0.01	0.24	0.07
$5d_{3/2}-6p_{1/2}$	−5.17		−5.35	
$5d_{3/2}-6p_{3/2}$	−7.32		−6.92	
$5d_{3/2}-7p_{1/2}$	4.83	−0.05	3.30	0.24
$5d_{3/2}-7p_{3/2}$	4.81	−0.04	3.24	0.20
$5d_{5/2}-6p_{3/2}$	−5.54		−6.02	
$5d_{5/2}-7p_{3/2}$	4.28	−0.04	3.02	0.20

To use the direct-summation method, the so-called B-spline technique [206] is employed to construct the set of single-electron orbitals used for the summation in Eq. (2.7), as well as for the calculation of the correlation potential, $\hat{\Sigma}$. The states used in the calculation of $\hat{\Sigma}$ are linear combinations of the B-splines which are eigenstates of the HF Hamiltonian (A.12), whereas those used for the evaluation of Eq. (2.7) are the Brueckner orbitals [eigenstates of the $\hat{H}_0+\hat{\Sigma}$ Hamiltonian; defined in Eq. (A.19)]. For the summation, 90 B-splines of order 9 are used for each partial wave in a cavity of radius 75 au.

Without any rescaling of the correlation potential (see Sec. 3.2.2) my energies agree with experiment to around 0.1%-0.5% for most levels, and the important *s*-*p* intervals are reproduced to about 0.3%. In Table 3.4 (page 24) I presented calculated energy levels for Cs using the second-order ($\Sigma^{(2)}$) and the all-order ($\Sigma^{(\infty)}$) CPSCI method, both with and without scaling. Table 3.13 presents the percentage discrepancies for the relevant energy intervals in Cs. This shows the small effect that scaling has directly on the energies, but the relatively large improvements it makes on the intervals. The rescaling of the correlation potential helps to numerically stabilize the results. The rescaling means there is no significant loss in the accuracy for the energy-levels when using $\Sigma^{(2)}$ instead of $\Sigma^{(\infty)}$. This is important for the case of Yb$^+$, where only the second-order correlation potential was used. Only the second-order method is used for the Yb$^+$, since the presence of a (full) $4f$ shell that sits very close to the valence $6s$ electron means that other missed effects (such as the ladder diagrams) are comparable in size to the higher-order correlations.

In Table 3.8 (page 26), I compared calculations of several of the relevant $E1$ reduced matrix elements for Cs with their corresponding experimental values. My calculations demonstrate very good agreement with experiment, to better than 0.5% for the lowest *s*-*p* transitions, and better than 5% for the transitions involving *d* and higher *p* states. Again, I present calculations using the second-order ($\Sigma^{(2)}$) and the all-order ($\Sigma^{(\infty)}$) CPSCI method, both with and without scaling. Importantly, this demonstrates that by including the rescaling of the correlation potential one can correct for the discrepancies that arise from using only the second-order correlation potential; effectively meaning that the rescaled

Table 3.14 Calculated reduced matrix elements (au) for $E1$ transitions of interest in Ba$^+$ and Yb$^+$ and comparison with experiment (where available).

	Ba$^+$			Yb$^+$		
Transition	Calc.	Exp.		Calc.	Exp.	
$6s_{1/2} - 6p_{1/2}$	3.322	3.36(4)	[207]	2.705	2.471(3)	[208, 209]
$6s_{1/2} - 6p_{3/2}$	4.690	4.55(10)	[207]	3.817	3.36(2)	[210]
$5d_{3/2} - 6p_{1/2}$	3.063	3.03(9)	[211]	3.094	2.97(4)	[208, 209]
		3.14(8)	[212]			
		2.90(9)	[207]			
$5d_{3/2} - 6p_{3/2}$	1.338	1.36(4)	[211]	1.366		
		1.54(19)	[207]			
$5d_{5/2} - 6p_{3/2}$	4.127	4.15(20)	[211]	4.271		

second order correlation potential method is just as good in practice as using the all-order method.

I present $E1$ reduced matrix elements for Ba$^+$ and Yb$^+$ in Table 3.14, along with experimental values for comparison where available. This demonstrates very good agreement between my calculations and experiment for Ba$^+$, and reasonably good agreement for Yb$^+$. The discrepancies for the Yb$^+$ values, on the order of 5% − 10%, are due mainly to the more complicated electron structure due to the closeness of the $4f^{14}$ core shell to the valence $6s$ state. The most important $E1$ transition for the $6s$–$5d_{3/2}$ PNC amplitude in Yb$^+$ is the $p_{1/2}$–$d_{3/2}$ transition. This transition corresponds to the weak s–$p_{1/2}$ mixing, which dominates the amplitude. This $p_{1/2}$–$d_{3/2}$ $E1$ matrix element agrees with experiment to about 4%. However, for the $6s$–$5d_{5/2}$ PNC amplitude considered here, the most important $E1$ amplitudes are the s–$p_{3/2}$ and $p_{3/2}$–$d_{5/2}$ transitions. The s–$p_{3/2}$ amplitude agrees to only 13% with experiment, and an experimental value for the $p_{3/2}$–$d_{5/2}$ transition is, to the best of our knowledge, not known.

The accuracy of the weak charge and AM induced PNC interaction matrix elements relies on the accuracy of the wavefunctions at short distances (near the nucleus). One way to test the accuracy of the wavefunctions at this distance scale is to calculate magnetic dipole hyperfine structure constants, which also depend on the wavefunctions close to the nucleus. The hyperfine structure constants are typically reproduced very well for s and p states, but not so well for d states (see, e.g., Ref. [213]). The direct applicability of using hyperfine structure calculations as a test for p-d $h_{\rm PNC}$ matrix elements has not been fully investigated. The uncertainty in the calculations of the hyperfine structure constants is dominated by core polarisation, which is much larger for the hyperfine constants than for the weak matrix elements. The implication of this is that the accuracy of the s-p PNC interaction matrix elements can be high, and importantly can be controlled by computing hyperfine constants. For the p-d weak matrix elements, however, there is no guarantee of high accuracy, and it is not clear how the accuracy can be reliably judged. In Table 3.15 I present calculations of magnetic-dipole hyperfine structure constants A, for the $6s$ and $6p_{1/2}$ states of Cs, Ba$^+$ and Yb$^+$, along with experimental values for comparison.

The $h_{\rm PNC}$ interaction, to lowest order, is effectively a contact interaction

Table 3.15 Calculated magnetic dipole hyperfine constants A (MHz) for the lowest valence states of Cs, Ba^+ and Yb^+, and a comparison with experiment.

	^{133}Cs			^{135}Ba$^+$			^{171}Yb$^+$		
Level	Calc.	Exp.		Calc.	Exp.		Calc.	Exp.	
$s_{1/2}$	2315	2298.2	[214]	3674	3593.3(22)	[215]	13202	12645(2)	[216]
$p_{1/2}$	290	291.89(8)	[217]	668	664.6(3)	[218]	2515	2104.9(13)	[216]

and as such only significantly mixes s and $p_{1/2}$ states. Due to core polarisation, however, mixing between s and $p_{3/2}$ states, as well as between $p_{3/2}$ and $d_{3/2,5/2}$ states, is not so small. For s-s PNC amplitudes there is nothing to worry about, since these contain only terms involving s–$p_{1/2}$ mixing. The s–$d_{3/2}$ amplitudes contain also terms involving p-d mixing, however the s–$p_{1/2}$ mixing is many times larger, meaning that these amplitudes are dominated by the s–$p_{1/2}$ mixing terms, which contribute between 70% and 90% to the total amplitude.

As discussed in the previous section, the accuracy of the NSI amplitudes (s–$d_{3/2}$), should be about 1%. This is due to the very good agreement with energy levels, hyperfine structure constants, and matrix elements. The NSD parts of the s–$d_{3/2}$ amplitudes are likely to be somewhat less accurate, due mainly to core-polarisation effects and the larger number of contributing states (since the spin-dependent PNC interaction can mix states with $\Delta J = 1$). Because of this, without the DCP contribution, the accuracy for these amplitudes is likely to be between 5% and 10%.

For the s–$d_{5/2}$ amplitudes, there are no s–$p_{1/2}$ mixing terms, instead there are terms involving s–$p_{3/2}$ and $p_{3/2}$–$d_{5/2}$ mixing. Due to core-polarisation, there is no significant difference between the extent of the PNC mixing between these two contributions, and the size of the respective matrix elements is roughly the same. For the part of these PNC amplitudes coming from the s–$p_{3/2}$ mixing, i.e. the second term in Eq. (3.1), the accuracy is likely to be very good. However, for the contribution from the $6p_{3/2}$–$5d_{5/2}$ $\hat{h}_{\rm NSD}$ matrix elements the accuracy will be significantly worse.

There is not enough information to reliably determine how accurate the $p_{3/2}$–$d_{5/2}$ $\hat{h}_{\rm NSD}$ matrix elements are, and as such the s–$d_{5/2}$ NSD-PNC amplitudes should be conservatively considered order-of-magnitude estimates. This low level of accuracy is sufficient for the purpose of the current work, which is to demonstrate the magnitude and relative sizes of these transitions in different elements. Note also that the very high accuracy that is required of the NSI-PNC calculations for the extraction of the nuclear weak charge is not required in the search for AMs.

In Table 3.16 I compare my calculations of the NSD-PNC amplitudes in Ba^+ and Ra^+ with several of those available in the literature. The agreement between results for the s–$d_{3/2}$ transitions is reasonable. For the s–$d_{5/2}$ transition, I agree with calculations of Ref. [204] but not of Ref. [205].

For atoms and ions similar to Yb^+, in which an external electron is close to the core and strongly interacts with its electrons, a different higher-order effect described by the so-called 'ladder diagrams' [190] becomes important. The inclusion of ladder diagrams also significantly improves the accuracy of calculations in ions, for which the valence electrons lie closer to the core, and improves the

Table 3.16 Reduced matrix elements $\langle J_b, F_b || d_{\rm NSD} || J_a, F_a \rangle$ [defined in Eq. (B.5)] of the spin-dependent PNC amplitudes of Ba$^+$ and Ra$^+$ and comparison with other works. Units: $10^{-13}\varkappa\,$au.

			$E_{\rm PNC}$		
	I	Transition	This work	Others	
^{135}Ba$^+$	1.5	$\langle 5d_{5/2}, 3 \| d_{\rm NSD} \| 6s, 2 \rangle$	0.85	0.82	[204]
				0.274	[205]
		$\langle 5d_{3/2}, 3 \| d_{\rm NSD} \| 6s, 2 \rangle$	17.15	19.44	[205]
^{223}Ra$^+$	1.5	$\langle 6d_{5/2}, 3 \| d_{\rm NSD} \| 7s, 2 \rangle$	11.4	12.7	[204]
				3.504	[205]
		$\langle 5d_{3/2}, 3 \| d_{\rm NSD} \| 6s, 2 \rangle$	210.9	234.690	[205]

accuracy of the d-states for atoms and ions, as discussed in the previous section. With the inclusion of ladder diagrams, as well as the double-core-polarisation effect, the accuracy for these calculations can potentially approach the level of several percent, though this would need further investigation. The accuracy could then be further improved by including the Breit [58] and QED [68, 103] corrections, as well as higher order non-Brueckner electron correlations, such as structure radiation, the weak correlation potential and renormalization of states (see e.g. Ref. [5, 8, 199, 219]).

3.3.3 Results and discussion

My calculations of the s–$d_{5/2}$ NSD-PNC amplitudes of several isotopes of Rb, Cs, Ba$^+$ and Yb$^+$ are presented in Table 3.17, and for Fr, Ra$^+$ and Ac^{2+} in Table 3.18. For ease of comparison I present both the reduced matrix elements [defined in Eq. (B.3) of appendix B.1], and the z-components. The s–$d_{5/2}$ are typically between one and two orders of magnitude smaller than the corresponding s–$d_{3/2}$ transitions, due primarily to the absence of s–$p_{1/2}$ weak mixing. The largest amplitudes presented are in Fr, consistent with its very large s-s and s–$d_{3/2}$ transitions. The amplitudes are large in fact for all the Fr-like ions, and are also large in Cs and Yb$^+$.

As well as the s–$d_{5/2}$ transitions, which have no NSI contribution, I have also performed calculations for several s–$d_{3/2}$ transitions for which both NSI and NSD contributions are non-zero. I express these amplitudes in the form

$$E_{\rm PNC} = P(1 + R), \tag{3.2}$$

where P is the NSI-PNC amplitude (including Q_W), and R is the ratio of the NSD to NSI parts. Here, both parts are calculated concurrently, using the same method and wavefunctions. This approach has the advantage that the relative sign difference between the NSI and NSD parts is fixed, ensuring no ambiguity in the sign of $\varkappa$. There is also typically a significant improvement in accuracy for the ratio over that for each of the amplitudes individually, due to the fact that the atomic calculations for both components are very similar and much of the theoretical uncertainty cancels in the ratio [213].

I present these amplitudes for Rb and Cs in Table 3.19, and for Fr and Ac^{2+} in Table 3.20. Not presented are amplitudes for Ba$^+$, Yb$^+$, or Ra$^+$, since these have been performed relatively recently in Ref. [213].

Table 3.17 NSD-PNC amplitudes of the $|5sF_a\rangle \to |4d_{5/2}F_b\rangle$ transition in Rb, and the $|6sF_a\rangle \to |5d_{5/2}F_b\rangle$ transitions in Cs, Ba$^+$ and Yb$^+$. Both the reduced matrix elements (RME) and the z components are shown. Units: $10^{-13}\varkappa$ au.

				$E_{\rm PNC}$						$E_{\rm PNC}$	
	I	F_a	F_b	RME	z-component		I	F_a	F_b	RME	z-component
^{85}Rb	2.5	2	1	0.224	0.0708	^{135}Ba$^+$	1.5	1	1	−0.311	−0.127
		2	2	0.409	0.149			1	2	−0.475	0.150
		2	3	0.448	−0.0977			2	1	−0.139	−0.0440
		3	2	0.219	0.0477			2	2	−0.475	−0.174
		3	3	0.501	0.164			2	3	−0.850	0.186
		3	4	0.733	−0.122	^{171}Yb$^+$	0.5	1	2	−11.3	3.57
^{87}Rb	1.5	1	1	0.273	0.112	^{173}Yb$^+$	2.5	2	1	−2.67	−0.845
		1	2	0.417	−0.132			2	2	−4.88	−1.78
		2	1	0.122	0.0386			2	3	−5.34	1.17
		2	2	0.417	0.152			3	2	−2.61	−0.569
		2	3	0.746	−0.163			3	3	−5.98	−1.96
^{133}Cs	3.5	3	2	3.40	0.743			3	4	−8.75	1.46
		3	3	5.03	1.65						
		3	4	4.89	−0.815						
		4	3	2.91	0.484						
		4	4	5.78	1.72						
		4	5	7.71	−1.04						

Table 3.18 NSD-PNC amplitudes of the $|7sF_a\rangle \to |6d_{5/2}F_b\rangle$ transitions in Fr, Ra$^+$ and Ac^{2+}. Units: $10^{-13}\varkappa$ au.

				$E_{\rm PNC}$						$E_{\rm PNC}$	
	I	F_a	F_b	RME	z-component		I	F_a	F_b	RME	z-component
^{211}Fr	4.5	4	3	24.3	4.05	^{223}Ra$^+$	1.5	1	1	4.16	1.70
		4	4	32.6	9.72			1	2	6.35	−2.01
		4	5	29.6	−3.99			2	1	1.86	0.588
		5	4	19.7	2.65			2	2	6.35	2.32
		5	5	36.3	10.0			2	3	11.4	−2.48
		5	6	45.8	−5.18	^{225}Ra$^+$	0.5	1	2	14.4	−4.55
^{221}Fr	2.5	2	1	13.2	4.17	^{229}Ra$^+$	2.5	2	1	3.41	1.08
		2	2	24.1	8.79			2	2	6.22	2.27
		2	3	26.4	−5.76			2	3	6.82	−1.49
		3	2	12.9	2.81			3	2	3.33	0.726
		3	3	29.5	9.65			3	3	7.62	2.49
		3	4	43.2	−7.20			3	4	11.2	−1.86
^{223}Fr	1.5	1	1	16.1	6.57	^{227}Ac^{2+}	1.5	1	1	4.59	1.88
		1	2	24.6	−7.77			1	2	7.02	−2.22
		2	1	7.20	2.28			2	1	2.05	0.650
		2	2	24.6	8.97			2	2	7.02	2.56
		2	3	44.0	−9.59			2	3	12.6	−2.74

Table 3.19 PNC amplitudes (z components) of the $|5sF_a\rangle \to |4d_{3/2}F_b\rangle$ transition in Rb, and the $|6sF_a\rangle \to |5d_{3/2}F_b\rangle$ transitions in Cs. Units: 10^{-11} au.

Q_W	I	F_a	F_b	$E_{\rm PNC}$	Q_W	I	F_a	F_b	$E_{\rm PNC}$
				^{87}Rb					^{133}Cs
-46.8	1.5	1	0	$-0.301\times[1+0.0805\varkappa]$	-73.2	3.5	3	2	$-2.05\times[1+0.0444\varkappa]$
		1	1	$-0.337\times[1+0.0796\varkappa]$			3	3	$-3.14\times[1+0.0431\varkappa]$
		1	2	$0.261\times[1+0.0779\varkappa]$			3	4	$1.35\times[1+0.0412\varkappa]$
		2	1	$-0.117\times[1-0.0439\varkappa]$			4	3	$-0.923\times[1-0.0305\varkappa]$
		2	2	$-0.301\times[1-0.0457\varkappa]$			4	4	$-2.86\times[1-0.0323\varkappa]$
		2	3	$0.301\times[1-0.0483\varkappa]$			4	5	$1.87\times[1-0.0345\varkappa]$

Table 3.20 PNC amplitudes of the $|7sF_a\rangle \to |6d_{3/2}F_b\rangle$ transitions in Fr and Ac^{2+}. Units: 10^{-11} au.

Q_W	I	F_a	F_b	$E_{\rm PNC}$	Q_W	I	F_a	F_b	$E_{\rm PNC}$
				^{223}Fr					^{227}Ac^{2+}
-128.3	1.5	1	0	$-38.4\times[1+0.0273\varkappa]$	-130.1	1.5	1	0	$-28.7\times[1+0.0250\varkappa]$
		1	1	$-43.0\times[1+0.0278\varkappa]$			1	1	$-32.0\times[1+0.0241\varkappa]$
		1	2	$33.3\times[1+0.0288\varkappa]$			1	2	$24.8\times[1+0.0223\varkappa]$
		2	1	$-14.9\times[1-0.0189\varkappa]$			2	1	$-11.1\times[1-0.0105\varkappa]$
		2	2	$-38.4\times[1-0.0179\varkappa]$			2	2	$-28.7\times[1-0.0123\varkappa]$
		2	3	$38.4\times[1-0.0164\varkappa]$			2	3	$28.7\times[1-0.0150\varkappa]$

Suitability for measurements A method has been proposed by Fortson for measuring PNC in a single atomic ion that has been laser trapped and cooled [92]. Originally proposed with measuring the $6s$–$5d_{3/2}$ transition of Ba$^+$ in mind, work has begun to use this method for the $7s$–$6d_{3/2}$ transition in Ra$^+$ at the KVI institute in the Netherlands [94, 97–100]. The use of this or a similar method to study spin-dependent PNC in s–$d_{5/2}$ transitions has been previously discussed [204, 205]. Though these transitions have significantly smaller PNC signals than the corresponding s–$d_{3/2}$ transitions, the main advantage here is that there is no NSI contribution. This is beneficial for the extraction of the nuclear AM since the (larger) NSI contribution would not need to be subtracted, and it would limit the possibility of spurious NSI-PNC acting as a false signal.

In [92] it was shown that to ensure accurate PNC measurements of a single trapped ion both the upper and lower levels of the transition should be long lived. The only significant contribution to the decay rate of the $5,6d_{5/2}$ states in Ba$^+$, Ra$^+$ are the $E2$ transitions to the s ground state. There are also $M1$ and $E2$ $d_{5/2}$–$d_{3/2}$ contributions, though these are highly suppressed. Both $E2$ transitions are suppressed in the case of Ac^{2+}, so I include both in the calculation. I calculate the lifetimes of the relevant $d_{5/2}$ states in Ba$^+$, Ra$^+$ and Ac^{2+} to be 35.9 s, 0.302 s, and 247 s respectively. These results are in good agreement with other recent calculations, e.g. [95, 220]. The upper states of the other elements presented here are unstable as they have allowed $E1$ transitions to lower levels. This is not a problem for neutral Cs or Fr where atomic-beam-type experiments could be used.

In the s–$d_{5/2}$ transitions considered here it is possible that the contribution to the amplitude coming from the combination of the weak charge and hyperfine interaction may not be as small as in other systems, due to the $d_{3/2}$–$d_{5/2}$ and $p_{1/2}$–$p_{3/2}$ hyperfine mixing. The ratio of the hyperfine to fine structure splitting goes as

$$\frac{Z\alpha^2 \frac{m_e}{m_p}}{Z^2\alpha^2} = \frac{1}{Z}\frac{m_e}{m_p} \sim 10^{-5}. \tag{3.3}$$

The PNC amplitude of the s–$d_{5/2}$ transitions due to the combined weak charge and hyperfine interaction would therefore be of the order

$$E_{\rm PNC}^{Q_W+{\rm hf}}(s\text{–}d_{5/2}) \sim 10^{-5}\, E_{\rm PNC}^{Q_W}(s\text{–}d_{3/2}). \tag{3.4}$$

For Cs, this leads to a $Q_W + \text{hf}$ contribution on the order of 10^{-16} au (including Q_W), whereas the AM contribution to this transition is $10^{-13}\varkappa$ au $\sim 10^{-14}$ au. Similarly for Ba$^+$, Fr, and Ra$^+$ the $Q_W + \text{hf}$ contribution is between one and two orders of magnitude smaller than the contribution from the AM. This is smaller than the assumed accuracy here, so this contribution can be safely neglected for now. An accurate calculation of this contribution is beyond the scope of this thesis.

3.4 Strongly enhanced atomic parity violation due to close levels of opposite parity

So far, the only observation of a nuclear AM comes from the ^{133}Cs measurement by the Wieman group [4]. The quest for new measurements is also partly motivated by the requirement to perform an independent test of the existing Cs result in other systems. This is a very important result and must be checked even if the accuracy is not improved. Moreover, the systems studied here have a very large enhancement in the PNC signal, which could make these systems even more favourable for observing the AM.

Additionally, some isotopes of each of these atoms are believed to exhibit a very large nuclear enhancement of parity and time-invariance violating effects [221] (see also [107, 222–224]). Protactinium is a particularly interesting case in this regard, with a possibility of very close nuclear levels of opposite parity, which may lead to a huge enhancement in the PNC effects. This is discussed in more detail in Section 3.4.6. Some isotopes of Fr, Ra and Ac also have close nuclear levels of opposite parity [222].

In this section, I present calculations of both NSD and NSI PNC effects that are enhanced by the presence of very close electronic levels of opposite parity. The AM-induced PNC transition in neutral Ra has been considered previously [119, 120]. The PNC amplitude between the even ground and $^3D_2$ states was found to be more than 10^3 times larger than the corresponding $6s$–$7s$ amplitude in Cs. I revisit these calculations in Section 3.4.2, improving the accuracy and verifying that the PNC signal is indeed greatly enhanced. In Sections 3.4.3 through 3.4.6 I then proceed to calculate PNC, due both to the AM and the nuclear weak charge, in Ba, Ac$^+$ (an analogue of Ra), Th, and Pa.

I believe the atoms and ions considered here are very promising candidates for experimental studies of parity violating nuclear effects. They may also be used to measure the ratio of weak charges in isotopic chain measurements.

There are several factors which contribute to the enhancement (or suppression) of the parity-violating signal in atomic transitions. The first, pointed out by the Bouchiats [24, 26], is that the PNC amplitude should scale a little faster than Z^3 (Z the atomic number). For this reason it is natural to expect larger amplitudes in heavy systems. Also, as is clear from Eq. (2.7) [page 7], the existence of close energy levels of opposite parity has the potential to produce a very large enhancement. It is with these motivations in mind that I pursue large PNC signals in the heavy elements chosen for this work. The transitions studied here have opposite parity levels with energy intervals of ~ 10 cm^{-1}. For comparison, the energy interval corresponding to the largest contributing term of the $6s$–$7s$ PNC transition in Cs is $\sim 10^4$ cm^{-1}.

Perhaps the most important and hardest to predict, the final factor is the size of the weak-interaction matrix element between the opposite-parity states. The most significant contribution to this comes from s–$p_{1/2}$ mixing [27]. Finding large atomic systems with close pairs of opposite parity levels is comparatively simple, however determining the extent of single-electron s–$p_{1/2}$ mixing generally requires complicated many-body calculations. In the heavy atoms studied here this tends to suppress the final amplitude; e.g., there is a 10^3 factor enhancement from the proximity of opposite parity states, but this does not necessarily transform directly to a 10^3 enhancement in the amplitude. As well as this, of course, is the fact that the NSI interaction cannot mix states of different total angular momentum, and the NSD interaction can only mix states with $\Delta J = 0, 1$ (and $J \neq 0 \to 0$).

Actually, the s–$p_{3/2}$ and $p_{3/2}$–$d_{3/2}$ weak mixing is not insignificant. This is mainly due to core polarisation, without which these contributions would be practically zero. This has the benefit of counteracting the suppression due to limited s–$p_{1/2}$ mixing, however it makes the calculations very sensitive to the usually smaller corrections such as correlations and core polarisation. This makes determining the accuracy particularly difficult, especially in cases for which the amplitudes are small. If there is only a small amount of s–$p_{1/2}$ mixing, then the amplitude becomes very sensitive to core polarisation, and is thus not particularly accurate, even if $E1$ amplitudes and energies are reproduced well. In all cases, the PNC matrix elements are sensitive to configuration mixing.

3.4.1 Calculations and accuracy

To perform the calculations, I make use of the combined configuration interaction and many-body perturbation theory (CI+MBPT) method [225], as described in Sec. A.7. For the considered atoms and ions with more than two valence electrons, sometimes a small deviation from the method here described was necessary. Where I have deviated from this method will be described in the text.

Interactions with external fields and core polarisation are taken into account using the time-dependent Hartree-Fock (TDHF) method, see Sec. A.6.1. Note, however, that I do not take into account the double core polarisation. This is because here I focus on the NSD amplitudes for which the accuracy of the analysis is less important (as discussed in Sec. 2.4.1).

I calculate the correlation potential $\hat{\Sigma}_1$ [see Eq. (A.48) in Sec. A.7] to both second-order and all-orders in perturbation theory. The difference between calculations using the second- and all-order methods gives a good indication of the uncertainty due to missed correlation effects.

Calculation of the PNC amplitude requires a summation of the complete set of states. I make use of a method based on the Dalgarno-Lewis technique [226] to perform the summation, as described in Sec. A.8 (without the double core polarisation). The presence of the small energy intervals leads to a complication that is resolved by making a minor modification to this method, which is discussed in the next section.

Calculating PNC with a small energy interval Radium, Ba, and Ac^{+} have two valence electrons above a closed-shell core. For these relatively simple systems the above method works quite well. I generate the wavefunctions and energies using a full CI calculation allowing double valence excitations, with core-valence correlations taken into account as described above. For Th and Pa, with more than two valence electrons, I use slight variations of the above method (discussed in later sections) and do not try to compute the entire sum. Due to the presence of the very close opposite parity levels, the transitions in question have a single dominating term, contributing upward of 95% to the total amplitude. For this reason it is a good first approximation to calculate this term alone. To do this I calculate the relevant matrix elements of the $E1$ and weak interactions including core polarisation, and use the experimental energy difference to compute the term.

For Ba, Ra and Ac^{+}, a determination of the whole amplitude is required. A problem that occurs though is that the existence of the close levels makes this method numerically unstable. Even if the energy levels are computed to very high accuracy, the relevant energy interval may be very wrong. For example, the experimental energy interval between the even $^3D_2$ and the odd $^3P_1$ levels in Ra is 5.41 cm^{-1}. My calculations for the energies of these states vary from experiment by just 5% and 1% respectively, however, I calculate this interval to be 828 cm^{-1}. This would lead to an error of several orders of magnitude. There are three methods one can use to remedy this.

The first and simplest method is to rescale the single-electron correlation potential, i.e. $\hat{\Sigma}_1 \to \lambda\hat{\Sigma}_1$ in Eq. (A.48). Different parameters are used for each of the orbital angular momentum states (s, p etc.), and are chosen to reproduce the relevant experimental energy interval exactly. For Ra, the ionisation energy of the the ground state was also made to match exactly with experiment in this way. It is worth noting that these scaling parameters are close to unity, indicating the already reasonable accuracy. For Ra the parameters chosen were $\lambda_s = 0.994$, $\lambda_p = 1.046$, and $\lambda_d = 0.893$. For Ac^{+} they were $\lambda_s = 0.957$, $\lambda_p = 1.016$ and $\lambda_d = 0.917$, and for Ba they were $\lambda_s = 1.010$, $\lambda_p = 0.897$, and $\lambda_d = 0.933$.

The second approach is not to perform any re-scaling of Σ, but to use orthogonality conditions in the summation to extract the dominating term, and rescale it by a factor $\Delta E^{\mathrm{Calc.}}/\Delta E^{\mathrm{Exp.}}$. To do this, the intermediate states in Eq. (A.53) temporarily forced to be orthogonal to the state causing the dominating term; then the amplitudes are computed using these ‘intentionally incomplete’ states. This is made more clear by considering a PNC transition $a \to b$, which is enhanced by the proximity of the state $|x\rangle$ to the state $|b\rangle$. The total PNC amplitude can then be expressed

$$E^{a\to b}_{\rm PNC} = \overbrace{\langle b|\widetilde{\boldsymbol{d}}_{E1}|\delta a\rangle + \langle\delta b'|\widetilde{\boldsymbol{d}}_{E1}|a\rangle}^{\text{non-dominating term}} + \overbrace{\frac{\langle b|\widetilde{h}_{\rm PNC}|x\rangle\langle x|\widetilde{\boldsymbol{d}}_{E1}|a\rangle}{E_b - E_x}}^{\text{`main' dominating term}}, \tag{3.5}$$

where the dashed states, $|\delta b'\rangle$, are the intentionally incomplete states—i.e. solutions to the mixed-states differential equation (A.53) with the condition enforced that they be orthogonal to the state causing the dominating contribution (in this example, $|x\rangle$). By comparing the results computed both with and without enforcing the orthogonality conditions, I can separate this 'main' term from the sum and proceed to re-scale it.

The third method is to separate the non-dominating term in the same way as above. This time, instead of re-scaling the dominant term, it is discarded and re-calculated "directly", by which I mean the $E1$ and PNC matrix elements are calculated separately, and combined with the experimental energy interval. This term is then added to the non-dominating tail to form the total PNC amplitude.

If good agreement exists between these three methods it is indicative of good numerical accuracy, and also of sufficient completeness in the basis. This is exactly what I find.

In Table 3.21 I present my calculated energy levels for Ba, Ra and Ac$^+$ along with experimental values for comparison. I present calculations using both the unscaled correlation potential (column Σ) as well as the calculations including the rescaled potential (column $\lambda\Sigma$). Here I have chosen the scaling parameters to reproduce the energies of the relevant close opposite parity levels, as opposed to with achieving good overall accuracy in mind. The unscaled energies for Ba and Ra are already very good, and in most cases this scaling improves the accuracy.

For Ac$^+$ the agreement with unscaled energies is not as good, however it should be noted that the intervals between levels are reproduced to a much better accuracy than the levels themselves, indicating most of the error is likely associated with determining the ground state energy. In this case the rescaling improves the accuracy for all levels.

Testing the method and accuracy Ytterbium, like Ba, Ra and Ac$^+$ has two valence electrons above a closed shell core. The parity violating $6s^2\,{}^1S_0 \to 6s5d\,{}^3D_1$ transition has contributions from both the NSI and NSD parts of the PNC Hamiltonian, and is enhanced by the proximity of the odd $6s6p\,{}^1P^o_1$ level to the upper ${}^3D_1$ level in the transition. The energy interval between these levels is just 579 cm^{-1}. Though not as small as the other intervals studied in this work, it still means this transition in Yb has a large dominating term, contributing more than 80% to the total amplitude. Several calculations exist in the literature for parity nonconservation in neutral Yb [40, 87, 88, 227–229]. Therefore studying PNC in this transition for Yb will serve as a useful test for the method.

Table 3.22 presents calculations of both the NSI and NSD parts of the PNC amplitude for this transition in Yb, and compares these values with those calculated in several other works, and demonstrates very good agreement. I present calculations using both methods described above; that is using a scaled correlation potential ($\lambda\Sigma$) that is chosen to reproduce exactly the energy interval of

Table 3.21 Comparison of calculated energy levels (cm^{-1}) with experiment (Ref. [188]) for Ba, Ra and Ac^{+}.

			Calc.						Calc.		
Atomic State			Σ	$\lambda\Sigma$	Exp.	Atomic State			Σ	$\lambda\Sigma$	Exp.
Ba	$6s^2$	$^1S_0$	0	0	0	Ra	$7s^2$	$^1S_0$	0	0	0
	$5d6s$	$^3D_1$	8180	8684	9034		$7s7p$	$^3P_0$	13285	13102	13078
		$^3D_2$	8368	8865	9216			$^3P_1$	14170	13999[a]	13999
		$^3D_3$	8765	9243	9597			$^3P_2$	16835	16694	16689
	$5d6s$	$^1D_2$	10772	11309	11395		$6d7s$	$^3D_1$	13079	13756	13716
	$6s6p$	$^3P_0$	12387	12677	12266			$^3D_2$	13342	13994[a]	13994
		$^3P_1$	12748	13031	12637			$^3D_3$	14067	14642	14707
		$^3P_2$	13617	13877	13515		$6d7s$	$^1D_2$	16742	17318	17081
	$6s6p$	$^1P_1$	17737	18080	18060		$7s7p$	$^1P_1$	20487	20432	20716
	$5d^2$	$^3F_2$	19669	20605	20934		$7s8s$	$^3S_1$	26691	26658	26754
		$^3F_3$	20007	20928	21250						
		$^3F_4$	20409	21314	21624	Ac$^+$	$7s^2$	$^1S_0$	0	0	0
	$5d6p$	$^3F_2$	21242	22015	22065		$6d7s$	$^3D_1$	3917	4355	4740
		$^3F_3$	22121	22866	22947			$^3D_2$	4406	4836	5267
		$^3F_4$	22955	23675	23757			$^3D_3$	6579	6911	7427
	$5d2$	$^1D_2$	22216	23062[a]	23062		$6d7s$	$^1D_2$	8403	8886	9088
	$5d6p$	$^1D_2$	22320	23074[a]	23074		$6d^2$	$^3F_2$	12023	12849	13236
	$5d^2$	$^3P_0$	22086	22949	23209			$^3F_3$	13762	14557	14949
		$^3P_1$	22340	23199	23480			$^3F_4$	15644	16281	16757
		$^3P_2$	22895	23727	23919		$6d^2$	$^3P_0$	16250	17039	17737
								$^3P_1$	17530	18290	19015
								$^3P_2$	21615	22199[a]	22199
							$6d^2$	$^1D_2$	18053	18773	19203
							$6d^2$	$^1G_4$	20692	20804	20848
							$7s7p$	$^3P_0$	21453	21048	20956
								$^3P_1$	22550	22181[a]	22181
								$^3P_2$	28612	28328	26447

[a] Levels match experiment exactly, by construction

Table 3.22 Calculations of the NSI (including Q_W) and NSD parts of the ${}^1S_0\,(F{=}1/2) \to {}^3D_1\,(F{=}1/2)$ PNC amplitude (z compnent, $F_z{=}0$) for ^{171}Yb ($I{=}1/2$) and comparison with other works. The signs have been omitted. Units: $10^{-11}\,iea_0$

	This work		Others	
	$\lambda\Sigma$[a]	Orthog.[b]	Value	Ref.
NSI-PNC	62.5	59.0	60	[88]
			61.8	[227]
			41.6	[228]
			61.5	[40]
NSD-PNC	$1.01\varkappa$	$0.965\varkappa$	$1.12\varkappa$	[87]
			$0.997\varkappa$	[229]
			$0.990\varkappa$	[40]

[a] Scaling correlation potential to reproduce the energy interval

[b] Using orthogonality conditions to subtract and re-scale the dominating term by factor $\Delta E^{\text{Calc.}}/\Delta E^{\text{Exp.}}$

Table 3.23 Comparison of calculated and experimental magnetic hyperfine structure constants, A (MHz), for low-lying states of ^{137}Ba.

	$6s5d\,{}^3D_1$	$6s5d\,{}^3D_2$	$6s6p\,{}^3P^o_1$
This work	-528	373	1216
Experiment	-521 [230]	416 [230]	1151 [231]

the dominating term, and also using the orthogonality conditions to extract the dominating contribution and then re-scaling it for the experimental interval.

In Table 3.23, I present the magnetic hyperfine structure constants, A, for the low-lying states of Ba along with experimental values for comparison. I include states dependent on the s and p single-electron wavefunctions, as these states dominate in the PNC interaction. The PNC matrix elements depend on the value of the wavefunction at short distances, as do the hyperfine structure constants. Thus, good accuracy is demonstrated for the important s and p wavefunctions near the nucleus.

To form an estimate of the uncertainty, I perform the calculations for Ra, Ba, and Ac$^+$ using both the all-order and second-order correlation potentials, as described above. The difference between these methods leads to about a 10% difference in the PNC amplitudes. Taking this into account, I conservatively expect the accuracy of the PNC calculations to be around 20% for Ra, Ba, and Ac$^+$. For Th and Pa, with a more complicated electron structure and less experimental data, it is harder to tell. Until a more detailed analysis can be performed these calculations should be considered order-of-magnitude estimates, which is more than sufficient for now. The accuracy of these CI+MBPT calculations can be improved as more experimental data becomes available.

3.4.2 Radium

Here, I study two relevant transitions for measuring PNC in Ra, the $7s^2\,{}^1S_0 \to 6d7s\,{}^3D_2$ transition, and the $7s^2\,{}^1S_0 \to 6d7s\,{}^3D_1$ transition. Both transitions are in the optical range ($\lambda \sim 700$ nm) and are enhanced by the proximity of the odd $7s7p\ ^3P_1$ level to the upper levels in the transitions.

There are several isotopes of Ra that have non-zero nuclear spin, required for measuring the AM. The nuclear spin of Ra is caused by a valence neutron, which makes these transitions especially interesting for the study of the neutron–nucleus parity violating potential [13, 14, 48]. The only measurement of an AM so far is for ^{133}Cs, which has only a valence proton [4].

In Table 3.24, I present calculations of reduced matrix elements of operators of interest for the $E1$, NSI-PNC and NSD-PNC interactions. My calculations of the $E1$ matrix elements, as well as the energy levels (in Table 3.21), agree well with previous calculations, e.g., Ref. [232, 233].

One can use the relevant values of the $E1$ and AM matrix elements to determine the amplitude of the dominating term of the PNC transition. Note that in Table 3.24 I present only the "electron-part" of the operators, without any additional factors. For example, the formula linking the matrix elements of $\gamma_5\rho$ to the NSI-PNC interaction is

$$\langle b||\hat{h}_{\rm NSI}||a\rangle = \frac{G_F}{2\sqrt{2}}(-Q_W)\langle b||\gamma_5\rho||a\rangle.$$

I present reduced matrix elements due to their lack of dependence on the projection of angular momentum; the NSD-PNC matrix elements also depend on nuclear spin. The reduced matrix elements obey the symmetry condition

$$\langle a||\hat{h}||b\rangle = (-1)^{J_b-J_a}\langle b||\hat{h}||a\rangle^*,$$

where the asterisk stands for complex conjugation and results in a change of sign for the PNC matrix elements but not for the $E1$ matrix elements. Also note that the actual matrix elements contain factors depending on the different angular momentum values, for example, the NSI-PNC matrix element contains the Wigner $3j$ symbol that has a term $1/\sqrt{2J+1}$, which makes these reduced matrix elements appear larger for large values of J. Full formulas are given in Appendix B.1.

The dominating contribution to the $^1S_0 - {}^3D_2$ transition is given by:

$$E_{\rm PNC}^{F_a\to F_b} \simeq k_{\rm NSD}\frac{\langle ^3D_2||\boldsymbol{\alpha}\rho||^3P_1^o\rangle\langle ^3P_1^o||-e\boldsymbol{r}||^1S_0\rangle}{E(^3D_2)-E(^3P_1^o)}, \tag{3.6}$$

where $k_{\rm NSD}$ is the coefficient (for the z component),

$$\begin{aligned} k_{\rm NSD} =& \frac{G_F}{\sqrt{2}}\varkappa\sqrt{(I+1)(2I+1)(2F_b+1)(2F_a+1)/I}\times(-1)^{F_b-F_z}\begin{pmatrix} F_b & 1 & F_a \\ -F_z & 0 & F_z\end{pmatrix} \\ &\times(-1)^{F_b-F_a}\begin{Bmatrix} J_n & J_b & 1 \\ I & I & F_b\end{Bmatrix}\begin{Bmatrix} J_n & J_a & 1 \\ F_a & F_b & I\end{Bmatrix} \end{aligned} \tag{3.7}$$

[see equations (B.3) and (B.5) in Appendix B.1]. Here $F_z = \min(F_a, F_b)$, and the index n refers to the intermediate state.

Due to the large dominating term in the transitions in Ra this gives a good first approximation, and was the method used in the earlier works [119, 120]. We, however, proceed to calculate the entire sum (with the mixed-states approach), using the rescaled correlation potential method to deal with the numerical sensitivity due to the close opposite parity levels, as discussed above.

Table 3.24 Reduced matrix elements $\langle a||\hat{H}||b\rangle$ (au) for the $E1$, NSI-PNC and NSD-PNC amplitudes between the lowest few states of Ra. No value means forbidden by selection rules.

Even state a	Odd state b	H_{ab}: $-er$[a]	H_{ab}: $\gamma_5\rho$[b]	H_{ab}: $\alpha\rho$[c]	Even state a	Odd state b	H_{ab}: $-er$	H_{ab}: $\gamma_5\rho$	H_{ab}: $\alpha\rho$
$7s^2$ $^1S_0$	$7s7p$ $^3P_0$		-22.8		$7s6d$ $^3D_2$	$7s7p$ $^3P_1$	4.38		-2.21
	$^3P_1$	1.22		46.4		$^3P_2$	2.60	-4.31	0.656
	$^1P_1$	-5.49		-12.3		$^1P_1$	0.797		6.44
$7s6d$ $^3D_1$	$7s7p$ $^3P_0$	2.99		3.36	$7s6d$ $^3D_3$	$7s7p$ $^3P_2$	-6.35		8.11
	$^3P_1$	-2.57	4.13	-5.45	$7s6d$ $^1D_2$	$7s7p$ $^3P_1$	-0.353		-4.68
	$^3P_2$	-0.688		-1.77		$^3P_2$	-0.519	-5.24	-5.24
	$^1P_1$	-0.440	-9.15	4.74		$^1P_1$	-3.23		-13.5

[a] For $E1$ matrix element
[b] For NSI-PNC martrix element
[c] For NSD-PNC martrix element

Table 3.25 Comparison of the different methods of determining the dominating term of the PNC amplitudes for ^{225}Ra.

NSD-PNC	units: $10^{-10}\varkappa iea_0$		
	Orthog.[a]		
	$\lambda\Sigma$[b]	Σ[c]	Direct[d]
$^1S_{0\,F=0.5} \rightarrow {}^3D_{2\,F=1.5}$	5.708	5.873	5.706
$^1S_{0\,F=0.5} \rightarrow {}^3D_{1\,F=1.5}$	0.1551	0.1557	0.1551
NSI-PNC	units: $10^{-10}(-Q_W/N)iea_0$		
$^1S_0 \rightarrow {}^3D_1$	13.67	14.00	13.75

[a] Subtracting the dominating term using orthogonality conditions
[b] Scaling the correlation potential to reproduce energy interval
[c] Re-scaling dominating term by $\Delta E^{\text{Calc.}}/\Delta E^{\text{Exp.}}$
[d] Calculate dominating term directly using Eq. (3.6)

Table 3.25 compares the three different methods of determining the dominating contribution to the amplitude as described above. There is very good agreement between these approaches, indicating good numerical accuracy in the calculations.

The $^1S_0 - {}^3D_2$ transition is of particular interest for the potential measurement of the AM. It is enhanced by very close levels of opposite parity, the interval between the upper $^3D_2$ state and the odd-parity $^3P_1$ state is just 5.41 cm^{-1}, and there is no NSI contribution. This leads to a huge enhancement in the parity violating signal caused by the interaction of the valence electrons with the AM of the nucleus.

Calculations of the PNC amplitudes between the different hyperfine components for this transition are presented in Table 3.26. I have performed the calculation of the entire sum, as opposed to just the leading term as was done in [120]. This amplitude is very large indeed, several orders of magnitude larger than the NSD amplitudes in Cs.

My value is about twice as large as the value calculated in Ref. [120]. I be-

Table 3.26 NSD-PNC amplitudes (z components) for the ${}^1S_0 \to {}^3D_2$ transition in Ra, with F_z=min(F_a,F_b). There is no NSI contribution to this transition. Units: $10^{-10} iea_0\,\varkappa$

I	F_a	F_b	This work	Ref. [120]
1.5	1.5	0.5	−1.39	−0.57
		1.5	−3.35	−1.37
		2.5	3.13	1.28
0.5	0.5	1.5	5.92	2.42

Table 3.27 Effect of the CI basis on the matrix element $\langle {}^3P_1 || \boldsymbol{\alpha}\rho || {}^3D_2 \rangle$ in Ra and comparison with Ref. [120].

CI-Method	A	B	C	Full	Ref. [120]
$\langle a \|\| \boldsymbol{\alpha}\rho \|\| b \rangle$	0.90	1.18	1.48	2.21	1.10

A: Allowing only single excitations from the main reference configuration: $7s^2$ for ${}^3D_2$ and $7s7p$ for ${}^3P_1$

B: Allowing only single excitations from two reference states: $7s^2$ and $6d7s$ for ${}^3D_2$, and $7s7p$ and $6d7p$ for ${}^3P_1$

C: Allowing double excitations, but with a reduced basis

Full: Allowing double excitations with the full basis (final value)

lieve this is mainly due to the effect of the basis used for the wavefunctions on the matrix elements of the NSD-PNC interaction. Only a minimal number of single-electron basis states calculated in a V^N potential were used in Ref. [120]. The use of the V^N approximation in Ref. [120] allowed the authors to attain reasonable accuracy for the wavefunctions without saturating the basis. In this thesis, however, I use a complete set of single-electron states calculated in the V^{N-2} potential. In this case, the single-electron orbitals are initially quite different from those in the neutral atom. However, high accuracy of the results is achieved when the basis is saturated by allowing all single and double excitations from the initial reference configuration. The best correspondence between two methods is achieved when only single excitations are allowed in the V^{N-2} potential. Single excitations correct the orbitals calculated in the V^{N-2} potential making them close to those calculated in the V^N potential. In Table 3.27 I present calculations of the reduced matrix elements of the $\boldsymbol{\alpha}\rho$ operator (which are proportional to the NSD-PNC matrix elements) using several different basis configurations, and demonstrate that by using wavefunctions similar to those used in [120] it is possible to account for the difference between the value determined in this work and that of Ref. [120]. Note that this change in the wavefunctions makes only a much smaller difference to the energy levels ($\sim 5\%$) and $E1$ matrix elements ($\sim 10\%$).

The measurement of the AM of ^{133}Cs was achieved by comparing measurements of the PNC amplitude, which contained contributions from both the NSD and NSI parts, between different hyperfine components [4]. The considered transition in Ra, however, offers the possibility to measure the effect of the AM directly, which may be more efficient due both to the the much larger amplitude and to the fact that the the NSI interaction does not contribute in this case at all due to the large change in total electron angular momentum $\Delta J = 2$.

As well as the ${}^1S_0 - {}^3D_2$ transition, which has no NSI contribution, I have also performed calculations for the ${}^1S_0 - {}^3D_1$ transition, for which both NSI and

Table 3.28 PNC amplitudes (z components) for the ${}^1S_0 \to {}^3D_1$ transition in Ra. Units: $10^{-10} iea_0$

Q_W	I	F_a	F_b	$E_{\rm PNC}$	Q_W	I	F_a	F_b	$E_{\rm PNC}$
			^{223}Ra					^{225}Ra	
-127.0	1.5	1.5	0.5	$-6.71 \times [1 - 0.0402\varkappa]$	-129.0	0.5	0.5	0.5	$-6.81 \times [1 - 0.0475\varkappa]$
			1.5	$-9.00 \times [1 - 0.0161\varkappa]$				1.5	$9.64 \times [1 + 0.0237\varkappa]$
			2.5	$7.35 \times [1 + 0.0241\varkappa]$					

NSD contributions are non-zero. This transition is also enhanced due to close levels of opposite parity, though not to the same extent. The interval between the even ${}^3D_1$ state and the odd ${}^3P_1$ states is 283.53 cm^{-1}.

These amplitudes are presented in Table 3.28. I express the amplitudes in the form

$$E_{\rm PNC} = P(1 + R), \tag{3.8}$$

where P is the NSI-PNC amplitude (including Q_W), and R is the ratio of the NSD to NSI parts. Here I calculate both parts concurrently, using the same method and wavefunctions. This approach has the advantage that the relative sign difference between the NSI and NSD parts is fixed, ensuring no ambiguity in the sign of $\varkappa$ [40]. There is also typically a significant improvement in accuracy for the ratio over that for each of the amplitudes individually, due to the fact that the atomic calculations for both components are very similar and much of the theoretical uncertainty cancels in the ratio [213].

The z component (J_z=0) of the F-independent electron part of the NSI-PNC amplitude (defined in Appendix B.1.3) for the ${}^1S_0 - {}^3D_1$ transition in ^{223}Ra is:

$$E_{\rm PNC}({}^{223}{\rm Ra}) = 12.4 \times 10^{-10} (-Q_W/N)\, iea_0, \tag{3.9}$$

an order of magnitude larger than the $7s$–$8s$ transitions in Fr and Ra$^+$, and about twice as large as the $7s$–$6d_{3/2}$ transitions in Fr and Ra$^+$ (see Section 3.2) and the ${}^1S_0 - {}^3D_1$ transition in Yb (see, e.g. [40]).

3.4.3 Barium

Barium, like Ra, has two valence electrons above a closed shell core, and I proceed with the calculations in the same way. Calculations of the reduced matrix elements of interest to PNC studies are presented in Table 3.29 (energies for Ba are presented in Table 3.21). The energies and $E1$ transition amplitudes agree reasonably with previous calculations, e.g., Ref. [233].

There are two transitions of interest in Ba that are enhanced by the presence of close levels of opposite parity. The first is between the meta-stable $5d6s\,{}^3D_1$ and the upper $5d^2\,{}^1D_2$ even states. Both NSI and NSD-PNC parts of this amplitude are enhanced by the proximity of the odd $5d6p\,{}^1D^o_2$ state to the upper state of the transition, with an interval of 12.34 cm^{-1}.

Calculations of the NSI and NSD contributions to the ${}^3D_1 - {}^1D_2$ PNC amplitude for Ba are presented in Table 3.30. I present these amplitudes in the form $E_{\rm PNC} = P(1 + R)$, as described above. The z component (J_z=1) of the F-independent NSI-PNC amplitude for this transition is:

$$E_{\rm PNC}({}^{135}{\rm Ba}) = -3.55 \times 10^{-10} (-Q_W/N)\, iea_0, \tag{3.10}$$

Table 3.29 Reduced matrix elements $\langle a||\hat{H}||b\rangle$ (in au) for the $E1$ ($-e\boldsymbol{r}$), NSI-PNC ($\gamma_5\rho$), and NSD-PNC ($\boldsymbol{\alpha}\rho$) amplitudes between the relevant states of Ba. No value means identically zero due to selection rules.

Even state	Odd state	H_{ab}			Even state	Odd state	H_{ab}		
a	b	$-e\boldsymbol{r}$	$\gamma_5\rho$	$\boldsymbol{\alpha}\rho$	a	b	$-e\boldsymbol{r}$	$\gamma_5\rho$	$\boldsymbol{\alpha}\rho$
$6s^2$ $^1S_0$	$6s6p$ $^3P_0$		2.02		$5d6s$ $^3D_2$	$6s6p$ $^3P_1$	−3.48		0.171
	$^3P_1$	−0.510		−4.12		$^3P_2$	−2.03	0.291	−0.494
	$^1P_1$	5.50		1.62		$^1P_1$	−0.461		−0.518
$5d6s$ $^3D_1$	$6s6p$ $^3P_0$	−2.34		−0.376		$5d6p$ $^3F_2$	2.88	2.61	3.80
	$^3P_1$	2.03	−0.245	0.675		$^1D_2$	0.372	0.675	−0.811
	$^3P_2$	0.532		0.335		$^3F_3$	−5.97		−1.76
	$^1P_1$	0.081	1.07	−0.309	$5d^2$ $^1D_2$	$6s6p$ $^3P_1$	1.26		0.815
	$5d6p$ $^3F_2$	4.23		3.89		$^3P_2$	−1.62	1.29	1.55
	$^1D_2$	−2.72		−0.147		$^1P_1$	−2.58		1.08
						$5d6p$ $^3F_2$	−0.899	−0.020	−0.427
						$^1D_2$	−2.49	−0.085	−0.356
						$^3F_3$	0.061		−0.165

Table 3.30 PNC amplitudes (z components) for the $^3D_1 \to {}^1D_2$ transition in Ba. Units: $10^{-10}iea_0$

	Q_W	I	F_a	F_b	$E_{\rm PNC}$
^{135}Ba	−74.0	1.5	0.5	0.5	$2.48 \times [1 + 0.144\varkappa]$
				1.5	$-2.48 \times [1 + 0.0945\varkappa]$
			1.5	0.5	$1.11 \times [1 + 0.1476\varkappa]$
				1.5	$2.66 \times [1 + 0.0977\varkappa]$
				2.5	$-2.49 \times [1 + 0.0145\varkappa]$
			2.5	1.5	$0.543 \times [1 + 0.1031\varkappa]$
				2.5	$2.18 \times [1 + 0.0199\varkappa]$
				3.5	$-2.51 \times [1 - 0.0966\varkappa]$

despite some suppression due to the small value of the NSI-PNC matrix element, it is still large.

The other transition is from the meta-stable $5d6s\,^3D_2$ state to the same upper $5d^2\,^1D_2$ even state. As with the first transition, both the NSI and NSD parts of this amplitude are enhanced by the proximity of the odd $5d6p\,^1D_2^o$ state to the upper state of the transition, with the same 12.34 cm^{-1} interval. However, in this case there is a second dominating term that contributes to the NSD-PNC amplitude only. This contribution comes from the odd $5d6p\,^3F_3$ state, and is enhanced by an energy interval of 114.6 cm^{-1}.

The fact that there are two dominating terms to this transition makes this case potentially more difficult numerically – the experimental energy intervals for both leading terms cannot be simultaneously reproduced with the same set of scaling parameters for the correlation potential. I proceed in this case using a mixture of the two above described methods; I use the same correlation potential scaling parameters as for the $^3D_1 - {}^1D_2$ transition (reproducing the 12.34 cm^{-1} interval exactly), and then enforce orthogonality conditions to separate off the remaining dominating term and rescale it for the 114.6 cm^{-1} experimental interval. As a test of the numerical accuracy I in fact separate off both dominating terms using the orthogonality conditions and compare them to the

Table 3.31 PNC amplitudes (z components) for the ${}^3D_2 \to {}^1D_2$ transition in Ba. Units: $10^{-10} iea_0$

	Q_W	I	F_a	F_b	$E_{\rm PNC}$
^{135}Ba	-74.0	1.5	0.5	0.5	$-0.233 \times [1 + 0.161\varkappa]$
				1.5	$-0.233 \times [1 + 0.190\varkappa]$
			1.5	0.5	$-0.233 \times [1 + 0.144\varkappa]$
				1.5	$-0.279 \times [1 + 0.0753\varkappa]$
				2.5	$-0.174 \times [1 + 0.146\varkappa]$
			2.5	1.5	$-0.174 \times [1 + 0.0686\varkappa]$
				2.5	$-0.366 \times [1 - 0.0179\varkappa]$
				3.5	$-0.115 \times [1 + 0.0724\varkappa]$
			3.5	2.5	$-0.115 \times [1 - 0.0360\varkappa]$
				3.5	$-0.466 \times [1 - 0.131\varkappa]$

values calculated directly using the matrix elements from Table 3.29 and the experimental intervals. I find excellent agreement between these values, within 0.3% for the NSI part and better than 0.1% for the NSD part, and conclude that the numerical accuracy is good. Calculations of the ${}^3D_2 - {}^1D_2$ PNC amplitude for ^{135}Ba are presented in Table 3.31, and the z component ($J_z = 2$) of the NSI-PNC amplitude for the ${}^3D_2 - {}^1D_2$ transition for Ba is:

$$E_{\rm PNC}({}^{135}{\rm Ba}) = -0.497 \times 10^{-10} (-Q_W/N)\, iea_0, \tag{3.11}$$

relatively small compared to the other transitions studied in this work (though still larger than the measured Cs amplitude).

While there are possible PNC transitions from the ground state, they are not enhanced. The ${}^3D_1$ state is practically stable with no allowed $E1$ or $E2$ transitions to the ground state, the only lower state. I calculate the lifetime of this state to be 4×10^6 s. For the ${}^3D_2$ state, which has only a significant contribution from an $E2$ transition to the ground state, I calculate a lifetime of 70 s, which agrees very well with the value of 69 s calculated in Ref. [232].

Though the here considered amplitudes are smaller than those in Ra, and despite the fact that the enhanced amplitudes are not from the ground state, there are advantages to working with Ba. The ^{135}Ba and ^{137}Ba nuclei, each with nuclear spin $I = 3/2$, are stable. There are obvious benefits to this over working with radioactive elements. Also, despite the smaller amplitudes and likely smaller nuclear enhancement (i.e. smaller $\varkappa$) than in Ra, the ratio of the NSD to NSI parts is very large for transitions between some hyperfine components. This is due to small values for the NSI-PNC matrix element of the dominating terms (see Table 3.29), which suppresses the NSI part of the amplitudes.

The transitions from the ground state, namely the ${}^1S_0 - {}^3D_1$, the ${}^1S_0 - {}^1D_2$, and the ${}^1S_0 - {}^3D_2$ transitions, may themselves in fact be promising options for searching for PNC. As well as searching for the AM by measuring PNC between different hyperfine components, each of the NSI transitions in Ba could be used for measurements of PNC in a chain of isotopes. There is currently much interest in this type of measurement, in particular for Yb [40, 87, 88, 227–229], where measurements have already been performed [36], and are continuing [85]. The atomic PNC amplitude in Yb constitutes the largest yet observed in any system. The NSI-PNC transitions in neutral Ba are of particular interest in this

Table 3.32 Reduced matrix elements $\langle b||\hat{H}||a\rangle$ (au) of the amplitudes between the lowest few states of Ac$^+$. No value means forbidden by selection rules.

Odd state		Even state		H_{ba}			Odd state		Even state		H_{ba}		
a		b		$-e\boldsymbol{r}$	$\gamma_5\rho$	$\boldsymbol{\alpha}\rho$	a		b		$-e\boldsymbol{r}$	$\gamma_5\rho$	$\boldsymbol{\alpha}\rho$
$7s7p$	$^3P_0$	$7s^2$	$^1S_0$		45		$7s7p$	$^3P_1$	$7s^2$	$^1S_0$	1.7		−85
		$6d7s$	$^3D_1$	−1.8		5.6			$6d7s$	$^3D_1$	1.7	16	−15
		$6d^2$	$^3P_0$		5.2					$^3D_2$	2.2		14
			$^3P_1$	−0.50		0.029				$^1D_2$	−0.10		3.1
									$6d^2$	$^3F_2$	0.56		−3.3
										$^3P_0$	0.66		12
										$^3P_1$	−0.42	1.6	−1.5
										$^3P_2$	0.40		−4.2
										$^1D_2$	0.82		−4.7

area. Like Yb, Ba has many stable isotopes, with both even and odd-nucleon numbers, that are significantly spread out. The $^3D_1 - {}^1D_2$ NSI-PNC amplitude in Ba is about half the size of the $^1S_0 - {}^3D_1$ transition of Yb, though the NSD contribution for Ba is several times larger than that for Yb.

3.4.4 Actinium II

The Ac$^+$ ion has a ground state configuration very similar to that of Ra, and thus the calculations can be approached in the same way. Here, the transition of interest is the $7s^2\,{}^1S_0 \to 6d^2\,{}^3P_2$ transition, for which there is no NSI contribution. This transition is enhanced by the proximity of the odd $7s7p\,{}^3P_1$ level to the even $6d^2\,{}^3P_2$ level, with an energy interval of 18.93 cm^{-1}.

In Table 3.32 I present calculations of the relevant reduced matrix elements for Ac$^+$, and in Table 3.33 I present z components of the NSD-PNC amplitudes. These amplitudes are almost as large as the corresponding $^1S_0 - {}^3D_2$ transitions in Ra. Despite the difficulties of working with ions, it is possible that there are advantages in using actinium. The ^{227}Ac nucleus has a half life of 22 yr, much longer than the 42 min half-life of the most stable odd-nucleon Ra isotope (^{227}Ra) or the 22 min of the most stable Fr isotope (^{223}Fr).

This transition in Ac$^+$ could be measured using a similar method to that put forward by Fortson in Ref. [92] for measuring PNC in single ions that have been laser trapped and cooled. The upper $6d^2$ level of the transition should be relatively stable, a condition for accuracy in this method, since the only allowed $E1$ transition to a lower level is suppressed by the small interval 18.93 cm^{-1}. Including all $E1$, $E2$ and $M1$ transitions to lower levels, I calculate the lifetime of this state to be about 0.2 s.

3.4.5 Thorium

Thorium has four valence electrons. Full-scale accurate calculations for this atom are beyond the scope of the present work, however I use the same methods outlined above (using a V^{N-4} potential; see Appendix A.7) to perform preliminary calculations here also.

Table 3.33 NSD-PNC amplitudes (z components) for the ${}^1S_0 \to {}^3P_2$ transition in Ac$^+$. There is no NSI contribution to this transition. Units: $10^{-10} iea_0\,\varkappa$

	I	F_a	F_b	$E_{\rm PNC}$
^{227}Ac$^+$	1.5	1.5	0.5	1.05
			1.5	2.51
			2.5	−2.35
^{231}Ac$^+$	0.5	0.5	1.5	−4.44

To perform the calculations of the PNC amplitudes I calculate only the dominating contribution using the matrix elements of the PNC and $E1$ interactions, without trying to evaluate the entire sum. For the wavefunctions I include the eight leading configurations and from these allow single excitations. This provides a fair compromise between completeness of the wavefunctions and ease of computation. Here I include correlation corrections, but I calculate these to second order in MBPT only. I also do not perform any re-scaling of the correlation potential. This is because the uncertainty here is dominated by the completeness of the basis, not by the effect of the correlation potential. I have performed calculations of several energy levels of interest to PNC in Th. These are presented in Table 3.34 (note that this is not a comprehensive list of states; the Th spectrum is very dense). Despite the lower level approximation for the more complex system the agreement is reasonably good, particularly for the lower states. Calculations of the relevant $E1$ and PNC reduced matrix elements are presented in Table 3.35.

It is worth noting that for Th (and also for Pa) the configuration mixing is very large, particularly for the higher states. The configurations given in Tables 3.34 and 3.35 are the leading configurations (taken from Ref. [189]), but other contributing configurations are important as well. For example, the NSI-PNC ($\gamma_5\rho$) reduced matrix element between the $6d7s^27p\ {}^3D_3$ and $6d^27s^2\ {}^3F_3$ states is rather large (see Table 3.35), which is unexpected since the leading configurations suggest this transition is essentially a single-electron p-d transition. (This particular matrix element does not contribute to the PNC amplitude studied here.) However, due to the large configuration mixing this matrix element also has a large contribution coming from single-electron s-p mixing, enhancing this amplitude. The extent of this mixing is detrimental to the accuracy of the calculations, especially when the overall accuracy is not high, since even relatively small errors in the calculated configurations may lead to large errors in the weak matrix elements. Fortunately, the weak matrix elements of relevance to the PNC amplitudes studied here are relatively stable in this regard. Still, this is a large contributing factor to the low accuracy for these calculations in Th and Pa.

Thorium has several isotopes of non-zero nuclear spin, e.g., ^{227}Th with $I = 1/2$, ^{225}Th with $I = 3/2$, and ^{229}Th with $I = 5/2$. The most long-lived of these is ^{229}Th, which has a half-life of about 7300 yr, and the most stable Th isotope is ^{232}Th, which has zero nuclear spin and a half life of 1.4×10^{10} yr. The nuclear spin of Th is produced by a valence neutron. There are two interesting PNC transitions in Th that are enhanced by close opposite parity levels.

The first is a transition between the meta-stable $6d^27s^2\,{}^3F_4$ state and the

Table 3.34 Calculated energy levels for Th and comparison with experiment (Ref. [189]). Units are cm^{-1}.

State[a]		Calc.	Exp.
$6d^27s^2$	$^3F_2$	0	0
	$^3P_0$	2546	2558
	$^3F_3$	3168	2869
	$^1P_2$[b]	4120	3688
	$^3P_1$	3926	3865
	$^3F_4$	5650	4962
$6d^37s$	$^5F_1$	5257	5563
	$^5F_2$	6232	6362
	$^3H_4$	18358	15493
	$^3F_3$	18536	17398
$5f6d7s^2$	$^3G^o_5$	18846	15490
$6d7s^27p$	$^3D^o_3$	20190	17411

[a] Not a comprehensive list of states

[b] Term determined in this work

Table 3.35 Reduced matrix elements $\langle b||\hat{H}||a\rangle$ of the amplitudes between the relevant states of Th. (a.u.)

Odd state		Even state		H_{ba}			Odd state		Even state		H_{ba}		
a		b		$-e\boldsymbol{r}$	$\gamma_5\rho$	$\boldsymbol{\alpha}\rho$	a		b		$-e\boldsymbol{r}$	$\gamma_5\rho$	$\boldsymbol{\alpha}\rho$
$6d7s^27p$	$^3D_3$	$6d^27s^2$	$^3F_2$	−0.17		−14	$5f6d7s^2$	$^3G_5$	$6d^27s^2$	$^3F_4$	1.7		53
			$^3F_3$	−0.20	−47	2.8			$6d^37s$	$^3H_4$	0.14		2.9
			$^3F_4$	−0.51		−32							
		$6d^37s$	$^3H_4$	−0.01		−7.1							
			$^3F_3$	0.15	−0.37	4.5							

higher $6d^3 7s\, ^3H_4$ state, which is induced by the nuclear AM. This transition is enhanced by the extremely small 3.1 cm^{-1} energy interval between the $5f6d7s^2\, ^3G^o_5$ state and the $^3H_4$ state. This transition is given by

$$E_{\text{PNC}} \simeq k_{NSD} \frac{\langle ^3H_4||\boldsymbol{\alpha}\rho||^3G^o_5\rangle\langle ^3G^o_5|| - e\boldsymbol{r}||^3F_4\rangle}{E(^3H_4) - E(^3G^o_5)}, \tag{3.12}$$

where the factor k_{NSD} is given in Eq. (3.7). The NSD-PNC amplitudes between various hyperfine components for this transition are given in Table 3.36. There is also a NSI contribution to this transition, though it is not enhanced by the proximity of opposite parity levels and doesn't contain a single dominating term. It is likely between one and two orders of magnitude smaller than the NSD contribution, below the current level of accuracy.

The second transition of interest in Th is between the ground $6d^2 7s^2\, ^3F_2$ state and the higher $6d^3 7s\, ^3F_3$ state. This transition is enhanced by a 12.8 cm^{-1} energy interval between the $6d7s^2 7p\, ^3D^o_3$ state and the $^3F_3$ state, and has contributions from both the AM and the nuclear weak charge. The amplitudes for this transition are presented in Table 3.37, where, as for Ra, I present the amplitudes in the form $E_{\text{PNC}} = P(1 + R)$. Note that the ratio of the NSD contribution to the NSI contribution is significantly larger for Th than for Ra.

The z component (J_z=2) of the NSI-PNC amplitude for the (F-independent) $^3F_2 - {}^3F_3$ transition in ^{232}Th is calculated to be

$$E_{\text{PNC}}(^{232}\text{Th}) = 9.9 \times 10^{-11}(-Q_W/N)\, iea_0. \tag{3.13}$$

There is no NSD-PNC contribution here due to the fact that ^{232}Th has nuclear spin $I = 0$. Despite suppression from both the $E1$ and PNC matrix elements the amplitude is large, an order of magnitude larger than the $6s$–$7s$ transition in Cs. Though the accuracy here is not high, this transition could be used in isotopic chain measurements to determine ratios of the weak charges for different isotopes of Th. ^{232}Th is practically stable, with a half-life of 1.5×10^{10} yr.

3.4.6 Protactinium

As well as the enhancement that is due to the presence of close electronic levels of opposite parity, there is some suggestion that there may also be a very large nuclear enhancement of P-, T-odd effects in ^{229}Pa [221] (see also [107, 222–224]), which has nuclear spin $I = 5/2$. The suggestion of large nuclear enhancement comes from experimental evidence that there is an extremely small energy splitting ($\sim$ 0.22 keV) between the members of a ground state parity doublet [234]. However, more recent experimental work has put the identification of these levels into doubt (see, e.g. [235]). Even so, the parity violating nuclear effects can reasonably be expected to be large, and along with the electronic enhancement this makes Pa an interesting case also.

To perform these calculations for Pa, which has five valence electrons, I follow a similar procedure as in Th, however I do not allow any excitations from the eight leading configurations in the production of the wavefunctions. The experimental energies of these states, as well as calculations of the reduced matrix elements of the relevant operators, are presented in Table 3.38.

Note that it would be preferable to perform calculations in Pa (and even Th) using the conventional CI method with a V^N potential. The benefits for

Table 3.36 NSD-PNC amplitudes (z components) for the ${}^3F_4 \to {}^3H_4$ transition in Th. The NSI contribution to this transition is not enhanced. Units: $10^{-10} i e a_0 \, \varkappa$

	I	F_a	F_b	$E_{\rm PNC}$		I	F_a	F_b	$E_{\rm PNC}$
^{227}Th	0.5	3.5	4.5	3.4	^{229}Th	2.5	1.5	2.5	1.4
		4.5	4.5	-1.0			2.5	2.5	-0.87
								3.5	1.7
							3.5	2.5	-0.12
								3.5	-1.4
								4.5	1.8
							4.5	3.5	-0.16
								4.5	-1.7
								5.5	1.8
							5.5	4.5	-0.14
								5.5	-1.5
								6.5	1.5
							6.5	5.5	-0.086
								6.5	-1.0

Table 3.37 PNC amplitudes (z components) for the ${}^3F_2 \to {}^3F_3$ transition in Th. Units: $10^{-10} i e a_0$

Q_W	I	F_a	F_b	$E_{\rm PNC}$	Q_W	I	F_a	F_b	$E_{\rm PNC}$
		^{227}Th					^{229}Th		
-128.9	0.5	1.5	2.5	$0.95 \times [1 + 0.22\varkappa]$	-130.8	2.5	0.5	0.5	$-0.79 \times [1 + 0.21\varkappa]$
		2.5	2.5	$-0.34 \times [1 + 0.22\varkappa]$				1.5	$0.72 \times [1 + 0.18\varkappa]$
			3.5	$0.83 \times [1 - 0.16\varkappa]$			1.5	0.5	$-0.42 \times [1 + 0.21\varkappa]$
								1.5	$-0.91 \times [1 + 0.18\varkappa]$
								2.5	$0.68 \times [1 + 0.13\varkappa]$
							2.5	1.5	$-0.28 \times [1 + 0.18\varkappa]$
								2.5	$-0.91 \times [1 + 0.13\varkappa]$
								3.5	$0.68 \times [1 + 0.054\varkappa]$
							3.5	2.5	$-0.17 \times [1 + 0.13\varkappa]$
								3.5	$-0.83 \times [1 + 0.053\varkappa]$
								4.5	$0.68 \times [1 - 0.042\varkappa]$
							4.5	3.5	$-0.091 \times [1 + 0.053\varkappa]$
								4.5	$-0.62 \times [1 - 0.043\varkappa]$
								5.5	$0.68 \times [1 - 0.16\varkappa]$

Table 3.38 Reduced matrix elements $\langle a||\hat{H}||b\rangle$ for the amplitudes between the relevant states of Pa. Also shown are the experimental energies of the levels [189].

Odd state	Even state	H_{ab} (a.u.)		
a	b	$-e\boldsymbol{r}$	$\gamma_5\rho$	$\boldsymbol{\alpha}\rho$
$5f6d^37s$ $^6I^o_{9/2}$ (8583 cm^{-1})	$5f^26d7s^2$ $^4K_{11/2}$ (0 cm^{-1})	0.22		−13.7
	$5f^26d7s^2$ $^4G_{11/2}$ (8571 cm^{-1})	0.36		−4.5
	$5f^26d7s^2$ $^4H_{9/2}$ (8596 cm^{-1})	−0.08	2.8	3.8

Table 3.39 NSD-PNC amplitudes (z components) for the $^4K_{11/2} \to {}^4G_{11/2}$ transition in Pa. The NSI contribution to this transition is not enhanced. Units: $10^{-10} iea_0\,\varkappa$

	I	F_a	F_b	$E_{\rm PNC}$		I	F_a	F_b	$E_{\rm PNC}$
^{229}Pa	2.5	3	3	0.039	^{231}Pa	1.5	4	4	0.041
			4	0.0061				5	0.0032
		4	3	−0.055			5	4	−0.078
			4	0.063				5	0.056
			5	0.0070				6	0.0024
		5	4	−0.071			6	5	−0.092
			5	0.072				6	0.043
			6	0.0056					
		6	5	−0.078					
			6	0.067					
			7	0.0028					
		7	6	−0.077					
			7	0.043					
		8	7	−0.064					

this type of Hartree-Fock potential when only a small basis is used for the valence wavefunctions was discussed in Section 3.4.2. However, I find that in these cases the convergence of the TDHF equations [Eqs. (A.40) and (A.41) of Appendix A.6.1] is problematic due to the open s, f, and d shells of the important configurations. This is especially true for the operator of the NSD-PNC interaction, which leads to unstable and unreliable results. It is for this reason that I make use of the V^{N-M} potential approach despite the reduction in accuracy.

There are two transitions of particular interest in Pa. The first is between the even $5f^26d7s^2\,{}^4K_{11/2}$ ground-state and the $5f^26d7s^2\,{}^4G_{11/2}$ upper state, and the other is between the ground-state and the $5f^26d7s^2\,{}^4H_{9/2}$ state. Both transitions are enhanced by the proximity of the odd $5f6d^37s\,{}^6I^o_{9/2}$ state to the upper state of the transitions with energy intervals of 12.0 cm^{-1} and 13.2 cm^{-1} respectively.

Table 3.40 PNC amplitudes (z components) for the ${}^4K_{11/2} \to {}^4H_{9/2}$ transition in Pa. Units: $10^{-10} iea_0$

Q_W	I	F_a	F_b	$E_{\rm PNC}$	Q_W	I	F_a	F_b	$E_{\rm PNC}$
			^{229}Pa					^{231}Pa	
-129.8	2.5	3	2	$-5.1\times[1+0.023\varkappa]$	-131.8	1.5	4	3	$-4.7\times[1+0.023\varkappa]$
			3	$3.0\times[1+0.018\varkappa]$				4	$2.2\times[1+0.012\varkappa]$
			4	$0.35\times[1+0.011\varkappa]$				5	$0.14\times[1-0.0022\varkappa]$
		4	3	$-4.4\times[1+0.018\varkappa]$			5	4	$-4.1\times[1+0.012\varkappa]$
			4	$3.5\times[1+0.011\varkappa]$				5	$2.3\times[1-0.0022\varkappa]$
			5	$0.32\times[1+0.0028\varkappa]$				6	$0.10\times[1-0.019\varkappa]$
		5	4	$-3.8\times[1+0.011\varkappa]$			6	5	$-3.8\times[1-0.002\varkappa]$
			5	$3.5\times[1+0.0028\varkappa]$				6	$1.9\times[1-0.019\varkappa]$
			6	$0.25\times[1-0.0073\varkappa]$			7	6	$-3.8\times[1-0.019\varkappa]$
		6	5	$-3.8\times[1+0.0028\varkappa]$					
			6	$3.0\times[1-0.0073\varkappa]$					
			7	$0.15\times[1-0.019\varkappa]$					
		7	6	$-3.5\times[1-0.007\varkappa]$					
			7	$2.3\times[1-0.019\varkappa]$					
		8	7	$-3.5\times[1-0.019\varkappa]$					

Calculations of the AM induced PNC amplitudes for the ${}^4K_{11/2} - {}^4G_{11/2}$ transition are presented in Table 3.39. There is also a NSI contribution to this transition but it is not enhanced and is smaller than the NSD part.

The ${}^4K_{11/2} - {}^4H_{9/2}$ transition transition has enhanced contributions from both the AM and Q_W induced contributions. The amplitudes for this transition are presented in Table 3.40. The NSD amplitudes in Table 3.39 and 3.40 are approximately 10 times smaller than those calculated for Th, however the AM, $\varkappa_a({}^{229}\text{Pa})$, may be much larger.

I calculate the z component (J_z=9/2) for the F-independent part of the ${}^4K_{11/2} - {}^4H_{9/2}$ NSI-PNC amplitude to be

$$E_{\rm PNC}({}^{231}\text{Pa}) = -44 \times 10^{-11}(-Q_W/N)\, iea_0. \tag{3.14}$$

As for Th, the accuracy here is not high, though the amplitude is very large, about the same size as the $7s$–$6d_{3/2}$ amplitudes in Fr and Ra$^+$, and about a third of the size of the ${}^1S_0 - {}^3D_1$ amplitude in neutral Ra. This transition would therefore be of interest for measuring the ratio weak charges for a number of different isotopes of Pa, the most stable of which being ^{231}Pa, with a half-life of about 32500 yr.

3.4.7 Discussion and conclusion

I have presented calculations of strongly enhanced atomic parity nonconservation due both to the nuclear weak charge and the nuclear AM in the hope of motivating experiment. Experiments, including the production of beams of various Ra isotopes, are currently under way with atomic parity violation in mind, see e.g. [236, 237]. These methods can also be exploited for other actinides, including neutral atoms and ions [237]. Parity violation experiments in Yb have already been performed [36], and improvements are under way [85]. In principle these could make use of the chain of isotopes method, and also lead to the extraction of the AM. For most of the atoms considered here, experiments similar to the type used to measure PNC in Yb would be applicable. In principle, an experiment like that currently being used to search for PNC in dysprosium could also be used [89]. In this method it is not directly the PNC amplitude that is measured, and the quantity of immediate interest is the weak matrix element of the dominating term, making this method particularly interesting for the transitions that would otherwise be from excited states. A condition here, however, is that the upper state be relatively stable [89]. For the Ac^+ ion, a method similar to that put forward by Fortson in Ref. [92] for measuring PNC in single ions that have been laser trapped and cooled could be used.

Note that I have not considered PNC in dysprosium in this chapter, since calculations for PNC in dysprosium have been performed fairly recently [91]. The feature of dysprosium that makes it a particularly interesting system for the study of atomic PNC is the existence of two nearly degenerate states of opposite parity and the same total angular momentum, $J = 10$, at $E = 19797.96\ \mathrm{cm}^{-1}$. Despite this close-level enhancement, the overall PNC effect in dysprosium has been found to be small, due to only very small amounts of s-p mixing in the relevant matrix element [89, 91], and a non-zero PNC signal has not yet been observed. This does not mean that this transition is not interesting, however, and it is still the subject of much interest and ongoing work, not only to measure PNC, but also as a test of other fundamental symmetries and as a possible sensitive test for variation of the fundamental constants [238, 239], as well as searching for evidence of a parity violating cosmic field, and dark matter, as discussed in Ch. 5 of this thesis.

Anapole moment induced transitions are presented for systems whose nuclear spin is caused both by a valence neutron (Ra, Ba, and Th) and a proton (Ac^+ and Pa). I expect the accuracy of the calculations to be approximately 20% for Ra, Ba, and Ac^+, and provide order-of-magnitude calculations for Th and Pa. Calculations for Th and Pa can be improved by extending the CI calculations and performing a summation for the entire PNC amplitude. More complete calculations for all systems can be performed if experimental work is under way. Due to the very large enhancement of the PNC amplitudes the atoms and ions considered here are promising candidates for experimental studies of parity violating nuclear forces and for studying PNC in a chain of isotopes.

CHAPTER 4:
Double Core Polarisation:
contribution to atomic parity-nonconservation and electric-dipole-moment calculations

In this chapter, I present a detailed study of the effect of the double core polarisation (the polarisation of the core electrons due to the simultaneous action of the electric dipole and parity-violating weak fields) for amplitudes of the ss and sd parity violating transitions, and for the atomic electric dipole moments for several atoms and ions of experimental interest. This effect is quite large, and may have been missed in several previous calculations. It therefore has the potential to resolve some disagreement between calculations in the literature, and has significant consequences for the use of experimental data in the accuracy analysis.

4.1 Introduction

Measurements of parity nonconservation (PNC), and atomic electric dipole moments (EDMs) provide important tests of the electroweak theory. The PNC amplitude of the $6s$–$7s$ transition in cesium is the most precise low-energy test of the standard model to date. This precision is a result of the highly accurate measurements [4, 53] as well as the almost equally accurate atomic calculations [9–11], which are needed for their interpretation (see also [5, 8]).

For calculations of PNC in Cs there is very good agreement between calculations, and the high accuracy is widely accepted. For other systems, however, there is disagreement between various calculations—in some cases by as much as 5%. Due to the potential significance of these calculations for probing physics beyond the standard model, it is very important that this disagreement be resolved.

In addition to the well known experiments for Cs, PNC measurements are under consideration for the Ba$^+$ ion [92] and are in progress for the Ra$^+$ ion [94, 97–100]. The FrPNC collaboration has begun the construction of a laser cooling and trapping apparatus with the purpose of measuring atomic parity nonconservation in microwave and optical transitions of francium [80–84]. There are also experiments under way at the Cyclotron and Radioisotope Centre (CYRIC) at Tohoku University to use Fr in an electron EDM measurement [240–242]. For more current and prospective EDM experiments see, e.g., Refs. [3, 28].

Reliable interpretation of all these measurements requires accurate atomic calculations. In this chapter, we consider a particular aspect of atomic calculations that has received little attention in previous publications. This is the effect of the double core polarisation (DCP), which arises due to the simultaneous action of the electric dipole ($E1$) and parity-violating weak fields [243]. The polarisation of the atomic core by the electric field of the laser is affected by the presence of the weak interaction and vice versa. This leads to an additional contribution to the PNC amplitude or atomic EDM, which varies significantly between different atoms and transitions. For example, it contributes only 0.26% to the $6s$–$7s$ PNC transition in Cs but is significantly larger for the *sd* PNC transitions—reaching 6% for the $6s$–$5d_{3/2}$ PNC transition in Ba$^+$. A special case is the thallium atom. If thallium is treated as a mono-valence system, then the double core polarisation contribution is about 40% for the $6p_{1/2}$–$6p_{3/2}$ PNC amplitude and about 60% for the EDM induced in the $6p_{1/2}$ ground state. If instead, Tl is treated as a three-valence system, then the majority of the DCP is included automatically via the configuration interaction equations.

The importance of the double core polarisation contribution is known, and is included in many PNC and EDM calculations (see, e.g., Refs. [8, 38, 179]). However, it was never studied in detail and its importance was never properly emphasised. Perhaps for this reason it may be that some calculations based on the sum-over-states approach have missed this contribution.

Here, we study the effect of the double core polarisation for the amplitudes of the *ss* and *sd* parity non-conserving transitions in Rb, Cs, Ba^+, La^{2+}, Tl, Fr, Ra^+, Ac^{2+}, and Th^{3+} as well as electron EDM enhancement factors for the ground states of the above neutral atoms and Au. We show that the effect is large and in some cases can explain the discrepancy between different calculations. We also show that this contribution affects the analysis of the accuracy of the calculations based on the use of the experimental data.

4.2 Calculations

4.2.1 PNC and EDM amplitudes

Some of the discussion and equations presented here is a repitition of that presented earlier and in the appendix. I present it again here, though, for completeness, and because it is directly relevant to the current discussion.

The PNC amplitude of a transition between states of the same nominal parity can be expressed via the sum over all intermediate opposite-parity states n,

$$E_{\rm PNC} = \sum_n \Big[\frac{\langle w|\hat{d}_{E1}|n\rangle\langle n|\hat{h}_{\rm PNC}|v\rangle}{\varepsilon_v - \varepsilon_n} + \frac{\langle w|\hat{h}_{\rm PNC}|n\rangle\langle n|\hat{d}_{E1}|v\rangle}{\varepsilon_w - \varepsilon_n}\Big], \tag{4.1}$$

where v, w, and n are many-electron wavefunctions of the atom with corresponding energies ε, $\hat{d}_{E1}$ is the electric dipole transition operator and $\hat{h}_{\rm PNC}$ is the operator of the weak interaction. Likewise, the contribution to an atomic EDM induced in the atomic state a by a mixing of opposite parity states n has the form

$$d_{\rm atom} = 2\sum_n \frac{\langle a|\hat{d}_{E1}|n\rangle\langle n|\hat{h}_{PT}|a\rangle}{\varepsilon_a - \varepsilon_n}, \tag{4.2}$$

where $\hat{h}_{PT}$ is the P- and T-odd operator that depends on the electron EDM and mixes states of opposite parity.

The amplitudes can then be evaluated via a direct summation of products of matrix elements and energy denominators over the states n. We refer to this method as the direct-summation (DS) method. We, however, bypass this technique in favour of a more numerically stable approach based on solving differential equations, the so-called mixed-states method (sometimes also the 'solving-equations' method), as described in Appendix A.8. This approach, which is outlined in the next section, has many important advantages, not least of which is that it allows the easy inclusion of the important double core polarisation (DCP) contribution.

4.2.2 Atomic structure calculations and core polarisation

The above 'exact' expressions (4.1) and (4.2) can be reduced to approximate formulas containing instead single-electron energies and matrix elements. Then, many-body effects are included by modifying the single-electron orbitals and the external field operators.

We begin with the relativistic Hartree-Fock approximation and proceed to include the dominating electron correlation effects using the correlation potential method [5, 70, 199, 219, 244, 245]. The correlation potential is used to construct the so-called Brueckner orbitals (BOs) for the valence electron, which are found by solving the Hartree-Fock-like equations with the extra operator $\hat{\Sigma}$:

$$(\hat{H}_0 + \hat{\Sigma} - E_n)\psi_n^{(\mathrm{BO})} = 0, \tag{4.3}$$

where $\hat{H}_0$ is the relativistic Hartree-Fock Hamiltonian and the index n denotes valence states. The BO $\psi_n^{(\mathrm{BO})}$ and energy E_n include correlations; see Appendix A.4.2 for more detail.

Interactions with the external fields are included via the time-dependent Hartree-Fock (TDHF) approximation (see, e.g., [5, 70, 199, 219, 243–245], and Appendix A.6.1). The external fields in question are the electric dipole ($E1$) interaction with the electric field of the photon, d_{E1}, and either the nuclear-spin–independent weak interaction h_{PNC}, or the P- and T-odd weak interaction h_{PT} in the case of atomic EDMs. It is with this method that we also include the important core-polarisation effects, which arise from the action of the external fields on the Hartree-Fock V^{N-1} core potential.

Within the framework of the TDHF method, the single-electron wavefunction in external weak and $E1$ fields is expressed

$$\psi = \psi_0 + \delta\psi + Xe^{-i\omega t} + Ye^{i\omega t} + \delta Xe^{-i\omega t} + \delta Ye^{i\omega t}, \tag{4.4}$$

where ψ_0 is the unperturbed state, $\delta\psi$ is the correction due to the weak interaction acting alone, X and Y are corrections due to the photon field acting alone, δX and δY are corrections due to both fields acting simultaneously, and ω is the frequency of the PNC transition. Since the EDM amplitude is a diagonal matrix element with no transition, $\omega = 0$ in the EDM case. This method is equivalent to the well-known random phase approximation (RPA).

The corrections δV to the core potential are found by solving the following system of RPA equations self-consistently for the core states.

The equations for the $E1$ core polarisation,

$$\begin{aligned} (\hat{H}_0 - E_c - \omega)X_c &= -(\hat{d}_{E1} + \delta\hat{V}_{E1})\psi_{0c}, \\ (\hat{H}_0 - E_c + \omega)Y_c &= -(\hat{d}_{E1}^{\dagger} + \delta\hat{V}_{E1}^{\dagger})\psi_{0c}, \end{aligned} \tag{4.5}$$

and for the weak core polarisation,

$$(\hat{H}_0 - E_c)\delta\psi_c = -(\hat{h}_f + \delta\hat{V}_f)\psi_{0c}, \tag{4.6}$$

are independent and can be solved separately. Here, the index c denotes core states, $\hat{h}_f$ is the operator of the external weak field, and $\delta\hat{V}_f$ and $\delta\hat{V}_{E1}$ are corrections to the core potential arising from the weak and $E1$ interactions respectively. Again, ω is the energy of the PNC transition, and is zero in the case of EDMs. An example set of diagrams corresponding to the PNC amplitude or

Figure 4.1 Example diagrams for the PNC amplitude $v \to w$ or atomic EDM (in which case $w = v$) including (single) core polarisation to the lowest-order in the Coulomb interaction. The solid line represents the HF or BO electron, the dashed line is the $E1$ interaction, the wavy line is the Coulomb interaction, and the cross denotes the weak interaction. There are also the corresponding diagrams with the weak and $E1$ interactions interchanged.

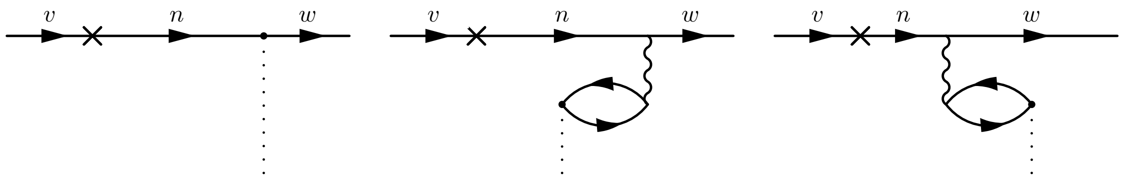

(a) Zeroth order (b) Direct ($E1$) (c) Direct ($E1$)

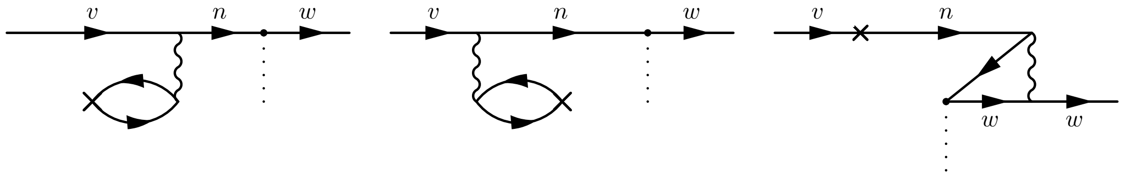

(d) Direct (weak) (e) Direct (weak) (f) Exchange ($E1$)

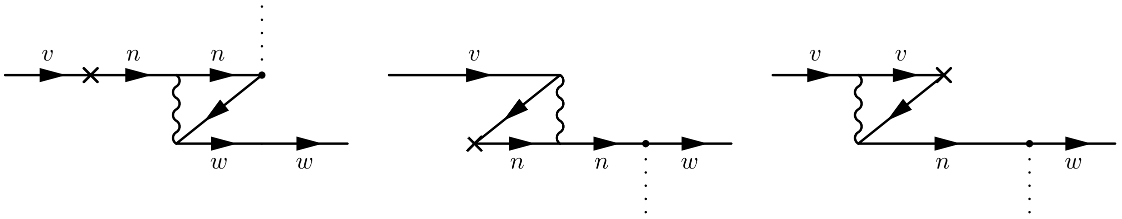

(g) Exchange ($E1$) (h) Exchange (weak) (i) Exchange (weak)

Figure 4.2 Example diagram for the lowest-order (in the Coulomb interaction) double core polarisation contribution to the PNC amplitude $v \to w$ or atomic EDM (in which case $w = v$). For PNC there is only the exchange diagrams (shown) but for EDM there are also direct diagrams. There is also a diagram with the order of the weak and $E1$ interactions interchanged.

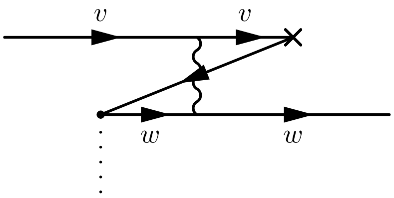

atomic EDM including the lowest-order (single) core polarisation are presented in Fig. 4.1.

There is also the set of equations corresponding to the double core polarisation:

$$\begin{aligned}(\hat{H}_0 - E_c - \omega)\delta X_c &= -\delta\hat{V}_{E1}\delta\psi_c - \delta\hat{V}_f X_c - \delta\hat{V}_{fE1}\psi_{0c} + \delta E_c\psi_{0c},\\ (\hat{H}_0 - E_c + \omega)\delta Y_c &= -\delta\hat{V}^{\dagger}_{E1}\delta\psi_c - \delta\hat{V}_f Y_c - \delta\hat{V}^{\dagger}_{fE1}\psi_{0c} + \delta E_c\psi_{0c}.\end{aligned} \tag{4.7}$$

Here, $\delta\hat{V}_{fE1}$ is the correction to the core potential arising from the simultaneous perturbation of the weak field and the electric field of the laser light, and δE_c is the corresponding correction to the core energy. An example diagram corresponding to the DCP correction is presented in Fig. 4.2. The correction to the core energy,

$$\delta E_c = \langle\psi_{0c}|\delta\hat{V}_{E1}|\delta\psi_c\rangle + \langle\psi_{0c}|\delta\hat{V}_f|X_c\rangle + \langle\psi_{0c}|\delta\hat{V}_{fE1}|\psi_{0c}\rangle, \tag{4.8}$$

is zero in the case of PNC (since the matrix elements of the weak PNC interaction are imaginary and cannot produce a shift in the energy, even in an electric field), but non-zero for EDMs.

The equations (4.7) depend on the solutions to equations (4.5) and (4.6), and must therefore be iterated after (4.5) and (4.6) are solved (and their convergence has been realised). In the mixed-states method, the PNC amplitude between valence states a and b is then given by

$$\begin{aligned}E_{\rm PNC} &= \langle\psi_b|\hat{d}_{E1} + \delta\hat{V}_{E1}|\delta\psi_a\rangle + \langle\psi_b|\hat{h}_{\rm PNC} + \delta\hat{V}_W|X_a\rangle + \langle\psi_b|\delta\hat{V}_{fE1}|\psi_a\rangle\\ &= \langle X_b|\hat{d}_{\rm PNC} + \delta\hat{V}_W|\psi_a\rangle + \langle\psi_b|\hat{h}_{\rm PNC} + \delta\hat{V}_W|X_a\rangle + \langle\psi_b|\delta\hat{V}_{fE1}|\psi_a\rangle\\ &= \langle\psi_b|\hat{d}_{E1} + \delta\hat{V}_{E1}|\delta\psi_a\rangle + \langle\delta\psi_b|\hat{d}_{E1} + \delta\hat{V}_{E1}|\psi_a\rangle + \langle\psi_b|\delta\hat{V}_{fE1}|\psi_a\rangle,\end{aligned} \tag{4.9}$$

and the corresponding atomic EDM is given by

$$d_{\rm atom} = 2\langle\psi_a|\hat{d}_{E1} + \delta\hat{V}_{E1}|\delta\psi_a\rangle + \langle\psi_a|\delta\hat{V}_{fE1}|\psi_a\rangle. \tag{4.10}$$

Note that the two different ways of expressing the PNC amplitude [second two lines in Eq. (4.9)] gives a very strong test of the numerical accuracy of the mixed-states approach. By using BOs for the valence states ψ_a and ψ_b in (4.9) and (4.10) we can include correlations in the calculation of the PNC and EDM amplitudes. The corrections $\delta\psi_a$ and $\delta\psi_b$ to the BOs ψ_a and ψ_b are also found with the use of the correlation potential $\hat{\Sigma}$:

$$(\hat{H}_0 - E_a + \hat{\Sigma})\delta\psi_a = -(\hat{h}_f + \delta\hat{V}_f)\psi_{0a}. \tag{4.11}$$

The last term in equations (4.9) and (4.10) represents the double core polarisation contribution (DCP), which is due to the simultaneous action of the two external fields. This term gives an important correction that is often not included in sum-over-states calculations.

It is possible to include a term for the DCP perturbatively directly after solving equations (4.5) and (4.6), and without iterating the equations (4.7). For example, by solving the equations (4.7) once without iterating, or by adding the term as a MBPT diagram (as in Fig. 4.2) that corresponds to a double core-excitation. This contribution corresponds to the lowest order DCP term, which we refer to as $\delta V_{fE1}^{\rm pert.}$. There is, however, another contribution that comes from further iterations of the pair of equations (4.7), which corresponds to the summation over all higher-order (in the Coulomb interaction) diagrams. This effect, which we refer to as the relaxation effect $\delta V_{fE1}^{\rm relax}$, has a significant impact on the value of the double core polarisation. The relative size of this relaxation effect means it is not enough to simply include the term perturbatively, and the total DCP term must be taken as $\delta V_{fE1} = \delta V_{fE1}^{\rm pert.} + \delta V_{fE1}^{\rm relax}$.

In these calculations we didn't include corrections such as structure radiation (the correction to the correlation potential Σ due to the $E1$ field, $\delta\Sigma_{E1}$, the weak correlation potential, $\delta\Sigma_W$, and the combined weak and $E1$ fields, $\delta\Sigma_{WE1}$), or other higher order corrections such as ladder diagrams, and renormalization of states. These corrections are typically small (with perhaps the exception of thallium when treated as a single valence system) though they should be taken into account for accurate calculations.

4.3 Results and discussion

4.3.1 PNC amplitudes

We have performed calculations of the double core polarisation correction to many PNC amplitudes, the results of which are presented in Table 4.1 along with several existing PNC calculations for comparison. We present the contributions of the double core polarisation that stem from including the term perturbatively, $\delta V_{fE1}^{pert.}$, and the subsequent relaxation effect, arising from further iterations of (4.7), δV_{fE1}^{relax}, separately.

Our results show that the double core polarisation term is quite large, especially for the *sd* PNC transitions, and also that the relaxation effect is not small and must be included along with the perturbative lower order term. We also demonstrate that in these cases the majority of the discrepancy between the mixed-states (MS) and direct sum-over-states (DS) calculations can be explained by the possible omission of the DCP term.

In Ref. [93], calculations of *sd* PNC transitions were performed for Cs, Ba$^+$, Fr and Ra$^+$ using both the mixed-states and the direct-summation methods. As discussed, the double core polarisation contribution was included in [93] in the MS calculations only. In that work there was about a 4% discrepancy between the DS and MS calculations for Cs and Fr, 8% for Ba$^+$ and 7% for Ra$^+$.

Table 4.1 Double core polarisation contribution to parity nonconservation amplitudes for transitions in several atoms and ions. We present several of the most complete calculations, and what their value would be if the DCP term was omitted ($E_{\rm PNC}^{-\delta V_{fE1}}$). Shown separately are the lowest order perturbative DCP term, $\delta V_{fE1}^{\rm pert.}$, and the relaxation contribution that comes from iterations of the equations (4.7), $\delta V_{fE1}^{\rm relax}$. Also shown are several available calculations and the methods they used for comparison. MS refers to the mixed-states (or solving-equations) method, which typically includes the DCP term, and DS is the direct-summation method, which may not. CC Means the coupled-cluster method, and MP means using many-body perturbation theory. Amplitudes are presented in units of $iea_B(-Q_W/N)\times 10^{-11}$.

		$E_{\rm PNC}$		$\Delta E_{\rm PNC}$(DCP) - This work				Other values		
Transition		Most complete		$\delta V_{fE1}^{pert.}$	δV_{fE1}^{relax}	δV_{fE1}^{total}	$E_{\rm PNC}^{-\delta V_{fE1}}$	$E_{\rm PNC}$		Method
^{85}Rb	$5s$–$6s$	0.1390(7)	[101]	−0.0004	0.0001	−0.24%	0.1393	0.139(2)	[38]	MS-MP
	$5s$–$4d_{3/2}$	−0.450	[a]	0.0065	0.0021	−2.0%	−0.459	—		
^{133}Cs	$6s$–$7s$	0.9041(45)	[8]	−0.0034	0.0010	−0.26%	0.907	0.8977(40)	[11]	DS-MP
								0.8906(24)	[9]	DS-CC
	$6s$–$5d_{3/2}$	−3.70(4)	[191][b]	0.070	0.030	−2.6%	−3.80	−3.76(7)	[93]	DS-MP
								−3.62(7)	[93]	MS-MP
^{137}Ba$^+$	$6s$–$7s$	0.658(7)	[191][b]	−0.007	0.001	−0.84%	0.664	—		
	$6s$–$5d_{3/2}$	−2.20(2)	[191][b]	0.073	0.067	−6.0%	−2.34	−2.34(9)	[93]	DS-MP
								−2.17(9)	[93]	MS-MP
								−2.46(2)	[220]	DS-CC
^{139}La^{2+}	$6s$–$5d_{3/2}$	−2.14(2)	[191][b]	0.051	0.085	−6.0%	−2.28	—		
^{223}Fr	$7s$–$8s$	15.49(16)	[197]	−0.05	0.05	−0.06%	15.5	15.41	[79]	DS-CC
								15.9(2)	[78]	MS-MP
	$7s$–$6d_{3/2}$	−58.0(6)	[191][b]	1.12	0.40	−2.6%	−59.5	−59.5(24)	[93]	DS-MP
								−57.1(23)	[93]	MS-MP
^{226}Ra$^+$	$7s$–$8s$	10.9(1)	[191][b]	−0.10	0.07	−0.28%	10.9	—		
	$7s$–$6d_{3/2}$	−44.3(4)	[191][b]	1.29	0.92	−4.8%	−46.5	−45.89	[95]	DS-CC
								−46.4(14)	[94]	DS-CC
								−45.9(19)	[93]	DS-MP
								−43.9(18)[c]	[93]	MS-MP
^{227}Ac^{2+}	$7s$–$6d_{3/2}$	−42.8(4)	[191][b]	1.01	1.21	−4.9%	−45.0	—		
^{232}Th^{3+}	$7s$–$6d_{3/2}$	−43.6(4)	[191][b]	0.75	1.44	−4.8%	−45.8	—		

[a] This work

[b] This work (see previous chapter)

[c] Rescaled from ^{223}Ra$^+$

Here, we calculate the contribution of the double core polarisation for these s–d transitions to be approximately 3% for Cs and Fr, 6% for Ba$^+$ and 5% Ra$^+$ – consistently making up for most of the disagreement. The rest of the difference likely comes from the numerical accuracy of the different methods and minor differences in correlation calculations. If the double core polarisation contribution is removed from the MS calculations then our MS and DS calculations match perfectly for Ba$^+$ and Fr, and are within 1% for the Cs and Ra$^+$ values from [93].

The sd transition in Ra$^+$ is a particularly useful case to study as there are a number of values available for comparison. Total DCP contribution is about -5% (see Table 4.1) which is very close to the difference between the most complete calculations (from the previous chapter of this thesis) and all calculations using the DS approach where this contribution may be missing. The range of values that do not include the double core polarisation term, including the DS values from Ref. [93], lie within 1% of each other. They also lie within 1% of the value obtained by removing the DCP contribution from the result of the previous chapter of this thesis.

Another value, calculated by Wansbeek *et al.* [94] using a relativistic coupled-cluster (CC) approach, also agrees with these values, lying within 0.3% of the value calculated in this work without double core polarisation and 0.2% of the Pal *et al.* [95] DS value. It is not clear if the DCP contribution was included in the works [94, 95]. (A brief overview of the CC and MP methods are given in Appendix A.5 and A.4, respectively.)

The difference between the $6s$–$7s$ PNC transitions in Cs for the mixed-states value 0.9041(45) of Ref. [8] and the sum-over-states value 0.8906(24) of Ref. [9, 10] is larger than the DCP term – it is mainly due to missed contributions to the core and tail parts of the summation in (4.1) (see [11] for full detail). It is worth noting however, that the double core polarisation contribution of 0.26% is of the same size as the uncertainty quoted in Refs. [9, 10] of 0.27%—meaning that this uncertainty can only be claimed if the DCP contribution is included. As we shall discuss in the next section, the double core polarisation contribution has particular impact on the accuracy analysis.

We have performed and presented detailed PNC calculations for these Fr- and Cs-like ions in the previous chapter. A more complete analysis of the accuracy of these calculations, including calculations of energy levels, lifetimes and matrix elements is given there.

4.3.2 Atomic EDM

As well as parity nonconservation, calculations for several atomic electric dipole moments (EDMs) induced by the dipole moment of the electron (d_e) have been performed. These calculations, along with several existing calculations for comparison, are presented in Table 4.2.

Some previous calculations of the EDM for Cs [180], as well as Fr and Au [250], do not include the double core polarisation term. These values, along with one for Rb calculated in this work, are presented in the $d^{(0)}_{atom}$ column of Table 4.2. They are then corrected by adding the DCP term with the corrected results given in the column $d^{\rm new}_{atom}$. We find here also that the double core polarisation term is quite a large contribution, and that by including this term we can improve the agreement between several previous calculations.

Table 4.2 Double core polarisation contribution to Atomic EDM calculations for several atoms including both the perturbative and relaxation parts. The values $d^{(0)}_{atom}$ do not include DCP, and the values $d^{\rm new}_{atom}$ do. Values in units of d_e.

State		$d^{(0)}_{atom}$	Δd_{atom}(DCP) - This work				Other values	
			$\delta V^{\rm pert.}_{fE1}$	$\delta V^{\rm relax.}_{fE1}$	% $\delta V^{\rm both}_{fE1}$	$d^{\rm new}_{atom}$	d_{atom}	Ref.
Rb	$5s$	26.8[a]	−0.59	−0.86	−5.4%	25.4	25.74(26)	[246]
							25.7	[247]
							24.6	[248]
Cs	$6s$	124(4)[b]	−3.0	−2.5	−4.4%	119(4)	120.5(12)	[246]
							114.9	[248]
Au	$6s$	260(39)[c]	−6.7	−3.4	−3.9%	250(39)	249.9	[248]
Fr	$7s$	910(46)[c]	−24.3	−12.1	−4.0%	874(46)	894.93	[249]

[a] This work.

[b] Reference [180].

[c] Reference [250].

It is interesting to note that if we include only the perturbative DCP term into the EDM calcualtions for Cs and Fr and don't include the relaxation term, we reproduce the values from References [246] and [249] almost exactly (see Table 4.2).

The Tl atom represents an interesting case for both PNC and EDM calculations. If we treat Tl as a mono-valence system, then the DCP contribution to the PNC amplitude is huge. It contributes 36% to the PNC amplitude of the $6p_{1/2}$–$6p_{3/2}$ transition and about 60% to the EDM of the ground state. The DCP contribution is strongly dominated by the $6s$ electrons. An example diagram for the DCP contribution to the $6p_{1/2}$–$6p_{3/2}$ PNC amplitude in Tl (where Tl is treated as a mono-valence system with the $6s$ electrons treated as part of the core) is presented in Fig. 4.3. This reflects the well-known fact that the correlations between the three outermost electrons in thallium are strong and should be treated accurately. In our view, the best approach is to treat thallium as a triple-valence-electron system and to use the configuration interaction (CI) technique combined with many-body perturbation theory (MBPT) for including valence–core correlations; as discussed in Appendix A.7. In this approach, the dominating DCP contribution is included automatically; see Fig. 4.4.

However, good results can be obtained in other approaches too if correlations between $6s$ and $6p$ electrons, including the DCP contribution, are treated accurately. For example, by treating Tl as a single-valence system, and including core-polarisation (but not DCP) and correlations to second-order in MBPT, we calculate the EDM of Tl to be $d(\mathrm{Tl}) = -2000\,d_e$ (many times larger in magnitude than the 'correct' value of $\sim -600\,d_e$ [181]). Including the DCP term, however, brings the value to $\sim -700\,d_e$, making up most of the difference. The rest of the difference comes from the higher-order correlation effects included in Ref. [181], but not included in our work.

In early calculations of the PNC in thallium [38] it was treated as a mono-valence system and the DCP contribution was included. Recent calculations of the EDM enhancement factor [180, 181] used the CI approach, the calculations of the Tl EDM based on the coupled-cluster approach [179, 182] seems to include

Figure 4.3 An example DCP contribution to the $6p_{1/2}$–$6p_{3/2}$ PNC amplitude in Tl when Tl is treated as a single-valence system (the $6s$ states are considered part of the core). Here, the solid lines correspond to HF or BO electron wavefunctions, the cross denotes the weak (PNC or EDM) interaction, the dotted line denotes the $E1$ interaction, and the wavy line is the Coulomb interaction (of multipolarity, k).

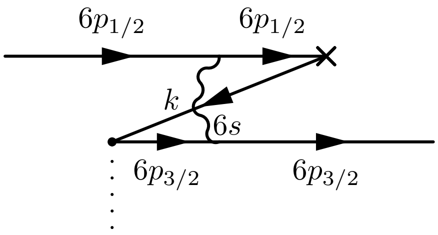

Figure 4.4 Contribution to the $6p_{1/2}$–$6p_{3/2}$ PNC amplitude in Tl corresponding to the DCP diagram presented in Fig. 4.3, when Tl is treated as a three-valence system. This diagram is included automatically when using the CI technique.

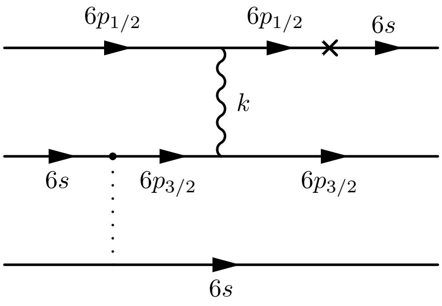

the DCP contribution too by introducing the perturbed excitation operators T_1 and T_2 (see [179] for detailes).

4.4 Implications for accuracy analysis

Most of the accuracy analysis in the literature assumes that the PNC and EDM amplitudes can be reduced to a sum of products of matrix elements and energy denominators that are all independent. The $E1$ matrix elements and energies can then be compared with experimental values in order to judge the accuracy of the calculations. The accuracy of the weak matrix elements can similarly be judged by calculating hyperfine structure constants, since both the weak interaction and the hyperfine structure rely on the form of the wavefunctions on short distances. The accuracy of this analysis, however, is limited by the value of the double core polarisation effect – which is by no means negligible. The DCP contribution cannot easily be presented as a product of weak and electric dipole matrix elements which are independent on each other. If the analysis of accuracy ignores this contribution it does not present the whole picture.

For example, the DCP contribution is 5% for the $7s$–$6d_{3/2}$ PNC transition in Ra$^+$. Some sophisticated calculations can give excellent agreement with the experimental data for the energies, electric dipole transition amplitudes and for the hyperfine structure. The accuracy for the PNC amplitude, however, would still only be 5% if the DCP contribution was not included.

CHAPTER 5:
Parity-Violating Interactions of Cosmic Fields with Atoms, Molecules, and Nuclei:
limits on parameters of Lorentz and CPT-violation

In this chapter, I present methods for extracting limits on the strength of P-odd interactions of various cosmic fields with electrons, protons, and neutrons, by exploiting the static and dynamic parity-nonconserving amplitudes and electric dipole moments they induce in atoms. Candidates for such fields are dark matter (including axions) and dark energy, as well as several more exotic sources described by Lorentz-violating standard model extensions. Atomic calculations are performed for several atoms and ions. From these calculations, and existing measurements in Dy, Cs, and Tl, constraints are placed on the interaction strengths of several parity-violating cosmic fields with electrons and neutrons. Note that in this chapter, I depart from the usual convention of atomic units, and employ the more standard natural relativistic units ($\hbar = c = 1$), in order to aid with comparisons with other works.

5.1 Introduction

Scalar and pseudoscalar cosmic fields (e.g. the Higgs and axion fields) have a strong theoretical underpinning. As well as these, many other background fields are invoked by theories which extend beyond the standard model (SM), for example, supersymmetric theories, and string theory. Many of these fields, including vector, pseudovector, and tensor fields, have been conveniently parametrised in the form of the so-called Standard Model Extension (SME) [254–256]. In this chapter, we examine the parity and time-reversal violating effects, including parity nonconservation (PNC) amplitudes and atomic electric dipole moments (EDMs), that such cosmic fields induce in atomic systems through their interaction with electrons, protons, and neutrons. In the next chapter, I discuss the specific case of axion and axion-like particle dark-matter detection in more detail.

The existence of a cosmic field that interacts with electrons in a parity-violating manner can contribute to the mixing of opposite-parity atomic states, leading to parity-violating effects in atoms. Parity nonconservation amplitudes are parity-violating $E1$ transitions between two states of the same nominal parity. They are generated by parity-violating forces; in the conventional case, these include Z^0-boson exchange between the electrons and nucleons and the electromagnetic interaction of the electrons with parity-violating nuclear moments that are borne by parity-violating forces inside the nucleus, as discussed in Ch. 1 (also see, e.g., Refs. [3, 27, 28]).

In addition to inducing PNC effects and EDMs, cosmic fields that interact with standard-model fermions can give rise to other fascinating phenomena. In the case of axions, this includes the axio-electric effect [257–264], nuclear anapole moments, and spin-gravity and spin-axion momentum couplings in atomic, molecular, solid-state and nuclear systems [265–268]. A general pseudoscalar cosmic field need not necessarily be restricted to an axionic one; dark energy and other exotic fields are also possibilities. We therefore present the atomic-structure calculations separately from any field parameters, to avoid any model dependence.

In Sec. 5.2, we first show that a static pseudoscalar cosmic field cannot give rise to observable P-odd effects in atoms in the lowest order, and then present the necessary theory and derive expressions for the PNC effects and EDMs induced in atoms and nuclei by pseudoscalar and pseudovector cosmic fields. We go on in Sec. 5.3 to present the methods used for our *ab initio* relativistic atomic calculations for pseudovector and dynamic pseudoscalar cosmic-field–induced PNC amplitudes and atomic EDMs for a number of neutral atoms and ions. These calculations are necessary for determining, or placing limits upon, important pseudoscalar and pseudovector cosmic-field parameters, in conjunction with appropriate experimental data. In Sec. 5.4, we present the results of our atomic calculations and combine these with existing PNC experiments in Cs, Tl, Yb, and Dy to give limits on the interaction strengths of static pseudovector and tensor cosmic fields with electrons, protons, and neutrons. We also discuss possible systems for experimentally obtaining limits on the interaction strengths of dynamic cosmic fields with standard model fermions.

5.2 Theory

5.2.1 Parity-violating interactions of fermions with cosmic fields

Except where explicitly noted, we use natural units, $\hbar = c = 1$, throughout. Here, we consider two distinct sources of cosmic fields. Pseudoscalar (PS) fields, such as axions, are described by the Lagrangian density

$$\mathcal{L}^{\rm PS} = -i\zeta m_f\,\phi\,\bar{\psi}\gamma^5\psi + \eta(\partial_\mu\phi)\,\bar{\psi}\gamma^\mu\gamma^5\psi, \tag{5.1}$$

where ζ and η are dimensionless constants quantifying the interaction strength of fermions with the PS cosmic field via a direct and derivative-type coupling, respectively, m_f is the mass of the fermion in question, ψ is the fermion wavefunction with the Dirac adjoint $\bar{\psi} \equiv \psi^\dagger\gamma^0$, and γ^μ (with $\mu = 0, 1, 2, 3$) and $\gamma^5 = i\gamma^0\gamma^1\gamma^2\gamma^3$ are the Dirac matrices. The factor m_f is factorised purely for convenience (to make ζ dimensionless); the coupling, in general, is not dependent on the fermion mass.

Here, $\phi = \phi(\boldsymbol{r}, t)$ is the dynamic PS field in question. In the next section we will see that an interaction of the form (5.1) with a static field will not lead to any parity-violating effects in atoms in the lowest order. The field ϕ (for example, an axion field or a light pseudoscalar dark-matter field) obeys the Klein-Gordon equation, $(\partial_\mu\partial^\mu + m^2)\phi = 0$. We take this field to be classical and real, so that

$$\phi(\boldsymbol{r}, t) = \cos(\omega_\phi t - \boldsymbol{p}_\phi \cdot \boldsymbol{r} + \xi), \tag{5.2}$$

where $\boldsymbol{p}_\phi$ and ω_ϕ are the momentum and energy of the pseudoscalar field particle (e.g. the axion), respectively, and ξ is a phase factor. We have absorbed the amplitude of the field into the constants η and ζ. With a redefinition of the phase factor at a fixed point in space, we can express this field more simply as $\phi(\boldsymbol{r}, t) = \cos(\omega_\phi t)$. This is valid so long as the time scale of an experiment is sufficiently short that the evolution of the $\boldsymbol{p}_\phi \cdot \boldsymbol{r}$ term in (5.2), which corresponds to the motion of the observer with respect to the coordinates, is small compared with the evolution of the $\omega_\phi t$ term over the course of the experiment. This will usually be the case, since the typical speed of a PS cosmic field relative to Earth is expected to be $v \sim 10^{-3}$, see, e.g., Ref. [269]; a brief discussion of the coherence time is given towards the end of this chapter.

We also consider terms from the Lorentz-invariance-violating SME [254–256]:

$$\mathcal{L}^{\rm SME} = \frac{1}{2} i\bar{\psi}\Gamma_\nu \overleftrightarrow{\partial}^\nu \psi - \bar{\psi}M\psi, \tag{5.3}$$

where

$$M = a_\mu\gamma^\mu + b_\mu\gamma^\mu\gamma^5 + \frac{1}{2}H_{\mu\nu}\sigma^{\lambda\mu}, \tag{5.4}$$

$$\Gamma_\nu = c_{\mu\nu}\gamma^\mu + d_{\mu\nu}\gamma^\mu\gamma^5 + e_\nu + if_\nu\gamma^5 + \frac{1}{2}g_{\lambda\mu\nu}\sigma^{\lambda\mu}, \tag{5.5}$$

$\sigma^{\lambda\mu} = i[\gamma^\lambda, \gamma^\mu]/2$, where $[A, B] = AB - BA$ is the commutator, and $A\overleftrightarrow{\partial}^\nu B \equiv A(\partial^\nu B) - (\partial^\nu A)B$, where the derivatives act on the wavefunctions only (not the fields). The relativistic interaction Hamiltonians due to Eqs. (5.4) and (5.5) are

$$\hat{h}^M = a_0 + a_j\gamma^0\gamma^j + b_0\gamma^5 + b_j\gamma^0\gamma^j\gamma^5 + iH_{0j}\gamma^j + \frac{1}{2}H_{jk}\epsilon^{jkl}\gamma_l\gamma^5 \tag{5.6}$$

and

$$\begin{aligned}\hat{h}^\Gamma &= c_{00}\gamma^0\gamma^j p_j - (c_{0j} + c_{j0})p^j - c_{jk}\gamma^0\gamma^j p^k - mc_{00}\gamma^0 \\ &+ d_{00}\gamma^0\gamma^j\gamma^5 p_j - (d_{0j} + d_{j0})\gamma^5 p^j - d_{jk}\gamma^0\gamma^j\gamma^5 p^k \\ &- m_f d_{j0}\gamma^j\gamma^5 - m_f e_0 - e_j\gamma^0 p^j - if_j\gamma^0\gamma^5 \\ &- \epsilon^{jkl}g_{j00}\gamma_l\gamma^5 p_k + i(g_{j0k} + g_{jk0})\gamma^j p^k \\ &+ \frac{1}{2}\epsilon^{jkl}g_{jkm}\gamma_l\gamma^5 p^m - \frac{1}{2}m_f\epsilon^{jkl}g_{kl0}\gamma^0\gamma_j\gamma^5,\end{aligned} \tag{5.7}$$

respectively [270]. (Also see Ref. [270] for a derivation of the non-relativistic form of the above Hamiltonian.) In the above equations, the Lorentz indices are separated into their time and space components, with Latin characters j, k, l, m running 1 through 3, and $\gamma^a = -\gamma_a$. We use the standard $(+---)$ metric, and a summation over repeated indices is assumed.

We note that interactions of cosmic fields with fermions are not limited to those described by the SME Lagrangian (5.3). For example, dimension-five operators that are linear in the electromagnetic gauge-field strength, see, e.g., [271, 272], can produce static electric dipole moments of fundamental particles [272], and contribute to the splitting of the magnetic dipole moments of fermions and their antifermion partners [253, 271].

5.2.2 Interaction of electrons with pseudoscalar and pseudovector cosmic fields

The direct PS interaction [first term of the right-hand side of (5.1)], and the time-derivative part of the derivative-type PS interaction [second term on the right-hand side of (5.1)], lead to interaction Hamiltonians of the form

$$\hat{h}^{\rm PS}_{i\gamma^0\gamma^5} = i\zeta m_f \cos(\omega_\phi t)\gamma^0\gamma^5, \tag{5.8}$$

(a) Pseudoscalar field ϕ (b) Pseudovector field b_μ

Figure 5.1 Fundamental vertices for the interaction of an electron with a pseudoscalar and pseudovector cosmic field.

and

$$\hat{h}^{\rm PS}_{\gamma^5} = \eta\omega_\phi \sin(\omega_\phi t)\gamma^5, \tag{5.9}$$

which we shall refer to as the PS $i\gamma^0\gamma^5$ and the PS γ^5 interactions, respectively[1]. The fundamental vertices for the interactions (5.8) and (5.9) are represented by the same Feynman diagram [presented in Fig. 5.1(a)]. Interactions of this form with atomic electrons will manifest themselves as oscillating contributions to PNC amplitudes and atomic EDMs.

It is also possible for parity-violating interactions of electrons with a cosmic field to produce static PNC effects in atoms. For this, we consider the Lagrangian corresponding to the interaction of electrons with the pseudovector (PV) field, b_μ [Fig. 5.1(b)]:

$$\begin{aligned}\mathcal{L}^{\rm PV}_{\gamma^5} &= -b_\mu\bar{\psi}\gamma^\mu\gamma^5\psi\\ &= -b_0\psi^\dagger\gamma^5\psi + \boldsymbol{b}\cdot\psi^\dagger\boldsymbol{\alpha}\gamma^5\psi,\end{aligned} \tag{5.10}$$

where $\boldsymbol{\alpha} = \gamma^0\boldsymbol{\gamma}$, and we have absorbed the strength of the interaction into the definition of the field $b_\mu = (b_0, -\boldsymbol{b})$. The temporal-component term of this coupling leads to the interaction Hamiltonian

$$\hat{h}^{\rm PV}_{\gamma^5} = b_0(t)\gamma^5, \tag{5.11}$$

which could be either static [$b_0(t) = b_0$] or dynamic [$b_0(t) = b_0\sin(\omega_b t)$] (the choice of phase here is entirely arbitrary, and is chosen for later convenience). We refer to this interaction as either the static or dynamic PV γ^5 interaction. In the dynamic case, the effects of (5.11) will mimic those of (5.9). In the static case, however, they will mimic the conventional nuclear-spin-independent (NSI) PNC signal induced by Z^0-boson exchange between the nucleus and electrons, described by the Hamiltonian

$$\hat{h}_{Q_W} = \frac{G_F}{2\sqrt{2}}Q_W\rho(\boldsymbol{r})\gamma^5, \tag{5.12}$$

where $G_F = 1.166\times10^{-5}$ GeV^{-2} is the Fermi weak constant, Q_W is the nuclear weak charge and ρ is the normalised nucleon density (see Ch. 1). In the standard model, $Q_W \approx -N$, where N is the number of neutrons in the nucleus.

---

[1] Note that the 'γ^5' interaction appears as $\gamma^0\gamma^5$ in the Lagrangian (and visa-versa); this possibly confusing notation stems from the extra γ^0 in $\bar{\psi} = \psi^\dagger\gamma^0$.

The spatial-derivative component terms in (5.1), and the spatial component terms in (5.10), lead to interaction terms of the form $\boldsymbol{\sigma}\cdot\boldsymbol{B}_{\text{eff}}$, where $\boldsymbol{\sigma}$ is the spin of a SM fermion and $\boldsymbol{B}_{\text{eff}}$ is an effective magnetic field due to the momentum of the PS or PV cosmic field, and thus give no parity-violating effects. The best current limits on such static interactions of a cosmic field with electrons, protons, and neutrons, using the notation of the SME parametrization [256], are: $|\tilde{b}^e_X| < 1.3\times10^{-31}$ GeV, $|\tilde{b}^e_Y| < 1.3\times10^{-31}$ GeV [273, 274], $|\tilde{b}^p_\perp| < 1.6\times10^{-33}$ GeV [275] and $|\tilde{b}^n_\perp| < 8.4\times10^{-34}$ GeV [276] (see also [275]), respectively, where the subscripts denote the field components in the sun-centred celestial-equatorial frame. Here and throughout this chapter, the superscripts e, p, and n denote the particle species: electron, proton, and neutron, respectively. For further details on the broad range of experiments performed in this field and a brief history of recent developments in the improvement of these limits, we refer the reader to Refs. [256, 273, 274, 276–283]. A comprehensive list of the limits extracted for the various interaction constants has been compiled in Ref. [284]. Indirect limits have been obtained for the SME parameter $\tilde{b}^e_T$ through linear combinations of several SME parameters, constrained at the level of $\sim 2\times10^{-27}$ GeV [273, 274]. Indirect limits have also been obtained for the SME parameter $\tilde{b}^n_T$ [279]. In this thesis, we consider the extraction of direct limits on the P-odd effects induced by the temporal component of the field, b_0 [as defined in Eq. (5.11)], for electrons, protons, and neutrons, which are complementary to the limits derived from P-even fermion effects discussed above. We do not consider the cosmic-field–induced interaction $\boldsymbol{\sigma}\cdot\boldsymbol{B}_{\text{eff}}$ further in this thesis, but note that such an interaction can also be sought in an oscillatory form (see, e.g., Refs. [267, 268]).

Note that any effective Hamiltonian that is proportional to the γ^5 or $i\gamma^0\gamma^5$ matrices will lead to a mixing of opposite-parity states in atoms and thus could contribute to parity nonconserving amplitudes. In this sense, the calculations provided in this chapter are general, and can be applied to any source leading to an interaction in the above forms.

The matrix elements of the γ^5 and $i\gamma^0\gamma^5$ operators are not entirely independent of one another. Considering the relativistic Hamiltonian for an N electron atom of nuclear charge Z in the presence of electrostatic interactions,

$$\hat{H} = \sum_{\imath=1}^{N}\left[\boldsymbol{\alpha}_\imath\cdot\boldsymbol{p}_\imath + m_e(\gamma^0_\imath - 1) - \frac{Ze^2}{r_\imath} + \sum_{\jmath<\imath}\frac{e^2}{r_{\imath\jmath}}\right], \tag{5.13}$$

where $\boldsymbol{p}_\imath$ is the relativistic (three-)momentum of the $\imath$th electron, $r_{\imath\jmath} = |\boldsymbol{r}_\imath - \boldsymbol{r}_\jmath|$, and $e = |e|$ is the elementary charge, the two operators in question are related via the useful identity

$$i\gamma^0_k\gamma^5_k = \frac{i}{2m_e}[\hat{H},\gamma^5_k] \tag{5.14}$$

(proved below), from which it follows that

$$\langle b|i\gamma^0_k\gamma^5_k|a\rangle = \frac{i}{2m_e}(E_b - E_a)\langle b|\gamma^5_k|a\rangle, \tag{5.15}$$

where the states a and b are eigenstates of the atomic Hamiltonian (5.13) with eigenvalues E_a and E_b, respectively. Note that for the standard choice of angular wavefunctions, the matrix elements of the $i\gamma^0\gamma^5$ operator are real and hence symmetric, whereas the γ^5 operator gives rise to imaginary matrix elements, and are antisymmetric. Equation (5.15) maintains this symmetry. To prove the relation in the case of the electrostatic Hamiltonian (5.13), note that the commutator in Eq. (5.14) reduces to

$$\begin{aligned}[\hat{H}, \gamma^5_k] &= \sum_{\imath} \left([\boldsymbol{\alpha}_\imath, \gamma^5_k] \cdot \boldsymbol{p}_\imath + m_e [\gamma^0_\imath, \gamma^5_k] \right) \\ &= 2 m_e \gamma^0_k \gamma^5_k. \end{aligned} \tag{5.16}$$

We have made use of the relation $\{\gamma^\mu, \gamma^5\} = 0$ ($\{x, y\} = xy + yx$ is the anti-commutator). This relation holds equally well if we had used the Hartree-Fock Hamiltonian (including core polarisation) in place of the 'exact' Hamiltonian (5.13). In that case, the many-body wavefunctions and energies that appear in Eq. (5.15) would be replaced by their single-particle counterparts.

The atomic PNC amplitude can then be written as

$$E^{a \to b}_{\mathrm{PNC}} = \sum_k \langle \widetilde{b(t)} | \boldsymbol{d}_k | \widetilde{a(t)} \rangle, \tag{5.17}$$

where $\boldsymbol{d}_k = -e\boldsymbol{r}_k$ is the operator of the electric dipole ($E1$) interaction, and $|\widetilde{a}\rangle = |a\rangle + |\delta a\rangle$ is the perturbed wavefunction associated with the atomic state a, with $|a\rangle$ the unperturbed wavefunction, and $|\delta a\rangle$ is the correction to the wavefunction due to the PNC interactions (5.8), (5.9) or (5.11). Likewise, the induced atomic EDM can be expressed as

$$d^a_{\mathrm{EDM}} = \sum_k \langle \widetilde{a(t)} | \boldsymbol{d}_k | \widetilde{a(t)} \rangle. \tag{5.18}$$

5.2.3 Interaction of atomic electrons with a static pseudoscalar field and other SME terms

Before we present the formulas for $|\widetilde{a}\rangle$, we discuss briefly the effects of a possible static pseudoscalar interaction, and show that such an interaction cannot give rise to observable P-odd amplitudes in atoms in the lowest order (though note that a static pseudovector field can). To see this for a derivative-type coupling, note that the time derivative in the interaction Lagrangian density (5.1) vanishes for a static field ϕ. The spatial derivative terms in (5.1) lead only to P-even effects, since they cannot lead to mixing of opposite parity atomic states.

To see this for the direct pseudoscalar coupling [first term on the right-hand side of (5.1)], we prove a general relation that states that any static interaction Hamiltonian, $\hat{h}$, that can be expressed in the form

$$\hat{h} = [\hat{H}, \hat{o}], \tag{5.19}$$

where $\hat{H}$ is the atomic Hamiltonian (5.13), will not give rise to any electromagnetic amplitudes, which have the form $j_\mu A^\mu = \psi_b^\dagger (A^0 + \boldsymbol{\alpha} \cdot \boldsymbol{A}) \psi_a$, in atoms, where $A^\mu = (A^0, \boldsymbol{A})$ is the photon field, so long as the commutator

$$[A^0 + \boldsymbol{\alpha} \cdot \boldsymbol{A}, \hat{o}] = 0. \tag{5.20}$$

Using time-independent perturbation theory, the wavefunction, $|\tilde{a}\rangle = |a\rangle + |\delta a\rangle$, perturbed to first-order by the interaction $\hat{h}$ (5.19) can be written as

$$\begin{aligned} |\tilde{a}\rangle &= |a\rangle + \sum_n \frac{|n\rangle\langle n|\hat{h}|a\rangle}{E_a - E_n} \\ &= |a\rangle - \hat{o}|a\rangle; \end{aligned} \tag{5.21}$$

similarly,

$$\langle\tilde{a}| = \langle a| + \langle a|\hat{o}. \tag{5.22}$$

With the use of the relation (5.19), the energy denominators have cancelled, and the summation was reduced to unity by closure. One can also check that $|\tilde{a}\rangle$ in (5.21) is the solution of the Dirac equation with the perturbation (5.19). Hence, the correction induced by the static interaction $\hat{h}$ to any general electromagnetic interaction is reduced to

$$\langle b|(A^0 + \boldsymbol{\alpha}\cdot\boldsymbol{A})|\delta a\rangle + \langle\delta b|(A^0 + \boldsymbol{\alpha}\cdot\boldsymbol{A})|a\rangle = \langle b|[A^0 + \boldsymbol{\alpha}\cdot\boldsymbol{A}, \hat{o}]|a\rangle. \tag{5.23}$$

There are thus no corrections to electromagnetic amplitudes if the commutator in (5.23) is equal to zero. Note also that any operator satisfying Eq. (5.19) automatically has no diagonal matrix elements and has null expectation values for an energy eigenstate.

In the case of PNC amplitudes and atomic EDMs, including (5.17) and (5.18), the relevant electromagnetic interaction operator is the $E1$ operator, $\boldsymbol{d}$. For the static pseudoscalar interaction [Eq. (5.8) with $\omega_\phi = 0$], $\hat{h} = i\gamma^0\gamma^5$, and from Eq. (5.14), $\hat{o} \propto \gamma^5$. Since $[\gamma^5, \boldsymbol{r}] = 0$, the static pseudoscalar field does not give rise to any observable P-odd transitions or EDMs in atoms in the lowest order. Also, since the commutator is equal to zero, the correction to the wavefunction (5.21) does not contribute to the Dirac charge or current densities j_μ.

The PV field (5.10) and the dynamic PS fields (5.1) will be examined in detail in the rest of this chapter. Here we turn our attention briefly to some of the other fields in the SME and discuss what possible parity-violating effects they could give rise to in atomic systems.

The a_μ term in the SME Lagrangian (5.4) is equivalent to interaction with a constant vector potential and does not give rise to observable effects in atoms. It is also easy to check directly that $a_\mu\boldsymbol{\alpha} = i[\hat{H}, a_\mu\boldsymbol{r}]$ and that therefore constant a_μ contributions vanish in atoms. We note, however, that due to the CPT-odd charge nonconservation — the fact that these fields may couple to different fermion species with different interaction strengths or charges — interactions involving more than one fermion species, such as in particle decays, may be affected.

The e_j interaction term can be expressed as $\hat{h}_{e_j} = \gamma^0\boldsymbol{e}\cdot\boldsymbol{p}$, which gives no effects in atoms. This can be demonstrated as follows. Using the relations $[\hat{H}, \boldsymbol{\gamma}] = -2\gamma^0\boldsymbol{p} + 2m_e\boldsymbol{\alpha}$, and $[\hat{H}, \boldsymbol{r}] = -i\boldsymbol{\alpha}$, which hold for the atomic Hamiltonian (5.13), this term can be expressed as

$$\hat{h}_{e_j} = \boldsymbol{e}\cdot[\hat{H}, im_e\boldsymbol{r} - \frac{1}{2}\boldsymbol{\gamma}], \tag{5.24}$$

which is in the form of Eq. (5.19) and hence gives no atomic effects due to Eqs. (5.21) and (5.23).

The d_{00} and d_{jk} terms in the SME (5.7) lead to interaction Hamiltonians proportional to $d_{00}\hat{\boldsymbol{\Sigma}}\cdot\boldsymbol{p}$, and $d_{jk}\hat{\Sigma}^j p^k$, respectively, where $\hat{\boldsymbol{\Sigma}} = \begin{pmatrix}\boldsymbol{\sigma} & 0\\ 0 & \boldsymbol{\sigma}\end{pmatrix}$ is the Dirac spin matrix. These terms both lead to parity-violating effects in atoms. We consider the d_{00} term for interactions with nucleons in Sec. 5.2.5. In the non-relativistic limit, this term will not lead to any atomic effects via an interaction with electrons, since in this limit it can be expressed $im_e[\hat{H}_{\rm NR}, \boldsymbol{\sigma}\cdot\boldsymbol{r}]$, where $\hat{H}_{\rm NR}$ is the non-relativistic Schrödinger Hamiltonian for the atomic system in question. The H_{0j}, g_{jkm}, and g_{j00} terms in (5.6) and (5.7) also lead to parity-violating effects in atoms, though we do not consider these in this thesis.

Many of the terms in the SME Lagrangian (5.3) are proportional to $\boldsymbol{p}$ in the non-relativistic limit and, because of the relation $\boldsymbol{p} = im_e[\hat{H}_{NR}, \boldsymbol{r}]$, give no atomic effects in this limit. The c_{0j} terms, which in the non-relativistic limit scale as $\boldsymbol{p}$, also produce P-odd effects due to relativistic corrections. Also, they introduce direction and frame dependent anisotropies in the electron energy-momentum relation [238, 279, 285].

The other terms in Eqs. (5.6) and (5.7) give rise to P-even interactions, and do not contribute to atomic parity-violating effects. These terms do, however, contribute to other interesting phenomena, such as bound-state energy shifts and modulations in clock transition frequencies. For more information and detailed discussions of many of these terms, see, e.g., Refs. [254–256, 284].

5.2.4 Perturbed wavefunctions and formulas for the atomic PNC amplitudes and EDMs

To analyse the dynamic effects, we apply first-order time-dependent perturbation-theory (TDPT) with a slow turn-on of the perturbation (see, e.g., Ref. [267] for further details), and find that the perturbed wavefunction corresponding to the unperturbed atomic state $|a\rangle$ due to the considered dynamic interactions is given by

$$|\widetilde{a(t)}\rangle = |a\rangle + \sum_n c_n^{(a)}(t)|n\rangle, \tag{5.25}$$

where

$$c_n^{(a)}(t) = \frac{\sum_\imath \langle n|\hat{V}_\imath|a\rangle}{(E_a - E_n)^2 - \omega_\phi^2}\left[-i\partial_t f(t) + (E_a - E_n)f(t)\right]. \tag{5.26}$$

Here, $f(t) = \eta\omega_\phi\sin(\omega_\phi t)$ and $\hat{V} = \gamma^5$ when we consider the PS γ^5 interaction (5.9), $f(t) = \zeta m_e\cos(\omega_\phi t)$ and $\hat{V} = i\gamma^0\gamma^5$ when we consider the PS $i\gamma^0\gamma^5$ interaction (5.8), and $f(t) = b_0\sin(\omega_b t)$ and $\hat{V} = \gamma^5$ when we consider the dynamic case of the PV γ^5 interaction (5.11). The index $\imath$ denotes summation over atomic electrons. In deriving Eq. (5.26), we have neglected the natural widths of the considered states. While we do not consider these widths in this chapter, they affect the phase in (5.26) when considering resonance phenomena, and will be discussed in more detail in the next chapter.

Therefore, the general PNC amplitude can be expressed to first order in the

PNC interaction as:

$$E^{a\to b} = \sum_{n,\imath,\jmath}\left\{\frac{\langle b|\boldsymbol{d}_\jmath|n\rangle\langle n|\hat{V}_\imath|a\rangle}{(E_a-E_n)^2-\omega_\phi^2}\left[-i\partial_t f(t)+(E_a-E_n)f(t)\right]\right.$$
$$\left.+\frac{\langle b|\hat{V}_\imath|n\rangle\langle n|\boldsymbol{d}_\jmath|a\rangle}{(E_b-E_n)^2-\omega_\phi^2}\left[i\partial_t f(t)+(E_b-E_n)f(t)\right]\right\}. \qquad (5.27)$$

Note that Eq. (5.27) also applies for induced atomic EDMs, for which the initial and final atomic states are identical; $b = a$.

It is now convenient to make one further approximation, namely that the energy of the field particle is much smaller than the energy separation between all opposite-parity states of interest, i.e. $\omega_\phi \ll |E_{a,b} - E_n|$ for all n. For a relatively light field particle, there is no loss of generality in making this assumption, except in the case where the atomic system of interest possesses close levels of opposite parity, which will be investigated for Dy, Yb, and Ba in the coming sections.

With this assumption we can present four comparatively simple formulas for the dynamic PNC amplitudes and atomic EDMs induced by the pseudoscalar interactions for both the γ^5 and $i\gamma^0\gamma^5$ cases presented in Eqs. (5.8) and (5.9):

$$E^{\rm PS}_{\rm PNC}(\gamma^5) = \eta\omega_\phi\sin(\omega_\phi t)K_{\rm PNC}, \qquad (5.28)$$

$$E^{\rm PS}_{\rm PNC}(i\gamma^0\gamma^5) = \frac{\zeta\omega_\phi}{2}\sin(\omega_\phi t)K_{\rm PNC}, \qquad (5.29)$$

$$d^{\rm PS}_{\rm EDM}(\gamma^5) = -2i\eta\omega_\phi^2\cos(\omega_\phi t)K_{\rm EDM}, \qquad (5.30)$$

and

$$d^{\rm PS}_{\rm EDM}(i\gamma^0\gamma^5) = -i\zeta\omega_\phi^2\cos(\omega_\phi t)K_{\rm EDM}. \qquad (5.31)$$

For the PV interaction presented in Eq. (5.11), the induced PNC amplitude is given by

$$E^{\rm PV}_{\rm PNC}(\gamma^5) = b_0(t)K_{\rm PNC}, \qquad (5.32)$$

where in the static case $b_0(t) = b_0$ is a constant, and in the dynamic case $b_0(t) = b_0\sin(\omega_b t)$ oscillates. In the dynamic case, the PV γ^5 interaction also gives rise to an oscillating atomic EDM, given by

$$d^{\rm PV}_{\rm EDM}(\gamma^5) = -2ib_0\omega_b\cos(\omega_b t)K_{\rm EDM}. \qquad (5.33)$$

In the above equations, we have defined $K_{\rm PNC}$ and $K_{\rm EDM}$ as

$$K_{\rm PNC} = \sum_{n,\imath,\jmath}\left[\frac{\langle b|\boldsymbol{d}_\imath|n\rangle\langle n|\gamma^5_\jmath|a\rangle}{E_a-E_n} + \frac{\langle b|\gamma^5_\jmath|n\rangle\langle n|\boldsymbol{d}_\imath|a\rangle}{E_b-E_n}\right] \qquad (5.34)$$

and

$$K_{\rm EDM} = \sum_{n,\imath,\jmath}\frac{\langle a|\boldsymbol{d}_\imath|n\rangle\langle n|\gamma^5_\jmath|a\rangle}{(E_a-E_n)^2}. \qquad (5.35)$$

These quantities will henceforth be referred to as the atomic structure coefficients.

The formulas (5.28–5.33) provide the connection between the atomic-structure calculations and the fundamental physics, which is necessary to extract quantitative information about the fields in question. In deriving these equations, we made use of the relation (5.15). Notice that the atomic structure coefficients are the same for both the γ^5 and $i\gamma^0\gamma^5$ cases. Note also that Eq. (5.35) shows that no EDMs are induced by these fields in atomic states of zero angular momentum, since in this case the scalar operator γ^5 couples only intermediate states of zero angular momentum, while the vector operator $\boldsymbol{d}$ cannot couple states of zero angular momentum.

For the dynamic fields, in the case where $\omega_\phi \sim |E_{a,b} - E_n|$, for a particular n, one has to use the complete equation (5.27) for the term corresponding to this n. In this case, which can occur in atomic systems which possess a pair of close opposite-parity levels, there may be additional enhancement from this term. The rest of the amplitude can be given by one of equations (5.28–5.33) with this particular term excluded. Note that in the limit that $\omega_{\phi/b} \gg |E_{a,b} - E_n|$ for all n (i.e. a heavy field particle), the expression (5.27) vanishes to lowest order.

In the non-relativistic limit, the matrix element of the γ^5 operator reduces to

$$\langle b|\gamma^5_\imath|a\rangle \overset{NR}{\to} i(E_b - E_a)\langle b'|\boldsymbol{\sigma}_\imath \cdot \boldsymbol{r}_\imath|a'\rangle, \tag{5.36}$$

where the wavefunctions $|n'\rangle$ are the two-component Pauli spinors (as opposed to the wavefunctions $|n\rangle$, which are four-component Dirac spinors). This term scales as $1/c$; the next lowest-order corrections are of order $1/c^3$. This means that in the non-relativistic case, the operator γ^5 can be replaced by the commutator $i[\hat{H}_{NR}, \boldsymbol{\sigma}\cdot\boldsymbol{r}]$, and therefore, by Eqs. (5.19–5.23), the $K_{\rm PNC}$ coefficients (5.34) vanish in the non-relativistic limit.

In the calculations, this leads to significant cancellation between the $\langle b|\boldsymbol{d}|\delta a\rangle$ and $\langle \delta b|\boldsymbol{d}|a\rangle$ terms in the summation (5.34). If the calculations were exact, this would eliminate the non-relativistic part of the amplitude and leave only the relativistic corrections, constituting the correct result. In practice, however, the cancellation leads to significant instabilities in the calculations. To bypass this problem, we express the γ^5 operator via the exact relation (proved below)

$$\gamma^5_\imath = i[\hat{H}, \hat{\boldsymbol{\Sigma}}_\imath \cdot \boldsymbol{r}_\imath] + 2\gamma^5_\imath \hat{K}_\imath, \tag{5.37}$$

which holds for the atomic Dirac-Coulomb Hamiltonian (5.13). Notice the similarity between the commutator term in (5.37) and the non-relativistic expression (5.36). Matrix elements of this commutator term between atomic states scale as $1/c$, whereas for the $\gamma^5\hat{K}$ term they scale as $1/c^3$. Here,

$$\hat{K} = \begin{pmatrix} \hat{k} & 0 \\ 0 & \hat{k} \end{pmatrix} \equiv \begin{pmatrix} -1 - \hat{\boldsymbol{\sigma}}\cdot\hat{\boldsymbol{l}} & 0 \\ 0 & -1 - \hat{\boldsymbol{\sigma}}\cdot\hat{\boldsymbol{l}} \end{pmatrix}, \tag{5.38}$$

where $\hat{\boldsymbol{l}}$ is the orbital angular momentum operator. Note that the spherical spinors, Ω_κ, are eigenstates of the $\hat{k}$ operator, with eigenvalue κ [the Dirac quantum number, $\kappa = (l - j)(2j + 1)$]:

$$\hat{k}\Omega_\kappa = \kappa\Omega_\kappa.$$

The commutator in Eq. (5.37) cancels exactly in the amplitude, and does not contribute; see Eqs. (5.19–5.23). We can, therefore, calculate the $K_{\rm PNC}$ coefficients free of large cancellation by using only the last term in (5.37). Note that there are no such cancellations in the summation in Eq. (5.35) for the $K_{\rm EDM}$ coefficients, which can be calculated directly with high numerical precision.

To prove Eq. (5.37), first let

$$G = -2\gamma^0\gamma^5(\gamma^0 K) = \begin{pmatrix} 0 & 2K \\ 2K & 0 \end{pmatrix}, \tag{5.39}$$

$$L = i[H, \boldsymbol{\Sigma}\cdot\boldsymbol{r}]. \tag{5.40}$$

Then,

$$\begin{aligned} L &= i\begin{pmatrix} 0 & -2i\boldsymbol{\sigma}\cdot\boldsymbol{L} - 3i \\ -2i\boldsymbol{\sigma}\cdot\boldsymbol{L} - 3i & 0 \end{pmatrix} \\ &= \begin{pmatrix} 0 & -2K \\ -2K & 0 \end{pmatrix} + \gamma^5 \\ \therefore \gamma^5 &= L + G \end{aligned} \tag{5.41}$$

(The above is valid for many-particle states, with the summation over electrons suppressed).

5.2.5 Interactions with nucleons and via hadronic mechanisms

Note that PS and PV cosmic fields can also interact with the nucleus, giving rise to nuclear anapole moments and nuclear Schiff moments, which contribute to nuclear-spin-dependent (NSD) PNC amplitudes and atomic EDMs respectively, see, e.g., [267, 268, 286]. In Ref. [267], it was shown that an interaction of the form (5.9) can give rise to a nuclear anapole moment (AM), a P-odd, T-even nuclear moment that normally arises due to parity-violating nuclear forces [14].

Here, we consider nuclear anapole moments induced by the interaction between nucleons and the static PV interaction of the form (5.11), which in the non-relativistic limit reads [267]

$$\hat{W}_{\rm NR} = b_0^N \boldsymbol{\sigma}\cdot\boldsymbol{p}/m_N, \tag{5.42}$$

where b_0^N is the cosmic-field amplitude including the interaction strength between the cosmic field and a nucleon, and $\boldsymbol{\sigma}$, $\boldsymbol{p}$ and m_N are the spin, momentum and mass of the nucleon. We also consider the interaction of the SME d_{00} term in (5.3) with nucleons. In the non-relativistic limit, this term leads to an interaction Hamiltonian of the form

$$\hat{W}_{\rm NR} = -d_{00}^N \boldsymbol{\sigma}\cdot\boldsymbol{p}. \tag{5.43}$$

Both interactions (5.42) and (5.43) will contribute to the nuclear AM. The Hamiltonian representing the NSD PNC interaction of a valence electron with the nuclear AM is given by

$$\hat{h}_{\rm AM} = \frac{G_F K_I}{\sqrt{2}}\frac{\boldsymbol{\alpha}\cdot\boldsymbol{I}}{I}\varkappa\,\rho(\boldsymbol{r}), \tag{5.44}$$

where $K_I = (I+1/2)(I+1)^{-1}(-1)^{I+1/2-l_N}$, with l_N being the orbital angular momentum of the valence nucleon, $\boldsymbol{I}$ is the nuclear spin, and ρ is the nuclear density [14] (see also [28]). The dimensionless constant $\varkappa = \varkappa_a + \varkappa_{\rm CF}$ quantifies the magnitude of the AM, and has contributions both from parity-violating nuclear forces, $\varkappa_a$ (the conventional AM), and from the interaction of the cosmic field with the nucleons, $\varkappa_{\rm CF}$.

From Eq. (5.44), we see that the interaction of atomic electrons with the cosmic-field–induced AM has exactly the same form as their interaction with the conventional (parity-violating nuclear-force–induced) AM, the only difference being the source of the moment. This means that no new atomic calculations are required, and a limit on the magnitude of $\varkappa_{\rm CF}$, and hence b_0^N and d_{00}^N, can be extracted directly from existing experiments and calculations.

The magnitude of the AM, $\varkappa_{\rm CF}$, is related to the field parameters b_0^N and d_{00}^N by the equation

$$\varkappa_{\rm CF} = \frac{2\sqrt{2}\pi\alpha\mu_N\langle r^2\rangle}{G_F m_N}(b_0^N - m_N d_{00}^N), \tag{5.45}$$

where $\langle r^2\rangle$ and μ_N are the mean-square radius and magnetic moment (in nuclear magnetons) of the valence nucleon, respectively, and $\alpha \approx 1/137$ is the fine-structure constant; see Refs. [14, 267] for more details. We take $m_N = 0.94$ GeV, $\mu_p = 2.8$, $\mu_n = -1.9$, and $\langle r^2\rangle = (3/5)r_0^2A^{2/3}$, where $r_0 = 1.2$ fm and A is the atomic mass number.

The dynamic PS and PV fields (5.9) and (5.11) also induce oscillating anapole moments in atomic nuclei. This was considered in Ref. [267]. In the case of a static PV cosmic-field–induced AM, one can immediately extract limits on the coupling of the fields with protons via the existing NSD PNC calculations and measurements in Cs [4] and Tl [34]. This is not the case for the dynamic interactions. For this reason, we consider only the static case.

5.3 Methods for atomic structure calculations

We examine a number of different systems, and use different computational methods for the *ab initio* relativistic calculations. We outline these briefly and refer the reader to the relevant sources for more detailed information.

5.3.1 Single-valence electron systems

For atoms and ions with one valence electron above a closed-shell core, we employ the correlation potential method [5, 199, 219, 244], as described in Appendix A.4.2. Core polarisation and the PNC and $E1$ interactions are included via the time-dependent Hartree-Fock (TDHF) method [5, 199, 219, 244], as described in appendix A.6.1. Note that in solving the TDHF equations (A.40), we have neglected the contribution from ω_ϕ, i.e. we have assumed that $\omega_\phi \ll |E_{\rm core} - E_{a,b}|$. The core excitation energy is very large, so this should be valid in all cases.

The PNC and EDM atomic structure coefficients (5.34) and (5.35) can then be calculated using single-particle energies and wavefunctions, with the operators $\boldsymbol{d}_\imath$ and $\gamma^5_\imath$ replaced by the effective single-particle operators including the core-polarisation corrections: $\sum_\imath \boldsymbol{d}_\imath \to \boldsymbol{d} + \delta\hat{V}_{E1}$, $\sum_\imath \gamma^5_\imath \to \gamma^5 + \delta\hat{V}_{\gamma^5}$. This is how we calculate the $K_{\rm EDM}$ values, however, for the $K_{\rm PNC}$ values we use a slightly different method due to the instabilities caused by the large cancellation discussed previously.

By expressing the second term on the right-hand side of Eq. (5.37) as

$$2\gamma^5\hat{K} = -2\gamma^0\gamma^5(\gamma^0\hat{K}),$$

and noting that single-particle states are eigenstates of $\gamma^0\hat{K}$ (with eigenvalue κ), we can use Eq. (5.15) to express the PNC (single-particle) matrix elements as

$$\langle\psi_n|2\gamma^5\hat{K}|\psi_a\rangle = \frac{-\kappa_a}{2m_e}(\mathcal{E}_n - \mathcal{E}_a)\langle\psi_n|\gamma^5|\psi_a\rangle. \tag{5.46}$$

Upon substitution into the summation for $K_{\rm PNC}$, we can invoke the closure relation and the amplitude for single-particle states reduces to

$$K_{\rm PNC} = \frac{1}{m_e}(\kappa_b + \kappa_a)\langle\psi_b|\gamma^5(\boldsymbol{d} + \delta V_{E1})|\psi_a\rangle, \tag{5.47}$$

where we have neglected the core polarisation due to the $2\gamma^5\hat{K}$ operator, since it is highly suppressed. This expression requires no summation over intermediate states, does not contain significant cancellation, and can be calculated with relatively high accuracy. We include correlations by using the BOs ψ_a and ψ_b for the valence states a and b in Eq. (5.47).

For the $K_{\rm EDM}$ coefficients, the first term on the right-hand side of Eq. (5.37) does not cancel. In fact, this term dominates the amplitude [since it leads almost directly to the non-relativistic approximation (5.36)] and scales as $1/c$, whereas the second term scales as $1/c^3$. Inserting $\gamma^5 \approx i[\hat{H}, \hat{\boldsymbol{\Sigma}}\cdot\boldsymbol{r}]$ [see Eq. (5.36) and (5.37)] into Eq. (5.35), we see that the $K_{\rm EDM}$ coefficients for ${}^2S_{1/2}$ states are approximately proportional to the static dipole polarisability, with corrections on the order of $(1/c)^3$. The constant of proportionality is determined by Eq. (5.37) and the angular integrals [287]:

$$\begin{aligned} K_{\rm EDM}(z) &\simeq -i\sum_n \frac{\langle a|d_z|n\rangle\langle n|\hat{\boldsymbol{\Sigma}}\cdot\boldsymbol{r}|a\rangle}{E_a - E_n} \\ &\approx \frac{i}{2e}\alpha_0, \end{aligned} \tag{5.48}$$

where the scalar electric dipole polarisability, α_0, is given by

$$\alpha_0 = -\frac{2e^2}{3(2J_a+1)}\sum_n \frac{|\langle a||r_z||n\rangle|^2}{E_a - E_n}, \tag{5.49}$$

where $\langle a||r_z||n\rangle$ is the z component of the reduced matrix element of the $\boldsymbol{r}$ operator. [Equation (5.48) relies on the fact that the radial integrals and energies depend only on the n, l quantum numbers, and not on j, in the non-relativistic limit.] This can be used as an independent test of the calculations. Rougher (and far less accurate) relations can also be derived for other states, e.g. the ${}^2P_{1/2}$ ground state of Tl, which are useful for order-of-magnitude estimates.

It is therefore an interesting possibility to consider effects arising in Rydberg atoms—atoms which contain one electron in a very highly excited state. Such atoms have hugely enhanced polarizabilities, and will therefore have correspondingly enhance effects due to parity-violating cosmic fields.

Note that in the methods described above we have not included the core polarisation contribution that comes from the simultaneous action of the $E1$ and

PNC fields, the so-called "double core polarisation", see Ch. 4. Core polarisation amounts to only a small correction to the quantities considered here, so the even smaller double core polarisation can be safely neglected in most cases. In the case of Tl, however, where the single-particle approach is less valid, this may have a significant impact on the accuracy.

5.3.2 Two valence electron atoms

We treat Yb and Ba as systems with two valence electrons above a closed shell core, and follow closely the methods employed recently [40, 123] to calculate conventional PNC effects in these atoms. We make use of the combined configuration interaction (CI) and many-body perturbation theory (MBPT) method developed in Ref. [225]; the specific form that we use is described in Appendix A.7. Interactions with external fields and core polarisation are taken into account using the TDHF method as above.

We also introduce a scaling parameter into the correlation potential, as in Ch. 3: $\hat{\Sigma}_1 \to \lambda_l \hat{\Sigma}_1$ in Eq. (A.48), where λ_l can take different values for different values of orbital angular momentum, l, (s, p, d etc.) and $\lambda_l \approx 1$. The scaling parameters serve two purposes. Firstly, since the single-particle energies in Eq. (5.46) are relatively sensitive to λ_l, whereas the radial integrals are comparatively insensitive, we can use this as a test of the stability of the calculations. We do this and find satisfactory stability for both the matrix elements and the overall PNC amplitudes. Secondly, in the case of the PNC transition in Yb, a system that possesses a pair of relatively close levels of opposite parity, we can use the scaling parameters to fit the important energy differences to the experimental energies, as was done in Sec. 3.4. This is important, since even modest errors in individual energy levels may lead to an error of orders-of-magnitude in an energy interval when it is particularly small. See Sec. 3.4 for a detailed discussion on this point.

The matrix elements are then computed from the sum of the single-particle contributions. For the single-particle contributions, we use Eq. (5.46), which removes all significant cancellation into a small factor $\sim 1/c^3$ [two factors of c come from the coefficient m_e in (5.46), the third comes from the lower (small) component of the Dirac radial wavefunction].

Note that we can also use Eq. (5.36) to approximately express Eq. (5.46) as

$$\langle\psi_n|2\gamma^5\hat{K}|\psi_a\rangle \approx \frac{-i\kappa_a}{2m_e}(\mathcal{E}_n-\mathcal{E}_a)^2\langle\psi'_n|\boldsymbol{\sigma}\cdot\boldsymbol{r}|\psi'_a\rangle, \tag{5.50}$$

which scales as $1/c$ (the next lowest corrections are of order $1/c^3$). Equations (5.46) and (5.50) have very different radial integrals; as such, performing the calculations using both these equations serves as a good numerical test of our method. We find good agreement between both the matrix elements and the amplitudes calculated using Eqs. (5.46) and (5.50). This is important, since it justifies neglect of core polarisation due to the $2\gamma^5\hat{K}$ operator.

5.3.3 Dysprosium

The feature of Dy that makes it a particularly interesting system for the study of atomic PNC is the existence of two nearly degenerate states of opposite parity and the same total angular momentum, $J = 10$, at $E = 19797.96$ cm^{-1}. We use the notation A for the even-parity state and notation B for the odd-parity state, following Ref. [89]. The PNC experiment in Dy is different to those done, for example, in Cs, and it is the quantity $\langle A|\gamma^5|B\rangle$ that is of most interest. This is because, in Dy, the mixing of the opposite parity A and B states is observed directly, whereas in in the other experiments it is transitions between states of the same parity that are observed [89] (the parity-violating part of these transitions is enabled by a mixing of many opposite-parity states).

The method we use for the calculations in Dy follows almost exactly previous calculations of conventional PNC effects in this system [91], with the only exception being the interchange of the operator of the electron-nucleus weak interaction (5.12) with those for the parity-violating interactions with cosmic fields, (5.9) and (5.11). We use the particular CI method described in much greater detail in Ref. [288]. To construct the single-electron orbitals, we use a V^N potential, where $N = 66$ is the total number of electrons.

A different V^N Hartree-Fock potential is used for each different configuration, then the valence states found in the Hartree-Fock calculations are used as basis states for the CI calculations. This helps account for the fact that single-electron states actually depend on the configurations. While it is possible to account for this dependence within the CI calculations, it requires a complete set of single-electron states. These would then be used to construct the many-electron basis states by redistributing the valence electrons over the single-electron basis states. Then the actual many-electron states are found by diagonalizing the matrix of the effective CI Hamiltonian [289]. This approach works well in the case of a few valence electrons, e.g. neutral Ba and Ra as discussed above. However, for the twelve valence electrons of Dy, it would lead to a matrix of enormous size making it practically impossible to saturate the basis with limited computing resources. The results with an unsaturated basis are unstable and strongly depend on where the basis is truncated. Therefore, it is preferable to account for the differences in the configurations at the Hartree-Fock, rather than the CI, stage of the calculations.

After the self-consistent Hartree-Fock procedure is done for each necessary configuration, the effective CI Hamiltonian for the valence states of Dy, with $M = 12$ valence electrons, is expressed as

$$\hat{H}^{\rm eff} = \sum_{i=1}^{M} \hat{h}_1(\boldsymbol{r}_i) + \sum_{j<i} \frac{e^2}{r_{ij}}, \tag{5.51}$$

where

$$\hat{h}_1 = \boldsymbol{\alpha}\cdot\boldsymbol{p} + m_e(\gamma^0 - 1) - V^{\rm nuc} + U^{\rm HF} + \delta V_{\rm p}. \tag{5.52}$$

Here $U^{\rm HF}$ is the Hartee-Fock potential due to the $N - M$ core electrons. We do not use the *ab initio* correlation potential as described above, instead it is the term $\delta V_{\rm p}$ in Eq. (5.52) that simulates the effect of valence-core correlations. It is known as the polarisation potential, and has the form

$$\delta V_{\rm p} = -\frac{\alpha_{\rm p}}{2(r^4 + a_0^4)}, \tag{5.53}$$

where $\alpha_{\rm p}$ quantifies the polarisation of the core, and a_0 is a cut-off parameter, for which we use the Bohr radius. The term $\alpha_{\rm p}$ is treated as a parameter and is scaled to reproduce the correct experimental energies. The effect that adding

Table 5.1 Calculations of the PNC and EDM atomic structure coefficients [$j_z = \min(j_a, j_b)$] for several atomic systems. Valid in the case that $\omega_\phi \ll |E_{a,b} - E_n|$. Values are presented in atomic units.

	PNC		EDM	
	Transition	$K_{\rm PNC}$ ($i10^{-6}$)	State	$K_{\rm EDM}$
H	$1s$–$2s$	0.1447(2)	$1s$	0.0164(1)
Li	$2s$–$3s$	0.219(3)	$2s$	0.60(1)
Na	$3s$–$4s$	0.224(4)	$3s$	0.61(1)
K	$4s$–$5s$	0.242(4)	$4s$	1.09(5)
	$4s$–$3d_{3/2}$	−0.307(6)		
Cu			$4s$	0.16(3)[a]
Rb	$5s$–$6s$	0.247(5)	$5s$	1.22(8)
Ag			$5s$	0.17(5)[a]
	$5s$–$4d_{3/2}$	−0.30(1)		
Cs	$6s$–$7s$	0.256(5)	$6s$	1.6(2)
	$6s$–$5d_{3/2}$	−0.22(3)		
Ba	${}^1S_0$–${}^3D_1$	−0.5(1)		
Ba$^+$	$6s$–$5d_{3/2}$	−0.02(1)		
Yb	${}^1S_0$–${}^3D_1$	−8(2)		
Au			$6s$	0.12(4)[a]
Tl	$6p_{1/2}$–$6p_{3/2}$	0.22(5)	$6p_{1/2}$	0.2(1)
Fr	$7s$–$8s$	0.253(6)	$7s$	1.3(2)
	$7s$–$6d_{3/2}$	−0.25(3)		
Ra$^+$	$7s$–$6d_{3/2}$	−0.08(3)		

[a] From polarisability calculations [290–292].

or removing basis configurations, and making small changes in the values $\alpha_{\rm p}$, has on the amplitude is a good way to test the accuracy of the calculations.

Since the states of interest in Dy are practically degenerate, the commutator term in Eq. (5.37) does not contribute to the matrix element. We therefore calculate the matrix elements of the PNC interaction directly from the single-particle contributions using Eq. (5.46). We use the same configurations and values for $\alpha_{\rm p}$ (≈ 0.4 a.u.) as in Ref. [91].

5.4 Results and discussion

5.4.1 Values and accuracy of the atomic structure coefficients

Results of our calculations for the atomic structure coefficients $K_{\rm PNC}$ and $K_{\rm EDM}$ [defined in equations (5.28) through (5.35)] are presented in Table 5.1. We present z-components, with $j_z = \min(j_a, j_b)$.

In order to estimate the uncertainty, we calculate the values $K_{\rm PNC}$ without including any correlations, including correlations to second-order ($\Sigma^{(2)}$), and including correlations to all-orders (see Sec. 5.3). We take the all-order results as the midpoint, and estimate the uncertainty as the difference between this and the pure Hartree-Fock (no correlations) calculations. The second-order results are used as an extra test; the deviation of the second-order results from the all-order ones is significantly smaller than the assumed uncertainty. We also examine the effect that including core polarisation has on the amplitudes and note that its effect is also smaller than the assumed uncertainty.

Note that we treat Tl here as a single valence electron system, where the $6s^2$ electrons are treated as core states. In order for this treatment of Tl to yield accurate results one needs to take into account many higher-order correlation corrections, such as ladder-diagrams [190]. In particular, the double core polarisation may give a significant contribution in this approximation, see Ch. 4. Therefore, for the Tl $K_{\rm PNC}$ we use only the second-order correlation potential, and the uncertainty is taken as the size of these correlation effects. The uncertainty attributed to Tl takes into account the omitted core-polarisation effects. An alternative method for calculations in Tl is to treat it as a three-valence-electron system, and use the CI+MBPT method, see, e.g., [181]. In this approach, the double core polarisation is taken into account automatically. The trivalent CI+MBPT method is significantly more computationally demanding than the methods we employ in this chapter, and is not necessary at the currently desired level of accuracy; more complete calculations can be performed when further experimental work in this area is undertaken.

For H, we perform the calculations both using exact Dirac-Coulomb wavefunctions and numerical wavefunctions including finite-nuclear-size effects. The difference between these two approaches is negligible at the desired accuracy. The $\langle 2s|\gamma^5|2p\rangle$ matrix element is almost identically zero numerically (without including radiative corrections). This means that despite being a seemingly good candidate for a Dy-type stark-interference experiment, where the PNC matrix element is measured directly (see [89]), H is unlikely to yield informative results in this case. The uncertainty estimates in the H $1s$–$2s$ $K_{\rm EDM}$ value comes mainly from a truncation of the basis used for the summation, and the uncertainty for the $1s$ $K_{\rm PNC}$ value reflects the omission of radiative quantum electrodynamics effects, which become important at this scale ($\sim 1/c^3$).

In the case of atomic EDMs, there is no cancellation as for the $K_{\rm PNC}$ values, and these magnitudes are comparatively stable. The accuracy of these calculations is expected to be relatively high, with the dominating uncertainty coming from the inclusion of electron correlations. We take as an estimate of the uncertainty the difference between the calculations performed with the second-order and the all-order correlation potential. As noted above, the expression for the EDM atomic structure coefficients (5.35) can be reduced to a form very similar to that of the electric dipole scalar polarisability (5.48). We use this fact as a test of our calculations and find excellent agreement using published polarisability values; better than 1% for Li and Na, and better than 5% for most other atoms, see, e.g., [293]. The decline in agreement for the higher Z systems is due to the larger role of relativistic effects here, since Eq. (5.48) is a non-relativistic approximation.

From the results in Table 5.1, we see that the magnitudes of PNC amplitudes in general increase with increasing atomic mass. This can be understood as a relativistic effect, since the amplitude vanishes in the non-relativistic limit. However, we note that the magnitudes increase considerably more slowly with Z than the Z^3 dependence of conventional NSI PNC effects induced by Z^0-boson exchange between atomic electrons and nucleons [24, 294]. This means that light atoms may also be suitable candidates for searches of pseudoscalar and pseudovector cosmic-field–induced effects.

Since the considered interaction is one with an external cosmic field, as op-

Table 5.2 Matrix elements of the $2\gamma^5\hat{K}$ operator for Ba, Ra, Dy, and Yb between nearly-degenerate opposite-parity levels.

	A	B	ΔE_{BA} (cm^{-1}) [188]	$\langle B\vert 2\gamma^5\hat{K}\vert A\rangle$ (i a.u.)[a]
Ba	$5d^2\,(^1D_2)$	$5d6p\,(^1D^o_2)$	-12.34	$0.3(1)\times 10^{-9}$
Dy	$4f^{10}5d6s\,(J=10)$	$4f^95d^26s\,(J=10)$		$0.7(2)\times 10^{-8}$
Yb	$5d6s\,(^3D_1)$	$6s6p\,(^1P^o_1)$	-579.12	$0.29(6)\times 10^{-8}$

[a] For ease of comparison with the literature, note that 0.7×10^{-8} a.u. = 50 MHz.

posed to a nuclear-sourced field as in the case of conventional atomic PNC, the amplitudes are not necessarily restricted by the value of the wavefunctions on the nucleus. In conventional PNC, this has the effect of greatly suppressing contributions from higher orbital angular momentum (l) states, in which electrons do not spend as much time near the nucleus. This limits the magnitude of the PNC effect in many transitions, such as the A–B matrix element in Dy, that have otherwise ideal conditions (high nuclear charge Z, very close opposite-parity levels). Such restrictions were noted very early, see, e.g., [27]. In the cosmic-field–induced PNC effect, however, this restriction does not apply.

For the dynamic interactions, the results presented in Table 5.1 are valid only in the case that $\omega_\phi \ll |E_{a,b}-E_n|$. As stated above, this should generally not be a problem, except for when there exists a pair of close opposite parity levels in the summation (5.27). Such a pair of close levels appears in Ba, Dy, and Yb. In Table 5.2, we present calculations of the $2\gamma^5\hat{K}$ matrix element between states that correspond to close levels of opposite parity in these atoms.

For Dy, it is actually the quantity $\langle B|\gamma^5|A\rangle$, as opposed to the PNC amplitude $E_{\rm PNC}$, that is directly of interest, since the transitions between B and A are directly measured in the Dy experiments. To determine the uncertainty in this quantity, we examine the effect of removing configuration states from the basis. Note that in the conventional PNC case, the $\langle A|\hat{h}_{Q_W}|B\rangle$ matrix element is highly dependent on the configurations used [91]. We perform the calculations including only the leading two configurations for each state, as well as including all twelve of the configurations considered in Ref. [91], and many combinations in between. We find, in fact, that this makes little difference to the final amplitude, meaning it is quite stable. We take the uncertainty in this value to cover the range of values obtained between using only the leading two configurations for each state and using all twelve considered basis configurations. Despite making relatively large changes to the energies, modest modifications to $\alpha_{\rm p}$ make only small changes to the amplitude; smaller than the assumed level of accuracy.

5.4.2 Limits on the interactions of a pseudovector cosmic field

For the static case, the PV interaction will manifest itself as a small addition to the PNC amplitude of a transition between two states of the same nominal parity. Therefore, by combining the results of the conventional (Q_W induced) PNC experiments and calculations with the calculations of the cosmic-field–induced PNC amplitude [given by Eq. (5.32) and Table 5.1], it is possible to extract limits on the values of the PV cosmic-field coupling constants b_0. We present these limits in Table 5.3.

Table 5.3 Comparison of calculated and observed PNC amplitudes in Cs, Tl and Yb, and the relevant weak matrix element in Dy, and extraction of limits on the electron–cosmic-field interaction parameter b_0^e.

		$E_{\rm PNC}^{Q_W}$ ($i10^{-11}$ a.u.)				
Transition		Experiment		Theory		$\lvert b_0^e\rvert$ limit (GeV)
Cs	$6s-7s$	0.8353(29)	[4]	0.8428(38)	[11]	$2{\times}10^{-14}$
Tl	$6p_{1/2}-6p_{3/2}$	24.8(2)	[34]	25.6(7)	[39]	$2{\times}10^{-12}$
Yb	${}^1S_0-{}^3D_1$	87(14)	[36, 85]	110(14)	[40]	$2{\times}10^{-12}$

	$\langle A\vert\hat{h}_{Q_W}\vert B\rangle$ ($i10^{-16}$ a.u.)[a]				
	Experiment		Theory		$\lvert b_0^e\rvert$ limit (GeV)
Dy	3.5(4.5)	[89]	6(6)	[91]	$7{\times}10^{-15}$

[a] 3.5×10^{-16} a.u. = 2.3 Hz; 6×10^{-16} a.u. = 4 Hz.

The most stringent limit comes from the results in Dy. This is due mainly to the significantly low absolute uncertainty in both the theoretical and experimental limits on the $\hat{h}_{Q_W}$ matrix element.

We have used the available NSD PNC measurements for Cs and Tl to extract limits on the constants b_0^p and b_0^n that quantify the interaction strength of a PV cosmic field (5.42) with protons and neutrons, respectively. We also use these measurements to constrain the constants d_{00}^p and d_{00}^n that appear in (5.43), which quantify the interaction strengths of protons and neutrons with the SME $d_{\mu\nu}$ tensor field (5.7). We present these limits in Table 5.4. In extracting the limits, we have taken the values of the conventional (nuclear-forced induced) AM as $\varkappa_a=0.19$ and assumed a 30% uncertainty for the nuclear theory for Cs, and $\varkappa_a=0.17$ with 60% uncertainty for Tl, see, e.g., Ref. [28]. The nuclear spin in both Cs and Tl is primarily due to the valence protons. For Tl, we use a single-particle picture and therefore extract limits for the proton only. For Cs, we use the expectation values of the spin occupation from Ref. [275] to determine limits for both protons and neutrons.

These field-nucleon coupling limits are to be compared with the field-electron coupling limits obtained from PNC amplitude measurements and from direct determination of weak interaction matrix elements, which are tabulated in Table 5.3. The latter limits are by far the more stringent. Note that ongoing AM measurements with Fr, Yb, and BaF will also lead to limits on PV cosmic-field couplings to protons and neutrons [36, 83, 85, 124, 128].

Table 5.4 Theoretical and observed values for the nuclear AM constant $\varkappa_a$ for Cs and Tl, and the extracted limits on the proton– and neutron–cosmic-field interaction parameters $b_0^{p,n}$ and $d_{00}^{p,n}$.

	$\varkappa_a$			b_0 limits (GeV)		d_{00} limits	
	Observed		Theory	$\lvert b_0^p\rvert$	$\lvert b_0^n\rvert$	$\lvert d_{00}^p\rvert$	$\lvert d_{00}^n\rvert$
^{133}Cs	0.364(62)	[4, 48]	0.15 — 0.23[a]	$4{\times}10^{-8}$	$2{\times}10^{-7}$	$5{\times}10^{-8}$	$2{\times}10^{-7}$
^{203,205}Tl	0.22(30)	[34, 118]	0.10 — 0.24[b]	$8{\times}10^{-8}$		$9{\times}10^{-8}$	

[a] Refs. [110, 113, 115, 116]

[b] Refs. [110, 113, 116]

5.5 Conclusion

In this chapter, relativistic calculations were performed for parity nonconservation amplitudes and atomic electric dipole moments induced by the interaction of pseudoscalar and pseudovector cosmic fields with atomic electrons for H, Li, Na, K, Cu, Rb, Ag, Cs, Ba, Ba$^+$, Dy, Yb, Au, Tl, Fr, and Ra$^+$. We have shown that a static pseudoscalar cosmic field cannot give rise to observable P-odd effects in atoms in the lowest order, but in contrast, a static pseudovector cosmic field can. Candidates for such cosmic fields include dark matter (such as axions) and dark energy, as well as a number of more exotic sources, e.g. those described by Lorentz-invariance violating standard-model extensions [255].

For the case of a static pseudovector field, these calculations can be combined with existing parity nonconservation measurements to extract limits on the strength of the electron–cosmic-field coupling. From existing data and calculations, we find that Dy gives the most stringent limit for the interaction strength between the temporal component of the pseudovector field and the atomic electrons: $|b_0^e| < 7\times10^{-15}$ GeV in the laboratory frame of reference (1σ). Also, using the existing measurement of the nuclear anapole moment of Cs and the limit on the value of the Tl nuclear anapole moment, in conjunction with their respective theoretically predicted values, we extract limits on the strength of the proton–cosmic-field couplings b_0^p and d_{00}^p. By taking into account nuclear many-body effects [275], we also extract 1σ limits on the strength of the neutron–cosmic-field couplings. We find that the more stringent limits of $|b_0^p| < 4\times10^{-8}$ GeV and $|d_{00}^p| < 5\times10^{-8}$ for protons, and $|b_0^n| < 2\times10^{-7}$ GeV and $|d_{00}^n| < 2\times10^{-7}$ for neutrons come from the anapole moment results for Cs. These limits on the temporal components b_0, which are derived from P-odd fermion effects, are complementary to the existing limits on the interaction of the spatial components $\boldsymbol{b}$ of a static PV field with electrons, protons, and neutrons, which are derived from the P-even fermion effects, see, e.g., Ref. [284].

Finally, we mention that cosmic-field searches need not be restricted only to atomic systems. Searches for cosmic-field–induced electric dipole moments can also be performed in solid-state systems. Static electron electric dipole moment experiments in ferro-electrics are discussed in Refs. [173, 174], for instance, and solid-state systems have already been proposed for use in the detection of axion dark matter (see, e.g., Refs. [295, 296]). We also mention that transient electric dipole moments may also be induced by cosmic fields in the form of topological defects [297]. Topological defect dark matter can also be detected with a global network of detectors that can be used to search for coherent-in-time signals, such as with magnetometers [298] or atomic clocks [299]. Note that such a global network of atomic clocks already exists in the form of GPS satellites, meaning that this form of dark matter can be searched for by simply analysing the existing GPS data [299].

CHAPTER 6:
New Methods for Axion Dark Matter Detection

In this chapter, I expand on the general results of the previous chapter, applying them to the specific case of axion dark matter in more detail. I present our calculations of the parity and time-invariance violating effects (specifically, electric dipole moments) that an axion field would induce in atoms. Crucially, the effects considered here are linear in the small parameter that quantifies the interaction strength between the dark matter particles and ordinary matter particles; most current dark matter and axion searches rely on effects that are proportional to quadratic and higher powers of this parameter. Oscillating electric dipole moments have the potential to be measured with very high accuracy, and experimental techniques in this field are evolving fast, making this a particularly exciting area for potential discovery in the near future. Pairs of closely spaced opposite parity levels that are found in atomic dysprosium and certain diatomic molecules may also lead to a significant enhancement in these effects. Note that in this chapter, I depart from the usual convention of atomic units, and employ the more standard natural relativistic units ($\hbar = c = 1$)*, in order to aid with comparisons with other works.*

6.1 Introduction

One of the most important unanswered questions in fundamental physics today is the so-called strong CP problem. This refers to the puzzling observation that quantum chromodynamics (QCD) does not appear to violate the combined charge-parity symmetry (CP), despite there being no known theoretical reason for its conservation, see, e.g., Refs. [303–308]. One compelling resolution to this problem comes from the Peccei-Quinn (PQ) theory, in which an additional global U(1) symmetry, known as the PQ symmetry, is introduced into the standard model (SM) QCD Lagrangian and is subsequently broken both spontaneously and explicitly [305, 306] (see also [309–312]). The breaking of the PQ symmetry gives rise to a pseudoscalar boson known as the axion. This particle causes the QCD CP symmetry breaking parameter to become effectively zero, thus in principle alleviating the strong CP problem. For more detail on this topic, the reader is directed to the review in Ref. [313] (see also Refs. [73, 314]).

Another crucial outstanding problem in modern physics is the question of dark matter (DM). The astrophysical evidence for the existence of DM is overwhelming, see, e.g., Refs. [269, 315]; however, its composition is not known, and despite years of searching no confirmed terrestrial observation has yet been made (see Ch. 7 for a discussion of a possible exception). There have been many suggestions put forward that attempt to provide a theoretical framework for DM, though no single theory is a clear leading candidate, see, e.g., Refs. [73, 269]. What we do know is that the energy content of the universe is dominated by DM ($\sim 23\%$) and dark energy ($\sim 73\%$), see, e.g., Ref. [316]. Dark energy is proposed to account for the observed accelerating expansion of the Universe [317, 318]; even less is known about the composition of dark energy than of DM.

The axion, since emerging as a compelling solution to the strong CP problem, has in fact been identified as a promising DM candidate [319] (see also [320]). Axions may constitute a large fraction of the DM in the observable universe. Thus axions, if detected, would have a real potential to resolve both the DM and strong CP problems. Many methods have been proposed and applied to the search for axions; for a recent review, I direct the reader to Ref. [321] (see also Refs. [73, 313, 322–324]).

The axion, though neutral, couples to photons via an effective electromagnetic anomaly [325]. This coupling is used in many currently running experiments to search for axions and other axion-like particles (ALPs) [325, 326]. Such experiments include attempts to convert DM axions into photons in the presence of very strong magnetic fields (e.g. the ADMX experiment [327]), as well as the "light shining through a wall" experiments, in which photons traverse an optical barrier by converting to axions and back again (e.g. ALPS [328]); see also the CAST [329] and IAXO [330] experiments. See, e.g., Ref. [322] for a review on searches for axion and ALP DM. These experiments rely on effects proportional to quadratic or higher powers of the axion-photon coupling constant, which, due to the anomalous nature of the interaction, is exceptionally small.

The nature of the effect that such searches exploit means that these experiments are useful for detecting axions only over a limited range of the relevant parameter space. There is no *a priori* reason to exclude the possibility of particles that lie outside this region; simultaneous experiments are necessary to search for axions and ALPs through as large a range of parameters as possible.

The prospect that atomic systems could be used as a probe for DM, axions, and other cosmic fields has been considered extensively in the literature, see, e.g., Refs. [258, 261, 267, 272, 285, 286, 295, 299, 331, 332]. Signatures of scalar DM (including axions) can also be sought using highly precise atomic spectroscopy, as recently considered in Ref. [333]. While the effects induced in atoms by such a cosmic field may be small, the advantage of using atoms is that atomic physics methods are highly advanced, and both the experimental and theoretical accuracy, and hence sensitivity, can be high.

6.2 Theory

Axions have the following effective couplings to standard model particles:

$$\begin{aligned} \mathcal{L} = \ & g_\gamma \frac{a}{f_a} F_{\mu\nu} \widetilde{F}^{\mu\nu} && (6.1) \\ & + g_g \frac{a}{f_a} G_{c\mu\nu} \widetilde{G}_c^{\mu\nu} && (6.2) \\ & + g_f \frac{\partial_\mu a}{f_a} \bar{\psi}_f \gamma^\mu \gamma_5 \psi_f , && (6.3) \end{aligned}$$

where F and G are the field strength tensors of quantum electrodynamics (QED) and QCD, respectively, ψ_f is the fermion wave function, a is the axion(-like particle) field, and f_a is the axion decay constant (unless otherwise stated, we work in units $\hbar = c = 1$), see, e.g., Refs. [268, 286]. The parameters g_γ, g_g, and g_f are model-dependent constants that quantify the strength of the coupling to photons, gluons, and fermions, respectively, and are typically taken to be of order unity. An exception is the electron coupling constant g_e, which in certain models (e.g., the KSVZ model [309, 310]) can be set to zero at tree level. In this case $g_e \sim 10^{-3}$ due to one-loop corrections; other models still allow $g_e \sim 1$. Axion-like particles are assumed the have the same general couplings, with f_a a free parameter.

The axion field can be taken as a classical, nonrelativistic, field such that for a particular choice of phase it can be expressed as

$$a(\boldsymbol{r},t) = a_0 \cos(m_a t), \tag{6.4}$$

where m_a is the axion mass. The axion mass is typically expected to lie within one of two windows; the "classical" region, with 10^{-6} eV $\lesssim m_a \lesssim 10^{-4}$ eV, or the "anthropic" region, with 10^{-10} eV $\lesssim m_a \lesssim 10^{-8}$ eV, see, e.g., Ref. [313]. These regions correspond to oscillations of (6.4) on the order of GHz and kHz, respectively.

For the standard "QCD axion", the axion decay constant is related to its mass $m_a \sim \Lambda^2_{\rm QCD}/f_a$ via the formula [334]

$$\frac{1}{f_a} \approx 2\times 10^{-20}\ {\rm eV}^{-1}\left(\frac{m_a}{10^{-4}\ {\rm eV}}\right). \tag{6.5}$$

Making the further assumption that axions saturate the local DM density, one can equate the axion potential with the known DM energy density:

$$\frac{1}{2}m_a^2 a_0^2 = \rho_{\rm DM} \approx 0.3\ {\rm GeV\,cm}^{-3}. \tag{6.6}$$

From this, it is seen that (for a QCD axion) the factor a_0/f_a that appears in the calculations is independent of m_a. With these assumptions one can take this factor to be

$$\frac{a_0}{f_a} \approx 4\times 10^{-19}, \tag{6.7}$$

which we use for estimates of the size of the considered effects.

It should be noted, however, that the results in this chapter are not restricted to the typical QCD axion. We use the word axion to refer to any axion-like particle (ALP). In this case, the equations (6.5) and (6.7) do not strictly apply, and the parameters a_0 and f_a can take on any values (that are not already excluded experimentally). If the ALPs constitute a large portion of the DM in the galaxy, however, it is still the case that $a_0 \sim 1/m_a$, due to Eq. (6.6). These differences mean that the effects due to ALPs may actually have slightly different scaling with m_a than those due to QCD axions. Assuming axion-like particles saturate the DM density of the galaxy, the amplitude parameter can be expressed as

$$a_0 = 2.15\times 10^{-12}\left(\frac{m_a}{\rm eV}\right)^{-1}\ {\rm GeV}, \tag{6.8}$$

where the factor g/f_a is a free parameter of the theory.

6.2.1 Atomic and molecular EDMs

It worth breaking briefly to discuss how EDMs of atoms and molecules arise. This is discussed in Sec. 2.4.2 of this thesis; for a recent review, we direct the reader to Ref. [3]. The EDM of an electron can induce an EDM in an atom or molecule. In fact, experiments using ThO currently place the best limit on the electron EDM: $|d_e| < 8.7 \times 10^{-29}\, e\,\mathrm{cm}$ [146] (see also [144, 150]). The atomic EDM due to the electron EDM arises both from the sum of the intrinsic EDMs of all the electrons as well as from from the mixing of opposite parity states induced by the interaction of the electron EDM with the atomic field. In heavy systems, the contribution from the mixing of opposite parity states dominates, and the contribution from the sum of electron EDMs can be safely ignored. In the nonrelativistic limit, both such contributions go to zero. As such, an entirely relativistic treatment of the electron wavefunctions is necessary. For a more detailed discussion see, e.g., Ref. [28].

An EDM of the nucleus is completely unobservable in neutral systems due to the total screening of the external electric field by the electrons; this is known as the Schiff theorem [140]. However, observable atomic and molecular EDMs may also be produced due to the interaction of the electrons with higher-order P-and T-violating nuclear moments, such as the Schiff and magnetic quadrupole moments, which will be discussed in Sec. 6.4.1; see also Sec. 2.4.2.

6.2.2 Oscillating EDMs

Studies of static EDMs have gained much attention over the past few decades, as discussed in Sec. 2.4.2 (see also, e.g., Ref. [28, 135]). The dynamic EDM effects we consider here, however, require a completely different style of experiment. Measurements of the frequency and amplitude of the oscillationg EDMs would enable one to extract values (or at least limits) on the relevant field parameters [268, 286, 295]. For example, if we consider an axion field, a determination of the frequency of oscillations would lead directly to a value for the mass of the particle. Combined with this information, the amplitude of these oscillatory effects would lead to a determination of the coupling constants.

Axions lying in the classical or anthropic regions would lead to oscillations with frequencies between GHz and kHz, respectively. For the case of axions, the coherence time, $\tau_c \sim 2\pi/m_a v^2$, may be estimated from $\Delta\omega/\omega \sim (\frac{1}{2}m_a v^2/m_a) \sim v^2$, where a virial velocity of $v \sim 10^{-3}$ would be typical in our local Galactic neighbourhood, and the frequency is set by the axion mass: $\omega \approx m_a$ [286, 295].

The amplitudes of the oscillating EDMs induced by axions and other cosmic fields are likely to be extremely small. Given that even a static EDM has not yet been observed, the measurement of such dynamic EDMs seems quite a daunting task. It should be noted, however, that in some respects, the search for oscillating EDMs may be significantly easier. One of the major sources of systematic uncertainties in EDM experiments comes from the requirement to reverse the electric field; the field reversals are always imperfect, and the act of reversing the field creates stray currents, heat, and magnetic fields which can limit the experimental sensitivity. To search for oscillating EDMs, however, no such field reversals are required; the EDM itself does the reversing for us. Also, since the frequency of the EDM (should it exist) is set by cosmic parameters that are unrelated to the laboratory set up, it would be difficult for experimental systematics to mimic the effects.

Such EDMs could potentially be measured using normal EDM techniques, and searching for a temporal oscillation in the measured energy shift. However, it may be optimal to exploit the oscillating nature of the effects to maximise the sensitivity. For example, it may be possible to use optical cavity interferometry, which, when tuned to the correct frequency, would allow a build up of phase over several oscillations. Such a scheme was suggested in Ref. [286]. Also, by using magnetic fields to Zeeman tune the atomic or molecular energy levels into a resonance with the axion mass it may be possible to gain a significant enhancement. Another approach is to use a nuclear (or electron) magnetic resonance-type search, where the magnetic field is used to tune the Larmor frequency of a spin-polarised sample to the axion-field frequency. The resulting magnetisation can be observed using highly-precise magnetometry. Though this could be done with an atomic or molecular beam, or with trapped particles, the use of solid-state systems allows for a large enhancement due to the spin coherence times, and large number (spin) densities. Such an experimental scheme has been considered in Ref. [268, 295].

6.3 Axion–electron interaction

The interaction of axions with atomic or molecular electrons, Eq. (6.3) with $\psi_f = \psi_e$ the bound-state electron wave function, leads to the mixing of opposite-parity states, which in-turn leads to the production of an oscillating atomic or molecular EDM. Such effects were considered in Ref. [267]. We note that there are also other observable effects also due to the axion–fermion coupling (6.3), including parity-conserving $M1$ atomic transitions [335], parity-violating $E1$ atomic transitions [251, 252], and spin-precession effects [267]. These effects can also arise due to the axion–nucleus coupling, via the interaction in Eq. (6.2). Current limits on the axion (and ALP) coupling to electrons from astrophysical and laboratory-based searches are shown graphically in Fig. 6.1.

Adapting the general formula derived in the previous chapter [Eq. (5.27), page 76] to the specific case of an axion–induced atomic EDM, and noting that the relevent electron matrix element is complex and hence anti-Hermitian (i.e. $\langle i|\gamma^5|f\rangle = -\langle f|\gamma^5|i\rangle$), we arrive at the expression

$$D^v = 2im_a^2\frac{a_0}{f_a}\sum_n\frac{\langle v|\boldsymbol{d}|n\rangle\langle n|\gamma^5|v\rangle}{(E_v-E_n)^2-m_a^2}\cos(m_a t). \tag{6.9}$$

Here the formula is presented in the single-particle picture, for simplicity. In general, a summation over atomic electrons is assumed for each operator; both the considered operators are single-particle operators, so this summation is trivial.

There are two regimes of interest. The simplest case is when all the relevant energy intervals are larger than the axion mass, i.e. $E_v - E_n \gg m_a$ for all states n. For most of the relevant axion and ALP parameter space, this condition holds true for most atomic systems. This situation is examined in Sec. 6.3.1.

The other case, though slightly less simple, is potentially more interesting. Here, we consider the case when the system of interest contains a pair of opposite-parity levels that are near degenerate. Such a situation naturally arises in polar diatomic molecules (see, e.g., Ref. [108]), and also in some heavy elements that have a very dense spectrum [12]. In this case, it may be that $E_v - E_n \sim m_a$, though the natural line-widths may play an important role. This situation is examined in Sec. 6.3.2.

Brief note about the γ^5 operator The matrix elements of the γ^5 operator [that appears in Eq. (6.9)] can be simplified using the relation presented in

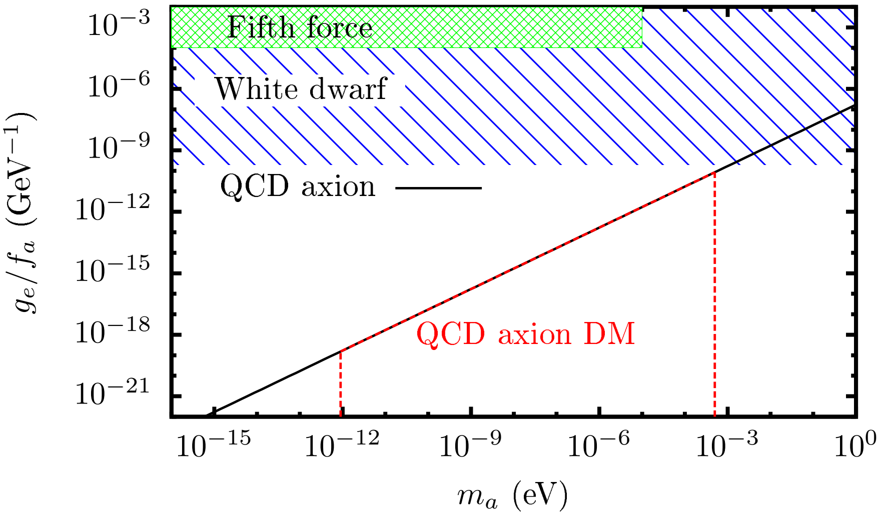

Figure 6.1 Parameter-space plot for the coupling of ALPs to electrons as a function of the ALP mass (adapted from Ref. [268]). The striped blue region is ruled out from observations of the cooling rate of white dwarfs [336]; the hatched green region is ruled out from searches for exotic spin-dependent new forces between electrons [337]. The area below the solid black line represents the possible parameter space for a QCD axion (if $g_e = 1$ the QCD axion must lie on this line), and the region bounded by the dashed red line is the available space for a QCD axion assuming it constitutes all of the DM. In general, ALPs may occupy any of the white areas.

Eq. (5.37) (proven in the previous chapter, see page 77)

$$\gamma^5_\imath = i[\hat{H}, \hat{\boldsymbol{\Sigma}}_\imath \cdot \boldsymbol{r}_\imath] + 2\gamma^5_\imath \hat{K}_\imath,$$

where $\hat{\boldsymbol{\Sigma}} = \mathbb{I}_2\boldsymbol{\sigma}$, with $\mathbb{I}_2$ the 2×2 identity matrix, and $\boldsymbol{\sigma}$ is the vector made from the Pauli spin matrices. The matrix elements of the first term above scale as $1/c$, whereas for the $\gamma^5\hat{K}$ term they scale as $1/c^3$. Therefore, in the nonrelativistic limit, γ^5 can be replaced by the commutator $i[\hat{H}, \boldsymbol{\sigma}_\imath \cdot \boldsymbol{r}_\imath]$. The difficulties associated with an operator that can be expressed in this way are discussed in Sec. 5.2.3 of the previous chapter.

Here, $\hat{K} = \mathbb{I}_2\hat{k}$, where $\hat{k}$ is defined in Eq. (5.38). Importantly, the spherical spinors Ω_κ [see Eq. (A.7)] are eigenstates of $\hat{k}$ with eigenvalues κ [the Dirac quantum number, $\kappa = (l - j)(2j + 1)$]. This means that single-particle states (orbitals) are eigenstates of the operator $\gamma^0\hat{k}$ with eigenvalues κ [see Eq. (A.6)]. Therefore, with the use of Eq. (5.15) [page 72], the (single-particle) matrix elements of the $2\gamma^5\hat{K}$ term can be expressed

$$\langle\phi_f|2\gamma^5\hat{K}|\phi_i\rangle = \frac{-\kappa_i}{2m_e}(\varepsilon_f - \varepsilon_i)\langle\phi_f|\gamma^5|\phi_i\rangle. \tag{6.10}$$

Combined with the above expressions, this means that for single-particle states the matrix elements of the γ^5 operator can be expressed via the *exact* (for single-particle state) expression:

$$\langle\phi_f|\gamma^5|\phi_i\rangle = \frac{i\Delta\varepsilon_{fi}}{1 + \frac{\kappa_i}{2m_e}\Delta\varepsilon_{fi}}\langle\phi_f|\hat{\boldsymbol{\Sigma}} \cdot \boldsymbol{r}|\phi_i\rangle, \tag{6.11}$$

where $\Delta\varepsilon_{fi} \equiv \varepsilon_f - \varepsilon_i$.

Table 6.1 Calculations for the amplitudes of the atomic EDM induced via the interaction of axions with electrons for several single-valence atoms. Values are presented in units of $10^{-12}\, g_e \frac{a_0}{f_a} \left(\frac{m_a}{\rm eV}\right)^2 |e|\,{\rm cm}$.

Atom	State	EDM
H	$1s$	0.118(1)
Li	$2s$	4.32(7)
Na	$3s$	4.39(7)
K	$4s$	7.8(4)
Cu	$4s$	1.2(2)
Rb	$5s$	8.8(6)
Ag	$5s$	1.2(4)
Cs	$6s$	11(1)
Au	$6s$	0.9(3)
Fr	$7s$	9(1)

6.3.1 Typical atomic effects

For atomic systems, typical energy intervals are on the order of $\Delta E \sim 10^3\,{\rm cm}^{-1} \simeq 1\,{\rm eV}$, whereas the mass of the axion is expected to be at most $m_a \sim 10^{-4}\,{\rm eV}$, and even as small as $10^{-10}\,{\rm eV}$. Therefore, in this case, $E_v - E_n \gg m_a$, and the m_a term in the denominator of Eq. (6.9) can be neglected. Taking only the non-relativistic part of the γ^5 matrix element leads to the simple expression

$$D^v = 2m_a^2 \frac{a_0}{f_a} \sum_n \frac{\langle v|\boldsymbol{d}|n\rangle\langle n|\boldsymbol{\sigma}\cdot\boldsymbol{r}|v\rangle}{E_v - E_n} \cos(m_a t), \tag{6.12}$$

which can be calculated with ease. Note in particular, that this expression is very similar to that for the static dipole polarisability, just as in Eq. (5.48) (on page 80), which means the accuracy of the calculations can be checked by scaling and comparing to the experimentally known polarisability values.

In Table 6.1, I present calculations for the size of the effects in several simple single-valence atomic systems. These accurate atomic calculations agree with the simple order-of-magnitude estimates presented in Ref. [267], and represent a significant improvement in the accuracy. Our calculations agree well with the observation that the atomic structure factor scales with the static dipole polarisability. The largest presented amplitude is for the $6s$ ground-state of cesium, which is not surprising, because this system has the largest ground-state polarisability of any atom [293]. Assuming $m_a \simeq 10^{-4}\,{\rm eV}$, and $a_0/f_a \simeq 4\times10^{-19}$ (i.e. assuming a QCD axion), the induced EDM in Cs is on the order of 10^{-38} e cm, which is 14 orders of magnitude smaller than the best limit on the EDM of a paramagnetic atom (Tl) [150], and 15 orders of magnitude smaller than the limit on the EDM of Cs [149]. We note, however, that the parameter space for axion-like particles is very broad, and spans many orders of magnitude. Using this effect in paramagnetic atoms, it may be possible to probe regions of the ALP parameter space, but it is unlikely to be possible to probe the QCD axion.

While EDM effects are typically much larger in paramagnetic systems, the measurements are typically much more precise in diamagnetics. The most precise limit on an atomic EDM was set using ^{199}Hg [147]. Simple estimates put

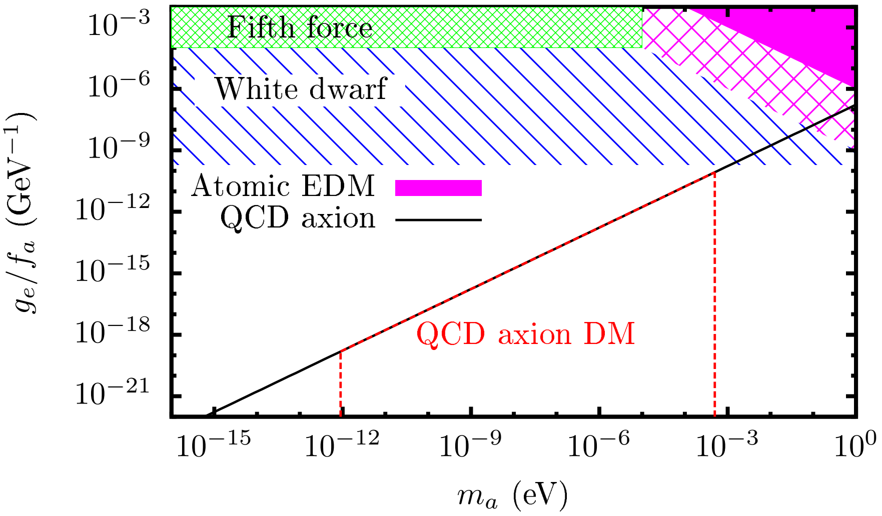

Figure 6.2 Potentially accessible region of the parameter-space for the coupling of ALPs to electrons from the axion-induced atomic EDM as a function of the ALP mass. The solid magenta region represents the parameters assuming the dynamic EDM search can be performed at the same level of sensitivity as the best atomic EDM search (set using Hg [147]). The hatched magenta region would be the accessible parameter space assuming an optimistic three orders-of-magnitude improvement over the current best limits. (See Fig. 6.1 for a description of the other regions.)

the axion-induced EDM of ground state of Hg at about 0.9, in the same units as those in Table 6.1, leading to an effect with the same assumptions as above on the order of 10^{-40} e cm, which is 12 orders of magnitude smaller than the limit on the Hg EDM.

In Fig. 6.2, I present the same parameter-space plot as that presented in Fig. 6.1, with two extra regions added. The first region (the solid magenta block) represents the potentially accessible region of the parameter space assuming a dynamic atomic EDM experiment using Cs (a paramagnetic atom) could reach the same level of sensitivity as the current most sensitive static EDM experiment, which was performed for the diamagnetic Hg atom [147]. We remind that one dominant source of uncertainty in atomic EDM experiments comes from the electric field reversals, which are not required in searches for dynamic EDMs. The other region (hatched magenta block) represents the potential set of parameters assuming that the dynamic Cs EDM could be probed at a level of sensitivity a few orders of magnitude better than the current best limits. Even with these especially optimistic assumptions, the axion-induced EDMs in alkali (group 1) atoms are likely too small to be competitive with other axion searches.

It is therefore unlikely that the EDM induced in atoms via the axion–electron interaction could be measured in the near future. This is not the end of the story, however. The axion-induced EDM via the same interaction in certain systems may be enhanced by many orders of magnitude.

One particular example of such an enhancement occurs in Rydberg atoms. Rydberg atoms, which are atoms that are in a very highly-excited state, are known to have a hugely enhanced polarizability. As shown above, the axion-induced oscillating EDMs in atoms are proportional to the atomic dipole polarizability; in this case, since the field is oscillating, it is proportional to the dynamic polarizability [338].

6.3.2 Resonant enhancement in atomic dysprosium and xenon

It may also possible to gain a further enhancement in the sensitivity of the EDM measurements by tuning the experiment to a specific frequency in order to bring about a resonance with $(E_v - E_n)^2 \simeq m_a^2$, see Eq. (6.9). Similar techniques have already been shown to work using the practically degenerate A and B states in Dy [89], and could potentially be implemented in systems such as barium, radium, thorium, and singly-ionised actinium, which also possess pairs of very close levels of opposite-parity, as discussed in Sec. 3.4 of this thesis. It was suggested in Ref. [286] to that searching for oscillating EDMs in cold molecules could be used to probe axion and ALP DM. The effects considered in that work were due to the axion–nucleus interaction, which produces a nuclear Schiff moment. Here, I consider the axion–electron interaction and consider the effects in atoms, such as Dy, in which the close pairs of opposite parity levels have the same total angular momentum and can be mixed.

In this regime it is allowed that $\Delta E \sim m_a$, and the expression for the EDM induced in state A, which is enhanced by the nearby state of opposite parity, B, is given by

$$D^A = 2m_a^2 \frac{a_0}{f_a} \frac{\langle A|\boldsymbol{d}|B\rangle\langle B|\boldsymbol{\sigma}\cdot\boldsymbol{r}|A\rangle}{(E_A - E_B + i\Gamma_A/2)^2 - m_a^2}(E_B - E_A)\cos(m_a t). \tag{6.13}$$

Since this EDM will be practically entirely due to the contribution from the mixing of the two nearby states, only one term from the usual summation needs to be considered.

In these systems it is possible to tune the already close levels into resonance using the Zeeman effect with modest magnetic fields. Such a procedure has been demonstrated to work in Dy, see, e.g., Refs.[239, 333, 339, 340]. Here, we consider such an effect on resonance, where a particular set of opposite-parity levels (denoted A and B) are brought into resonance with the axion mass $E_A - E_N \approx m_a$; for simplicity, we also consider only the case where $m_a \gg \Gamma$, which is a reasonable assumption for Dy and Xe. In this case, the EDM induced in the state A is given

$$D_A \approx -D^B \approx \langle A|\boldsymbol{d}|B\rangle\langle B|\boldsymbol{\sigma}\cdot\boldsymbol{r}|A\rangle \frac{a_0}{f_a} m_a \cos(m_a t). \tag{6.14}$$

In deriving this equation, we have assumed that the width of the state A is much greater than that of B, and that that ALP mass is much larger than the widths: $m_a \gg \Gamma_A \gg \Gamma_B$. Note that, contrary to the simple atomic case, this EDM scales (directly) as m_a, not m_a^2 (though for DM we also have, $a_0 \sim 1/m_a$).

The feature of Dy that makes it a particularly interesting system for the study of atomic PNC is the existence of two nearly degenerate states of opposite parity and the same total angular momentum, $J = 10$, at $E = 19797.96$ cm^{-1}. We use the notation A for the even-parity state and notation B for the odd-parity state, following Ref. [89]. Unfortunately, the enhancement in the signal is not as strong as one might have expected. This is due to two factors. Firstly,

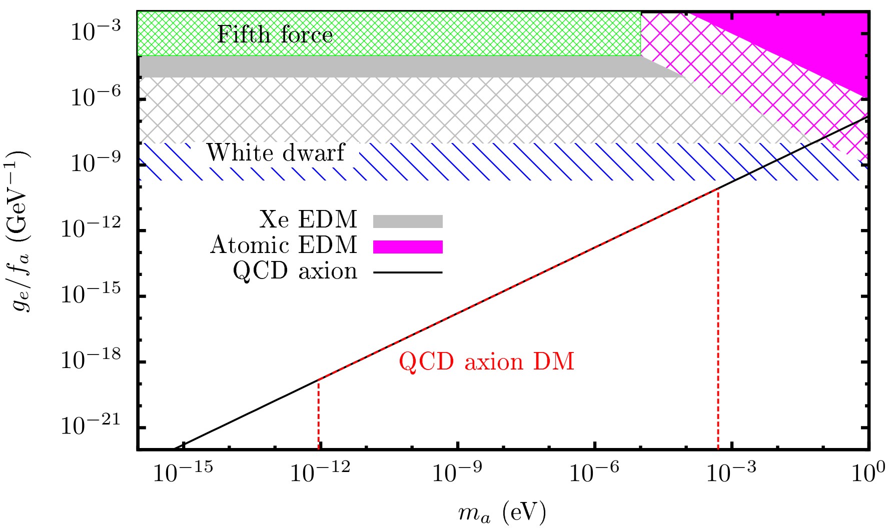

Figure 6.3 Potentially accessible region of the parameter-space for the coupling of ALPs to electrons from the axion-induced EDM in atomic Xe as a function of the ALP mass. The solid grey region represents the parameters assuming the dynamic EDM search can be performed at the same level of sensitivity as the best atomic EDM search. The hatched grey region would be the accessible parameter space assuming an optimistic three orders-of-magnitude improvement over the current best limits.

the small factor that appears in the denominator from the closeness of the levels is compensated by the small parameter ΔE in the numerator [see Eq. (5.37)], which in this case, does not cancel. Also, specifically for Dy, the relevant electric dipole matrix elements are particularly small in Dy [91]. This is because the A and B states have different spin, meaning the matrix element is zero in the non-relativistic limit.

It may be much more fruitful to examine the effects in other atomic systems that also posses near-degenerate opposite parity levels, such as Xe [341], however the calculations are rather complicated due to the large number of electrons involved; a full analysis is beyond the scope of this thesis. The levels of interest in Xe are the $J = 2$ levels at $E = 94759.9\,\mathrm{cm}^{-1}$ [188]. In Ref. [341], calculations were performed for Xe, with the intention of motivating a parity-violation experiment. Taking calculations of the relevant radial integrals from that work, it is possible to extract order-of-magnitude estimates on the size of the axion-induced EDM for Xe. Unlike in the Dy case, the relevant radial integral is not highly suppressed, which leads to a much larger effect. The resulting parameter-space plot is shown in Fig. 6.3.

It may also be possible to use a molecular interferometry experiment (such as that proposed in Ref. [286]), which would allow a build up of phase over several oscillations through an optical cavity on resonance. This may allow an improvement in the sensitivity of several orders of magnitude [286].

6.4 Axion–nucleon interactions

6.4.1 Nuclear Schiff and magnetic quadrupole moments

The QCD axion was previously shown to give rise to oscillating P- and T-odd nuclear Schiff moments [267, 268, 286], which arise from P- and T-odd intranuclear forces and from the EDMs of constituent nucleons. This follows from the observation that the QCD Lagrangian contains the P- and CP-violating term

$$\mathcal{L}^{\theta}_{\rm QCD} = \theta \frac{g^2}{32\pi^2} G^{\mu\nu}_a \widetilde{G}_{a\mu\nu}, \tag{6.15}$$

and that θ may be cast in the form $\theta(t) = a(t)/f_a$. Here, $a(t) = a_0 \cos(m_a t)$ is the oscillating QCD axion field with f_a the axion decay constant, θ is the dimensionless parameter that quantifies the degree of CP-violation, G_a and $\widetilde{G}_a$ are the gluonic field tensor and its dual, respectively, (with color index a) and g is the QCD gauge coupling constant.

Though an EDM of the nucleus is completely unobservable in neutral systems, the EDMs of individual nucleons, whether static or oscillating, contribute to the so-called nuclear Schiff moment [107, 342] (see also Ref. [139] where the contribution of the proton EDM was considered). The interaction of the atomic electrons with the nuclear Schiff moment leads to mixing of atomic and molecular states of opposite parity, which in turn leads to the creation of EDMs. The relation between the individual nucleon EDMs and the Schiff moment depends on the nuclear structure. It can be roughly estimated as $S \sim r_N^2 d_N$, where r_N is the nuclear radius and d_N is the nucleon EDM, though large enhancements are found in systems that posses octopole deformation. The relation between the Schiff moment and the induced atomic or molecular EDM depends on the electronic structure.

Such moments can arise due to the axion coupling to gluons inside the nucleus, producing an effective oscillating $\theta_{\rm QCD}$ term in the Lagrangian. In Ref. [286], Graham and Rajendran demonstrated that the axion–gluon coupling in Eq. (6.2) would induce an oscillating EDM in nucleons of $d_n \simeq 1.2\times10^{-16}\frac{a}{f_a}\, e\cdot$cm. (The expression for the nucleon EDM induced by the regular $\theta_{\rm QCD}$ term was derived in Ref. [343]; see also [344]). Assuming that axions saturate the DM density of the galaxy, and using the estimates for the axion couplings discussed above, this leads to an oscillating EDM of [286]

$$d_n \approx 4\times 10^{-35} \cos(m_a t)\, e\,{\rm cm}. \tag{6.16}$$

Also produced is a Schiff moment on the order of $S \sim 10^{-9} Z^3 d_n$ [107], meaning that it is preferable to use heavy systems (note that although the EDM of the nucleons do contribute to the nuclear Schiff and magnetic quadrupole moments, the dominant contribution actually comes from the axion perturbation to the pion exchange inside the nucleus [267]; the parametrisation of the induced Schiff moment in terms of the nucleon EDM is purely for convenience). For Hg and Tl, this evaluates to around three orders of magnitude further suppression. However, nuclei that posses octopole deformation gain a significant enhancement in the Schiff moment. For example, the Schiff moment of ^{225}Ra is more than two orders of magnitude larger than that of Hg [221, 222]. For heavier actinides such as ^{229}Pa, the enhancement means that the Schiff moment is actually enhanced compared to the bare nucleon EDM, $S(^{229}\mathrm{Pa}) \sim 10\, d_n$ [222, 286]. In Ref. [295] a thorough experimental proposal was put forward to search for axions and ALPs by detecting such a Schiff moment in solid state systems.

Here, we note that as well as nuclear Schiff moments, the axion–gluon coupling (6.2) also produces a nuclear magnetic quadrupole moment via the effective oscillating θ_{QCD}. The magnetic quadrupole moment is the lowest order P- and T-violating magnetic moment of the nucleus. As in the case of the Schiff moment, the magnetic quadrupole moment leads to the production of atomic and molecular EDMs by mixing electronic states of opposite parity. In Ref. [107] it was shown that the nuclear magnetic quadrupole moment creates larger EDMs in paramagnetic atoms and molecules than the Schiff moment. Also, in contrast to the Schiff moment, ordinary quadrupole deformation—which exists in 50% of nuclei, and in all nuclei of experimental interest—is sufficient to allow a significant enhancement (octopole deformation is required to enhance Schiff moments).

Here we point out that, as well as Schiff moments, axions may also induce oscillating P- and T-odd effects in molecules through the generation of oscillating nuclear magnetic quadrupole moments (MQMs), which arise from P- and T-odd intranuclear forces and from the EDMs of constituent nucleons. We note that nuclear MQMs, unlike nuclear EDMs, are not screened by the atomic electrons. Both of these mechanisms contribute to nuclear MQMs, which are linear in θ, and so recasting θ in the form $\theta(t) = a(t)/f_a$ leads to our noted inference. The approximate magnitudes of such oscillating nuclear MQMs and the effects they induce in molecules can be obtained for various cases from the numerical values in Ref. [345] (see also Refs. [107, 122, 224]) by the substitution $\theta \to a_0 \cos(m_a t)/f_a$, with $a_0/f_a \sim 4\times 10^{-18}$ from consideration of the local DM density, see, e.g., Ref. [267, 268, 286, 319, 346, 347].

6.4.2 Diatomic molecules

The Schiff moment can then produce an atomic or molecular EDM by inducing a mixing of opposite parity states. In paramagnetic systems, this EDM can be further enhanced, particularly in the diatomic molecules which posses Λ or Ω doubling—resulting in very closely spaced rotational levels of opposite parity. Note that the application of a modest external electric field ($\sim 10^2$ kV cm^{-1}) will lead to a maximally polarised molecular state. In this regime, the energy shift caused by the molecular EDM is actually independent of the applied electric field strength (since it is due to the internal effective electric field).

In Ref. [345], the authors used the relations between QCD and the nuclear P- and T-odd forces derived in Ref. [344] to show that the magnetic quadrupole moment of a valence neutron or proton is

$$M_n \approx M_p \approx 2\times 10^{-29}\, \theta_{\mathrm{QCD}}\, e\,\mathrm{cm}^2. \tag{6.17}$$

The moment of the nucleus depends on the nuclear structure, and can be quantified by the "collective enhancement" parameter, η: $M(N) = \eta_N M_n$. Here, N denotes the nucleus in question.

In much the same way as for the nucleon EDMs, the interaction of the axion field with gluons inside the nucleus would also give rise to oscillating nuclear magnetic quadrupole moments, with a magnitude given by $\eta M_{n/p}$, with the

Table 6.2 Nuclear spins I, molecular ground states, the enhancement factor η (for the heavy nucleus), calculations of the molecular structure W_M (from the literature), and the resulting energy shift factor $W_M M\Omega$ for several paramagnetic diatomic molecules of experimental interest.

System				$\lvert W_M\rvert$	$\lvert W_M M\Omega\rvert$
Molecule	I	State	η^a	$10^{33}\,\frac{\text{Hz}}{e\,\text{cm}^2}$	$10^{10}\frac{a_0}{f_a}\,\mu\text{Hz}$
^{135,7}BaF	3/2	$^2\Sigma_{1/2}$	−1.2	0.83^b	1
^{173}YbF	5/2	$^2\Sigma_{1/2}$	−20	2.1^c	42
^{201}HgF	3/2	$^2\Sigma_{1/2}$	2	4.8^b	10
^{181}TaN	7/2	$^3\Delta_1$	−25	1.1^d	50
^{229}ThO	5/2	$^3\Delta_1$	−19	1.9^e	72

[a] Ref. [345]
[b] Ref. [122]
[c] Ref. [348]
[d] Ref. [349]
[e] Ref. [350]

substitution $\theta_{\rm QCD}\to a_0\cos(m_a t)/f_a$ in Eq. (6.17). This leads to energy shifts due to the axion field of

$$\delta E \simeq C_{JF} M_W M\Omega\cos(m_a t), \tag{6.18}$$

where C_{JF} are angular coefficients of order ~ 0.1, Ω is the projection of the total electronic angular momentum onto the molecular axis, and the parameter W_M is found from molecular structure calculations (which we take from the literature):

$$W_M = \frac{3}{2\Omega}\langle 0|\sum_i\left(\frac{\boldsymbol{\alpha}_i\times\boldsymbol{r}_i}{r_i^5}\right)\cdot\boldsymbol{r}|0\rangle. \tag{6.19}$$

The values of the parameters η, M_W, and $M_W M\Omega$ for several paramagnetic diatomic molecules of experimental interest are given in Table 6.2.

For example, the energy shift in ^{229}ThO for the values $J=1$ and $F=5/2$ where the angular coefficient reaches its maximal value $|C_{JF}|=0.16$ and taking $a_0/f_a\simeq 4\times10^{-18}$ as above, is

$$\delta E(^{229}\text{ThO}) \simeq 2.1\times10^{-28}\,\text{eV}\,\cos(m_a t). \tag{6.20}$$

More generally, the energy shift is given

$$\delta E(^{229}\text{ThO}) \simeq 1.0\times10^{-21}\left(\frac{m_a}{\text{eV}}\right)^{-1}\left(\frac{g_N/f_a}{\text{GeV}^{-1}}\right)\,\text{eV}\,\cos(m_a t). \tag{6.21}$$

In Ref. [286], it was considered to search for the induced nuclear Schiff moment in cold molecules, using a molecular interferometry experiment (see also Ref. [159]). The authors reasoned that using such techniques, it may be possible to detect energy shifts as small as 10^{-25} eV. In Fig. 6.4, I plot the potentially accessible parameter space assuming that a search can be performed at this level of sensitivity. I also plot the potentially more realistic region, assuming the sensitivity is around six orders of magnitude worse. This demonstrates that such a search can potentially be competitive with existing searches. The

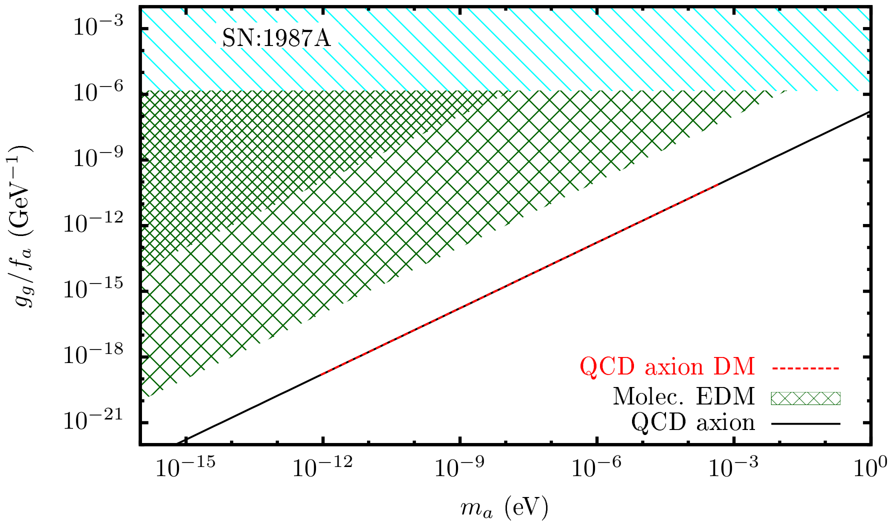

Figure 6.4 Potentially accessible region of the parameter-space for the coupling of ALPs to nucleons from the axion-induced nuclear magnetic quadrupole moment in diatomic polar molecules as a function of the ALP mass. The striped blue region is excluded from cooling rates in supernova 1978A (see, e.g., Ref. [268]). The densely hatched green region represents the accessible parameters assuming the dynamic EDM search can be performed at the $\delta E \sim 10 \times 10^{-19}$ eV level; the more sparsely hatched green region would be the accessible parameter space assuming the optimistic case that the search can be sensitive to the $\delta E \sim 10 \times 10^{-25}$ eV level, as in Ref. [286].

large effects of the MQM, compared to the Schiff moment, mean that in certain systems a significant enhancement can be found. Searches based on both nuclear Schiff and magnetic quadrupole moments could be complimentary, and may help to constrain systematic effects, which can be different in the different materials. Note that the analysis performed here is only a simple one, using order-of-magnitude estimates. A more detailed exploration concerning the particulars of the experimental techniques must be performed, though is beyond the scope of this thesis. Such an analysis will be saved for a future work.

6.4.3 Paramagnetic solids

In Ref. [295], a thorough experimental proposal was put forward to use the axion-induced nuclear Schiff moments that are produced in solid-states diamagnetic systems (see also Refs. [268, 286]) – the so-called CAPSEr experiment (cosmic axion spin precession experiment). Experimental work is currently under way at Mainz, in Germany. The authors plan to use highly precise magnetometry to detect the transverse magnetisation on resonance. The resonance condition is found by using magnetic fields to tune the Larmor frequency of the nuclear spins into resonance with the frequency of the axion field, m_a. By slowly scanning over values for the magnetic field, a resonance can be sought over a wide range of frequencies (i.e. a wide range of potential values for the axion mass). The induced signal can be expressed [295]:

$$M \approx np\mu(ED_A)\frac{\sin[(2\mu B_{\rm ext} - m_a)t]}{(2\mu B_{\rm ext} - m_a)}\sin(2\mu B_{\rm ext}t), \tag{6.22}$$

where n is the number density of nuclear spins, p is the polarisation fraction, μ is the magnetic dipole moment of the nucleus in question, $B_{\rm ext}$ is the applied magnetic field, and ED_A is the size of the energy shift, due to the atomic electric dipole moment (which is caused by the axion-induced nuclear Schiff moment).

Here, we note, that such effects can also be sought for using paramagnetic systems, in which the effect is mainly due to the axion-induced nuclear MQM (instead of the Schiff moment). The use of paramagnetic systems and the associated MQMs has several advantages, but also several disadvantages. The EDM produced in paramagnetic systems due to the MQM can be several orders of magnitude larger than those produced by the Schiff moment. In particular, nuclei that posses quadrupole deformation have a huge collective enhancement in the size of the MQM; most nuclei (and all of experimental interest) posses quadrupole deformation. In order to gain the collective enhancement of the Schiff moment, nuclear octopole deformation is required. Roughly, this should lead to around three or four orders of magnitude enhancement in the signal, depending on the system. Also to their advantage, is that in paramagnetic systems, the Larmor frequency is set by the electronic spin. So, the magnetic moment μ that appears in Eq. (6.22) becomes the electron magnetic moment (as opposed to the nuclear magnetic moment), which is three orders of magnitude larger.

The six orders of magnitude enhancement discussed above is, however, compensated by about a six orders of magnitude suppression, which is due to the fact that the total sensitivity is also proportional to the spin-coherence time (the spins must be polarised to gain a coherent signal). The diamagnetic systems considered in Ref. [295] have spin coherence times of around one million times larger than those in paramagnetic systems (depending on the specific materials).

So, overall, it may appear that there is no main advantage or disadvantage. However, the difference in the magnetic moments leads to another difference between the diamagnetic and paramagnetic experiments. The larger magnetic moment of the paramagnetic systems means that significantly higher frequencies (i.e. larger axion masses) can potentially be reached with the same magnetic fields. This means that, even if the overall sensitivity is substantially lower, experiments using paramagnetic systems can potentially probe a different region of the axion mass parameter space than the diamagnetic experiments. Therefore, such experiments would be complementary to each other and could be run in parallel. A full analysis of the size of the induced effects, including calculations for specific systems, is beyond the scope of this thesis and will be presented in a later work.

6.5 Axion electromagnetic anomaly

Recently, it was put forward in Ref. [351] that any particle with a static magnetic dipole moment would gain an induced oscillating EDM due to the axion electromagnetic anomaly. The author considered the tree-level perturbative correction to the electron magnetic dipole operator due to the axion anomaly, shown diagrammatically in Fig. 6.5, and concludes that such a moment may be detectable in molecules. The magnitude of the EDM derived in Ref. [351] is $\sim 10^{-32}\,e\,$cm, very large compared to the typical axion-induced EDMs (see, e.g., [252, 267, 286]), and only a few orders of magnitude smaller than the current

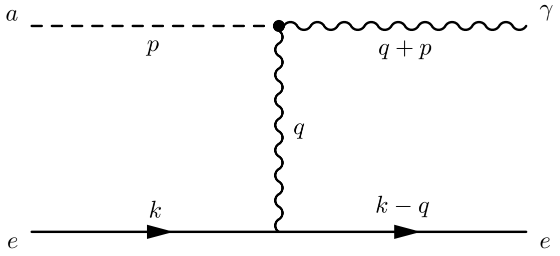

Figure 6.5 First-order Feynman diagram for the oscillating P- and T-odd EDM field induced from the interaction of an axion with an electron [351]. The solid line is an electron, the internal and external wavy lines are the virtual (exchanged) and real photons, respectively, and the dashed line is the axion.

limit on the (static) electron EDM [146]. Note that this result has since been called into question [352].

Such an effect (if correct) would require a frequency ($\omega = m_a$) and phase matched oscillating electric field in order to detect the EDM-like linear Stark shifts [351]. Such an effect relies on the frequency and phase of the applied field to be in resonance with the axion field in order to be detectable, which poses distinct problems from an experimental standpoint (due at least partly to the fact that neither of these quantities are known; see also Ref. [352].

We consider whether such an effect may be observable instead with an applied static electric field. That is, we consider the diagram as in Fig. 6.5, except with the external photon line replaced with a transverse line corresponding to the interaction with a static external electric field. Note that in Ref. [351], the author considers the photon-electron vertex as the effective anomalous magnetic interaction. For a more general treatment, we consider the vertex structure $\Gamma_\mu = \gamma_\mu + \frac{1}{2m_e}\sigma_{\mu\nu}q^\nu$, which contains the normal vector current as well as the effective anomalous current. A direct evaluation leads to the amplitude

$$ie\frac{g_\gamma a_0}{f_a}\sin(m_a t)\frac{1}{q^2}\epsilon_{\alpha\beta\nu\mu}p^\alpha q^\nu \varepsilon^\beta \bar{u}(k)\Gamma^\mu u(k'), \tag{6.23}$$

where $k' = k - q$, and ε is the polarization vector of the external photon. Here, we have assumed that the axion is nonrelativistic, i.e. $p^\mu \approx (m_a, \mathbf{0})$, meaning the index $\alpha = 0$. However, note that for a static field we are free to choose the gauge where $\varepsilon^\mu = (\varepsilon^0, \mathbf{0})$. Clearly, in this gauge (and thus in every gauge), such a treatment in fact does not lead to observable effects [352].

Instead, we consider the observable effect due to the Coulomb interaction between the nucleus and the electrons perturbed by the interaction of the axion field with the exchanged photon. The interaction mediated by the direct exchange of an axion between two fermions was considered in Ref. [308]. Evaluating the Feynman diagram for this process (presented in Fig. 6.6) leads to an effective single-electron interaction Hamiltonian

$$\hat{h}^{\text{int}} = \frac{\alpha}{2}\frac{g_\gamma a_0}{f_a}m_a \sin(m_a t)\,(\boldsymbol{\alpha}_p \times \boldsymbol{n})\cdot\boldsymbol{\alpha}_e, \tag{6.24}$$

where the operator $\boldsymbol{\alpha}_{e(p)} = \gamma^0\boldsymbol{\gamma}$ acts on the electron (proton) wave functions and $\boldsymbol{n}$ is the unit vector pointing from the nucleus to the electron. In arriving at

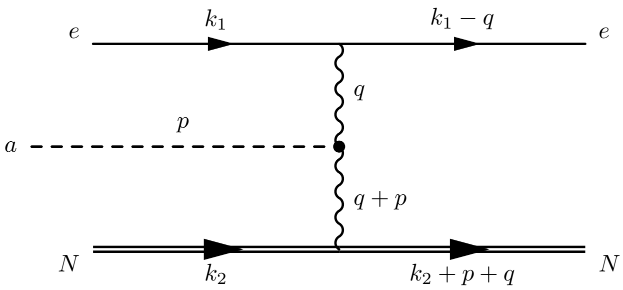

Figure 6.6 First-order Feynman diagram for the oscillating P- and T-odd interaction between an electron and the nucleus induced by the axion field. The fermion line denotes an atomic or molecular electron, the double line denotes the nucleus (sum of protons), the dashed line is the axion, and the wavy line is the exchanged photon. Note there are also diagrams with both fermions being electrons, and with both fermions being nucleons.

this formula we have assumed the axion to be nonrelativistic, i.e. $p^\mu \approx (m_a, \mathbf{0})$, and have taken the limit of zero nuclear recoil, $q^\mu \approx (0, \boldsymbol{q})$. Note that the $\boldsymbol{\alpha}$ matrices each introduce a small factor ($1/c$ in regular units); a suppression that makes this effect at least four orders of magnitude smaller than the other relevant effects considered in this thesis, so we consider it no further.

CHAPTER 7:

Direct Detection of Electron-Interacting WIMPs:

accurate atomic calculations and implications for the DAMA, XENON and CoGeNT annual modulation signals

A very promising claim of a positive direct detection of WIMPs was made by the DAMA Collaboration. Their result is currently the only long-standing claim for a positive dark matter detection. However, null results from many other experiments all but rule out the possibility that the DAMA result is due to a WIMP–nucleus interaction. The DAMA experiment is sensitive to scattering off both electrons and nuclei. Most other DM detection experiments, however, reject pure electron events, meaning that DM particles that interact favourably with electrons could potentially explain the DAMA modulation without being ruled out by the other null results. Newer hints on annual modulations from both the CoGeNT and XENON experiments (which are also sentive to electron recoils) makes this idea particularly exciting. In this chapter, I employ the relativistic Hartree-Fock method to calculate model-independent cross sections and event rates for the atomic ionisation induced by the interaction with dark matter for several atoms of experimental interest. This is the first time relativistic effects have been taken into account. Moreover, I demonstrate here that relativistic effects are crucial, dominating the amplitude. By assuming the DAMA modulation is a positive detection, I calculate the event rates that would be expected in the XENON and CoGeNT detectors. The CoGeNT results are more-or-less consistent with DAMA, however, the XENON results are not. From this we are able to set extremely tight constraints, and completely rule out electron-interacting WIMPs as the source of the DAMA modulation.

7.1 Introduction

The astronomical evidence for the existence of dark matter (DM) is overwhelming. Despite this, no definitive observation of DM has yet been confirmed, and its composition remains one of the most important outstanding problems facing physics today.

One intriguing potential detection was made by the DAMA Collaboration, which uses a NaI-based scintillation detector to search for possible DM interactions within the crystal in the underground laboratory at the Gran Sasso National Laboratory, INFN, Italy [356] (see also Ref. [357] and references therein). The data from the combined DAMA/LIBRA and DAMA/NaI experiments indicates an annual modulation in the event rate at around 3 keV electron-equivalent energy deposition with a 9.3σ significance (the low-energy threshold for DAMA is ~ 2 keV) [356, 358, 359]. The phase of this modulation agrees very well with the assumption that the signal is due to the scattering of DM particles (e.g., WIMPs) present in the DM galactic halo. The annual modulation is one of the key expected observables for WIMP dark matter detection and is expected due to the motion of the earth around the sun which results in an annual variation of the dark matter flux through a detector, see, e.g., Refs. [360, 361]. This result stands as the only enduring DM direct-detection claim to date.

However, null results from several other sources such as, for example, the XENON100 [362], LUX [363, 364], and SuperCDMS [365] experiments, all but rule out the possibility that the DAMA signal is due to a WIMP–nucleus interaction (see also Refs. [360, 366, 367]). While the DAMA experiment is sensitive to scattering of DM particles off both electrons and nuclei, most other DM detection experiments reject pure electron events in order to search for nuclear recoils with as little background as possible. This means that DM particles that interact favourably with electrons rather than nucleons could potentially explain the DAMA modulation without being ruled out by the other null results (see, e.g., Refs. [367, 368]). This possibility has been investigated previously in the literature—see, e.g., Refs. [361, 369–373]. It has also been noted [374] that such leptonically interacting DM models could explain the anomalous cosmic ray detections measured by, for example, the AMS [375], ATIC [376], Fermi [377], and PAMELA [378, 379] experiments (see also Refs. [380–382]).

In Ref. [370], the authors employ a general effective field theory approach to write down effective interactions between DM particles and electrons, assuming that the DM has interactions only with leptons at tree-level. They show, however, that due to a suppression in the WIMP–electron-scattering ionisation cross section, loop-induced WIMP–nucleus scattering would dominate the relevant event-rate if an interaction with nucleons can be generated at the one- or two-loop level, even if the DM particles only interacted with leptons at tree level. In this case, the previous constraints from nuclear recoil experiments [362, 363, 365] still apply (except in the case of an pseudovector electron coupling, in which the loop corrections do not arise). However, these conclusions are based on calculations that employed simple nonrelativistic wave functions. A rigorous *ab initio* relativistic treatment of the atomic structure has not yet been implemented. As is demonstrated in this thesis, a proper relativistic treatment is in fact crucial.

A recent analysis of data from the XENON100 experiment has also investigated WIMP-induced electron-recoil events [383, 384]. These experiments have also observed modest evidence for an annual modulation (at the 2.8σ level). However, based on their analysis of the average unmodulated event-rate, DM that interacts with electrons via an pseudovector coupling was excluded as an explanation for the DAMA result at the 4.4σ level [383]. This means that for DM–electron scattering to be consistent with both the DAMA and XENON experiments, the event rate would have to have a very large modulation fraction. It has been suggested that electron-interacting "mirror" DM may satisfy this criteria [385] (see also Ref. [373]). By assuming the DAMA result was due to an pseudovector coupling, and using the theoretical analysis from Ref. [370], the corresponding modulation amplitude that would be expected in the XENON experiment was calculated in Ref. [384]. The observed amplitude was smaller than this by a factor of a few, and it was concluded that the XENON results were inconsistent with the DAMA results at the 4.8σ level [384]. We note, however, these conclusions are not entirely model independent, and a rigorous relativistic analysis is required. We also note that there is no *a priori* reason to believe that the fraction of the modulated signal should be small or proportional to the fractional annual change in the DM velocity distribution. In fact, the scattering amplitude is very highly dependent on the values of momentum transfer involved, which depend on the velocity of the DM particles. As we shall show, electron relativistic effects must be taken into account properly to recover the correct momentum-transfer dependence of the cross section, which is a significant point.

The recent work in Ref. [353] demonstrated that the ionisation cross section due to a WIMP–electron interaction is actually dominated by relativistic effects. This is due to the non-analytic cusp-like behaviour of the Coulomb-like wave functions at very small radial distances, and the slight difference in the radial dependence of the Dirac wave functions (compared to the Schrödinger wave functions). The implication is that the suppression from the electron matrix elements may not be as strong as previously assumed, meaning the nonrelativistic calculations may significantly underestimate the cross section.

Furthermore, as several new experiments designed to test the DAMA results are currently under way [357, 386–390], it is crucial that the relevant theory required for their interpretation is correct, and as free of model dependencies as possible.

In this paper, we employ the relativistic Hartree-Fock method to calculate model-independent cross-sections and event rates for the atomic and molecular ionisation induced by the interaction of atomic electrons with dark matter for several systems of experimental interest. Atomic ionisation has been considered previously for the case of axions [261, 262, 391]. By performing the atomic structure calculations in an *ab initio* manner including all relativistic effects we are able to keep the discussion as model independent as possible. Also, our method allows the inclusion of all relativistic effects for the electron wavefunctions, which we show is important, but was neglected in previous analyses. Most current analysis parametrises the DM–electron scattering in terms of the "free electron" cross section. We, however, parametrise the interaction in terms of the mass of the DM particle, the mass of the mediating exchange particle, and the effective DM–electron coupling constant. This is a more useful parametrisation that more easily allows comparison with specific DM models.

In Sec. 7.2, I derive the scattering cross sections and other relevant quantities, and discuss how the approach taken in this paper differs from the previous investigations into this matter. In Sec. 7.3, I demonstrate the importance of relativistic effects, and note that a non-relativistic analysis (such as those performed previously) may significantly underestimate the size of the effects. In Sec. 7.4, I outline the techniques utilised for the accurate relativistic atomic calculations, and go on in Sec. 7.5 to present my results and to discuss the implications of these for the interpretation of the DAMA annual modulation in terms of DM interactions with atomic electrons. Finally, in Sec. 7.6 I present the summary and conclusions.

7.2 Theory

7.2.1 Scattering cross-section and event rate

We consider the case in which the scattering of an incident DM particle from the galactic halo off the atomic electrons leads to the ionisation of the atom or molecule. This situation is shown diagrammatically in Fig. 7.1.

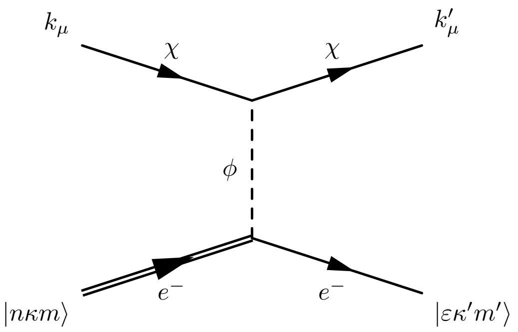

Figure 7.1 Example diagram for interaction of a dark matter particle (χ), with an electron via the exchange of mediator ϕ. Double electron line denotes a bound atomic electron ($E < 0$), and the single electron line denotes a continuum state electron with energy $\varepsilon > 0$.

First, we assume the well-motivated case that the DM particle interacts with electrons via the exchange of a heavy vector-boson mediator. We initially model this interaction as a simple four-fermion vertex described by an effective Yukawa-type potential,

$$\hat{h}_{\rm int} = \alpha_\chi \frac{{\rm e}^{-m_v r}}{r}, \tag{7.1}$$

and use the Born approximation to write down the cross section [353]. In the limit that $m_v \to 0$, the interaction (7.1) corresponds to a Coulomb-like interaction, and in the opposite limit ($m_v \to \infty$) it corresponds to a purely contact (delta-function–type) interaction. Treating the DM nonrelativistically, the partial differential cross section corresponding to the ejection of a bound electron initially in the state a to a state in the continuum is given by

$$\mathrm{d}\sigma_a = \frac{8\pi\alpha_\chi^2}{v_\chi^2}\int_{q_-}^{q_+} \frac{q\,\mathrm{d}q}{(q^2+m_v^2c^2)^2}\left|\langle\varepsilon|e^{i\boldsymbol{q}\cdot\boldsymbol{r}}|a\rangle\right|^2 \frac{p^2\,\mathrm{d}p\,\mathrm{d}\Omega_p}{(2\pi)^3}, \tag{7.2}$$

where $q_\pm = k \pm \sqrt{k^2 - 2m_\chi\Delta E}$, $|\varepsilon\rangle$ is an atomic state in the continuum with energy $\varepsilon \simeq p^2/2m_e$, the state $|a\rangle$ is a bound atomic state, and Ω_p denotes the momentum-space angular variables for the outgoing electron. The total energy deposition, $\Delta E \equiv \varepsilon - E_a$, is related to the change in energy of the DM particle and to the energy of the ejected electron:

$$\Delta E = \frac{k^2 - k'^2}{2m_\chi} = I_a + \varepsilon, \tag{7.3}$$

where I_a is the ionisation potential for the state $|a\rangle$.

The event rate is proportional to the function σv_χ, which must be averaged over the distribution for the DM particle velocity v_χ:

$$\langle\sigma v_\chi\rangle = \int_0^\infty f_\chi(v)\,\sigma\,v\,\mathrm{d}v \tag{7.4}$$

(note that the cross section σ itself depends strongly on v_χ, since this sets the incident energy of the DM particles). We take the velocity distribution to be

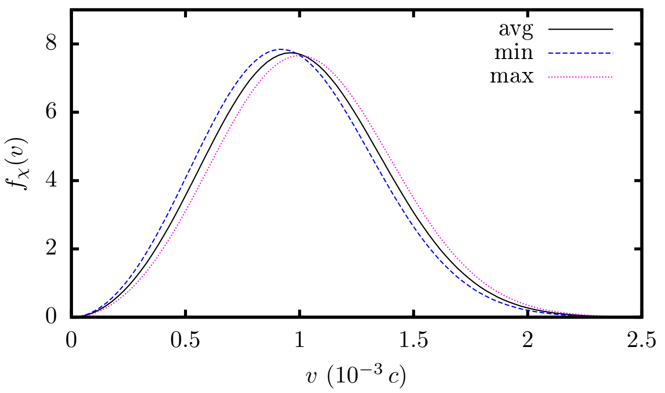

Figure 7.2 Normalised distributions for the DM velocity in the earth frame [see Eq. (7.5)]. The solid black line (avg) corresponds to the DM velocity distribution in the solar frame, and the dotted blue (min) and dashed magenta (max) lines refer to the distributions in the earth frame around December 2 and June 2, respectively.

pseudo-Maxwellian (see, e.g., Ref. [360]):

$$f_\chi(v) \propto v^2 \int_{-1}^{1} \exp\left[-\frac{3(\boldsymbol{v}+\boldsymbol{v}_e)^2}{2v_{\rm rms}^2}\right] \mathrm{d}(\cos\gamma)\,\Theta, \tag{7.5}$$

where, $v_{\rm rms}$ is the root-mean-square (rms) velocity of the DM particles in the galactic frame, γ is the angle between $\boldsymbol{v}$ and $\boldsymbol{v}_e$, and $\boldsymbol{v}_e$ is the velocity of the earth in the galactic frame:

$$v_e^2 \simeq v_\odot^2 + v_\oplus^2 + 2v_\odot v_\oplus \cos\beta\cos(\omega t), \tag{7.6}$$

where $v_\odot$ is the speed of the sun in the galactic frame, $v_\oplus$ is the orbital speed of the earth in the solar frame, and $\beta \approx 60°$ is the inclination of the earth's orbit relative to the galactic plane. Time $t = 0$ is when the velocities of the earth and sun add maximally in the galactic frame (corresponding to around June 2), and $\omega = \frac{2\pi}{T}$ with $T \sim 1\,\text{yr}$. The Heaviside-theta function Θ acts as the appropriate escape velocity ($v_{\rm esc}$) cut-off (the maximum allowed velocity of the DM particles in the galactic frame). The proportionality constant is determined from the normalization condition: $\int_0^\infty f_\chi(v)\,\mathrm{d}v = 1$. We take $v_{\rm rms} = 0.73\times10^{-3}\,c$, $v_\odot = 0.77\times10^{-3}\,c$, $v_{\rm esc} = 2.2\times10^{-3}\,c$, and $v_\oplus = 0.10\times10^{-3}\,c$ [360]. The particular distributions of interest are shown in Fig. 7.2. We note, however, that the above Maxwell distribution (7.5) is not the only candidate; in fact non-Maxwellian distributions are well-motivated, and, in certain circumstances, may have a significant impact on the modulation rate [392] (see also Ref. [393] and references therein).

In the experiment, neither ε or I_a are measured individually; instead it is the combination ΔE (7.3) that is important. The number of "single-hit" events in certain energy intervals (2–4 keV, 2–5 keV, and 2–6 keV) are recorded; only the single-hit rate is recorded, since the likelihood that a double-hit event would be caused by a dark matter interaction is vanishingly small. Therefore, the quantity of interest is

$$\langle \mathrm{d}\sigma\, v_\chi \rangle = \frac{4\alpha_\chi^2}{\pi}\int_0^\infty \mathrm{d}v \frac{f_\chi(v)}{v}\int_{q_-}^{q_+} \mathrm{d}q \frac{q}{(q^2+m_v^2c^2)^2} \\ \times \sum_{n,\kappa} m_e\sqrt{2m_e(\Delta E - I_{n\kappa})}K_{n\kappa}\, \mathrm{d}(\Delta E), \tag{7.7}$$

where $\kappa = (l-j)(2j+1)$ is the Dirac quantum number[1] with l and j the orbital and total (single-electron) angular momentum quantum numbers, respectively, and the "atomic kernel" is defined

$$K_{n\kappa}(\Delta E, q) = \sum_{\kappa'}\sum_{m,m'} \left|\langle \varepsilon\kappa' m' |\, \mathrm{e}^{i\boldsymbol{q}\cdot\boldsymbol{r}} | n\kappa m\rangle\right|^2. \tag{7.8}$$

Here, m is the projection of $\boldsymbol{j}$ onto the axis of quantization.

Then, the differential event rate per unit energy per kilogram, is given by

$$\mathcal{R}_{m_\chi, m_v, \alpha_\chi}(\Delta E) = \frac{n\rho_\chi}{m_\chi}\frac{\langle \mathrm{d}\sigma\, v_\chi\rangle}{\mathrm{d}(\Delta E)}, \tag{7.9}$$

where $\rho \approx 0.4\,\mathrm{GeV\,cm^{-3}}$ is the assumed local DM energy density, and n is the number of target atoms per kilogram. The total average event rate per kilogram in the energy interval $\Delta E \in [a,b]$ is given by

$$R_{a\to b} = \frac{1}{\Delta E_b - \Delta E_a}\frac{n\rho_\chi}{m_\chi}\int_a^b \langle \mathrm{d}\sigma\, v_\chi\rangle, \tag{7.10}$$

which is expressed in units of counts per day (cpd) per kg/keV.

7.3 Importance of electron relativistic effects

7.3.1 Exponential suppression (and lack thereof)

The large magnitude of the momentum transfer q relative to the typical electron momenta means that the exponent in the atomic structure factor $\langle f |\, \mathrm{e}^{-i\boldsymbol{q}\cdot\boldsymbol{r}} | i\rangle$ oscillates much more rapidly than the electron wave functions involved. The value of this integral is thus determined by small electron–nucleus separations, and the dominant contribution to the cross section is proportional to the probability of finding the electron close to the nucleus.

In general, rapid oscillations of $\mathrm{e}^{-i\boldsymbol{q}\cdot\boldsymbol{r}}$ lead to an exponential suppression of the amplitude. The simplest way to see this is by assuming that the electron wave functions have an oscillator-like behaviour, $\psi_{i,f}(r) \sim A\,\mathrm{e}^{-\beta r^2}$. The matrix element for large q will then be

$$\langle f |\, \mathrm{e}^{-i\boldsymbol{q}\cdot\boldsymbol{r}} | i\rangle \propto \mathrm{e}^{-q^2/8\beta}, \tag{7.11}$$

which is exponentially suppressed. This behaviour will be observed for any electron wave functions that are smooth near the origin. As mentioned above, exponential suppression of the amplitude for large v_e/V is also the general result of the adiabatic nature of the perturbation by a slow projectile [394, 395].

---

[1] $\kappa = -1$ for $s_{1/2}$, $\kappa = 1$ for $p_{1/2}$, $\kappa = -2$ for $p_{3/2}$, etc.

We demonstrate, however, that the behaviour of the electron wave functions near the origin of the Coulomb field leads to contributions to the amplitude that are not exponentially suppressed. These terms are proportional to the nuclear charge Z and decrease only as a power of q at large q.

Consider the ejection of an electron with energy ε from an atomic orbital nl. The contribution of the final-electron partial wave l' to the amplitude $\langle\varepsilon l'|\,\mathrm{e}^{-i\boldsymbol{q}\cdot\boldsymbol{r}}|nl\rangle$ is proportional to the radial integral

$$\int_0^\infty R_{\varepsilon l'}(r)R_{nl}(r)j_L(qr)r^2\,\mathrm{d}r, \tag{7.12}$$

where $R_{nl}(r)$ and $R_{\varepsilon l'}(r)$ are the radial wave functions of the initial and final states, $j_L(x)$ is the spherical Bessel function, the values of l, l' and L must satisfy the triangle inequality, and $l+l'+L$ must be even due to parity selection. The leading contribution to this integral at large q comes from small $r\sim 1/q$, where the radial functions behave as (in atomic units: $a_0=1$, $c=1/\alpha\approx 137$)

$$R_{nl}(r)\simeq Ar^l\left[1-\frac{Z}{l+1}r+\dots\right], \tag{7.13}$$

A being the normalization factor, and with a similar expression for $R_{\varepsilon l'}(r)$. From Eqs. (7.12) and (7.13), it appears that the leading contribution to the amplitude at high q is proportional to

$$\int_0^\infty r^{l+l'+2}j_L(qr)\,\mathrm{d}r=\frac{1}{q^{l+l'+3}}\int_0^\infty x^{l+l'+2}j_L(x)\,\mathrm{d}x. \tag{7.14}$$

However, the integral

$$\int_0^\infty x^{l+l'+2}j_L(x)\,\mathrm{d}x=2^{l+l'+1}\sqrt{\pi}\frac{\Gamma\left[\frac{3}{2}+\frac{1}{2}(L+l+l')\right]}{\Gamma\left[\frac{1}{2}(L-l-l')\right]}$$

is identically zero for even $l+l'+L$, since the gamma function in the denominator has poles for nonpositive integer arguments. This also shows that including any even-power corrections to the small-r expansion of the wave functions, Eq. (7.13) (which appear for any potential regular at the origin), also leads to zero contributions. Therefore the amplitude in this case would decrease faster than any power of q, i.e., exponentially.

On the other hand, the lowest-order, linear correction in either $R_{nl}(r)$ and $R_{\varepsilon l'}(r)$, is proportional to Z [see Eq. (7.13)], and the integral $\int_0^\infty x^{l+l'+3}j_L(x)\,\mathrm{d}x$ is *nonzero*. This determines the leading asymptotic behaviour of the amplitude,

$$\int_0^\infty R_{\varepsilon l'}(r)R_{nl}(r)j_L(qr)r^2\,\mathrm{d}r\propto\frac{Z}{q^{l+l'+4}}. \tag{7.15}$$

This shows that the largest cross section for large q (i.e., the least suppression, $\left|\langle f|\,\mathrm{e}^{-i\boldsymbol{q}\cdot\boldsymbol{r}}|i\rangle\right|^2\propto q^{-8}$) is obtained for both initial and final s states ($l=l'=L=0$). Similar integrals arise in the problem of atomic photoionisation at high energies, see, e.g., Ref. [396, 397].

This power, instead of the exponent, emerges due to the Coulomb singularity of the electron wave function at the nucleus. The singularity for the s-wave electrons is stronger than in higher partial waves, whose expansions contain extra powers of r. The ionisation by slow, heavy particles is thus dominated by s-wave contributions from small electron–nuclear distances. This means that there is an effective atomic-structure enhancement of such scattering processes involving s-waves, and that relativistic effects may be significantly larger than expected.

7.3.2 Relativistic enhancement

Indeed, the situation in the relativistic case is quite different. Consider the Dirac wave function for an electron in the central field of the atom,

$$\psi_{n\kappa m} = \begin{pmatrix} F_{n\kappa}(r)\,\Omega_{\kappa m}(\theta_r,\phi_r) \\ iG_{n\kappa}(r)\,\Omega_{-\kappa,m}(\theta_r,\phi_r) \end{pmatrix}, \tag{7.16}$$

where κ is the Dirac quantum number [$\kappa = -(l+1)$ for $j = l + 1/2$, and $\kappa = l$ for $j = l + 1/2$, j being the total angular momentum], and $\Omega_{\kappa m}$ is the two-component spherical spinor. At small r, the radial functions of the large and small Dirac components behave as [398]

$$F_{n\kappa}(r) \simeq B\,r^{\gamma-1}\,(\gamma - \kappa + Cr + \dots), \tag{7.17a}$$

$$G_{n\kappa}(r) \simeq -Z\alpha B\,r^{\gamma-1}(1 + Dr + \dots), \tag{7.17b}$$

where B is a normalization constant, $\gamma = \sqrt{\kappa^2 - (Z\alpha)^2}$,

$$C = -\frac{Z}{2\gamma+1}[1 + (2\gamma - 2\kappa + 1)(1 + \alpha^2\varepsilon_{n\kappa})], \tag{7.18}$$

$\varepsilon_{n\kappa}$ is the electron energy, and $D \sim C$.

In the nonrelativistic limit ($Z\alpha \to 0$, $\gamma = |\kappa|$) $G_{n\kappa}$ vanishes, and Eq. (7.17a) reduces to Eq. (7.13). However, the corrections in $\gamma = |\kappa| - (Z\alpha)^2/2|\kappa| + \dots$ actually change the power of r that appears in the expansion. As a result, the lowest-order in r term, which vanished in the nonrelativistic case [see Eq. (7.14)], now becomes

$$\int_0^\infty r^{\gamma+\gamma'} j_L(qr)\,\mathrm{d}r = \frac{2^{\gamma+\gamma'-1}}{q^{\gamma+\gamma'+1}}\sqrt{\pi}\frac{\Gamma\left[\frac{1}{2}(L+\gamma+\gamma'+1)\right]}{\Gamma\left[\frac{1}{2}(L-\gamma-\gamma'+2)\right]}, \tag{7.19}$$

which is *nonzero*. For example, for the initial and final s-wave states [$\kappa = -1$, $\gamma = \gamma' \simeq 1 - (Z\alpha)^2/2$], we have

$$\int_0^\infty r^{2\gamma} j_0(qr)\,\mathrm{d}r = \frac{\Gamma(2\gamma)\sin[\pi(1-\gamma)]}{q^{2\gamma+1}} \simeq \frac{\pi(Z\alpha)^2}{2\,q^{3-(Z\alpha)^2}}. \tag{7.20}$$

If one considers the contribution from a $p_{1/2}$ state ($\kappa = 1$) for either the bound or continuum electron, or both, the power of the q remains the same, but the coefficient is further suppressed by a power of $Z\alpha$. This is true for scalar, pseudoscalar, vector, and pseudovector interactions[2]. The small component (G) is suppressed by $\sim Z\alpha$, while the lowest-order term in the large component is suppressed by the factor $\kappa - \gamma \sim (Z\alpha)^2$ [see Eqs. (7.17a) and (7.17b)].

---

[2] For vector, scalar, pseudovector, and pseudoscalar interactions, the atomic structure factor is proportional to integrals of the form $\int(FF' \pm GG')j_L r^2\,\mathrm{d}r$ and $\int(FG' \mp GF')j_L r^2\,\mathrm{d}r$, respectively

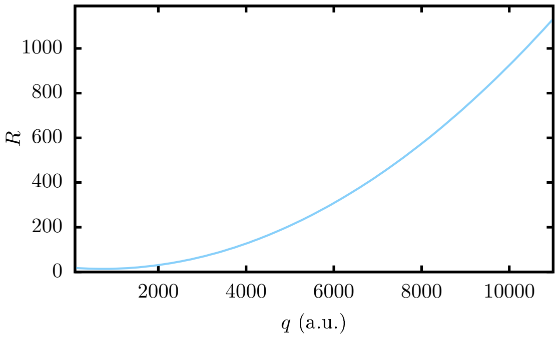

Figure 7.3 The ratio R of the atomic structure factor $\left|\langle\varepsilon s_{1/2}|\,\mathrm{e}^{-i\boldsymbol{q}\cdot\boldsymbol{r}}|3s_{1/2}\rangle\right|^2$ for the ionisation of $3s_{1/2}$ electrons in iodine ($I_{3s_{1/2}} = 1.1$ keV, $\varepsilon = 2$ keV) calculated with relativistic (hydrogen-like Dirac) wave functions to that obtained with nonrelativistic wave functions, using the true nuclear charge $Z = 53$. (The momentum conversion factor is 1 MeV/$c \approx 268$ a.u.)

Thus we see that not only is the exponential suppression removed, but even the power suppression is significantly weaker than that found in the nonrelativistic case. Note that the cross section goes as the square of the amplitude, meaning that the momentum-transfer dependence of the leading atomic structure contribution to the cross section is proportional to $q^{-6+2(Z\alpha)^2}$ (compared to q^{-8} in the nonrelativistic case, and $\mathrm{e}^{-(q/p_e)^2}$ in the "naive" adiabatic case). For a finite-range interaction, the cross section, which is to be integrated over q, contains the squared propagator $(q^2 + m_p^2c^2)^{-2}$ (m_p is the mass of the exchange particle); the atomic structure factor is unchanged, and our conclusions remain the same. This result indicates that relativistic effects actually give the dominating contribution to the amplitude, and that therefore a nonrelativistic treatment of such problems can greatly underestimate the size of the effect.

We have verified this enhancement numerically. In Fig. 7.3, we plot the ratio of the atomic structure factor calculated using relativistic Dirac-Coulomb wave functions to those calculated using nonrelativistic Schrödinger functions. The calculations were performed for the $3s$ state of iodine, which would give the dominant contribution to the ionisation rate due to WIMP–electron scattering at the energy scale relevant to the DAMA experiment [370] (the $1s$ and $2s$ electrons are bound too tightly in I and Xe to become ionised with the energy deposition observed by DAMA). We use the true nuclear charge ($Z = 53$ for iodine) instead of the effective nuclear charge $\widetilde{Z}$. The standard definition $\widetilde{Z} = n\sqrt{2I_{nl}}$, where n is the principal quantum number and I_{nl} is the electron ionisation energy, provides a sensible approximation for the wave function at intermediate distances. At very small distances, however, the nuclear charge is essentially unscreened. Therefore, the atomic wave functions at small distances are proportional to the pure Coulomb wave functions. Given the importance of small electron–nuclear separations, such processes are strongly dependent on the atomic number, and using a too-small $\widetilde{Z}$ can lead to orders-of-magnitude underestimation of the probability. The best way to treat this problem is to use a self-consistent field approach, such as the relativistic Hartree-Fock method.

A full comparison of the relativistic and nonrelativistic calculations of the atomic kernel of iodine is presented in Fig. 7.4 for relatively high values of the

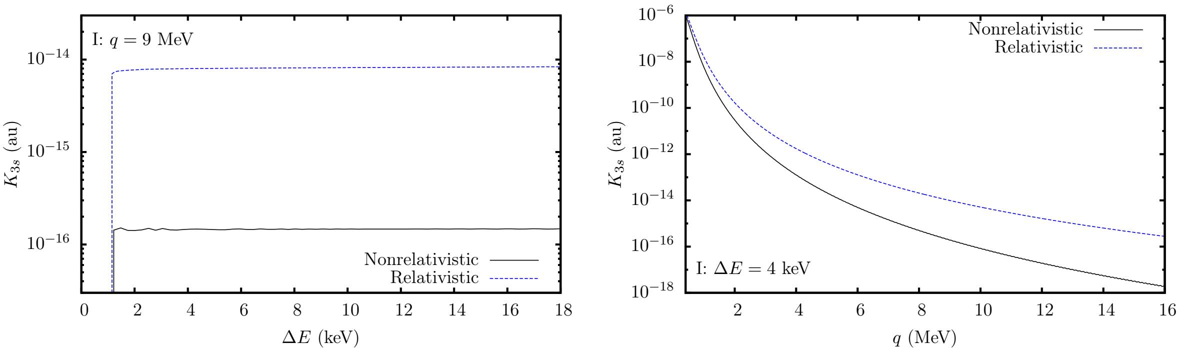

Figure 7.4 Comparison of the contribution of the $3s$ state to the atomic kernel of iodine in the relativistic and nonrelativistic approximations: (*left*) as a function of the energy deposition (ΔE) for a value of the momentum transfer of $q \simeq 9\,\text{MeV}$, and (*right*) as a function of q for $\Delta E \simeq 4\,\text{keV}$.

momentum transfer, q (only high values of q can contribute the cross section). For consistency, the relativistic and nonrelativistic calculations are performed using the exact same methods and computer codes (the relativistic Hartree-Fock method, described below); the nonrelativistic limit is achieved by letting the speed of light approach infinity in the code before the Dirac equation is solved. As $q \to 0$, the difference between the relativistic and nonrelativistic approaches diminishes, as expected. There are slight numerical instabilities in the nonrelativistic calculations visible in the plots in Fig. 7.4 (solid black line); these instabilities do not appear in the relativistic calculations. This is because in the relativistic case the atomic kernel is dominated by a single contribution coming from very low r, while the nonrelativistic case has contributions from larger r which cover several oscillations of the (very rapidly oscillating) j_L function. (Of course, the instabilities in the nonrelativistic calculations can be removed by increasing the parameters of the numerics, however, this is not necessary for the current purpose.)

7.4 Calculations

7.4.1 Calculations of the atomic kernel

To perform the atomic structure calculations we use the relativistic Hartree-Fock method, which is described briefly in Appendix A. Calculations of the bound-state energies for the core orbitals of atomic Na, Ge, I, Xe, and Tl are given in Table 7.1.

In Fig. 7.5, we plot the contributions of the different core states to the atomic kernel (7.8) for iodine as a function of the energy deposition, for a fixed momentum transfer. It is seen that the s-states dominate the amplitude, as expected. In Fig. 7.6 we plot the $3s$ core contribution to the iodine atomic kernel for different values of the maximum included continuum-state angular momentum as a function of the momentum transfer for fixed energy deposition. For very low values of momentum transfer, only the $j = 1/2$ states give significant contributions. For intermediate values, higher angular momentum states become important. For the high momentum transfer values, which are those relevant to

Table 7.1 Relativistic Hartree-Fock ionisation energies for the core states of Na, Ge, I, Xe, and Tl in atomic units (1 au = 27.211 eV).

Atom Z	Na 11	Ge 32	I 53	Xe 54	Tl 81
$1s_{1/2}$	40.54	411.1	1226	1277	2851
$2s_{1/2}$	2.805	53.46	193.0	202.5	484.5
$2p_{1/2}$	1.522	47.33	180.6	189.7	465.7
$2p_{3/2}$	1.515	46.15	169.6	177.7	465.7
$3s_{1/2}$	0.182	7.410	40.53	43.01	117.1
$3p_{1/2}$		5.325	35.34	37.66	108.2
$3p_{3/2}$		5.157	32.21	35.33	108.2
$3d_{3/2}$		1.616	24.19	26.02	91.71
$3d_{5/2}$		1.592	23.75	25.54	91.71
$4s_{1/2}$		0.569	7.759	8.430	26.88
$4p_{1/2}$		0.282	5.869	6.453	22.92
$4p_{3/2}$		0.273	5.450	5.983	22.92
$4d_{3/2}$			2.342	2.711	15.65
$4d_{5/2}$			2.274	2.634	15.65
$5s_{1/2}$			0.876	1.010	4.617
$5p_{1/2}$			0.434	0.493	3.230
$5p_{3/2}$			0.390	0.440	3.230
$4f_{5/2}$					5.784
$4f_{7/2}$					5.784
$5d_{3/2}$					0.967
$5d_{5/2}$					0.967
$6s_{1/2}$					0.360
$6p_{1/2}$					0.201
$6p_{3/2}$					0.201

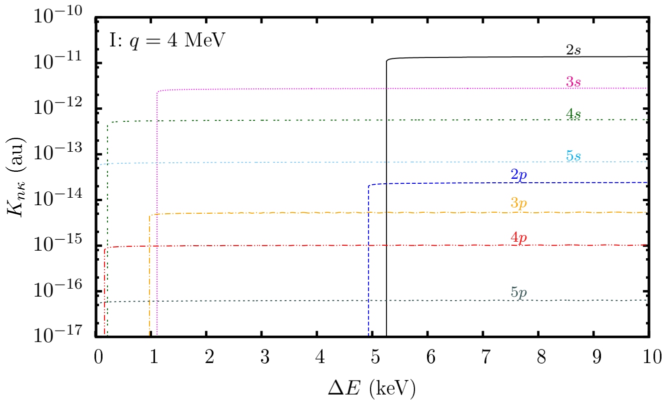

Figure 7.5 Core-state contributions to the atomic kernel [defined in Eq. (7.8)] for I as a function of the energy deposition, ΔE, at momentum transfer $q \simeq 4$ MeV. The s states dominate the amplitude; this domination only increases at larger q. The contributions from the d states (not shown) are orders of magnitude smaller again.

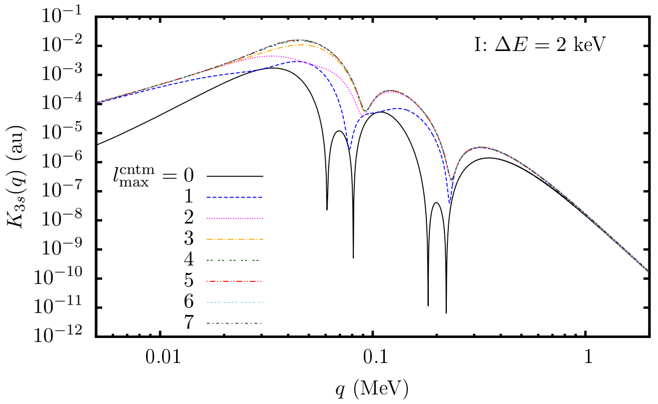

Figure 7.6 Contribution of the $3s$ core state to the atomic kernel for I as a function of the momentum transfer, q, at $\Delta E \simeq 2$ keV. Shown separately are the kernels with different values for the high-l cut-off for the continuum-state electron orbital angular momentum. The higher l continuum states contribute significantly at low values of q, however, at the values relevant to this work ($q >\sim$MeV), they contribute negligibly.

the ionisation problem, the higher angular momentum states contribute negligibly and only s-wave continuum states are important. Note that this is a result of the relativistic effects; in the nonrelativistic limit higher angular momentum states contribute non-negligibly because the s-state contribution is significantly underestimated. The general result is that in the calculations, only s-states need to be considered both for the bound states and for the continuum states, as suggested above; p-states contribute at the few-percent level. We have checked this in the direct calculations of the cross section as well, and it continues to hold true. We note, however, that in our full atomic structure calculations we keep all higher angular momentum states until the cross section converges explicitly to the $\sim 0.1\%$ level. For lower values of energy deposition ($\Delta E \lesssim 1\,$keV) this condition becomes less strong. Though not directly relevant to the DAMA experiment, this may be important for other types of electron-recoil experiments, such as those suggested in Refs. [399, 400].

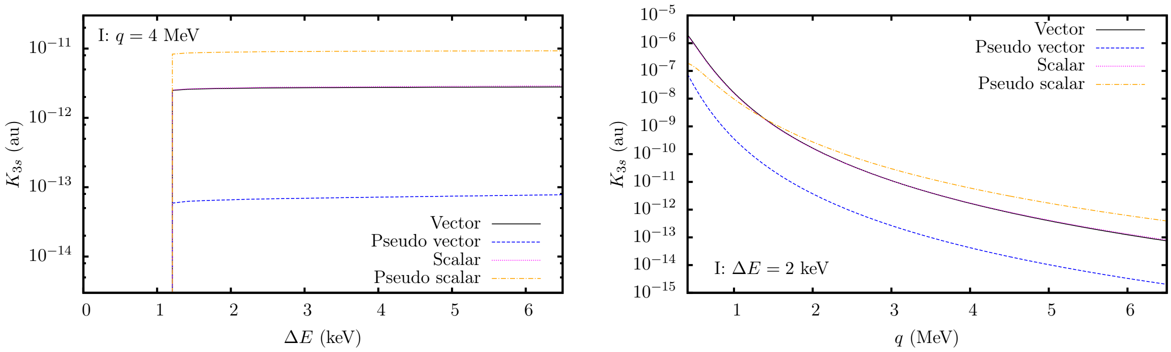

Figure 7.7 Comparison of the different Lorentz structures for the $3s$ core-state contribution to the atomic kernel for I as a function of the energy deposition, ΔE (with $q \simeq 4$ MeV), and of the momentum transfer, q (with $\Delta E \simeq 2$ keV). The pseudoscalar case gives the largest effect, since in this case the radial integrals include a contribution from initial and final s-states with $L = 1$ ($L = 0$ for the s-s contribution to the vector and scalar cases); the pseudovector case (zero/temporal component) gives by far the smallest contribution due to very large cancellations in the radial integrals, see Appendix B.2.

In Fig. 7.7, we present calculations of the atomic structure factors for the vector, scalar, pseudovector, and pseudoscalar electron interactions (see Appendix B.2). It is evident here that the electron pseudoscalar interaction gives the largest result (for very high momentum transfer), while the pseudovector case gives by far the smallest. The largeness of the pseudoscalar case can be understood as follows. The Factor $(Z\alpha)^2$ in the numerator of Eq. (7.20) comes from the expansion of the gamma function in the denominator of Eq. (7.19), which approaches infinity as γ approaches unity for $L = 0$. For the case where $L = 1$, however, this denominator is finite even in the $Z\alpha \to 0$ limit. Considering an initial (bound) s-state, there appears a contribution for the pseudoscalar and pseudovector cases that comes from the final $s_{1/2}$ continuum state with $L = 1$. In this case, the $(Z\alpha)^2$ suppression from Eq. (7.20) is removed, instead it is replaced by just a $\sim Z\alpha$ suppression which comes from the small Dirac component that appears in the radial integral for the pseudoscalar case (B.24). There is another enhancement by a factor of ~ 4 due to the few roughly equal terms in Eq. (B.24). In the pseudovector case (zero component), on the other hand, this situation does not lead to an enhancement. Instead there is huge suppression, which comes from the very large cancellation of terms in Eq. (B.25). This means that calculations of the electron structure for the pseudovector case are very susceptible to numerical instabilities and must be treated with great care (if high accuracy is to be achieved). The spatial components of the pseudovector interaction, however, are not small; in fact that scale essentially the same as the vector component. For s and $p_{1/2}$ waves (the only states relevant here) the deviation of the spatial components in pseudovector case from the temporal component of vector case is negligible; see Appendix B.2.

7.4.2 Scaling of the analytic results: a simple parametric model

In Figs. 7.8 and 7.9 we plot the contribution of several dominating core states to the atomic kernels (7.8) for Na, Ge, I, and Xe. Several orders-of-magnitude enhancement of the Xe/I atomic kernel compared to that of Na is observed, which is expected from the high-power of the Z-scaling of the electron matrix element, and the larger relativistic factor. Using the simple expression given in Eq. (7.20) to formulate the momentum transfer dependence of the atomic kernel for high values of q, one may use simple Z-dependent scaling factors to reproduce our full-scale calculations. For values below $q = 1$ MeV, the non-relativistic calculations using screened hydrogen-like wave functions are sufficient, though it should be noted that the usual notion of the effective nuclear charge $\widetilde{Z}_{nl} = n\sqrt{2I_{nl}}$ is not valid. This value is chosen to reproduce the correct energies, and gives a reasonable approximation of the wave functions at medium distances. The ionisation cross section, however, is dominated by the wave function at very small distances. Instead, the correct value for $\widetilde{Z}_{nl}$ should be chosen to reproduce the curves in Fig. 7.8.

7.5 Results

7.5.1 DAMA analysis

For our calculations of the atomic structure, we employ the system of atomic units ($\hbar = a_B = e = 1$, $c = 1/\alpha$). The conversion factor for the total cross section from atomic units is $a_B^2 \approx 2.8 \times 10^{-17}\,\text{cm}^2$, and for the function $\frac{\langle \mathrm{d}\sigma\cdot v\rangle}{\mathrm{d}\Delta E}$ is $a_B^2 c\alpha/2Ry \approx 0.019\,\text{cm}^3/\text{keV/day}$. We present the event rates in the standard units of counts per day (cpd) per kg/keV.

In Fig. 7.10, we plot the differential cross section (7.7) for Na, I, Xe, Ge, and Tl as a function of the total energy deposition, ΔE, for a specific set of DM parameters and assuming the standard halo velocity distribution (7.5). Note that the NaI detector in the DAMA experiment is doped with Tl. With a significantly higher atomic number, the effect arising from thallium is substantially larger than that from iodine; however, the small amount present in the detector means that the DAMA signal would still be dominated by the iodine contribution.

To a first approximation, the expected event-rate due to scattering of WIMPs from the galactic halo can be expressed as

$$R(t) = R_0 + R_m \cos(\omega t), \tag{7.21}$$

where R_0 is the constant or average part of the event-rate, which comes from the velocity distribution of the WIMPs in the solar frame, and R_m is the amplitude of the modulations in the event rate, which come from the relative motion of the earth around the sun; the factor ωt is defined in Eq. (7.6). We do note, however, that due to the very strong dependence of the scattering cross section on the incident energy of the DM particles (and therefore on the DM velocity), R_m itself depends on the phase of the earths orbit and therefore the event rate is not purely sinusoidal. The deviations from a sinusoidal shape, however, are modest for most of the parameter space, and do not affect the analysis substantially.

The so-called oscillation fraction, defined as R_m/R_0, has a strong dependence on the energy deposition, and on the mass of the DM particles. Fig. 7.11 shows the m_χ dependence of the differential cross section and the oscillation fraction for iodine as a function of the deposited energy, ΔE. The energy dependence

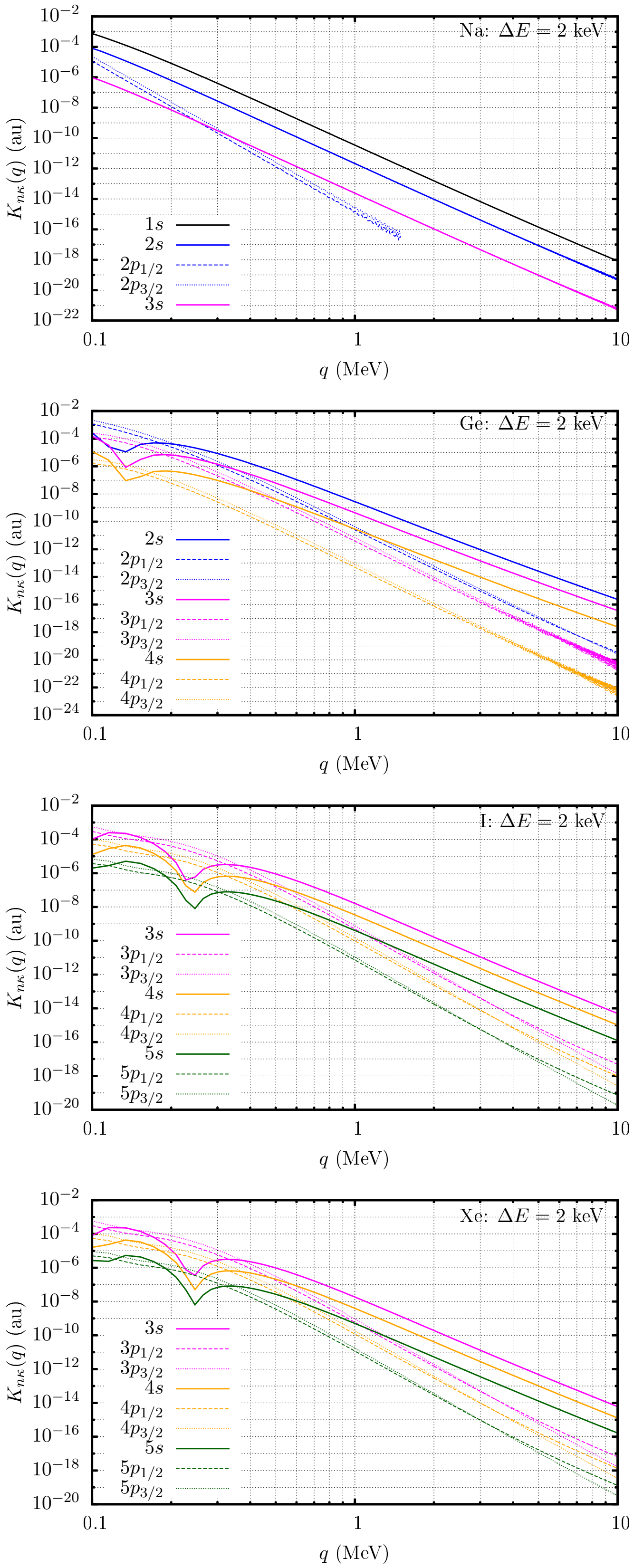

Figure 7.8 Plots of the atomic kernel (7.8) for several dominating core states of Na, Ge, I, and Xe, as a function of momentum transfer q, for a fixed energy deposition $\Delta E = 2.0$ keV.

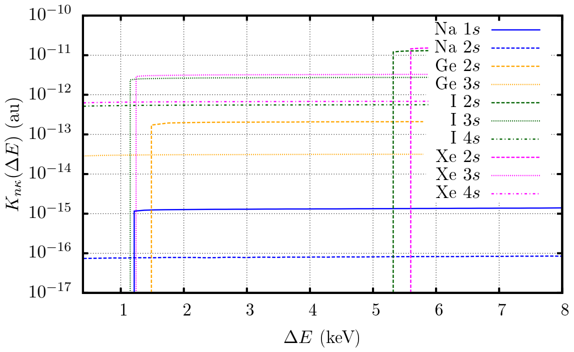

Figure 7.9 Plots of the atomic kernel (7.8) for a few dominating core states of Na, Ge, I, and Xe, as a function of energy deposition ΔE, for a fixed momentum transfer $q = 3.73$ MeV.

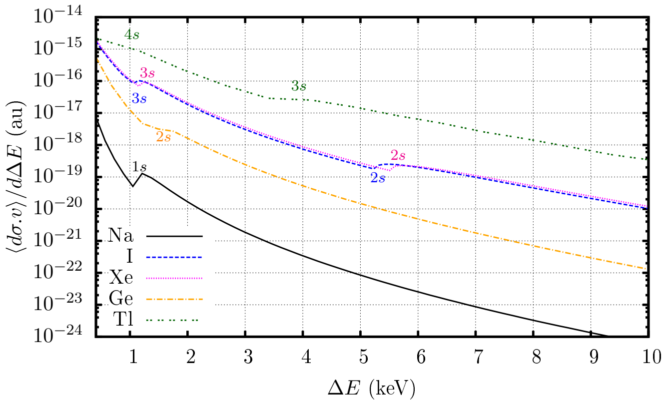

Figure 7.10 Plot of the differential cross section [defined in Eq. (7.7), with $m_\chi = 10\,\text{GeV}$, $m_v = 10\,\text{MeV}$, and for simplicity $\alpha_\chi = 1$] for Na, I, Xe, Ge, and Tl as a function of the total energy deposition, ΔE. The kinks in the curves correspond to the opening of deeper atomic shells; see Table 7.1. There is a clear and significant Z dependence, which is due to the low-r scaling of the wave functions and the relativistic effects.

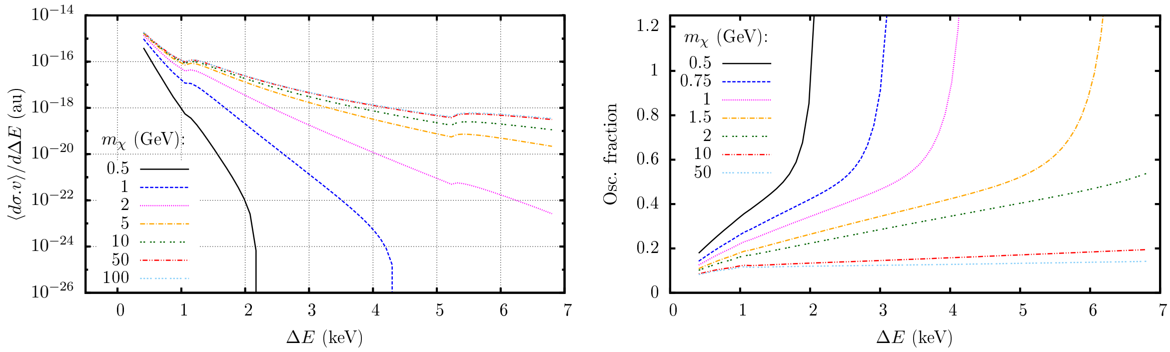

Figure 7.11 Plots showing the m_χ dependence of (*left*) the differential cross section, and (*right*) the oscillation fraction, for ionisation of iodine as a function of the deposited energy, ΔE. For the plots we have taken $m_v = 10$ MeV, and $\alpha_\chi = 1$. Low values of m_χ lead to significantly lower cross-sections, however, as m_χ increases the increase in the effect wanes. The energy dependence of the oscillations increases with decreasing m_χ, since in these regions only part of the DM velocity distribution can give rise to an effect.

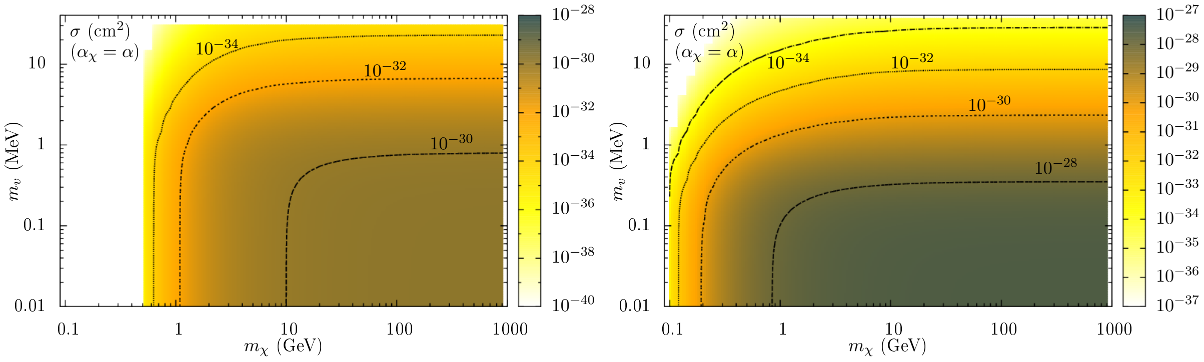

Figure 7.12 Total cross section (cm^2) for the ionisation of NaI in the 2 – 6 keV interval assuming $\alpha_\chi = \alpha$ for the average (i.e. spring/fall) DM velocity distribution: (*left*) assuming perfect detector resolution; (*right*) including the Gaussian resolution profile (7.22).

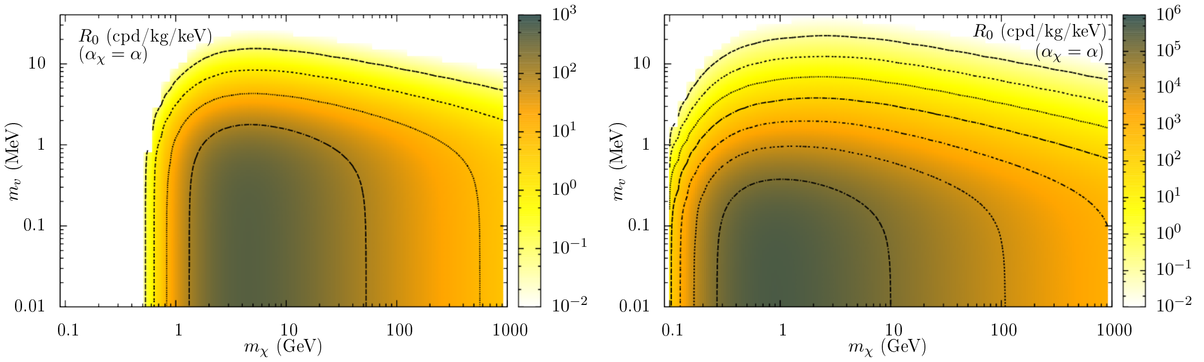

Figure 7.13 Unmodulated event-rate R_0 for NaI in the 2 – 6 keV interval assuming $\alpha_\chi = \alpha$ in units of cpd/kg/keV: (*left*) assuming perfect detector resolution; (*right*) including a Gaussian resolution profile (7.22).

of the oscillations increases with decreasing m_χ, since in these regions only part of the DM velocity distribution can give rise to an effect.

In order to calculate the number of events detected within a particular energy range, the energy resolution of the detectors must be taken into account. To do this, we convolute the calculated rate with a Gaussian:

$$\widetilde{R}(\Delta E) = \int R(\varepsilon) g_{\Delta E}(\varepsilon)\, \mathrm{d}\varepsilon, \tag{7.22}$$

where $g_{\Delta E}(\varepsilon)$ is a Gaussian function centred at ΔE, with standard deviation $\sigma = 0.448\sqrt{\Delta E/\mathrm{keV}} + 0.0091\Delta E/\mathrm{keV}$ as measured by the DAMA Collaboration [401]. This has the effect of "smearing out" the 2 keV low threshold, allowing a small fraction of events that originate from lower energies to be accepted. Note that since there is essentially an exponential enhancement in the event rate at lower energies (see Fig. 7.10) this has a significant impact on the results. We also assume that the DAMA detectors are 100% efficient, and importantly, that the efficiency is not a function of the energy deposition. This is a generous assumption which we make in order to be as conservative as possible.

Figure 7.12 shows the dependence of the cross section for the ionisation of NaI by DM–electron scattering on the DM particle mass and the mass of the

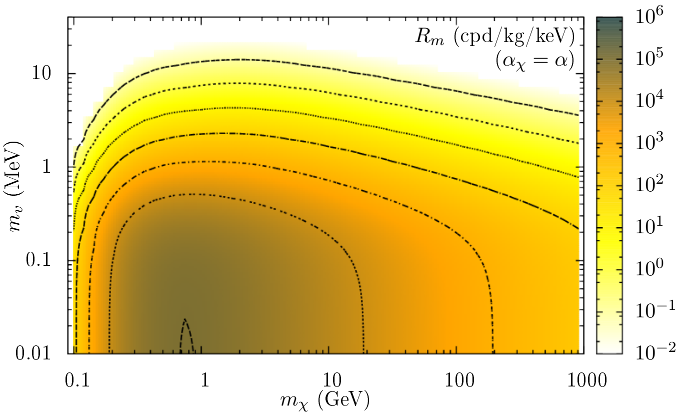

Figure 7.14 Modulation amplitude R_m for NaI in the 2 – 6 keV interval assuming $\alpha_\chi = \alpha$ in units of cpd/kg/keV (including the Gaussian resolution profile).

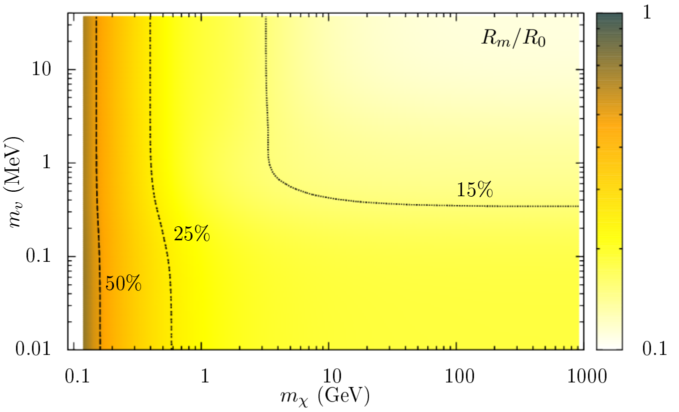

Figure 7.15 The calculated modulation fraction (R_m/R_0) expected for the scintillation signal in the 2 – 6 keV interval for NaI (including the Gaussian resolution profile).

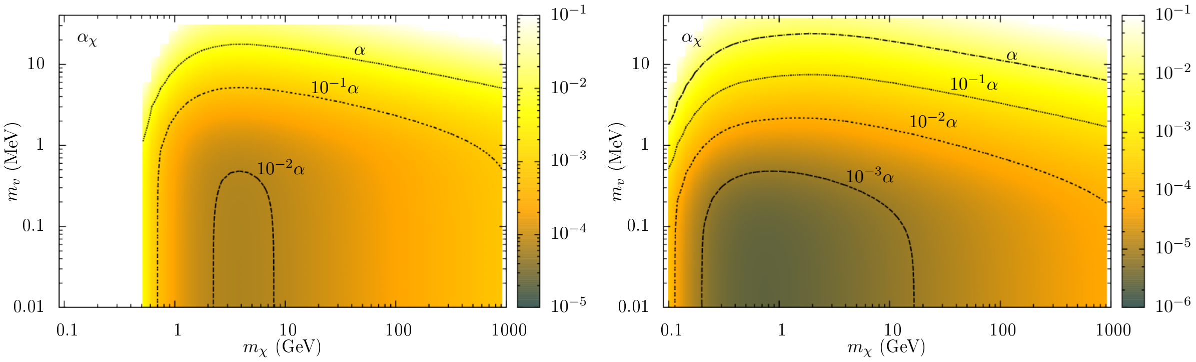

Figure 7.16 The value that α_χ must take in order to reproduce the DAMA modulation signal of 0.0112 cpd/kg/keV in the 2 – 6 keV interval: (*left*) assuming perfect detector resolution; (*right*) including the Gaussian resolution profile (7.22).

(vector) exchange particle. The plot is made arbitrarily with $\alpha_\chi = \alpha$; the cross section is linear in α^2, so with $\alpha_\chi = 10^{-2}\alpha$, for example, the value cross section would be smaller by a factor of 10^{-4}. The unmodulated event rate in the energy interval 2–6 keV, relevant to the DAMA experiment, is shown in Fig. 7.13. Shown separately are the event rates calculated assuming a perfect detector resolution, and assuming the Gaussian resolution as in Eq. (7.22). Note in particular, that the Gaussian profile allows events in this region to be caused by significantly smaller DM masses, and also greatly increases the observed event rate. This is entirely due to the fact that events originating at smaller energies (which have a much greater amplitude) are allowed to "leak" into the detection interval. As is clear, the dependence on the detector resolution is extreme. We note in particular, there is a clear favour of low m_χ, and that the modulation fraction is large. The corresponding modulated event rate (including the Gaussian profile) is shown in Fig. 7.14.

The DAMA collaboration observes a significant modulation in the event in this 2–6 keV interval, as described above. The amplitude of the observed modulation is [356]

$$R_m^{\rm DAMA} = 1.12(12) \times 10^{-2}\,{\rm cpd/kg/keV}, \tag{7.23}$$

amongst a background signal of approximately 1 cpd/kg/keV, which is attributed mostly to noise. To perform our analysis, we assume this modulation signal can be entirely attributed to ionisation of NaI by the scattering of WIMPs on the electrons. Figure 7.16 shows the value that the effective DM–electron coupling constant (α_χ) must take in order to give the required modulation amplitude.

In the WIMP–electron scattering scenario, the large modulation fractions (as reported by the DAMA [356], CoGeNT [402] and XENON100 [384] Collaborations) are reproduced naturally. The expected modulation fraction R_0/R_m is plotted explicitly for DAMA in Fig. 7.15. The fraction is very large, over 20% for large portions of the parameter space, even reaching as high as 50% for reasonable values. Note that this is assuming just the standard Maxwellian halo model for the DM velocity distribution (7.5). The large modulation is due to the fact that the ionisation cross section is highly velocity dependent. This is in contrast to WIMP–nucleon scattering cross section, where exotic DM distributions need to be assumed in order to replicate the large modulation fraction.

It is also seen that the mass m_v of the mediating particle (e.g., a dark photon) must be light. In order to keep the DM–electron coupling small ($\alpha_\chi \lesssim 10^{-2}\alpha$, required from collider searches, e.g., Ref. [403]), it is seen in Fig. 7.16 that $m_v \lesssim 1$ MeV. Note that, from stellar constraints, the mass of the mediator cannot be smaller than ~ 200 keV [404]. It is possible to reproduce the DAMA modulation within these constraints for a relatively wide range of parameters.

Note that in performing the analysis, we have paid no attention to the shape of the recoil spectrum, just choosing the parameters to reproduce the total number of counts in the given interval. This procedure represents the most conservative case; if the detectors were any less efficient, the acceptable values of α_χ would be forced to be larger. Taking these factors into account can therefore only strengthen out conclusions. In Fig. 7.17, the calculated spectrum is compared to the results of the DAMA experiment for a few specific sets of DM parameters that can reproduce the observed modulation amplitude averaged over the $2-6$ keV interval.

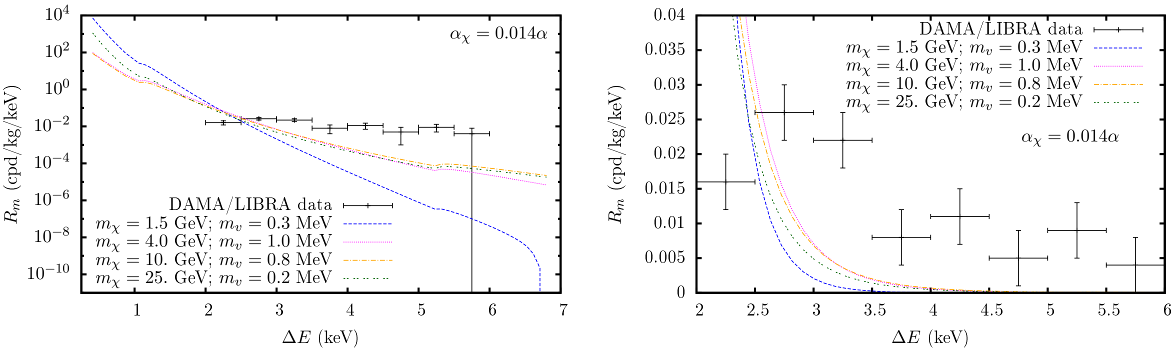

Figure 7.17 Calculated modulated event rate spectrum R_m for DAMA for a few specific choices of DM parameters which are able to replicate the amplitude of the observed modulation.

7.5.2 XENON100 analysis

A recent analysis of data from the XENON100 experiment has also investigated WIMP-induced electron-recoil events [383, 384]. These experiments also observed modest evidence for an annual modulation (at the 2.8σ level) – though the phase does not match perfectly with that observed by DAMA [384]. By assuming their result was a positive measurement of an annual modulation, the XENON Collaboration [384] (see also Ref. [383]) determined the best fit for their data to indicate an unmodulated event rate of

$$R_0^{\rm Xe100} = 5.5(6) \times 10^{-3}\,\text{cpd/kg/keV}, \tag{7.24}$$

with a modulation amplitude of

$$R_m^{\rm Xe100} = 2.7(8) \times 10^{-3}\,\text{cpd/kg/keV}, \tag{7.25}$$

with a quoted a background of $5.3{\times}10^{-3}$ cpd/kg/keV [383]. Note that the background (or unmodulated signal) is smaller than the DAMA modulation amplitude by a factor of two.

The XENON100 Collaboration has performed a detailed analysis of the electron recoil acceptance and efficiency [391, 406]. The electron recoil acceptance is given as a function of the observable scintillation photoelectrons is given in Fig. 1 (bottom) of Ref. [391]. Roughly, the acceptance rate can be given by the expression

$$ER_{\rm acc}(S1) \approx C_{\rm eff}\left(1 - {\rm e}^{-S1/3}\right), \tag{7.26}$$

where $C_{\rm eff}$ is an efficiency parameter with a best-fit value around 0.9 [391]. To be conservative, we take $C_{\rm eff} = 0.85$.

There is also the need to convert between 'S1' – the observed scintillation signal in photoelectrons (PE) – and the deposited energy deposition, ΔE. The conversion is given in Fig. 2 of Ref. [391]. We model this as a power law $S1(\Delta E) = \Delta E^x$, and take $x = 1.58$, which gives the best fit at 3 PE (2 keV), noting that the signal is dominated by lower energies. Then, the event rate for n detected photoelectrons is then obtained by applying "Poisson smearing" to the calculated

$$\widetilde{R}_n = \int R(\varepsilon)P_n(\varepsilon)ER_{\rm acc}(n), \tag{7.27}$$

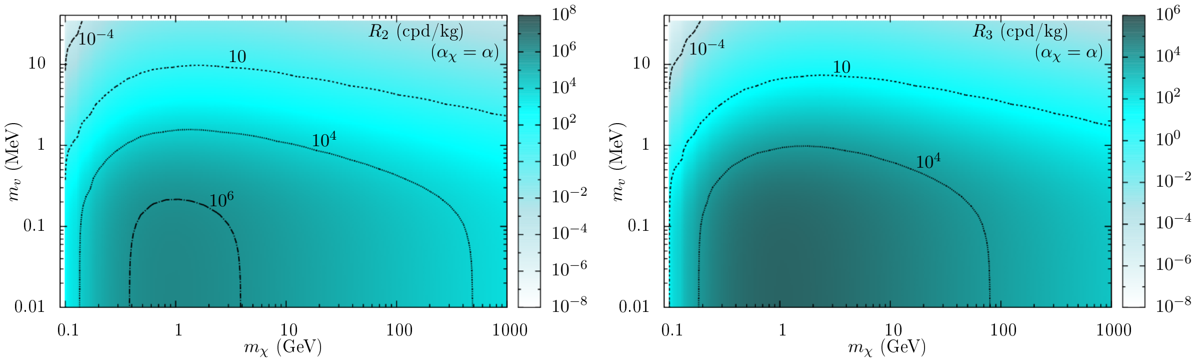

Figure 7.18 Calculated scintillation event rate for Xe (*left*) for 2 PE, and (*right*) for 3 PE.

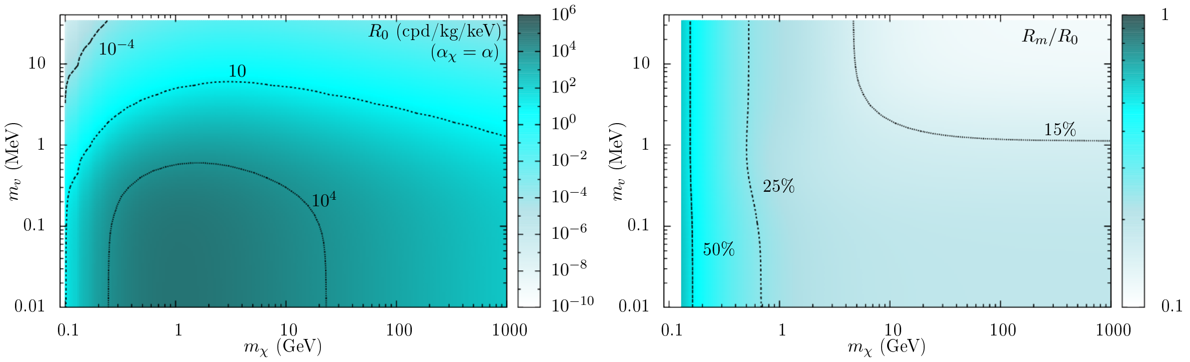

Figure 7.19 The calculated (*left*) unmodulated event rate (for fixed $\alpha_\chi = \alpha$), and (*right*) modulation fraction (R_m/R_0), for the scintillation signal in the 3 – 14 PE interval (corresponding to 2 – 6 keV) for Xe.

where the Poisson distribution is

$$P_n(\varepsilon) = \mathrm{e}^{-S1(\varepsilon)}\,\frac{S1(\varepsilon)^n}{n!}.$$

Note also, that we do not take into account the PMT resolution, $\sigma_{\rm PMT} = 0.5$PE [391, 407]. Taking this into account would allow a small fraction of the events at 2 PE to survive the cut and enter the observed rate. Since the rate at 3 PE is highly suppressed compared to the rate at 2 PE, as shown in Fig. 7.18, this choice should be considered conservative. We do note, however, that the Poisson smearing itself allows events that originate at energies lower than 2 keV to be detected with 3 PE, and is in this way similar to the simplistic Gaussian smearing employed for the DAMA analysis.

In Fig. 7.19 we present our calculations for the unmodulated event rate R_0 (for a fixed coupling $\alpha_\chi = \alpha$) and the modulation fraction R_m/R_0 for the XENON100 scintillation experiment, in the 3 – 14 PE range. The modulation fraction observed in the XENON100 experiment (7.25) is extremely large. We find, however, that this alone is not enough to discount the WIMP hypothesis as a source for the modulations. The calculated modulation fraction is very large, easily reaching 50% for very low values of $m_\chi < 1$ GeV. Note that the oscillation fraction is independent of the coupling constant.

By assuming the DAMA result is due to electron-interacting WIMPs, we can

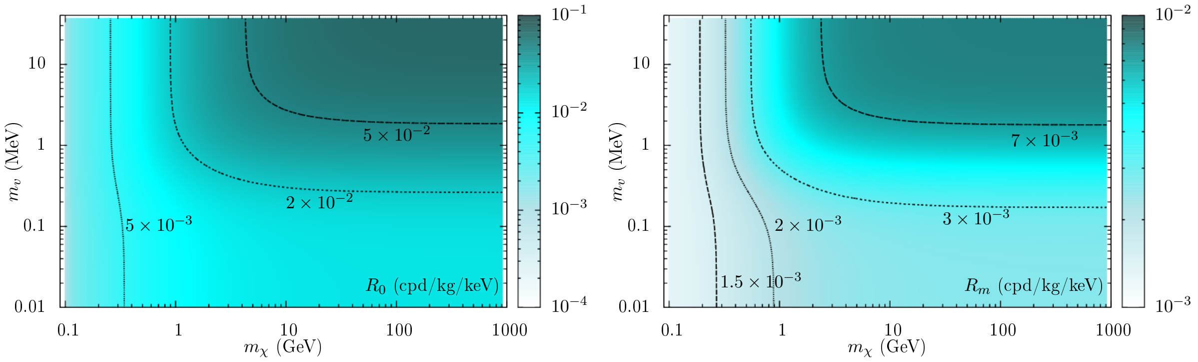

Figure 7.20 (*Left*) The umodulated event rate, and (*Right*) the modulation amplitude, that would be expected in the XENON100 scintillation experiment in the 3 – 14 PE interval (corresponding to 2 – 6 keV) assuming the DAMA modulation signal is a positive WIMP detection (the value of α_χ for each point on the parameter plot is shown in Fig. 7.16).

calculate the expected scintillation signal in xenon relevant to the XENON100 electron-recoil experiment. For each set of DM and mediator masses, we calculate the coupling required to reproduce the DAMA modulation signal in the 2 – 6 keV interval, assuming it is due to WIMP–electron scattering on the NaI crystal. These couplings, shown in Fig. 7.16 (*bottom*), are used as inputs into the calculations for xenon. Figure 7.20 shows the resulting calculated event rates that would be generated in liquid xenon summed between 3 and 14 photoelectrons (PE), as in the XENON100 electron recoil experiment [383, 384]. For convenience of comparison with the DAMA calculations, the rate is given in units of cpd/kg/kev – for which we calculate the total cpd/kg, and divide by 4 keV (corresponding to the 2 – 6 keV interval).

The XENON100 Collaboration sees an average (background) signal of around 0.005 cpd/kg/keV, with a potential annual modulation of about half this size. As is seen from the calculations of the unmodulated event rate R_0 for xenon, presented in Fig. 7.20 (left), there is room in the parameter space that can account for the DAMA modulation and still be consistent with XENON100. The modulated rate, presented in Fig. 7.20 (bottom), is also in reasonable agreement. We note, however, that these results are extremely dependent on the parameters of the detector acceptance, efficiency, and resolution.

In Fig. 7.21, we plot the modulated part of the ionisation event rate for xenon for a few specific choices of DM parameters that are able to reproduce (the amplitude of) the DAMA modulation signal. This shows that a detailed knowledge of the detector efficiency at very low energies is crucial for interpreting observed scintillation signal in terms of electron interacting DM. A discussion of the low energy efficiency is presented in Ref. [391] (see also Refs. [362, 405, 406, 408] and Ref. [409]).

7.5.3 XENON10 ‘ionisation only’ analysis

The XENON10 Collaboration [410] has performed an analysis of the ionisation-only signal in their liquid xenon detector. This data has been analysed in terms of low mass electron-interacting WIMPs [399], and limits have been set [411].

In Fig. 7.22 we plot the event rate for the primary ionisations generated

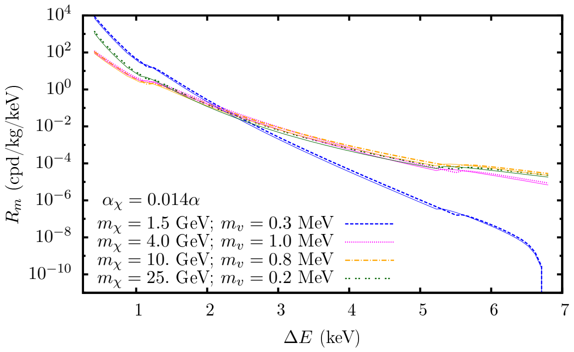

Figure 7.21 Calculation of the modulated ionisation event rate spectrum R_m for xenon (relevant to XENON100) for a few specific choices of DM parameters which are able to replicate the amplitude of the observed DAMA modulation. The corresponding signals generated in NaI are plotted in thin solid lines (almost indistinguishable from the xenon rates on this scale).

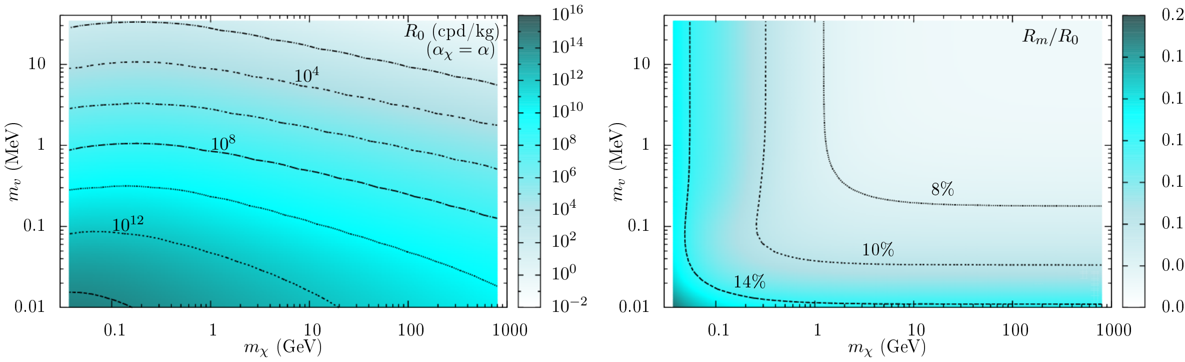

Figure 7.22 Calculation of (*left*) the unmodulated single primary-electron ionisation signal in xenon (relevant to the XENON10 experiment [410]) for a fixed coupling of $\alpha_\chi = \alpha$, and (*right*) the modulation fraction.

in a xenon detector due to the scattering of electron-interacting WIMPs. Note that this is a lower-bound on the generated events, since the primary ionisations (particularly from lower shells) will also induce secondary ionisations with some probability. The dominating contribution at low DM masses comes from the upper most shells; this is in line with previous calculations [411]. For very large DM masses (and large mediator masses) higher energy ranges play a significant role also. The spectrum of events for a few selected values of the DM mass is given in Fig. 7.23.

Figure 7.24 shows calculations of the ionisation rate for xenon integrated over all energy depositions (relevant to the ionisation-only XENON10 experiment [410]), assuming the DAMA modulation is due to electron-interacting WIMPs. Note that presented here is the calculation of "first-order" ionisation events only; i.e. the rate of ionised electrons Some fraction of these ionised electrons will recombine emitting photons which may also ionise other atoms. Also, when it is not the outermost electron which is ionised, the decay of the outer electrons to fill the created vacancy will also release photons which will ionise subsequent atoms with some probability. For a discussion, see Ref. [411].

The modulation fraction for the ionisation-only signal is substantially smaller

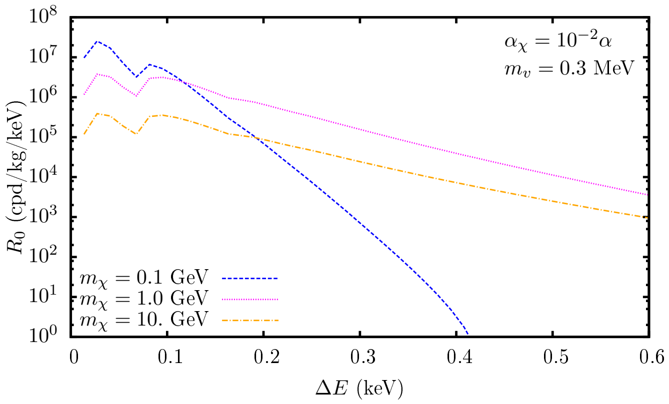

Figure 7.23 Calculation of the spectral shape for the single primary-electron ionisation signal (unmodulated) in xenon for a fixed coupling of $\alpha_\chi = 10^{-2}\alpha$ and $m_v = 0.3$ MeV, for a few DM masses.

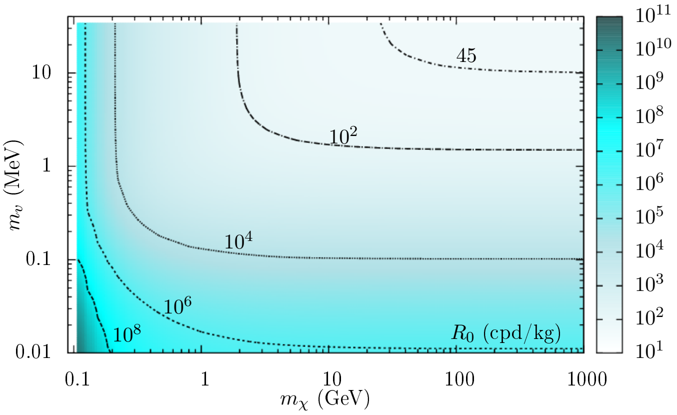

Figure 7.24 Calculation of the expected unmodulated ionisation-only signal in xenon (relevant to the XENON10 experiment [410]) assuming the DAMA modulation signal (7.23) is a positive WIMP detection.

than for the scintillation signal; it is below 10% for most of the parameter space. This is because the low-energy cut-off required for the scintillation signal means the observed signal can only originate from the high-energy (and high momentum transfer) tail of the cross section. In this region, the cross section becomes highly velocity dependent, hence the large modulation fraction; see Fig. 7.11.

The XENON10 Collaboration [410] observes at most 30 cpd/kg; at the 90% confidence level, the authors of Ref. [411] put a bound on the single-electron ionisation rate at 23.4 cpd/kg. The two-electron rate is substantially smaller at < 4.23 cpd/kg. As is clear from the calculations of the expected rate in xenon Fig. 7.24, there is no room in the relevant parameter space that can satisfy the DAMA modulation and escape the XENON10 limits. The very small error bars on the DAMA modulation ensure that even taking the DAMA modulation amplitude as many standard deviations smaller than the actually observed midpoint cannot significantly change this conclusion.

Note that we do not take into account any secondary ionisation that occurs.

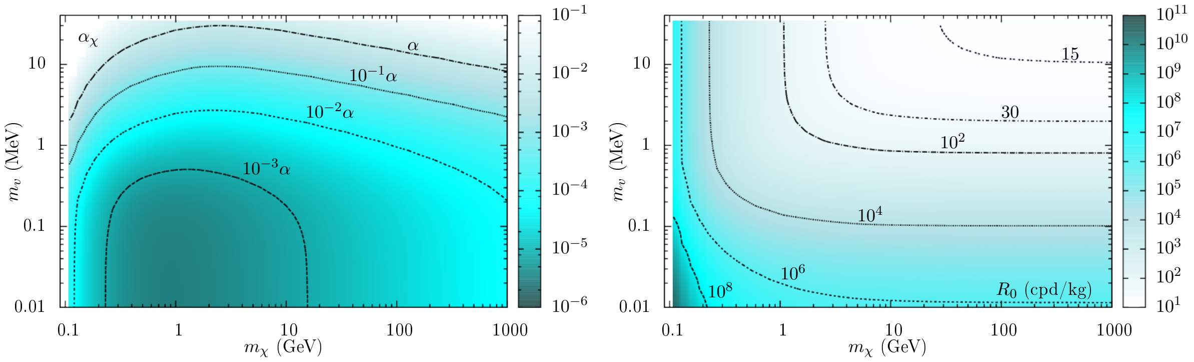

Figure 7.25 Calculations for the expected ionisation-only signal in xenon (relevant to the XENON10 experiment [410]) assuming the modulation signal observed in the XENON100 scintillation experiment [384] is due to WIMP–electron scattering. (*Left*) Value that α_χ must take to explain the XENON100 modulation (midpoint); (*right*) the resulting unmodulated event rate R_0 for XENON10 (single-electron primary ionisations only).

This is an effect which would have between $1 - 10\%$ effect on the calculated rates, acting to increase them. The efficiencies of the detector is essentially unity [411]. Therefore, our calculations represent a lower bound on the expected event rate, and are in this sense as conservative as reasonably possible. Taking the higher-order ionisations into account would only act to strengthen our conclusion that the DAMA modulation is incompatible and XENON10 limits.

We can also perform calculations to investigate weather the XENON100 scintilation and XENON10 ionisation experiments can be mutually consistent with the electron-interacting WIMP assumption. Figure 7.25 shows calculations of the "ionisation-only" event rate for xenon (integrated over all energy depositions), assuming the modulation observed in the XENON100 experiment (7.25) is due to electron-interacting WIMPs. This shows that for relatively large values of m_χ and m_v the XENON100 modulation may be compatible with the XENON10 limits.

7.5.4 CoGeNT analysis

Another direct-detection experiment, CoGeNT, employs a *p*-type point-contact germanium detector to search for WIMPs, in particular for low mass ($m_\chi \lesssim 10$ GeV) [402, 412, 413]. The CoGeNT Collaboration also sees modest evidence of an annual modulation in the event rate (at the $2.2\,\sigma$ level), with a phase that agrees with the standard halo assumption [402]. The modulation is seen in the "bulk" events (see Ref. [402]) in the $0.5 - 2$ keV interval; an annual modulation in the $2 - 4$ keV interval is consistent with zero. From their data, we extract a modulation amplitude of

$$R_m^{\rm CoGeNT} = 0.34\,{\rm cpd/kg/keV} \tag{7.28}$$

in the $0.5 - 2$ keV interval [402, 412]. The CoGeNT rate in the higher energy energy bins is consistent with zero annual modulation.

The CoGeNT modulation has been previously analysed in terms of nuclear recoils [414] (see also Refs. [415, 416]). It has also been noted that the CoGeNT modulation may be consistent with electron recoils [366]. Here, we present a more detailed analysis of the CoGeNT modulation in terms of electron recoils.

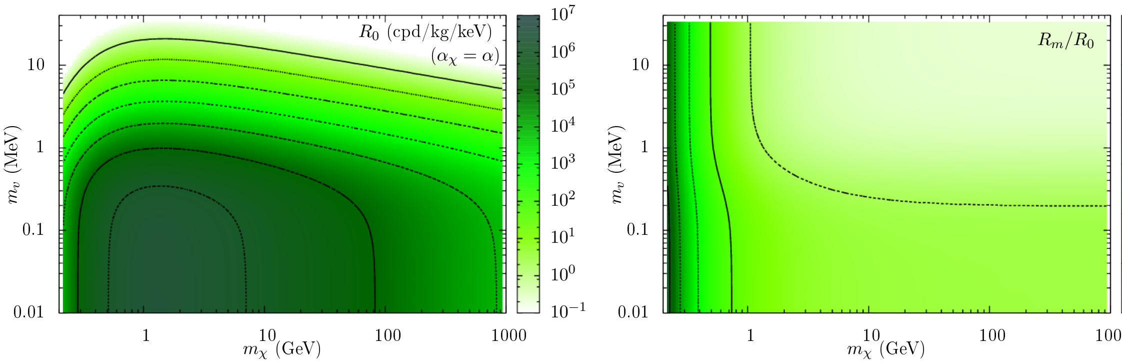

Figure 7.26 Unmodulated event-rate R_0 (*left*) and the modulation fraction R_m/R_0 (*right*) for germanium in the 0.5 – 2 keV interval assuming $\alpha_\chi = \alpha$ in units of cpd/kg/keV.

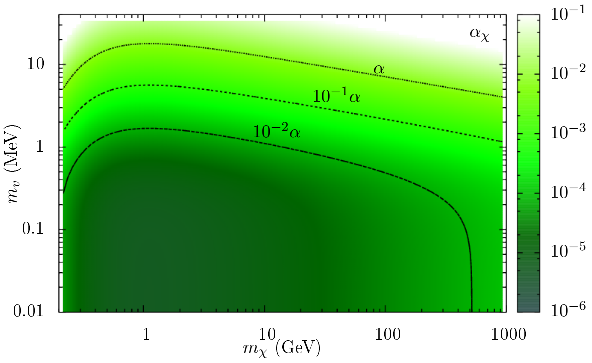

Figure 7.27 The value that α_χ must take in order to reproduce the CoGeNT modulation signal of $\sim$ 0.34 cpd/kg/keV in the 0.5 – 2 keV interval.

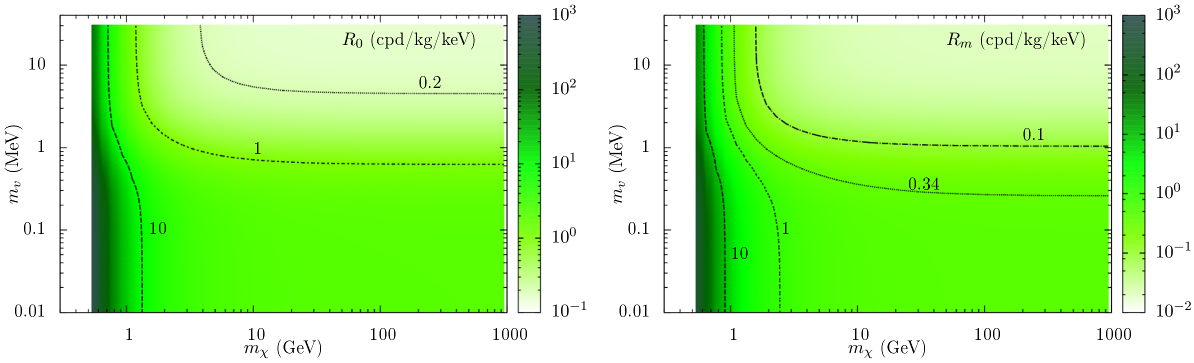

Figure 7.28 Calculation of the expected CoGeNT signal (germanium) in the 0.5 – 2 keV interval assuming the DAMA modulation signal (in the 2 – 6 keV interval) is a positive WIMP detection. The value of α_χ for each point on the parameter plot is shown in Fig. 7.16.

Figure 7.26 presents the event rate that would be generated (from atomic ionisation due to electron-interacting WIMPs) in a germanium detector averaged over the 0.5 – 2 keV energy interval for a fixed coupling constant ($\alpha_\chi = \alpha$). The dominant contributions at these energy scales come from the 3s and 2s shells (see Table 7.1). In Fig. 7.27 we present the values that α_χ must take for each value of DM mass m_χ and mediator mass m_v in order to reproduce the observed modulation (7.28). Note that for fairly light DM particles ($m_\chi \sim 1 - 10$ GeV) and reasonable values for the mediator mass ($m_v \sim 0.1 - 1$ MeV), the signal can be reproduced with values for the couling as small as $\alpha_\chi \sim 5 \times 10^{-4}\alpha$; this can be considered as reasonably consistent.

Figure 7.28 shows the signal expected to be generated in the germanium detector of the CoGeNT experiment in the 0.5 – 2 keV interval, assuming the the DAMA modulation signal of ∼ 0.01 cpd/kg/keVin the 2 – 6 keV interval is due to WIMP–electron scattering. Since the CoGeNT experiment is sensitive to lower energy depositions than the DAMA experiment, the expected signal is very large, but more or less consistent with the amplitude of the DAMA modulation (though note that for these parameters, the spectral shape of the DAMA modulation is not reproduced well). Also immediately noticeable is the large relative proportion of the oscillating signal, which is well above 20% for large portions of the parameter space.

In Fig. 7.29 we plot the energy dependence of the modulation amplitude for several specific choices of DM parameters that roughly agree both with the DAMA and CoGeNT modulations. Also shown is the data point for the CoGeNT modulation in the 0.5 – 2 keV window. Is is seen that the electron-recoil spectrum agrees fairly well with the CoGeNT data, and that the calculations are consistent with the observation of a modulation below 2 keV, but not above. We do note, however, that the data from the CoGeNT experiment is insufficient to draw any significant conclusions, and that this analysis does not rule out other potential sources for the CoGeNT modulation.

Figure 7.30 shows the signal that would be generated in xenon for the 2 – 5.8 keV energy range assuming the CoGeNT modulation was due to electron-interacting WIMPs. The generated signal is very small, and easily consistent with the XENON100 limits [384].

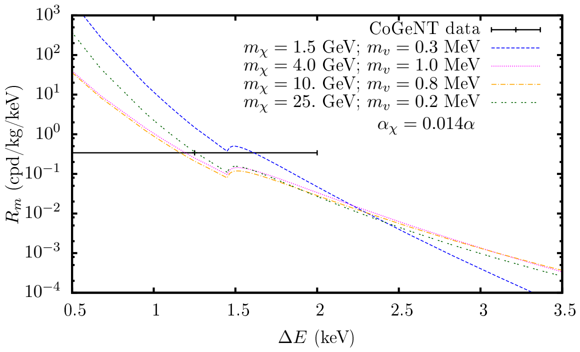

Figure 7.29 Calculation of the modulated event rate spectrum R_m for germanium (relevant to the CoGeNT experiment) for a few specific choices of DM parameters which are able to replicate the amplitude of the observed DAMA modulation.

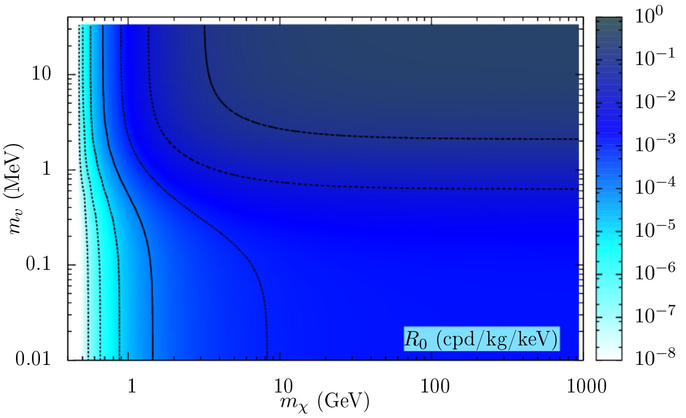

Figure 7.30 The umodulated event rate that would be expected in the XENON100 scintillation experiment for the 2 – 5.8 keV interval assuming the CoGeNT modulation signal (in the 0.5 – 2 keV interval) is a positive WIMP detection (the value of α_χ for each point on the parameter plot is shown in Fig. 7.27).

7.6 Conclusion

The DAMA Collaboration [356] observes a significant modulation in the event rate in the 2–6 keV interval with an amplitude of

$$R_m^{\rm DAMA} = 1.12(12) \times 10^{-2}\,{\rm cpd/kg/keV}. \tag{7.29}$$

One of the leading hypotheses for the source of this modulation is that it is due to atomic ionisation due to scattering of WIMP dark matter of atomic electrons [369]. In this chapter, I performed high-accuracy calculations of the expected event rates for the NaI detector of DAMA, as well as the germanium detector for the CoGeNT Collaboration [402, 412, 413], and the liquid xenon detectors used by the XENON10 [410] and XENON100 [362, 383, 384, 391, 405, 406] Collaborations.

The favoured region from the comparison of DAMA with the XENON100 experiment is for low DM masses, $m_\chi \lesssim 10\,$GeV and low mediator masses $m_v \lesssim$ 1 MeV. We note that in lieu of a more thorough investigation of the detector efficiency, acceptance, and resolution by the DAMA Collaboration, we employed a simple Gaussian resolution profile (based on resolution measurements of the DAMA Collaboration [401]). This amounts to a very generous assumption for the DAMA modulation, while we take very conservative assumptions for the XENON100 rate.

Still, large portions of the parameter space can be excluded based on the XENON100 constraints [383]. For the region above $m_\chi \gtrsim 10\,$GeV and $m_v \gtrsim 2\,$MeV (corresponding to the $5\times10^{-2}\,$cpd/kg/keV contour of Fig. 7.20 (left), the exclusion is 7.5σ, taking into account both the DAMA and XENON100 uncertainties. For the region above $m_\chi \gtrsim 1\,$GeV and $m_v \gtrsim 0.3\,$MeV (corresponding to the $2 \times 10^{-2}\,$cpd/kg/keV contour of Fig. 7.20 (left), the exclusion is 5.2σ. The region below $m_v \lesssim 0.2$ MeV is ruled out based on stellar bounds [404], and the region above $m_v \gtrsim 2$ MeV is ruled out based on the size of the coupling strength.

The XENON10 Collaboration [410] observes at most 30 cpd/kg; at the 90% confidence level, the authors of Ref. [411] put a bound on the single-electron ionisation rate at 23.4 cpd/kg. The two-electron rate is substantially smaller at < 4.23 cpd/kg. This allows us to place very tight constraints on the DM parameter space. For the region below $m_\chi \lesssim 25\,$GeV and $m_v \lesssim 10\,$MeV (corresponding to the $45\,$cpd/kg contour of Fig. 7.24, the exclusion is 3.1σ. For the region below $m_\chi \lesssim 2\,$GeV and $m_v \lesssim 1.5\,$MeV (corresponding to the $10^2\,$cpd/kg contour of Fig. 7.24, the exclusion is 6.5σ. For all the regions below $m_\chi \lesssim 0.2\,$GeV and $m_v \lesssim 0.1\,$MeV (corresponding to the $10^4\,$cpd/kg contour of Fig. 7.24, the exclusion is 9.3σ.

Note that these limits are conservative. We ignored the (very poor) fit the DAMA data in the best-case scenario, and calculated only lower bounds on the expected rates in both XENON10 and XENON100 experiments. Taking the DAMA spectrum into account, and including the higher-order processes in the xenon experiments would lead to significantly more stringent limits. Also, all of my calculations are relative impervious to errors, since they are based on ratios of calculations performed using the same code. Any DM parameters outside those considered directly in our analysis either cannot account for the DAMA modulation (as demonstrated in Fig. 7.16) or have been previously ruled out from stellar bounds [404].

Importantly, we note that the XENON10 and XENON100 constraints are complementary, in that they each “favour” opposite ends of the parameter space (with XENON100 favouring low m_χ and low m_v, and XENON10 favouring large m_χ and m_v). Therefore, by combining the two sets of constraints, we can exclude the entire parameter space for electron-interacting WIMPs as the source of the DAMA annual modulation. All regions of the parameter space are excluded by at least 5.2σ, with most of the parameter space excluded by at least 7σ. The part of the parameter space that is favoured by the “DAMA-only” analysis (that is, requires the smallest coupling constants, see Fig. 7.16) corresponds to very low values of m_χ and m_v, and is excluded by more than 9σ.

CHAPTER 8:
Concluding Remarks

8.1 Conclusions and summary

This thesis explored the possibility of using of high precision atomic and molecular physics to study fundamental interactions at low energy and to search for dark matter. Several approaches were considered, which reflects the broad range of physics that can be probed in this way. This avenue is complementary to the physics tests which are performed at very high energy (e.g. at CERN).

I presented new calculations of parity-violating effects in atoms. By considering several approaches, including exploiting the very high accuracy that is possible in simple systems, the very large effects that can be found in more complex systems, and studying processes that are sensitive to hadronic parity violation, I show that several new systems may be particularly stong candidates for future experimental work.

I then considered the interaction of atomic systems with various background "cosmic" fields. Candidates for such fields include dark matter (e.g. axions) and physics described by extensions to the standard model. By combining my calculations with existing experimental results, new limits on several parameters of physics beyond the standard model were set. Subsequently, I considered the specific case of axion dark matter in greater detail. By calculating several new effects that an axion field would induce in atoms, I show that axion searches based on these new effects can be complimentary to the existing searches. Crucially, the effects I consider are linear in the (extremely small) parameter that quantifies the axion interaction strength; most current search techniques are based on effects that are at least quadratic in this parameter.

Finally, I also considered the interaction of WIMPs (weakly interacting massive particles) with electrons, more specifically the WIMP-induced ionisation of atoms and molecules. By demonstrating that relativistic effects actually give the dominant contribution to such a process, I showed that non-relativistic calculations may underestimate the cross section by many orders of magnitude. This is a particularly significant finding, since all previous calculations relating to this problem were done using non-relativistic wavefunctions. Then, by employing accurate relativistic methods to calculate model-independent cross sections and event rates, I investigated implications this has for the interpretation of the annual modulation signals from the DAMA, XENON, and CoGeNT direct-detection experiments. By calculating the event rate that would be expected in the XENON100 and XENON10 experiments assuming the DAMA modulation was due to electron-interacting WIMPs, and comparing this to the limits set by those experiments, I rule out electron-interacting WIMPs as the source of the DAMA modulation by more than 5σ for all relevant parameter space.

8.2 Future work

- There is currently extensive experimental work under way with the aim of measuring nuclear spin independent (and nuclear spin dependent) parity nonconservation amplitudes in Ba^+, Ra^+, and Fr, see Sec. 2.4. It is imperitive that the accuracy of the theoretical calculations is at the same level as that of the experiment in order to obtain useful information about the see electroweak parameters. However, currently, there is less than perfect agreement between the calculations of several groups, see Sec. 3.2. The double core polarisation effect considered in Sec. 4 may account for some of the discrepancy, however, a full *ab initio* analysis with improved atomic structure techniques is required. One way to do this would be to extend the correlation potential method (see Sec. A.4.2) to include the so-called ladder diagrams [190].

- Recently, the group from Heraklion, Greece, has developed an optical cavity that can enhance parity violating (optical rotation) signals by around four orders of magnitude [106]. If combined with the further parity violation enhancement found in diatomic molecules, this signal enhancement can be significantly increased. Accurate measurements of parity violation in molecules is a very exciting prospect that may lead to important discoveries, including in searching for physics beyond the standard model, and in the study of parity violation in the hadron sector. So far, however, a successful measurement of parity violation in molecules has not been achieved. Theoretical considerations and calculations are crucial for success in this field. Accurate calculations are required in order to interpret the measurements in terms of fundamental physics parameters. This is needed to be able to place constraints on physics beyond the standard model, and to interpret the results in terms of nuclear theory. Also of equally high importance is the requirement to identify suitable systems for study. Future work is to perform calculations of parity violation (optical rotation) for molecules suitable for the "optical cavity enhanced"-type measurements discussed above.

- In Ch. 6, I presented calculations for the atomic electric dipole moments induced via the interaction of axions with electrons. I presented an order of magnetide estimate for the size of the effect in Xe, which is enhanced by the presence of near-degenerate opposite-parity states. What still needs to be done is a proper analysis of the experimental techniques that can be used to measure such a moment, to determine the efficacy of using such an effect to probe axion dark matter. Also, I discussed the electric dipole moments that are produced via the axion-induced nuclear magnetic quadrupole moments in diatomic molecules. The results in this case seem promising, however, a full analysis of the experimental feasibility is still required.

- Also in Ch. 6, I discuss the possibility of using paramagnetic solid state systems to search for axion-induced oscillating magnetic quadrupole moments. Such an experiment would complement the CASPEr proposal, and may have the potential to probe much larger axion masses. A more complete analysis is required to determine whether the advantages outweigh the disadvantages in terms of sensitivity, and to determine if the spin-coherence times can be long enough to make meaningful measurements at the higher frequencies (i.e. larger masses).

- In Ch. 7, I demonstrated that relativistic effects gave the dominant contribution to the ionisation of atoms by slow, heavy particles. In this chapter, I was concerned primarily with WIMPs and dark matter direct detection experiments. However, the general results I derived, as well as the code that was written, are also applicable to the study of ionisation of molecules by scattering of ions. Such a process is currently used as a cancer treatment. It may be possible to apply the methods and codes developed here to this problem, potentially increasing the efficiency of the treatment by identifying the optimal conditions.

APPENDIX A: Methods for Atomic Calculations

A.1 Overview

Though I use atomic units ($\hbar = |e| = m_e = 1$; $c = 1/\alpha \approx 137$) throughout this section, the factors e and m_e are left in the equations for the sake of clarity.

A.2 Dirac equation and relativistic orbitals

This section gives a brief overview of the Dirac theory and its application to atomic systems. It is provided in the interest of completeness, and to give context to the proceeding sections. The reader with a knowledge of elementary atomic theory will likely want to skip this section; and can do so without interrupting the continuity of the chapter.

For accurate calculations, a correct treatment of spin and relativistic effects must be included. This is particularly important for applications like the calculations of PNC effects, which are proportional to the wavefunction density on the nucleus, where the typical electron speed is on the order of $Z\alpha$, and for calculations of EDMs, which are zero in the non-relativistic limit. The Dirac equation for an electron in the presence of the vector potential A_μ is $(i\alpha\gamma^\mu D_\mu - m_e)\psi = 0$, where $D_\mu = \partial_\mu + ieA_\mu$ is the covariant derivative operator.

For an N-electron atom of nuclear charge Z, and including only the electrostatic part of the potential (magnetic corrections are discussed later), the Dirac equation can be expressed in the form $\hat{H}|A\rangle = \mathcal{E}_A|A\rangle$ for an atomic state A with corresponding eigenvalue (energy) $\mathcal{E}_A$, where

$$\hat{H} = \sum_{i=1}^{N}\left[c\boldsymbol{\alpha}_i \cdot \boldsymbol{p}_i + m_e c^2(\gamma^0_i - 1) - V^{\rm nuc}(\boldsymbol{r}_i) + \sum_{j=i+1}^{N}\frac{e^2}{r_{ij}}\right], \tag{A.1}$$

is the relativistic Dirac-Coulomb Hamiltonian (the inclusion of magnetic effects is discussed below). Here, $\boldsymbol{\alpha}(=\gamma^0\boldsymbol{\gamma})$ and γ^0 are Dirac matrices, $\boldsymbol{p}_i$ is the relativistic (three-)momentum of the ith electron, $r_{ij} \equiv |\boldsymbol{r}_i - \boldsymbol{r}_j|$, and for large distances the nuclear potential is given by $V^{\rm nuc} \simeq Z/r$. Note that, for convenience, we have subtracted the electron rest-energy from the eigenvalues of the above Hamiltonian. The total relativistic energy is given by $W_{n\kappa} = \mathcal{E}_{n\kappa} + m_e c^2$.

For single-electron (hydrogen-like) atoms, the solutions to the Dirac equation with this Hamiltonian represent the wavefunctions of the system. For atoms with $N > 1$, however, the Dirac equation with the Hamiltonian (A.1) cannot be exactly solved. It is the $\sum_{i,j} 1/r_{ij}$ term—that corresponds to the Coulomb interaction between each pair of electrons—that causes the problem. Therefore, in order to obtain approximate wavefunctions, this term must be approximated. This may be done by considering the single-particle "mean-field" Hamiltonian

$$\hat{h}^{\rm MF} = c\boldsymbol{\alpha}\cdot\boldsymbol{p} + m_e c^2(\gamma^0 - 1) - V^{\rm nuc} + U^{\rm MF}, \tag{A.2}$$

where each individual electron is assumed to move in the average potential ($U^{\rm MF}$) that is created by all the other electrons. The total Hamiltonian is then given by $\hat{H}^{\rm MF} = \sum_i \hat{h}^{\rm MF}_i$. Clearly, how this potential is calculated will determine the accuracy of this model; this will be the focus of the coming sections.

We will consider the single-electron solutions to the (mean-field) Dirac equation; i.e. $\hat{h}^{\rm MF}\phi_a(r_1) = \varepsilon_a\phi_a(r_1)$. These solutions are known as single-particle *orbitals* (sometimes also referred to as single-particle wavefunctions). We use the notation Ψ_A and $\mathcal{E}_A$ to represent the ("exact") atomic wavefunction and eigenvalue (energy) corresponding to an atom in the state A, respectively. Similarly, we employ ϕ_a and ε_a to represent the single-particle orbital and eigenvalue (also referred to as the single-particle energy, or sometimes the quasi-energy) corresponding to orbital a.

The atomic wavefunctions are then linear combinations of one or more Slater determinants made of these single-particle orbitals. For example, an N electron atom in the state A with energy $\mathcal{E}_A$ is described by the wavefunction

$$\Psi_A(\boldsymbol{r}_1,\boldsymbol{r}_2,...\boldsymbol{r}_N) = \sum_{i_1}\sum_{i_2}...\sum_{i_N} c_{i_1,i_2,...,i_N}\Phi_{i_1,i_2,...,i_N}(\boldsymbol{r}_1,\boldsymbol{r}_2,...,\boldsymbol{r}_N), \tag{A.3}$$

where the Slater-determinant is

$$\Phi_{i_1,i_2,...,i_N}(\boldsymbol{r}_1,\boldsymbol{r}_2,...,\boldsymbol{r}_N) = \frac{1}{\sqrt{N!}}\begin{vmatrix} \phi_{i_1}(\boldsymbol{r}_1) & \phi_{i_2}(\boldsymbol{r}_1) & \dots & \phi_{i_N}(\boldsymbol{r}_1) \\ \phi_{i_1}(\boldsymbol{r}_2) & \phi_{i_2}(\boldsymbol{r}_2) & \dots & \phi_{i_N}(\boldsymbol{r}_2) \\ \vdots & \vdots & \ddots & \vdots \\ \phi_{i_1}(\boldsymbol{r}_N) & \phi_{i_2}(\boldsymbol{r}_N) & \dots & \phi_{i_N}(\boldsymbol{r}_N) \end{vmatrix}. \tag{A.4}$$

Here, $\boldsymbol{r}$ denote the $3N$ spatial coordinates, and the indices i denote the basis states (i.e. all quantum numbers). The coefficients c are subject to the normalisation condition in the usual way. Note that if any two of the i indices in (A.4) are the same, the Slater determinant is zero, e.g., $\Phi_{i_1,i_a,...,i_a,...,i_N} = 0$ (ensuring the famous Pauli exclusion principle), and that an interchange of any two indices results in a change of sign, e.g., $\Phi_{i_1,i_a,...,i_b,...,i_N} = -\Phi_{i_1,i_b,...,i_a,...,i_N}$ (ensuring the anti-symmetry). In practical calculations, of course the wavefunction Eq. (A.3) cannot be used. Instead, approximate wavefunctions, which we denote ψ, are formed from one or more Slater-determinants. How this is done specifically depends on the approximation methods, which will be discussed below.

A.2.1 Single-particle orbitals

Employing the Dirac basis,

$$\gamma^0 = \gamma_0 = \begin{pmatrix} 1 & 0 \\ 0 & -1 \end{pmatrix}, \quad \gamma^i = -\gamma_i = \begin{pmatrix} 0 & \sigma_i \\ -\sigma_i & 0 \end{pmatrix}, \quad \gamma^5 = -\gamma_5 = \begin{pmatrix} 0 & 1 \\ 1 & 0 \end{pmatrix}, \tag{A.5}$$

the four-component eigenfunctions of the Hamiltonian (A.1), which correspond to the single-electron orbitals, can be expressed as

$$\phi_{n\kappa m}(\boldsymbol{r}) = \frac{1}{r}\begin{pmatrix} f_{n\kappa}(r)\Omega_{\kappa m}(\boldsymbol{n}) \\ i\alpha g_{n\kappa}(r)\Omega_{-\kappa,m}(\boldsymbol{n}) \end{pmatrix}, \tag{A.6}$$

where $f_{n\kappa}$ and $g_{n\kappa}$ are the large and small radial components of the Dirac wavefunction, respectively, and

$$\Omega_{\kappa m}(\boldsymbol{n}) = \begin{pmatrix} (-1)^{j-l-1/2}\sqrt{\frac{\kappa+1/2-m}{2\kappa+1}}Y_{l,m-1/2}(\theta,\phi) \\ \sqrt{\frac{\kappa+1/2+m}{2\kappa+1}}Y_{l,m+1/2}(\theta,\phi) \end{pmatrix} \tag{A.7}$$

are the two-component spherical spinors[1]. Here, $\kappa = (l - j)(2j + 1)$ is the Dirac quantum number that specifies the values of both the orbital (l) and total ($j = l \pm s$) angular momentum, $m = j_z$ is the projection of the total angular momentum $\boldsymbol{j} = \boldsymbol{l} + \boldsymbol{s}$ on the (z-)axis of quantisation, $l = |\kappa + 1/2| - 1/2$ is the value of the orbital angular momentum, $\boldsymbol{n} = \boldsymbol{r}/r$, and Y_{lm} are the spherical harmonics. The small number α is "pulled out" of the function g to increase numerical stability, and to make the relativistic scaling explicit.

The radial functions f and g satisfy the pair of first-order coupled differential equations,

$$\left(\frac{\mathrm{d}}{\mathrm{d}r} - \frac{\kappa}{r}\right) g_{n\kappa}(r) = \left(V(r) - \varepsilon_{n\kappa}\right) f_{n\kappa}(r), \tag{A.8}$$

$$\left(\frac{\mathrm{d}}{\mathrm{d}r} + \frac{\kappa}{r}\right) f_{n\kappa}(r) = \alpha^2 \left(\varepsilon_{n\kappa} + 2/\alpha^2 - V(r)\right) g_{n\kappa}(r). \tag{A.9}$$

This separation also ensures the pleasing normalisation conditions:

$$\int_0^\infty \mathrm{d}r \, \left(f_{n'\kappa} f_{n\kappa} + \alpha^2 g_{n'\kappa} g_{n\kappa}\right) = \delta_{n'n}, \tag{A.10}$$

$$\int_0^\pi \sin(\theta)\,\mathrm{d}\theta \int_0^{2\pi} \mathrm{d}\phi \; \Omega^\dagger_{\kappa' m'}(\boldsymbol{n}) \Omega_{\kappa m}(\boldsymbol{n}) = \delta_{\kappa'\kappa}\delta_{m'm}. \tag{A.11}$$

The Dirac basis is a convenient choice of basis (and therefore separation of radial functions) for atomic physics because the "large component" f gives the main contribution to most atomic effects, and the "small component" g gives the relativistic corrections. In fact, in the non-relativistic limit, $f(r)/r \overset{NR}{\to} R(r)$, where $R(r)$ is the radial solution to the central-field non-relativistic Schrödinger equation. Both the bound-state and continuum-state wavefunctions take the same form, except that the continuum functions do not depend on the principal quantum number n, and are instead numerated by their energy. For an orbital with energy ε, we denote the orbital, and the large and small Dirac components as $\phi_{\varepsilon\kappa m}$, $f_{\varepsilon\kappa}$, and $g_{\varepsilon\kappa}$, respectively.

Note that $\boldsymbol{j} (= \boldsymbol{l} + \boldsymbol{s})$ commutes with the Hamiltonian (clear from the rotational symmetry); we can therefore construct eigenstates of j^2 and j_z, which are the spherical spinors. Note, however, that neither $\boldsymbol{l}$ nor $\boldsymbol{s}$ individually commute with the Hamiltonian. In fact, as can be seen from Eq. (A.6), the upper and lower components of the wavefunction have values of orbital angular momentum that differ by one unit. However, since the lower component is significantly smaller-valued than the upper component (roughly by the ratio $v/c = v\alpha$), when relativistic effects can be considered small, the quantum number l can be considered conserved (i.e. a good quantum number) to a reasonable approximation.

A.3 Hartree-Fock method

We now discuss exactly how the mean-field potential introduced above is calculated. There are many ways to form such a potential, but the best method is to use what is known as a *self-consistent field* method. By a "self-consistent"

---

[1] For ease of comparison, I note that this choice is slightly different to that employed in some places in the literature; for example, the relation between this choice and that of Johnson *et al.*, is $f(r) = P(r)$, and $g(r) = -Q(r)/\alpha$; see Ref. [417].

method, we mean one in which the electrostatic potential derived from the electron density (i.e. from the known electron orbitals) is the same as the electrostatic potential that appears in the Dirac equation. The *best* such method is the Hartree-Fock method, which includes both the direct and exchange parts of the electron–electron repulsion.

In the calculations, we use the Relativistic Hartree-Fock (HF) method, in which Eq. (A.1) is replaced by the single-electron HF Hamiltonian:

$$\hat{h}^{\rm HF} = c\boldsymbol{\alpha}\cdot\boldsymbol{p} + m_e c^2(\gamma^0 - 1) - V^{\rm nuc} + U^{\rm HF}. \tag{A.12}$$

We use a Fermi-type distribution for the nuclear potential,

$$\rho(r) = \frac{\rho_0}{1 + {\rm e}^{(r-c)/a}}, \tag{A.13}$$

where $t = a(4\ln 3)$ is the "skin-thickness" and c is the "half-density radius", see, e.g., Ref. [418], and ρ_0 is found from the normalisation condition $\int\rho(r)\,{\rm d}^3r = 1$. The charge distribution is then given $Ze\rho(r)$. This is important since many of the effects considered in this thesis depend strongly on the form of the wavefunctions at short distances (and, in general, because high accuracy is required). In general, the atomic wavefunctions are then given by linear combinations of Slater determinants of the orbitals $\phi_{n\kappa m}$, which are found for each of the N_c states in the core by solving the Dirac equation

$$\hat{h}^{\rm HF}\phi_{n\kappa} = \varepsilon_{n\kappa}\phi_{n\kappa}, \tag{A.14}$$

as described above. In practice, the wavefunction for the atomic core is assumed in the Hartree-Fock method to be given by a single Slater-determinant; extensions to the Hartree-Fock method are discussed below.

The key to the Hartree-Fock method is the fact that a knowledge of the orbitals of the electrons in the core is the same as a knowledge of the electron (and therefore charge) distribution inside the atom, from which one can easily determine the electric potential from Gauss' law. So, using a basic form of the potential, one can generate a set of core orbitals. Using these orbitals, one can generate a mean field potential that is better than the original potential. In this better potential one can generate a better set of orbitals and so on.

The Hartree-Fock potential is given by the sum of the direct and exchange parts of the electron–electron Coulomb interaction, $U^{\rm HF} = U^{\rm dir} + U^{\rm exch}$, with

$$\begin{aligned} U^{\rm dir}\phi_a(\boldsymbol{r}) &= e^2\sum_{i\neq a}^{N_c}\int\frac{\phi_i^\dagger(\boldsymbol{r}')\phi_i(\boldsymbol{r}')}{|\boldsymbol{r}-\boldsymbol{r}'|}\,{\rm d}^3r'\phi_a(\boldsymbol{r}) \\ U^{\rm exch}\phi_a(\boldsymbol{r}) &= -e^2\sum_{i\neq a}^{N_c}\int\frac{\phi_i^\dagger(\boldsymbol{r}')\phi_a(\boldsymbol{r}')}{|\boldsymbol{r}-\boldsymbol{r}'|}\,{\rm d}^3r'\phi_i(\boldsymbol{r}), \end{aligned} \tag{A.15}$$

where the summation runs over all N_c atomic core orbitals. Diagrams representing the direct and exchange integrals correponding to these equations are shown in Fig. A.1. The equations (A.14) and (A.15) are solved iteratively until an acceptable level of convergence has been reached. When convergence has been achieved the method is said to be self-consistent. To start the iterative procedure, an initial approximation for the potential is required. For this, we

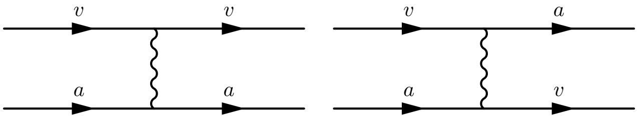

(a) Feynman Diagrams

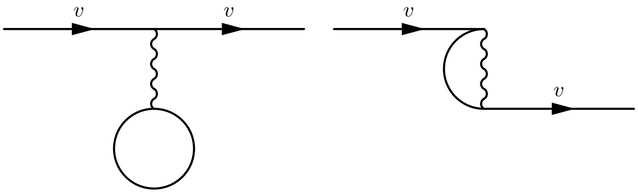

(b) Feynman-Goldstone Diagrams

Figure A.1 Feynman diagrams (and corresponding Feynman-Goldstone diagrams) for the direct and exchange interactions for electron v; the index a denotes the core electrons (over which a summation is assumed). The wavy line denotes the Coulomb interaction.

use a simple parametric potential. We note, however, that this should still be considered an entirely *ab initio* process, since one can use a Thomas-Fermi potential. The use of a parametric potential only acts to increase the speed of convergence; the self-consistent nature of the procedure ensures the starting approximation has no bearing on the final result (so long as convergence is reached).

For closed-shell atoms all the electrons are treated as core electrons, $N_c = N$. This procedure can calculate the ground state energy and wavefunction for closed-shell atoms to a very high accuracy. For atoms with M valence electrons, it is more convenient to separate the atomic electrons into two groups; the closed-shell "core", and the valence electrons, $N = N_c + M$. In this case, the Hartree-Fock equations are solved for the core electrons, and then the Hartree-Fock potential is kept constant and the orbitals for the valence electrons are found in this "frozen core" potential.

For single-valence atoms, this procedure leads to an accuracy on the order of 10%. To do better than this, one needs to consider perturbative corrections corresponding to valence–core interactions:

$$\delta V = \sum_{i<j} \frac{e^2}{r_{ij}} - U^{\rm HF}. \tag{A.16}$$

The interaction δV is known as the *residual Coulomb interaction*. The corrections to the wavefunctions and energies are known as the correlation corrections, and are discussed in Sec. A.4.

For atoms with more than one valence electron, a single Slater-determinant can be formed from the Hartree-Fock orbitals, however this typically does not lead to an acceptable accuracy, especially for the more highly excited states. For better accuracy, a linear combination of determinants is required. Note that the Hartree-Fock model itself cannot predict the value of the expansion coefficients, c in Eq. (A.3). A common method used in this case to determine the valence wavefunctions (and the method used in this thesis) is the *configuration interaction* method, discussed in Sec. A.7.

A.4 Correlation corrections

Correlation corrections are the deviation from the pure single-particle picture. They correspond to the electron–electron interactions of the valence electrons with the electrons in the core.[2] In this section, we restrict the discussion to atoms and ions with just one valence electron. A treatment of correlations in atoms with more than one valence electron is discussed in Sec. A.7.

In this section, we use the notation where the indices labelled by letters from the end of the alphabet (e.g. v and w) denote occupied valence states, letters from the start of the alphabet (a, b, c) denote denote occupied states in the core, and those from the middle of the alphabet (l, m, n) denote virtual states that are either unoccupied valence states (states above the core) or states in the core. Greek indices (α, β, γ) denote unoccupied core states (holes).

As mentioned above, the next step to improve the wavefunctions and energies after the Hartree-Fock procedure is to add perturbatively back the excluded electron–electron repulsion term, as in Eq. (A.16). As mentioned above, for single-valence systems, we employ a so-called V^{N-1} potential, in which the Hartree-Fock equations are solved for the $N-1$ electrons of the core. The wavefunction for the valence electron is then solved in this frozen core potential. In this case, the correlation corrections are greatly simplified. To the first order in perturbation theory, the correlation corrections to the (single-particle)[3] energy and wavefunction are given

$$\delta E_v^{(1)} = \sum_a \langle\psi_v|\frac{1}{r_{va}}|\psi_v\rangle - \langle\psi_v|U^{\rm HF}|\psi_v\rangle = 0, \tag{A.17}$$

$$|\delta\psi_v^{(1)}\rangle = \sum_n |\psi_n\rangle \frac{\sum_a \langle\psi_n|\frac{1}{r_{va}}|\psi_v\rangle}{E_v^{(0)} - E_n^{(0)}} - \sum_n |\psi_n\rangle \frac{\langle\psi_n|U^{\rm HF}|\psi_v\rangle}{E_v^{(0)} - E_n^{(0)}} = 0, \tag{A.18}$$

where the sum over a runs over all states in the core (note that there is an implicit sum over a in $U^{\rm HF}|\psi_v\rangle$), and the sum over n runs over the complete set of core, valence, and exited (virtual) states (including negative energy positron states, and states in the continuum). Notice that the first term, $\langle\psi_v|\frac{1}{r_{va}}|\psi_v\rangle$, is given by the same diagrams in Fig. A.1, and therefore exactly cancels with the $\langle\psi_a|U^{\rm HF}|\psi_a\rangle$ term. Therefore, there are no first-order corrections to the energies. Of course, this is not a coincidence; in fact it is the definition of the Hartee-Fock potential. Physically, this means that there are no corrections to the Hartree-Fock potential that involve only single excitations (in the absence of external fields).

---

[2] In some other places, the term "correlations" is defined as the difference between the experimental and HF energies.

[3] Note that for the single-particle wavefunctions here, $E = \varepsilon$, and $\psi = \phi$

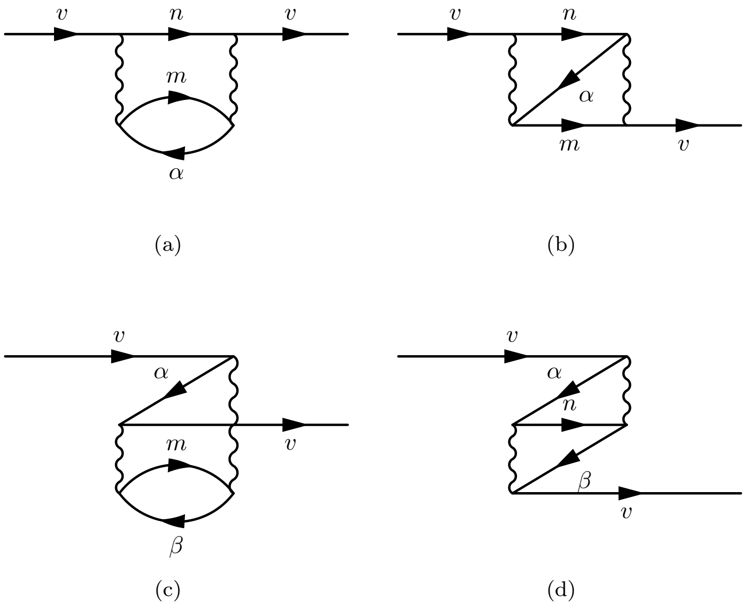

(a) (b)

(c) (d)

Figure A.2 Feynman-Goldstone diagrams for the second-order (in the residual Coulomb interaction) correlation corrections to the single-electron wavefunction ψ_v. The indices m and n denote virtual excited states, and α and β denote unoccupied core states (holes).

A.4.1 Second-order correlations

The lowest-order corrections are those from the second-order perturbation theory. These corrections can be expressed in the form of four Goldstone diagrams, which are presented in Fig. A.2. In Fig. A.3, I present the same diagrams using a different notation.

The corrections to the energies can be computed directly; via a direct summation over states of the diagrams presented in Fig. A.2 (as in Ref. [419]). In this thesis, however, we use a more numerically stable method developed in Ref. [420]; the so-called correlation potential method. In the correlation potential method, a non-local operator, $\hat{\Sigma}$, is added to the single-electron HF Hamiltonian Eq. (A.12). The wavefunctions for the valence electron are then solved in this modified HF potential:

$$\left(\hat{h}^{\mathrm{HF}} + \hat{\Sigma}(\varepsilon_a)\right)\phi_a^{\mathrm{BO}} = \varepsilon_a^{\mathrm{BO}}\phi_a^{\mathrm{BO}}. \tag{A.19}$$

The wavefunction ϕ^{BO} is reffered to as a “Brueckner” orbital. The Brueckner orbitals and their corresponding energies include the correlation effects. (Not that, in general, the correlation potential operator, Σ is energy dependent.) This method also allows one to include higher-order effects, including a summation of a series of diagrams to all orders in perturbation theory.

The correlation potential, related to the correlation potential operator via the formula

$$\hat{\Sigma}\phi_v = \int \Sigma(\boldsymbol{r}_1, \boldsymbol{r}_2, \varepsilon_v)\phi_v(\boldsymbol{r}_1)\,\mathrm{d}^3r_1, \tag{A.20}$$

can be expressed explicitly. For example, the potentials corresponding to the four second-order diagrams in Fig. A.2, are:

$$\Sigma^{A.2(a)}(\boldsymbol{r}_1,\boldsymbol{r}_2,\varepsilon_v) = \\ e^4\sum_{\alpha,n,m}\iint \mathrm{d}^3r_3\,\mathrm{d}^3r_4 \frac{\phi^\dagger_\alpha(\boldsymbol{r}_4)\phi_m(\boldsymbol{r}_4)\phi_n(\boldsymbol{r}_2)\;\phi_\alpha(\boldsymbol{r}_3)\phi^\dagger_m(\boldsymbol{r}_3)\phi^\dagger_n(\boldsymbol{r}_1)}{r_{24}r_{13}(\varepsilon_v-\varepsilon_n-\varepsilon_m+\varepsilon_\alpha)}, \tag{A.21}$$

$$\Sigma^{A.2(b)}(\boldsymbol{r}_1,\boldsymbol{r}_2,\varepsilon_v) = \\ -e^4\sum_{\alpha,n,m}\iint \mathrm{d}^3r_3\,\mathrm{d}^3r_4 \frac{\phi_m(\boldsymbol{r}_2)\phi^\dagger_\alpha(\boldsymbol{r}_3)\phi_n(\boldsymbol{r}_3)\;\phi^\dagger_m(\boldsymbol{r}_4)\phi_\alpha(\boldsymbol{r}_4)\phi^\dagger_n(\boldsymbol{r}_1)}{r_{23}r_{14}(\varepsilon_v-\varepsilon_n+\varepsilon_\alpha-\varepsilon_m)}, \tag{A.22}$$

$$\Sigma^{A.2(c)}(\boldsymbol{r}_1,\boldsymbol{r}_2,\varepsilon_v) = \\ -e^4\sum_{\alpha,n,m}\iint \mathrm{d}^3r_3\,\mathrm{d}^3r_4 \frac{\phi^\dagger_\beta(\boldsymbol{r}_4)\phi_n(\boldsymbol{r}_4)\phi^\dagger_\alpha(\boldsymbol{r}_1)\;\phi_\beta(\boldsymbol{r}_3)\phi^\dagger_n(\boldsymbol{r}_3)\phi_\alpha(\boldsymbol{r}_2)}{r_{23}r_{14}(\varepsilon_v+\varepsilon_\alpha-\varepsilon_n+\varepsilon_\beta)}, \tag{A.23}$$

$$\Sigma^{A.2(d)}(\boldsymbol{r}_1,\boldsymbol{r}_2,\varepsilon_v) = \\ e^4\sum_{\alpha,n,m}\iint \mathrm{d}^3r_3\,\mathrm{d}^3r_4 \frac{\phi^\dagger_\beta(\boldsymbol{r}_4)\phi_n(\boldsymbol{r}_4)\phi^\dagger_\alpha(\boldsymbol{r}_1)\;\phi_\beta(\boldsymbol{r}_2)\phi^\dagger_n(\boldsymbol{r}_3)\phi_\alpha(\boldsymbol{r}_3)}{r_{14}r_{23}(\varepsilon_v+\varepsilon_\alpha-\varepsilon_n+\varepsilon_\beta)}. \tag{A.24}$$

The integrals over r_{ij}^{-1} are performed by expanding over the spherical harmonics and summing over the multipolarities, as usual.

The second-order correlation potential, which we denote as $\Sigma^{(2)}$, is the sum of the four potentials above. In the next section we discuss the inclusion of higher-order effects into the correlation potential, including an all-orders summation of a dominating series of diagrams.

A.4.2 All-order correlation potential in the screened coulomb interaction

The second-order correlation method described above greatly increases the accuracy of the energies and wavefunctions for single-valence systems, however, it overestimates the corrections. Higher-order correlations must be taken into account to improve the accuracy. This task, however, is not so simple; the inclusion of third-order correlations actually worsens the agreement with experiment for single-valence systems such as Cs [421]. Therefore, one requires an all-order technique. For this, we use the correlation potential in the screened Coulomb interaction (CPSCI) method as developed in Refs. [199, 219] (see also Refs. [5, 243–245, 419, 420]). In general, when we refer to the correlation potential method, we mean the all-order CPSCI method as described here. Sometimes it is also necessary to refer to just the second-order version, as described above. When necessary, we distinguish between the two correlation potentials with the notation $\Sigma^{(2)}$ and $\Sigma^{(\infty)}$, respectively.

The CPSCI method allows the inclusion of three sets of dominating diagrams to all-orders of perturbation theory:

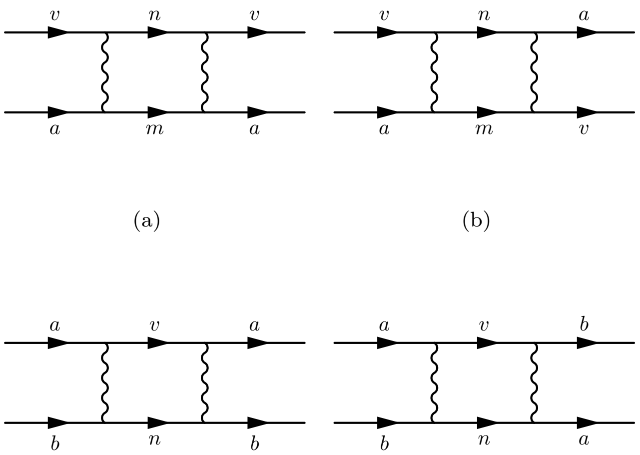

(a) (b)

(c) (d)

Figure A.3 Diagrams corresponding to those presented in Fig. A.2. The indices m and n denote virtual excited states, and a and b denote occupied core states.

(i) the screening of the electron–electron interaction due to the polarisation of the core electrons,

(ii) the electron–hole Coulomb interaction,

(iii) non-linear effects of the correlation potential (chaining of the self-energy).

The largest correction to the second-order correlation potential comes from the screening of the electron–electron Coulomb interaction by the other core electrons [245]. Examples of the screening diagrams are presented in Fig. A.4. The electron–hole interaction also gives an important contribution, which is typically around half the size of the screening correction [219]. An example diagram for the electron–hole interaction correction is presented in Fig. A.5. The screening and electron–hole diagrams are included into the correlation potential. The non-linear corrections are then included via iterations of the correlation potential within the HF equations. All other sets of diagrams are suppressed by a small parameter, and can be safely neglected [219], especially for the s and p states, which are typically of most interest.

Method for calculating the correlation potential In order to form the all-order correlation potential, the Feynman diagram technique is used. The reason for this is that it allows for a more convenient inclusion of higher-order correlations; the drawback is that it requires a numerical integration over frequencies.

In the Feynman technique, the second-order correlation corrections are expressed by the two diagrams presented in Fig. A.6. Then the second-order correlation potential, $\hat{\Sigma}^{(2)} = \hat{\Sigma}^{(2)}_{\rm dir} + \hat{\Sigma}^{(2)}_{\rm exch}$, is expressed via the Hartree-Fock

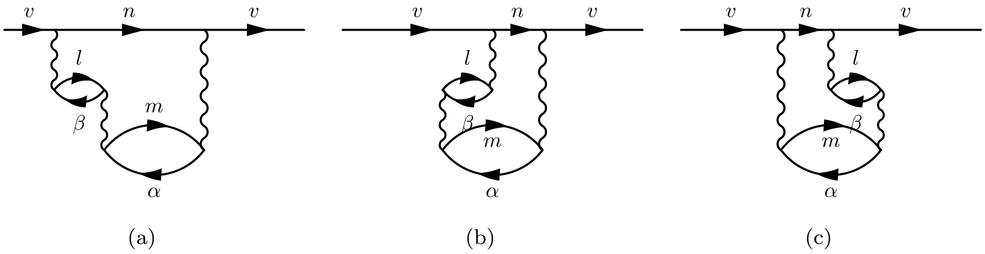

Figure A.4 Feynman-Goldstone diagrams for the lowest-order screening corrections to the second-order correlation diagram presented in Fig. A.2(a). There are also corresponding screening corrections for the other three diagrams in Fig. A.2. The indices l, m, and n denote virtual excited states, α and β denote unoccupied core states (holes), and v is the valence electron for which the corrections are calculated.

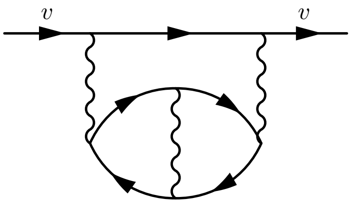

Figure A.5 Feynman-Goldstone diagram for the lowest-order electron–hole corrections to the second-order correlation diagram presented in Fig. A.2(a). There are also corresponding electron–hole interaction corrections for the other diagrams in Fig. A.2.

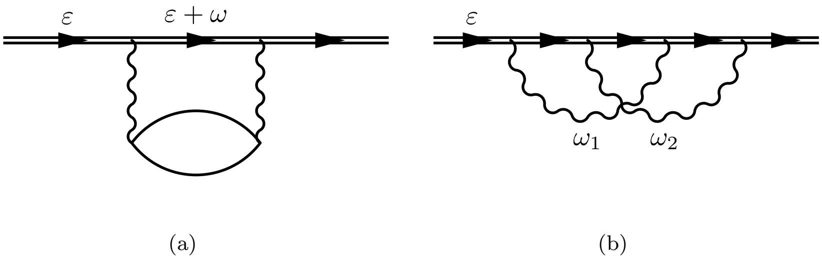

Figure A.6 Second-order direct (a) and exchange (b) correlation corrections in the Feynman diagram technique. The double line represents the Green's function for the external electron. The wavy line is the residual Coulomb interaction, and the loop represents polarisation of the core electrons. After integration over frequencies (ω), diagram (a) transforms to the diagrams A.2(a) and A.2(c), and (b) transforms to the diagrams A.2(b) and A.2(d) from Fig. A.2.

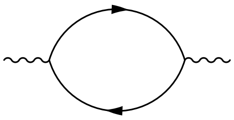

Figure A.7 Polarisation operator for the atomic core.

Feynman Green's function:

$$\hat{\Sigma}^{(2)}_{\rm dir}(\varepsilon, \boldsymbol{r}_1, \boldsymbol{r}_2) = \sum_{ij} \int \frac{{\rm d}\omega}{2\pi}\, G_{12}(\varepsilon+\omega)\, \hat{Q}_{1i}\, \hat{\Pi}_{ij}(\omega)\, \hat{Q}_{j2}, \tag{A.25}$$

$$\hat{\Sigma}^{(2)}_{\rm exch}(\varepsilon, \boldsymbol{r}_1, \boldsymbol{r}_2) = \sum_{ij} \iint \frac{{\rm d}\omega}{2\pi}\frac{{\rm d}\omega'}{2\pi}\, \hat{Q}_{1i}\, G_{1j}(\varepsilon+\omega)\, G_{ji}(\varepsilon+\omega+\omega')\, \hat{Q}_{j2}\, G_{i2}(\varepsilon+\omega'), \tag{A.26}$$

where $Q_{12} = \frac{e^2}{r_{12}}$ is the Coulomb interaction, G is the Green's function, Π is the polarisation operator, and the summation over i and j is the numerical implementation of the integrals over $\boldsymbol{r}_{i,j}$. The Green's function is expressed

$$G_{12}(\varepsilon) = \sum_n \frac{\phi_n(\boldsymbol{r}_1)\phi_n^\dagger(\boldsymbol{r}_2)}{\varepsilon - \varepsilon_n + i\delta} + \sum_a \frac{\phi_a(\boldsymbol{r}_1)\phi_a^\dagger(\boldsymbol{r}_2)}{\varepsilon - \varepsilon_a - i\delta} \qquad ; \qquad \delta \to 0, \tag{A.27}$$

where n is a (virtual) state above the core, and a is an occupied core state. The polarisation operator (Fig. A.7) is expressed

$$\begin{aligned} \hat{\Pi}_{12}(\omega) &= \int \frac{{\rm d}\omega'}{2\pi}\, G_{12}(\omega+\omega')\, G_{12}(\omega') \\ &= \sum_{a=1}^{N-1} \phi_a^\dagger(\boldsymbol{r}_1)\, [G_{12}(\varepsilon_a+\omega) + G_{12}(\varepsilon_a-\omega)]\, \phi_a(\boldsymbol{r}_2). \end{aligned} \tag{A.28}$$

The electron–hole interaction perturbs the polarisation operator. This effect (shown to lowest-order for one particular second-order diagram in Fig. A.5) is essentially due to the deviation of the direct Hartree-Fock potential for the excited core electron from that for the non-excited electron. It is calculated by replacing the $\hat{V}^{N-1}$ HF potential by the $\hat{V}^{N-2}$ potential when calculating $\hat{\Pi}$. Since this calculation involves iterations of the modified HF equations as above, the electron–hole interaction is included to all orders (once the convergence of the HF equations has been realised). This amounts to replacing the polarisation operator by the fully-chained operator, as shown in Fig. A.8.

To include the effect of the screening of the Coulomb interaction to all-orders is slightly more involved. The chain of polarisation diagrams can be obtained from the lowest-order diagram (Fig. A.7) by successive insertions of extra electron–hole loops into the Coulomb lines, as shown in Fig. A.9. Before the integration over frequencies, this series forms a geometrical progression

$$\hat{\Pi} + \hat{\Pi}\hat{Q}\hat{\Pi} + \hat{\Pi}\hat{Q}\hat{\Pi}\hat{Q}\hat{\Pi} + \ldots,$$

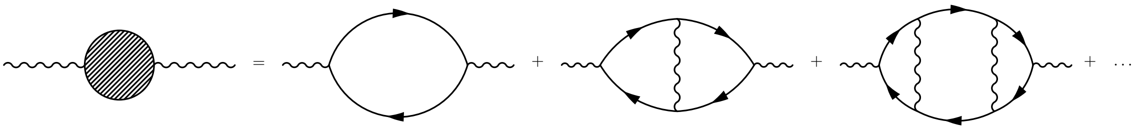

Figure A.8 Diagram for the electron–hole correction to the polarisation operator, chained to all-orders by iterations of the modified HF equations.

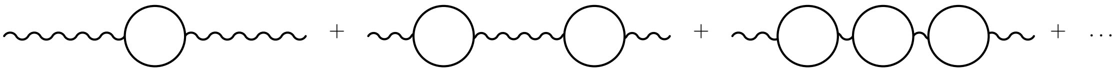

Figure A.9 Chain of all higher-order polarisation diagrams.

which can be summed analytically:

$$\hat{\pi}(\omega) = \hat{\Pi}(\omega)\left[1 - \hat{Q}\hat{\Pi}(\omega)\right]^{-1}. \tag{A.29}$$

Then, the screening of the Coulomb interaction is included to all-orders by making the substitution $\hat{\Pi} \to \hat{\pi}$ in the direct part of the correlation operator Eq. (A.25):

$$\hat{\Sigma}_{\rm dir}(\varepsilon, \boldsymbol{r}_1, \boldsymbol{r}_2) = \sum_{ij}\int\frac{{\rm d}\omega}{2\pi}\, G_{12}(\varepsilon+\omega)\,\hat{Q}_{1i}\,\hat{\pi}_{ij}(\omega)\,\hat{Q}_{j2}. \tag{A.30}$$

It is also possible to express the direct part of the correlation operator via the screened Coulomb operator $\hat{q}(\omega)$:

$$\hat{q}(\omega) = \hat{Q}(\omega)\left[1 - \hat{\Pi}(\omega)\hat{Q}\right]^{-1}, \tag{A.31}$$

which is found in the same way as Eq. (A.29). This equates to a redefinition of the Coulomb line that includes screening to all-orders (and the electron–hole interaction), as shown in Fig. A.10. The direct potential can then be expressed

$$\hat{\Sigma}_{\rm dir}(\varepsilon, \boldsymbol{r}_1, \boldsymbol{r}_2) = \sum_{ij}\int\frac{{\rm d}\omega}{2\pi}\, G_{12}(\varepsilon+\omega)\,\hat{Q}_{1i}\,\hat{\Pi}_{ij}(\omega)\,\hat{q}_{j2} \tag{A.32}$$

(note that only one Coulomb operator has been replaced). With this definition, one can also include screening into the exchange diagrams with the substitution $\hat{Q} \to \hat{q}$ in Eq. (A.26):

$$\hat{\Sigma}_{\rm exch}(\varepsilon, \boldsymbol{r}_1, \boldsymbol{r}_2) = \sum_{ij}\iint\frac{{\rm d}\omega}{2\pi}\frac{{\rm d}\omega'}{2\pi}\,\hat{q}_{1i}\,G_{1j}(\varepsilon+\omega)\,G_{ji}(\varepsilon+\omega+\omega')\,\hat{q}_{j2}\,G_{i2}(\varepsilon+\omega'), \tag{A.33}$$

The total correlation potential operator (self-energy operator) that includes an all-orders summation of the dominating screening and electron–hole interactions is given by the equations (A.32) and (A.33). This is shown diagrammatically in Fig. A.11. In order to compute the correlation potential, a complete set

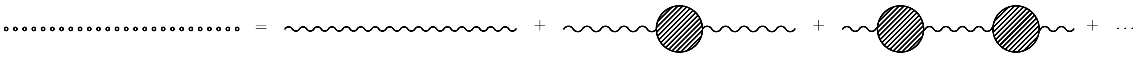

Figure A.10 Screening of the Coulomb interaction to all-orders (including the electron–hole interaction).

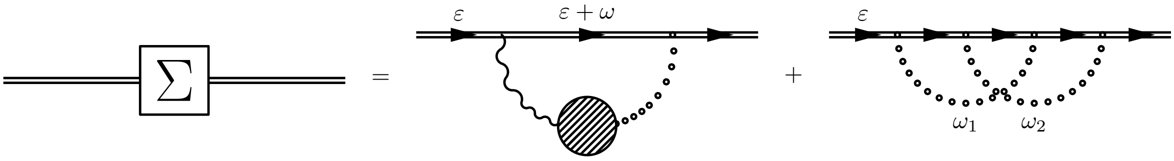

Figure A.11 The correlation potential operator (electron self-energy operator) including screening and the electron–hole interactions to all-orders.

of single-electron orbitals is required. One could construct the "complete" set of single-electron orbitals using the Hartree-Fock orbitals, however, for convenience we instead use the B-spline technique [206]. We find that the basis used to construct to correlation potential can typically be saturated with the use of between 40 and 70 B-splines of order 9 in a cavity of $40\,a_B$.

Then, the accuracy of the calculations is further improved by including the effects which are non-linear in the correlation potential. These effects are included by chaining the correlation potential to all-orders, as in Fig. A.12, which is achieved by adding the correlation potential to the Hartree-Fock potential, and solving the resulting modified Hartree-Fock equations iteratively for the valence states, as in Eq. (A.19). As for the case of the second-order potential, the resulting orbitals are referred to as Brueckner orbitals, which now contain these correlation effects to all-orders.

A.5 Coupled cluster method

An alternative approach to the CPSCI method described above that is very common in the literature is the coupled-cluster method. This method is not used directly in this thesis, however a brief outline is given here for completeness, and for useful comparison. Here, I outline only the simplest version of the coupled-cluster method; the linearised singles-doubles method. For a more detailed review of all-order coupled-cluster methods, see, e.g., Ref. [421].

In the linearised singles-doubles method, the many-electron wave function

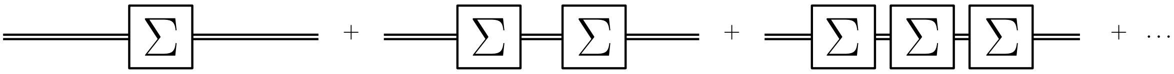

Figure A.12 Chaining of the correlation potential operator (electron self-energy operator) to all-orders.

of an atom is written as an expansion over terms containing single and double excitations of core or valence electrons from the reference Hartree-Fock wave function into basis states above the core, see, e.g., Ref. [422]. Here, we consider for simplicity the case of a single-valence system, for which the wavefunction is expressed as

$$|\psi_v\rangle = \Bigg[1 + \sum_{ma} \rho_{ma} a_m^\dagger a_a + \frac{1}{2}\sum_{mnab} \rho_{mnab} a_m^\dagger a_n^\dagger a_b a_a + \sum_{m\neq v} \rho_{mv} a_m^\dagger a_v + \sum_{mna} \rho_{mnva} a_m^\dagger a_n^\dagger a_a a_v\Bigg] |0_v^{HF}\rangle, \tag{A.34}$$

where $|0_v^{HF}\rangle = a_v^\dagger|0^{HF}\rangle$ is the lowest order wavefunction, with $|0^{HF}\rangle$ the Hartree-Fock wavefunction for the frozen core, and $a^\dagger$ and a are the single-electron creation and annihilation operators, respectively (see, e.g., Ref. [423]). Here, the sums over a and b run over all $N-1$ occupied core electrons, while the sums over m and n run over all unoccupied virtual states outside the core. The factors ρ are the expansion coefficients, and are found by solving the SD equations [422]. First, the SD equations

$$(\varepsilon_a - \varepsilon_m)\rho_{ma} = \sum_{bn} \tilde{g}_{mban}\rho_{nb} + \sum_{bnr} g_{mbnr}\tilde{\rho}_{nrab} - \sum_{bcn} g_{bcan}\tilde{\rho}_{mnbc}, \tag{A.35}$$

$$\begin{aligned}(\varepsilon_a + \varepsilon_b - \varepsilon_m - \varepsilon_n)\rho_{mnab} = g_{mnab} &+ \sum_{cd} g_{cdab}\rho_{mncd} + \sum_{rs} g_{mnrs}\rho_{rsab} \\ &+ \sum_{r} g_{mnrb}\rho_{ra} - \sum_{c} g_{cnab}\rho_{mc} + \sum_{rc} \tilde{g}_{cnrb}\tilde{\rho}_{mrac} \\ &+ \sum_{r} g_{mnra}\rho_{rb} - \sum_{c} g_{cmba}\rho_{nc} + \sum_{rc} \tilde{g}_{cmra}\tilde{\rho}_{nrbc},\end{aligned} \tag{A.36}$$

are solved self consistently for the core electrons to determine the core excitation coefficients ρ_{ma} and ρ_{mnab}. The iterative procedure needs a starting point, which is

$$\rho_{mnij} = \frac{g_{mnij}}{\varepsilon_i + \varepsilon_j - \varepsilon_m - \varepsilon_n}, \qquad \rho_{ma} = 0.$$

The g terms in the above equations are the Coulomb integrals,

$$g_{mnij} = \iint \phi(\boldsymbol{r}_1)_m \phi(\boldsymbol{r}_2)_n \, \frac{e^2}{r_{12}} \, \phi(\boldsymbol{r}_1)_i \phi(\boldsymbol{r}_3)_j \, \mathrm{d}^3 r_1 \, \mathrm{d}^3 r_2,$$

and the tilde above g or ρ means antisymmetrisation, e.g., $\tilde{g}_{mban} = g_{mban} - g_{mbna}$. The correction to the core energy is given by

$$\delta E_c = \frac{1}{2}\sum_{mnab} g_{abmn}\tilde{\rho}_{nmba}, \tag{A.37}$$

and is used to control the convergence of the self-consistent procedure.

In order to achieve high-accuracy for single-valence systems, some dominating triple excitations must be included, see, e.g., Ref. [424, 425].

For systems with more than one valence electron, higher accuracy can be achieved by combining the singles-doubles method with the configuration interaction method (which is discussed below) [426] (see also [427]). The coupled-cluster equations allow for a highly accurate treatment of core–valence correlations, while the configuration interaction technique allows for a much more accurate treatment of valence–valence correlations. In order to achieve this, some modifications of the singles-doubles equations are required; for example, all terms that have only excitations of valence electrons must be removed, since these are included in the configuration interaction calculations.

A.6 Interaction with external fields

A.6.1 Time-dependant Hartree-Fock method

In the presence of external fields the core becomes polarised, and a modification of the Hartree-Fock potential is required. We take this core polarisation into account using the time-dependent Hartree-Fock (TDHF) method as in Ref. [243] (see also Refs. [38, 244]). This is equivalent to the random phase approximation with exchange (RPA), as in Ref. [428].

Consider the (single-particle) interaction Hamiltonian due to an applied time-dependent external field (e.g., the electric field from a laser):

$$\hat{h}_f = \hat{f}\,\mathrm{e}^{-i\omega t} + \hat{f}^\dagger\,\mathrm{e}^{i\omega t}. \tag{A.38}$$

The total interaction Hamiltonian is the sum of each single-electron Hamiltonian for each electron in the atom $\hat{H}_f = \sum_i \hat{h}_{fi}$. Within the framework of the TDHF method, the Hartree-Fock potential is rewritten $U^{\rm HF} \to U^{\rm HF} + \delta V_f$, where δV_f is the correction to the core potential arising from the perturbing field. Then, the all single-particle orbitals for the core electrons are expressed as

$$\phi'_a = \phi_a + \eta_a\,\mathrm{e}^{-i\omega t} + \zeta_a\,\mathrm{e}^{i\omega t}, \tag{A.39}$$

where ϕ is the unperturbed orbital, η and ζ are corrections due to the external field, and ω is the frequency of the external field. The corrections to the core potential (δV) are found by solving the following system of TDHF equations self-consistently for all of the core orbitals:

$$\begin{aligned}(\hat{h}^{\rm HF} - \varepsilon_a - \omega)\eta_a &= -(\hat{h}_f + \delta V_f - \delta\varepsilon_a)\phi_a\\ (\hat{h}^{\rm HF} - \varepsilon_a + \omega)\zeta_a &= -(\hat{h}_f^\dagger + \delta V_f^\dagger - \delta\varepsilon_a)\phi_a,\end{aligned} \tag{A.40}$$

where the correction δV is calculated from

$$\begin{aligned}\delta V_f\phi_a &= U^{\rm HF}(\phi'_1,\ldots,\phi'_N)\phi_a - U^{\rm HF}(\phi_1,\ldots,\phi_N)\phi_a\\ &= \sum_{n\neq a}^{N_c}\int\Bigg[\frac{\zeta_n^\dagger(\boldsymbol{r}')\phi_n(\boldsymbol{r}') + \phi_n^\dagger(\boldsymbol{r}')\eta_n(\boldsymbol{r}')}{|\boldsymbol{r}-\boldsymbol{r}'|}\phi_a(\boldsymbol{r})\\ &\qquad\qquad - \frac{\zeta_n^\dagger(\boldsymbol{r}')\phi_n(\boldsymbol{r}) + \phi_n^\dagger(\boldsymbol{r}')\eta_n(\boldsymbol{r})}{|\boldsymbol{r}-\boldsymbol{r}'|}\phi_a(\boldsymbol{r}')\Bigg]\,\mathrm{d}^3r'.\end{aligned} \tag{A.41}$$

In deriving Eq. (A.40), we have kept terms only to first order in the perturbation, and the energy shift is given by $\delta\varepsilon_a = \langle\phi_a|\hat{h} + \delta V|\phi_a\rangle$. This iterative procedure requires an initial value for δV to begin; it suffices to start with $\delta V = 0$.

A.6.2 Matrix elements with core polarisation

We wish to determine the effect of this core polarisation on the matrix elements of transitions between external electrons. For now, we will consider the case of a single valence system, for simplicity. Consider now the valence wave function for a state v using the regular time-dependent perturbation theory,

$$\psi'_v = \psi_v + \frac{M_{wv}}{E_v - E_w + \omega}\psi_w\,\mathrm{e}^{-i\omega t}, \tag{A.42}$$

where M_{wv} is the transition matrix element (from initial state v to final state w), and we have kept only the resonant term $\omega \approx E_w - E_v$. Comparing this equation with the valence-wavefunction equivalents of Eqs. (A.39) and (A.40):

$$\begin{aligned} \psi' &= \psi + X\,\mathrm{e}^{-i\omega t} + Y\,\mathrm{e}^{i\omega t}, \\ (\hat{H}^{\mathrm{HF}} - E - \omega)X &= -(\hat{h}_f + \delta V_f - \delta E)\psi, \\ (\hat{H}^{\mathrm{HF}} - E + \omega)Y &= -(\hat{h}_f^\dagger + \delta V_f^\dagger - \delta E)\psi, \end{aligned} \tag{A.43}$$

which together imply

$$\begin{aligned} \langle\psi_w|\psi'_v\rangle &= \langle\psi_w|X_v\rangle\,\mathrm{e}^{-i\omega t} \\ &= \frac{\langle\psi_w|\hat{h}_f + \delta V_f|\psi_v\rangle}{E_v - E_w + \omega}\,\mathrm{e}^{-i\omega t}, \end{aligned} \tag{A.44}$$

it is clear that

$$M_{wv} = \langle\psi_w|\hat{h}_f + \delta V_f|\psi_v\rangle. \tag{A.45}$$

Then, for many-electron wavefunctions, the electron transition matrix elements M_{BA} (from initial state A to final state B) induced by the interaction $\hat{h}$ are given by the sum of single-electron contributions (see, e.g., Ref. [423]). Using this method, once convergence of equations (A.40) and (A.41) has been realised, core polarisation is included to all orders in perturbation theory (see, e.g., Refs. [38, 244]). The first-order core-polarisation correction diagrams are shown in Fig. A.13. Note that to include just the first-order core polarisation (as in Fig. A.13) corresponds to solving the equations (A.40) and (A.41) once, without further iterations. Further iterations of the equations give an important contribution, called relaxation, and in general can not be neglected.

This means that core-polarisation effects can be taken into account with a redefinition of the external field operators. We adopt the notation that a tilde over an operator means that operator has been redefined to include the core-polarisation correction:

$$\widetilde{h} \equiv \hat{h} + \delta V. \tag{A.46}$$

The TDHF corrections to matrix elements are extremely important. They often give corrections on the order of 10% or more. In fact, sometimes, without core polarisation the matrix element is zero and the entire amplitude is due to this correction. Note also, that including the core polarisation in this self-consistent way makes the matrix elements self-consistent in the same way that including the Hartree-Fock potential in the way described above makes the Hamiltonian and energies self consistent. For example, without including core polarisation, it is seen that the matrix elements of the $E1$ interaction are not

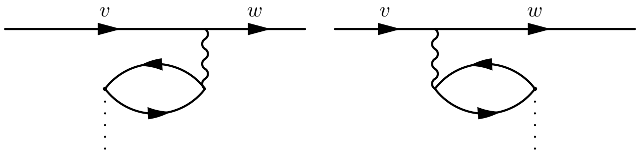

(a) Direct

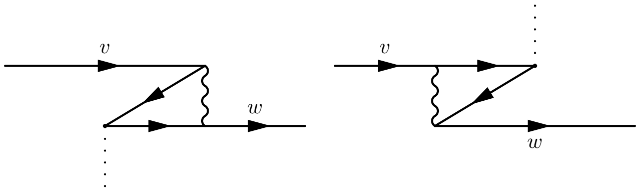

(b) Exchange

Figure A.13 Feynman-Goldstone diagrams for the lowest-order direct and exchange contributions to the core polarisation. The wavy line denotes the Coulomb interaction, and the dotted line denotes the interaction with the external field.

gauge independent; in the TDHF method this is corrected, see, e.g., Refs. [38, 244, 429]).

Note that we can easily include correlation corrections into the matrix elements by using Brueckner orbitals in place of the Hartree-Fock orbitals for the valence electrons in the above equations. The corrections to the Brueckner orbitals are found by including the correlation potential into the TDHF equations for the valence electrons.

A.7 Configuration interaction with many-body perturbation theory

In order to calculate the wavefunctions of systems with two or more valence electrons, we use a method that is based on the configuration interaction (CI) method. We make use of what is called the *configuration Interaction with many-body perturbation theory* (CI+MBPT) method, which was developed in Ref. [225] (also see Ref. [430]). The CI method very accurately takes into account the valence–valence electron correlations, while the MBPT very accurately treats the core–valence correlations; the combined CI+MBPT method gives the best of both techniques.

Typically, we use what we call the "V^{N-M} potential", as developed in Ref. [289]. In this case, the atomic electrons are broken into the $N_c (= N - M)$ core and M valence electrons. The Hartree-Fock equations are then solved for the N_c core orbitals, and the orbitals of the valence electrons are found in this frozen potential (as described below). Note that in some cases, particularly when there are many valence electrons, this method is impractical, and other approaches are needed. We therefore sometimes deviate from this method; when this happens it will be explained in the text.

The effective CI+MBPT Hamiltonian for the system of M valence electrons has the form:

$$\hat{H}^{\text{eff}} = \sum_i \hat{h}_1(r_i) + \sum_{i<j} \hat{h}_2(r_i, r_j), \tag{A.47}$$

where $\hat{h}_1$ is the single-electron part of the Hamiltonian,

$$\hat{h}_1 = c\boldsymbol{\alpha} \cdot \hat{\boldsymbol{p}} + c^2(\beta - 1) - V^{\text{nuc.}} + U^{\text{HF}} + \hat{\Sigma}_1, \tag{A.48}$$

and $\hat{h}_2$ is the two-electron part,

$$\hat{h}_2(r_i, r_j) = \frac{1}{|\boldsymbol{r_i} - \boldsymbol{r_j}|} + \hat{\Sigma}_2(r_i, r_j), \tag{A.49}$$

and the sum runs over the M valence electrons. In the above equations U^{HF} is the RHF potential created by the $N - M$ electrons of the closed-shell core. The additional $\hat{\Sigma}$ terms are the correlation potentials, without which these equations would correspond to the conventional CI method. The correlation potential is used to take into account core-valence correlations (see Refs. [225, 430] for details). The single electron correlation potential, $\hat{\Sigma}_1$, represents the interaction of a single valence electron with the atomic core, and is the same potential described as described in Sec. A.4.2 (sometimes we use the all-order potential, and sometimes only to second order). The two-electron operator, $\hat{\Sigma}_2$, represents the screening of the valence–valence Coulomb interaction by the core electrons.

Note that the method described here is not exhaustive; for certain systems and in certain cases deviations from this method are required. Where we deviate from this method will be described in the text.

A.8 Mixed states method for summation over intermediate states

Consider, for example, the first-order correction to an electric dipole transition induced by the interaction with some external field described by the Hamiltonian $\hat{h}$:

$$\boldsymbol{d}' = \sum_n \sum_{i,j}^{N} \left[\frac{\langle \Psi_b | \hat{\boldsymbol{d}}_i | \Psi_n \rangle \langle \Psi_n | \hat{h}_j | \Psi_a \rangle}{\mathcal{E}_a - \mathcal{E}_n} + \frac{\langle \Psi_b | \hat{h}_j | \Psi_n \rangle \langle \Psi_n | \hat{\boldsymbol{d}}_i | \Psi_a \rangle}{\mathcal{E}_b - \mathcal{E}_n} \right], \tag{A.50}$$

where the sum n runs over all unoccupied states, and the sums over i and j run over all atomic electrons. In order to perform the calculations, the above "exact" formula is replaced by one built from approximate wavefunctions in the single-particle picture:

$$\boldsymbol{d}' = \sum_n \sum_{i,j}^{\text{valence}} \left[\frac{\langle \psi_b | \widetilde{\boldsymbol{d}}_i | \psi_n \rangle \langle \psi_n | \widetilde{h}_j | \psi_a \rangle}{E_a - E_n} + \frac{\langle \psi_b | \widetilde{h}_j | \psi_n \rangle \langle \psi_n | \widetilde{\boldsymbol{d}}_i | \psi_a \rangle}{E_b - E_n} \right]. \tag{A.51}$$

This equation looks similar to Eq. (A.50), but has some important differences. Firstly, the wavefunctions and energies are replaced with their approximate counterparts (these matrix elements are determined in terms of matrix elements of single-particle orbitals as above, and the tilde over the operators means that core-polarisation is included). The sums over i and j now extend only over the valence electrons (the core contribution is included in the core-polarisation using the TDHF method as described above). Also, the sum over n now extends over *all* states, including the occupied core states. Extending the summation to the core states corresponds to inclusion of highly excited autoionising states.

One can then use Eq. (A.51) to perform calculations by a direct determination and summation of matrix elements and energy denominators; we refer to this apprach as the *direct summation*, or sum-over-states approach. In our calculation, however, we use a numerically more stable approach based on the Dalgarno-Lewis exact summation method [226], which we refer to as the *mixed states* (or sometimes, the solving-equations) method.

Consider the first-order correction to the wavefunction $|\psi_a\rangle$ due to the perturbation $\hat{h}$:

$$|\delta\psi_a\rangle = \sum_{n,j} \frac{|n\rangle\langle n|\hat{h}_j|\psi_a\rangle}{E_a - E_n}, \tag{A.52}$$

where $|n\rangle$ and $|\psi_a\rangle$ are eigenfunctions of the unperturbed Hamiltonian H_0, with eigenvalues E_n and E_a, respectively. Note that this correction satisfies the differential equation

$$(\hat{H}_0 - E_a)|\delta\psi_a\rangle = -\sum_j \hat{h}_j|\psi_a\rangle, \tag{A.53}$$

which can be solved numerically. In general, the interaction is time dependent, so time-dependent perturbation theory must be used. In fact, the relevant equations which must be solved are just the TDHF equations (A.40), though now there are two external fields, instead of one (e.g. $\hat{\boldsymbol{d}}$ and $\hat{h}$ above).

The wavefunction in the external $\hat{h}$ and $E1$ fields is expressed

$$\psi = \psi_0 + \delta\psi + Xe^{-i\omega t} + Ye^{i\omega t} + \delta Xe^{-i\omega t} + \delta Ye^{i\omega t}, \tag{A.54}$$

where ψ_0 is the unperturbed state, $\delta\psi$ is the correction due to the $\hat{h}$ interaction acting alone, X and Y are corrections due to the $E1$ field acting alone, δX and δY are corrections due to both fields acting simultaneously, and $\omega = E_a - E_b$ is the frequency of the transition. The corrections to the wavefunctions and to the core HF potential are found by solving the relevant TDHF equations self-consitantly for the core:

$$(\hat{H}_0 - E_c - \omega)X_c = -(\hat{d}_{E1} + \delta\hat{V}_{E1})\psi_{0c}, \tag{A.55}$$

$$(\hat{H}_0 - E_c + \omega)Y_c = -(\hat{d}^\dagger_{E1} + \delta\hat{V}^\dagger_{E1})\psi_{0c}, \tag{A.56}$$

$$(\hat{H}_0 - E_c)\delta\psi_c = -(\hat{h} + \delta\hat{V}_h)\psi_{0c}, \tag{A.57}$$

$$(\hat{H}_0 - E_c - \omega)\delta X_c = -\delta\hat{V}_{E1}\delta\psi_c - \delta\hat{V}_h X_c - \delta\hat{V}_{hE1}\psi_{0c} + \delta E_c\psi_{0c}, \tag{A.58}$$

$$(\hat{H}_0 - E_c + \omega)\delta Y_c = -\delta\hat{V}^\dagger_{E1}\delta\psi_c - \delta\hat{V}_h Y_c - \delta\hat{V}^\dagger_{hE1}\psi_{0c} + \delta E_c\psi_{0c}. \tag{A.59}$$

Here, the index c denotes core states, and $\delta\hat{V}_h$ and $\delta\hat{V}_{E1}$ are corrections to the core potential arising from the $\hat{h}$ and $E1$ interactions, respectively, and $\delta\hat{V}_{hE1}$ is the correction to the core potential arising from the simultaneous perturbation of the $\hat{h}$ field and the electric field of the laser light, and δE_c is the corresponding correction to the core energy, given by

$$\delta E_c = \langle\psi_{0c}|\delta\hat{V}_{E1}|\delta\psi_c\rangle + \langle\psi_{0c}|\delta\hat{V}_h|X_c\rangle + \langle\psi_{0c}|\delta\hat{V}_{hE1}|\psi_{0c}\rangle. \tag{A.60}$$

In the mixed-states method, the PNC amplitude between valence states a and b is then given by

$$\boldsymbol{d}' = \langle\psi_b|\sum_i \widetilde{\boldsymbol{d}}_i|\delta\psi_a\rangle + \langle\delta\psi_b|\sum_i \widetilde{\boldsymbol{d}}_i|\psi_a\rangle + \langle\psi_b|\sum_i \delta\hat{V}_{hE1i}|\psi_a\rangle, \tag{A.61}$$

The last term in the above equation represents the double core polarisation contribution, which is due to the simultaneous action of the two external fields. This term gives an important correction that is often not included in sum-over-states calculations. This effect is the subject of Ch. 4.

Note that no summation has been performed, and only calculations of the initial and final state wavefunctions and energies are needed. Alternatively, in the direct summation method, a complete set of intermediate wave functions and energies must be calculated. A comparison of calculations performed using the direct-summation and mixed-states approaches is a very good way of testing the completeness of the basis, since the two approaches (neglecting double core polarisation) must be identical if the basis is complete and fully self-consistent.

APPENDIX B: *Formulas*

B.1 Parity nonconservation amplitudes

The Hamiltonian describing the parity violating electron–nucleus interaction can be expressed as the sum of the nuclear-spin-independent (SI) and nuclear-spin-dependent (SD) parts (using atomic units, $\hbar = |e| = m_e = 1$, $c = 1/\alpha \approx 137$):

$$\hat{h}_{\rm PNC} = \hat{h}_{\rm SI} + \hat{h}_{\rm SD} = \frac{G_F}{\sqrt{2}}\left(-\frac{Q_W}{2}\gamma_5 + \frac{\boldsymbol{\alpha}\cdot\boldsymbol{I}}{I}\varkappa\right)\rho(r), \tag{B.1}$$

where $G_F \approx 2.2225 \times 10^{-14}$ a.u. is the Fermi weak constant, Q_W and $\varkappa$ are dimensionless constants quantifying the strength of the SI and SD PNC interactions, respectively, $\boldsymbol{\alpha} = \gamma_0\boldsymbol{\gamma}$ and $\gamma_5 = i\gamma_0\gamma_1\gamma_2\gamma_3$ are Dirac matrices, $\boldsymbol{I}$ is the nuclear spin and $\rho(r)$ is the normalised nuclear density, $\int \rho\,{\rm d}^3r = 1$. Eq. (B.1) contains only single-particle operators, so it transforms to the many-body operator in the trivial way: $H_{\rm PNC}(r_1, ..., r_N) = \sum_i h_{\rm PNC}(r_i)$.

The amplitude of a parity-violating $E1$ transition between two states of the same parity can be expressed via the sum over all opposite parity states n:

$$\boldsymbol{E}_{\rm PNC}^{a\to b} = \sum_n \left[\frac{\langle b|\hat{\boldsymbol{D}}_{E1}|n\rangle\langle n|\hat{H}_{\rm PNC}|a\rangle}{E_a - E_n}\,\frac{\langle b|\hat{H}_{\rm PNC}|n\rangle\langle n|\hat{\boldsymbol{D}}_{E1}|a\rangle}{E_b - E_n}\right], \tag{B.2}$$

where $\hat{\boldsymbol{D}} = -e\sum_i \boldsymbol{r}_i$ is the operator of the electric dipole ($E1$) interaction. In the calculations, Eq. (B.2) is determined in terms of single-particle orbitals and energies, as discussed in Ch. A. Note that due to the vector nature of the $E1$ transition, the $E_{\rm PNC}$ transition is also a vector quantity; in the tables we typically present the z-component, defined below.

Consider a transition between states of definite $\boldsymbol{F}$, $\boldsymbol{J}$, and M; where $\boldsymbol{F} = \boldsymbol{I} + \boldsymbol{J}$ is the total angular momentum of the atom, and M is its projection onto the axis of quantisation. With use of the Wigner-Eckart theorem, this amplitude can be expressed as:

$$E_{\rm PNC} = (-1)^{F_b - M_b}\begin{pmatrix} F_b & 1 & F_a \\ -M_b & q & M_a \end{pmatrix}\langle J_bF_b||d_{\rm PNC}||J_aF_a\rangle, \tag{B.3}$$

where $\langle f||h||i\rangle$ is called a “reduced matrix element”, and $(\cdots)$ is a Wigner $3j$ symbol (see, e.g., Ref. [287]), and $q = M_b - M_a$. Crucially, the reduced matrix elements are independent of projections of the angular momenta. Unless explicitly stated, we display z-components in all tables, and take $M = F_z = \min(F_a, F_b)$. The reduced matrix elements obey the symmetry rule

$$\langle J_aF_a||d_{\rm PNC}||J_bF_b\rangle = (-1)^{F_b - F_a}\langle J_bF_b||d_{\rm PNC}||J_aF_a\rangle^*, \tag{B.4}$$

where * means complex conjugation and results in a change of sign for the PNC amplitudes.

B.1.1 Spin-dependent PNC

For the SD-PNC amplitude, the reduced matrix element is given by

$$\langle J_bF_b||d_{\rm SD}||J_aF_a\rangle = \frac{G_F}{\sqrt{2}}\varkappa\sqrt{(I+1)(2I+1)(2F_b+1)(2F_a+1)/I}$$
$$\sum_n\Bigg[(-1)^{J_b-J_a}\begin{Bmatrix}J_n & J_a & 1\\ I & I & F_a\end{Bmatrix}\begin{Bmatrix}J_n & J_b & 1\\ F_b & F_a & I\end{Bmatrix}\frac{\langle J_b||\hat{d}_{\rm E1}||J_n\rangle\langle J_n||\boldsymbol{\alpha}\rho||J_a\rangle}{E_a-E_n}+$$
$$(-1)^{F_b-F_a}\begin{Bmatrix}J_n & J_b & 1\\ I & I & F_b\end{Bmatrix}\begin{Bmatrix}J_n & J_a & 1\\ F_a & F_b & I\end{Bmatrix}\frac{\langle J_b||\boldsymbol{\alpha}\rho||J_n\rangle\langle J_n||\hat{d}_{\rm E1}||J_a\rangle}{E_b-E_n}\Bigg], \quad \text{(B.5)}$$

where $\{\cdots\}$ is a Wigner $6j$ symbol (see, e.g., Ref. [287]).

For single-particle states, the reduced matrix elements of the SD-PNC interaction take the form

$$\langle j_a||\boldsymbol{\alpha}\rho||j_b\rangle = iR_{\rm 1SD}C_{\rm 1SD}+iR_{\rm 2SD}C_{\rm 2SD}, \quad \text{(B.6)}$$

where

$$\begin{aligned}R_{\rm 1SD} &= -\alpha\int\rho(r)\,g_a(r)\,f_b(r)\,{\rm d}r,\\ R_{\rm 2SD} &= -\alpha\int\rho(r)\,f_a(r)\,g_b(r)\,{\rm d}r,\end{aligned} \quad \text{(B.7)}$$

are the radial integrals with $\rho(r)$ the normalised (Fermi-type) nuclear density, and $C_{\rm 1,2SD}$ are the angular coefficients:

$$\begin{aligned}C_{\rm 1SD} &= (-1)^{j_a+l_b+1/2}\sqrt{6(2j_a+1)(2j_b+1)}\begin{Bmatrix}1/2 & j_a & l_b\\ j_b & 1/2 & 1\end{Bmatrix},\\ C_{\rm 2SD} &= (-1)^{j_a+l_a+3/2}\sqrt{6(2j_a+1)(2j_b+1)}\begin{Bmatrix}1/2 & j_a & l_a\\ j_b & 1/2 & 1\end{Bmatrix}.\end{aligned} \quad \text{(B.8)}$$

For many-particle states, the reduced matrix elements that appear in Eq. (B.5) are then given by sums of single-particle integrals (B.6).

Also for single-particle states, the reduced matrix elements of the electric dipole ($E1$) operator take the form

$$\langle j_a||\hat{d}_{\rm E1}||j_b\rangle = R_{E1}(-1)^{j_a+1/2}\sqrt{(2j_a+1)(2j_b+1)}\begin{pmatrix}j_a & j_b & 1\\ -1/2 & 1/2 & 0\end{pmatrix}, \quad \text{(B.9)}$$

where the radial integral is

$$R_{E1} = -e\int\big(f_a(r)f_b(r)+\alpha^2g_a(r)g_b(r)\big)\,{\rm d}r. \quad \text{(B.10)}$$

B.1.2 Spin-independent PNC

For the (Q_W-induced) SI-PNC amplitude, the reduced matrix element is

$$\begin{aligned}\langle J_bF_b||d_{\rm SI}||J_aF_a\rangle\\
&= i\frac{G_F}{2\sqrt{2}}(-Q_W)(-1)^{I+F_a+J_b+1}\sqrt{(2F_b+1)(2F_a+1)}\begin{Bmatrix}J_a & J_b & 1\\ F_b & F_a & I\end{Bmatrix}\\
&\times\sum_n\left[\begin{pmatrix}J_a & 0 & J_a\\ -m & 0 & m\end{pmatrix}\frac{\langle J_b||\hat{d}_{\rm E1}||J_n\rangle\langle J_n||\gamma_5\rho||J_a\rangle}{E_a-E_n}\right.\\
&\qquad\left.+\begin{pmatrix}J_b & 0 & J_b\\ -m & 0 & m\end{pmatrix}\frac{\langle J_b||\gamma_5\rho||J_n\rangle\langle J_n||\hat{d}_{\rm E1}||J_a\rangle}{E_b-E_n}\right],\end{aligned} \tag{B.11}$$

with $m = \min(J_a, J_b)$.

The single-particle reduced matrix element of the SI-PNC interaction is defined:

$$\langle j_a||\gamma_5\rho||j_b\rangle = iR_{\rm SI}C_{\rm SI}, \tag{B.12}$$

where

$$R_{\rm SI} = -\alpha\int\rho(r)\,[f_a(r)\,g_b(r) - g_a(r)\,f_b(r)]\,{\rm d}r \tag{B.13}$$

is the single-electron radial integral, and $C_{\rm SI} = \begin{pmatrix}J_a & 0 & J_a\\ -m & 0 & m\end{pmatrix}^{-1} = \sqrt{2J_a+1}$ is the angular coefficient (note that the coefficient $C_{\rm SI}$ and the $3j$ symbol in (B.11) cancel). The $\gamma_5\rho(r)$ operator is a scalar operator; the reduced matrix element of a scalar operator is just the matrix element divided by the $3j$ symbol, so the $3j$ symbols always cancel. We do this purely for convenience in the calculations.

B.1.3 F-independent form of spin-independent amplitude

When the spin-dependent part does not contribute to the PNC amplitude, it is usually more convenient to express the PNC amplitudes in a form completely independent of F. The electron (F-independent) part of the SI-PNC amplitude [i.e. with $|a\rangle = |J_a, l_a, m_a\rangle$ in (B.2)] is given by the formula

$$\begin{aligned}E_{\rm PNC} &= \frac{G_F}{2\sqrt{2}}(-Q_W)\sum_n(-1)^{J_b+J_n-2m}\\
&\times\left[\begin{pmatrix}J_b & 1 & J_n\\ -m & 0 & m\end{pmatrix}\begin{pmatrix}J_n & 0 & J_a\\ -m & 0 & m\end{pmatrix}\frac{\langle J_b||\hat{d}_{\rm E1}||J_n\rangle\langle J_n||\gamma_5\rho||J_a\rangle}{E_a-E_n}\right.\\
&\quad\left.+\begin{pmatrix}J_b & 0 & J_n\\ -m & 0 & m\end{pmatrix}\begin{pmatrix}J_n & 1 & J_a\\ -m & 0 & m\end{pmatrix}\frac{\langle J_b||\gamma_5\rho||J_n\rangle\langle J_n||\hat{d}_{\rm E1}||J_a\rangle}{E_b-E_n}\right],\end{aligned} \tag{B.14}$$

where for the z component we take $m = \min(J_a, J_b)$.

B.2 Angular decomposition for the atomic kernel

The atomic structure coefficient relevant to the process of atomic ionisation by scattering of dark matter particles, term the "atomic kernel", is defined

$$K_{n\kappa}(\Delta E, q) = \sum_{\kappa'} \sum_{m,m'} \left|\langle \varepsilon\kappa' m'|\, \mathrm{e}^{i\boldsymbol{q}\cdot\boldsymbol{r}} |n\kappa m\rangle\right|^2, \tag{B.15}$$

where $|\varepsilon\kappa' m'\rangle$ is an atomic state in the continuum with energy $\varepsilon = p^2/2m_e$, the state $|n\kappa m\rangle$ is a bound atomic state, and $\boldsymbol{q}$ is the momentum transfer; see Ch. 7. Here, m is the projection of $\boldsymbol{j}$ onto the axis of quantisation. Note that this matrix element is relevant to the case of an electron vector interaction (for a heavy mediator). We consider the scalar, pseudoscalar, and pseudovector cases below; only minor modifications are required.

To evaluate the sum of matrix elements in Eq. (B.15), we first write the exponential function in terms of the irreducible (spherical) tensor operators,

$$\mathrm{e}^{i\boldsymbol{q}\cdot\boldsymbol{r}} = \sum_{L=0}^{\infty} \sum_{M=-L}^{L} T_{LM},$$

where

$$T_{LM} = 4\pi (i)^L j_L(qr) Y_{LM}(\theta_r, \phi_r) Y^*_{LM}(\theta_q, \phi_q), \tag{B.16}$$

with Y_{LM} the spherical harmonics, and j_L the spherical Bessel function. Then, using the standard angular momentum summation rules (see, e.g., [287]), we express Eq. (B.15) as

$$\begin{aligned} K_{n\kappa}(\Delta E, q) &= \sum_{\kappa'} \sum_{m,m'} \sum_{L,M} \left|\langle \varepsilon\kappa' m'|T_{LM}|n\kappa m\rangle\right|^2 \\ &= \sum_{\kappa'} \sum_{L} \left|\langle \varepsilon\kappa'||T_L||n\kappa\rangle\right|^2 x(n,j), \end{aligned} \tag{B.17}$$

where $x(n,j)$ is the fractional occupation number for a given shell (for the shells of interest here $x = 1$, however, $x < 1$ for open shells). The factor $\langle p\kappa'||T_L||n\kappa\rangle$ is known as the reduced matrix element, and is defined via the Wigner-Eckart theorem:

$$\langle \varepsilon\kappa' m'|T_{LM}|n\kappa m\rangle \equiv (-1)^{j'-m'} \begin{pmatrix} j' & L & j \\ -m' & M & m \end{pmatrix} \langle \varepsilon\kappa'||T_L||n\kappa\rangle, \tag{B.18}$$

where $\begin{pmatrix} j' & L & j \\ -m' & M & m \end{pmatrix}$ is a $3j$ symbol. Importantly, the reduced matrix elements are independent of the quantum numbers m and m', as well as the index M.

Therefore, the atomic kernel is reduced to a summation over reduced matrix elements, which are found from Eq. (B.18) with, e.g., $M = 0$ and $m = m' = 1/2$:

$$\begin{aligned} \left|\langle \varepsilon\kappa'||T_L||n\kappa\rangle\right|^2 &= \begin{pmatrix} j' & L & j \\ -\frac{1}{2} & 0 & \frac{1}{2} \end{pmatrix}^{-2} \left|\langle \varepsilon\kappa' \tfrac{1}{2}|T_{L0}|n\kappa \tfrac{1}{2}\rangle\right|^2 \\ &= C^L_{\kappa\kappa'} \left(R_f^2 + 2\alpha^2 R_f R_g + \alpha^4 R_g^2\right), \end{aligned} \tag{B.19}$$

where R_f and R_g are the radial integrals,

$$R_f = \int f_{\varepsilon\kappa'} f_{n\kappa} j_L(qr)\,\mathrm{d}r \tag{B.20}$$

$$R_g = \int g_{\varepsilon\kappa'} g_{n\kappa} j_L(qr)\,\mathrm{d}r, \tag{B.21}$$

and the angular coefficient is

$$\begin{aligned} C^L_{\kappa\kappa'} =& \frac{1}{4}(-1)^{j+j'-l-l'}(2L+1)\begin{pmatrix} l' & l & L \\ 0 & 0 & 0 \end{pmatrix}^2 \begin{pmatrix} j' & L & j \\ -\frac{1}{2} & 0 & \frac{1}{2} \end{pmatrix}^{-2} \\ &\times \Bigg[(-1)^{j+j'-l-l'}(2j+1)(2j'+1)\begin{pmatrix} l' & l & L \\ 0 & 0 & 0 \end{pmatrix}^2 \\ &\quad + 8\sqrt{l'(l'+1)l(l+1)}\begin{pmatrix} l' & l & L \\ 0 & 0 & 0 \end{pmatrix}\begin{pmatrix} l' & l & L \\ -1 & 1 & 0 \end{pmatrix} \\ &\quad - 4(\kappa'+1)(\kappa+1)\begin{pmatrix} l' & l & L \\ -1 & 1 & 0 \end{pmatrix}^2 \Bigg]. \end{aligned} \tag{B.22}$$

For $s_{1/2}$ and $p_{1/2}$ states, this reduces simply to $C = 2$ (with $L = 0$ for $\kappa = \kappa' = \pm 1$, and $L = 1$ for $\kappa = -\kappa' = \pm 1$). Note that, since the reduced matrix elements do not depend on M, m, or m', we can choose any values for these indices that leave the $3j$ symbol in (B.18) nonzero, however the minimal values are typically the simplest to compute.

Similarly, if instead we consider a scalar, pseudoscalar, or pseudovector electron coupling, the relevant electron operator is replaced with $T_{LM}\gamma^0$, $T_{LM}\gamma^0\gamma_5$, or $T_{LM}\gamma_5$, respectively. Then the atomic structure factors can be expressed as

$$\left|\langle\varepsilon\kappa'||T_L\gamma^0||n\kappa\rangle\right|^2 = C^L_{\kappa\kappa'}\left(R_f^2 - 2\alpha^2 R_f R_g + \alpha^4 R_g^2\right), \tag{B.23}$$

$$\left|\langle\varepsilon\kappa'||T_L\gamma^0\gamma_5||n\kappa\rangle\right|^2 = D^L_{\kappa\kappa'}\alpha^2\left(R_{fg}^2 + 2R_{fg}R_{gf} + R_{gf}^2\right), \tag{B.24}$$

$$\left|\langle\varepsilon\kappa'||T_L\gamma_5||n\kappa\rangle\right|^2 = D^L_{\kappa\kappa'}\alpha^2\left(R_{fg}^2 - 2R_{fg}R_{gf} + R_{gf}^2\right), \tag{B.25}$$

where the radial integrals are

$$R_{fg} = \int f_{\varepsilon\kappa'} g_{n\kappa} j_L(qr)\,\mathrm{d}r \tag{B.26}$$

$$R_{gf} = \int g_{\varepsilon\kappa'} f_{n\kappa} j_L(qr)\,\mathrm{d}r. \tag{B.27}$$

The angular coefficient D is related to C via the transformation $\kappa \to \tilde{\kappa} = -\kappa$, with $l \to \tilde{l} = |\tilde{\kappa} + 1/2| - 1/2$ (κ' and l' remain unchanged). For $s_{1/2}$ and $p_{1/2}$ states we also have $D = 2$ (with $L = 0$ for $\kappa = -\kappa' = \pm 1$, and $L = 1$ for

$\kappa = \kappa' = \pm 1$). The full formula for D is given

$$\begin{aligned}
D^L_{\kappa\kappa'} &= \frac{1}{4}(2L+1)\begin{pmatrix} l' & \tilde{l} & L \\ 0 & 0 & 0 \end{pmatrix}^2 \begin{pmatrix} j' & L & j \\ -\frac{1}{2} & 0 & \frac{1}{2} \end{pmatrix}^{-2} \\
\times \Bigg[&- (2j+1)(2j'+1)\begin{pmatrix} l' & \tilde{l} & L \\ 0 & 0 & 0 \end{pmatrix}^2 \\
&- 4(i)^{j+j'-l-l'+1}\sqrt{(2j+1)(2j'+1)(\kappa-1)(\kappa'+1)}\begin{pmatrix} l' & \tilde{l} & L \\ 0 & 0 & 0 \end{pmatrix}\begin{pmatrix} l' & \tilde{l} & L \\ -1 & 1 & 0 \end{pmatrix} \\
&+ 4(-1)^{j+j'-l-l'}(\kappa'+1)(\kappa-1)\begin{pmatrix} l' & \tilde{l} & L \\ -1 & 1 & 0 \end{pmatrix}^2 \Bigg]. \qquad \text{(B.28)}
\end{aligned}$$

List of Tables

List of Figures

References

[1] C. S. Wu, E. Ambler, R. W. Hayward, D. D. Hoppes, and R. P. Hudson, Phys. Rev. **105**, 1413 (1957).

[2] T. D. Lee and C. N. Yang, Phys. Rev. **104**, 254 (1956).

[3] B. M. Roberts, V. A. Dzuba, and V. V. Flambaum, Annu. Rev. Nucl. Part. Sci. **65**, 63 (2015).

[4] C. S. Wood, S. C. Bennett, D. Cho, B. P. Masterson, J. L. Roberts, C. E. Tanner, and C. E. Wieman, Science **275**, 1759 (1997).

[5] V. A. Dzuba, V. V. Flambaum, and O. P. Sushkov, Phys. Lett. A **141**, 147 (1989).

[6] S. A. Blundell, W. R. Johnson, and J. Sapirstein, Phys. Rev. Lett. **65**, 1411 (1990).

[7] M. G. Kozlov, S. G. Porsev, and I. I. Tupitsyn, Phys. Rev. Lett. **86**, 3260 (2001).

[8] V. A. Dzuba, V. V. Flambaum, and J. S. M. Ginges, Phys. Rev. D **66**, 076013 (2002).

[9] S. G. Porsev, K. Beloy, and A. Derevianko, Phys. Rev. Lett. **102**, 181601 (2009).

[10] S. G. Porsev, K. Beloy, and A. Derevianko, Phys. Rev. D **82**, 036008 (2010).

[11] V. A. Dzuba, J. C. Berengut, V. V. Flambaum, and B. M. Roberts, Phys. Rev. Lett. **109**, 203003 (2012).

[12] V. A. Dzuba, V. V. Flambaum, and I. B. Khriplovich, Z. Phys. D **1**, 243 (1986).

[13] V. V. Flambaum and I. B. Khriplovich, Sov. Phys. JETP **52**, 835 (1980).

[14] V. V. Flambaum, I. B. Khriplovich, and O. P. Sushkov, Phys. Lett. B **146**, 367 (1984).

[15] W. C. Haxton and C. E. Wieman, Annu. Rev. Nucl. Part. Sci. **51**, 261 (2001).

[16] O. P. Sushkov and V. V. Flambaum, Sov. Phys. JETP **48**, 608 (1978).

[17] Y. B. Zeldovich, Sov. Phys. JETP **6**, 1184 (1958).

[18] B. A. Brown, A. Derevianko, and V. V. Flambaum, Phys. Rev. C **79**, 035501 (2009).

[19] A. Derevianko and S. G. Porsev, Phys. Rev. A **65**, 052115 (2002).

[20] A. Derevianko, Phys. Rev. Lett. **85**, 1618 (2000).

[21] V. V. Flambaum and I. B. Khriplovich, Sov. Phys. JETP **62**, 872 (1985).

[22] C. C. Bouchiat and C. A. Piketty, Phys. Lett. B **269**, 195 (1991).

[23] Y. B. Zeldovich, Sov. Phys. JETP **9**, 682 (1959).

[24] M.-A. Bouchiat and C. C. Bouchiat, Phys. Lett. B **48**, 111 (1974).

[25] M.-A. Bouchiat and C. C. Bouchiat, J. Phys. **35**, 899 (1974).

[26] M.-A. Bouchiat and C. C. Bouchiat, J. Phys. **36**, 493 (1975).

[27] I. B. Khriplovich, *Parity Nonconservation in Atomic Phenomena* (Gordon and Breach, Philadelphia, 1991).

[28] J. S. M. Ginges and V. V. Flambaum, Phys. Rep. **397**, 63 (2004).

[29] L. M. Barkov and M. S. Zolotorev, JETP Lett. **27**, 357 (1978).

[30] M. Macpherson, K. Zetie, R. B. Warrington, D. N. Stacey, and J. Hoare, Phys. Rev. Lett. **67**, 2784 (1991).

[31] R. B. Warrington, C. D. Thompson, and D. N. Stacey, Europhys. Lett. **24**, 641 (1993).

[32] D. M. Meekhof, P. A. Vetter, P. K. Majumder, S. K. Lamoreaux, and E. N. Fortson, Phys. Rev. Lett. **71**, 3442 (1993).

[33] S. J. Phipp, N. H. Edwards, P. E. G. Baird, and S. Nakayama, J. Phys. B **29**, 1861 (1996).

[34] P. A. Vetter, D. M. Meekhof, P. K. Majumder, S. K. Lamoreaux, and E. N. Fortson, Phys. Rev. Lett. **74**, 2658 (1995).

[35] N. H. Edwards, S. J. Phipp, P. E. G. Baird, and S. Nakayama, Phys. Rev. Lett. **74**, 2654 (1995).

[36] K. Tsigutkin, D. R. Dounas-Frazer, A. Family, J. E. Stalnaker, V. V. Yashchuk, and D. Budker, Phys. Rev. Lett. **103**, 071601 (2009).

[37] V. A. Dzuba, V. V. Flambaum, P. G. Silvestrov, and O. P. Sushkov, Europhys. Lett. **7**, 413 (1988).

[38] V. A. Dzuba, V. V. Flambaum, P. G. Silvestrov, and O. P. Sushkov, J. Phys. B **20**, 3297 (1987).

[39] M. G. Kozlov, S. G. Porsev, and W. R. Johnson, Phys. Rev. A **64**, 052107 (2001).

[40] V. A. Dzuba and V. V. Flambaum, Phys. Rev. A **83**, 042514 (2011).

[41] M.-A. Bouchiat, J. Guéna, L. R. Hunter, and L. Pottier, Phys. Lett. B **117**, 358 (1982).

[42] M.-A. Bouchiat, J. Guéna, L. Pottier, and L. R. Hunter, J. Phys. **47**, 1709 (1986).

[43] M. C. Noecker, B. P. Masterson, and C. E. Wieman, Phys. Rev. Lett. **61**, 310 (1988).

[44] S. L. Gilbert and C. E. Wieman, Phys. Rev. A **34**, 792 (1986).

[45] S. L. Gilbert, M. C. Noecker, R. N. Watts, and C. E. Wieman, Phys. Rev. Lett. **55**, 2680 (1985).

[46] J. Guéna, M. Lintz, and M.-A. Bouchiat, Phys. Rev. A **71**, 042108 (2005).

[47] J. Guéna, D. Chauvat, P. Jacquier, E. Jahier, M. Lintz, S. Sanguinetti, A. Wasan, M.-A. Bouchiat, A. V. Papoyan, and D. Sarkisyan, Phys. Rev. Lett. **90**, 143001 (2003).

[48] V. V. Flambaum and D. W. Murray, Phys. Rev. C **56**, 1641 (1997).

[49] M. Lintz, J. Guéna, and M.-A. Bouchiat, Eur. Phys. J. A **32**, 525 (2007).

[50] D. Antypas and D. S. Elliott, Phys. Rev. A **87**, 042505 (2013).

[51] D. Antypas and D. S. Elliott, Can. J. Chem. **92**, 144 (2014).

[52] V. A. Dzuba and V. V. Flambaum, Phys. Rev. A **62**, 052101 (2000).

[53] S. C. Bennett and C. E. Wieman, Phys. Rev. Lett. **82**, 2484 (1999).

[54] D. Cho, C. S. Wood, S. C. Bennett, J. L. Roberts, and C. E. Wieman, Phys. Rev. A **55**, 1007 (1997).

[55] A. Derevianko, Phys. Rev. A **65**, 012106 (2001).

[56] V. A. Dzuba, C. Harabati, W. R. Johnson, and M. S. Safronova, Phys. Rev. A **63**, 044103 (2001).

[57] O. P. Sushkov, Phys. Rev. A **63**, 042504 (2001).

[58] V. A. Dzuba, V. V. Flambaum, and M. S. Safronova, Phys. Rev. A **73**, 022112 (2006).

[59] M. Y. Kuchiev and V. V. Flambaum, J. Phys. B **35**, 4101 (2002).

[60] M. Y. Kuchiev and V. V. Flambaum, Phys. Rev. Lett. **89**, 283002 (2002).

[61] M. Y. Kuchiev, J. Phys. B **35**, L503 (2002).

[62] M. Y. Kuchiev and V. V. Flambaum, J. Phys. B **36**, R191 (2003).

[63] A. I. Milstein, O. P. Sushkov, and I. S. Terekhov, Phys. Rev. Lett. **89**, 283003 (2002).

[64] A. I. Milstein and O. P. Sushkov, Phys. Rev. A **66**, 022108 (2002).

[65] A. I. Milstein, O. P. Sushkov, and I. S. Terekhov, Phys. Rev. A **67**, 062103 (2003).

[66] W. R. Johnson, I. Bednyakov, and G. Soff, Phys. Rev. Lett. **87**, 233001 (2001).

[67] J. Sapirstein, K. Pachucki, A. Veitia, and K. T. Cheng, Phys. Rev. A **67**, 052110 (2003).

[68] V. V. Flambaum and J. S. M. Ginges, Phys. Rev. A **72**, 052115 (2005).

[69] V. M. Shabaev, K. Pachucki, I. I. Tupitsyn and V. A. Yerokhin, Phys. Rev. Lett.

94, 213002 (2005).

[70] V. A. Dzuba, V. V. Flambaum, P. G. Silvestrov, and O. P. Sushkov, Phys. Lett. A **103**, 265 (1984).

[71] V. A. Dzuba, V. V. Flambaum, P. G. Silvestrov, and O. P. Sushkov, Phys. Scr. **36**, 69 (1987).

[72] W. R. Johnson, S. A. Blundell, Z. W. Liu, and J. Sapirstein, Phys. Rev. A **37**, 1395 (1988).

[73] J. Beringer *et al.* (Particle Data Group), Phys. Rev. D **86**, 010001 (2012).

[74] M. E. Peskin and T. Takeuchi, Phys. Rev. D **46**, 381 (1992).

[75] J. L. Rosner, Phys. Rev. D **65**, 073026 (2002).

[76] W. J. Marciano and J. L. Rosner, Phys. Rev. Lett. **65**, 2963 (1990).

[77] The Q-weak Collaboration, Phys. Rev. Lett. **111**, 141803 (2013).

[78] V. A. Dzuba, V. V. Flambaum, and O. P. Sushkov, Phys. Rev. A **51**, 3454 (1995).

[79] M. S. Safronova and W. R. Johnson, Phys. Rev. A **62**, 022112 (2000).

[80] E. Gomez, S. Aubin, G. D. Sprouse, L. A. Orozco, and D. DeMille, Phys. Rev. A **75**, 033418 (2007).

[81] S. Aubin *et al.*, AIP Conf. Proc. **1441**, 555 (2012).

[82] S. Aubin *et al.*, AIP Conf. Proc. **1525**, 530 (2013).

[83] S. Aubin *et al.*, Hyperfine Interact. **214**, 163 (2013).

[84] M. Tandecki *et al.*, J. Instrum. **9**, P10013 (2014).

[85] K. Tsigutkin, D. R. Dounas-Frazer, A. Family, J. E. Stalnaker, V. V. Yashchuk, and D. Budker, Phys. Rev. A **81**, 032114 (2010).

[86] D. R. Dounas-Frazer, K. Tsigutkin, D. English, and D. Budker, Phys. Rev. A **84**, 023404 (2011).

[87] S. G. Porsev, M. G. Kozlov, and Y. G. Rakhlina, Hyperfine Interact. **127**, 395 (2000).

[88] D. DeMille, Phys. Rev. Lett. **74**, 4165 (1995).

[89] A. T. Nguyen, D. Budker, D. DeMille, and M. S. Zolotorev, Phys. Rev. A **56**, 3453 (1997).

[90] N. Leefer, L. Bougas, D. Antypas, and D. Budker, arXiv:1412.1245.

[91] V. A. Dzuba and V. V. Flambaum, Phys. Rev. A **81**, 052515 (2010).

[92] E. N. Fortson, Phys. Rev. Lett. **70**, 2383 (1993).

[93] V. A. Dzuba, V. V. Flambaum, and J. S. M. Ginges, Phys. Rev. A **63**, 062101 (2001).

[94] L. W. Wansbeek, B. K. Sahoo, R. G. E. Timmermans, K. Jungmann, B. P. Das, and D. Mukherjee, Phys. Rev. A **78**, 050501 (2008).

[95] R. Pal, D. Jiang, M. S. Safronova, and U. I. Safronova, Phys. Rev. A **79**, 062505 (2009).

[96] S. R. Williams, A. Jayakumar, M. R. Hoffman, B. B. Blinov, and E. N. Fortson, Phys. Rev. A **88**, 012515 (2013).

[97] O. O. Versolato *et al.*, Phys. Rev. A **82**, 010501 (2010).

[98] O. O. Versolato *et al.*, Can. J. Phys. **89**, 65 (2011).

[99] M. Nuñez Portela *et al.*, Hyperfine Interact. **214**, 157 (2013).

[100] M. Nuñez Portela *et al.*, Appl. Phys. B **114**, 173 (2013).

[101] V. A. Dzuba, V. V. Flambaum, and B. M. Roberts, Phys. Rev. A **86**, 062512 (2012).

[102] N. N. Dutta and S. Majumder, Phys. Rev. A **90**, 012522 (2014).

[103] B. M. Roberts, V. A. Dzuba, and V. V. Flambaum, Phys. Rev. A **87**, 054502 (2013).

[104] B. M. Roberts, V. A. Dzuba, and V. V. Flambaum, Phys. Rev. A **88**, 042507

(2013).

[105] L. Bougas, G. E. Katsoprinakis, W. von Klitzing, J. Sapirstein, and T. P. Rakitzis, Phys. Rev. Lett. **108**, 210801 (2012).

[106] D. Sofikitis, L. Bougas, G. E. Katsoprinakis, A. K. Spiliotis, B. Loppinet, and T. P. Rakitzis, Nature **514**, 76 (2014).

[107] O. P. Sushkov, V. V. Flambaum, and I. B. Khriplovich, Sov. Phys. JETP **60**, 873 (1984).

[108] V. V. Flambaum and I. B. Khriplovich, Phys. Lett. A **110**, 121 (1985).

[109] I. B. Khriplovich, Phys. Scr. **T112**, 52 (2004).

[110] W. C. Haxton, C.-P. Liu, and M. J. Ramsey-Musolf, Phys. Rev. C **65**, 045502 (2002).

[111] A. Y. Kraftmakher, Phys. Lett. A **132**, 167 (1988).

[112] W. R. Johnson, M. S. Safronova, and U. I. Safronova, Phys. Rev. A **67**, 062106 (2003).

[113] W. C. Haxton, C.-P. Liu, and M. J. Ramsey-Musolf, Phys. Rev. Lett. **86**, 5247 (2001).

[114] M. G. Kozlov, Phys. Lett. A **130**, 426 (1988).

[115] V. F. Dmitriev and V. B. Telitsin, Nucl. Phys. A **613**, 237 (1997).

[116] V. F. Dmitriev and V. B. Telitsin, Nucl. Phys. A **674**, 168 (2000).

[117] W. C. Haxton and B. R. Holstein, Prog. Part. Nucl. Phys. **71**, 185 (2013).

[118] I. B. Khriplovich, Phys. Lett. A **197**, 316 (1995).

[119] V. V. Flambaum, Phys. Rev. A **60**, 2611 (1999).

[120] V. A. Dzuba, V. V. Flambaum, and J. S. M. Ginges, Phys. Rev. A **61**, 062509 (2000).

[121] L. N. Labzowsky, Sov. Phys. JETP **48**, 434 (1978).

[122] M. G. Kozlov and L. N. Labzowsky, J. Phys. B **28**, 1933 (1995).

[123] B. M. Roberts, V. A. Dzuba, and V. V. Flambaum, Phys. Rev. A **89**, 042509 (2014).

[124] S. B. Cahn, J. Ammon, E. Kirilov, Y. V. Gurevich, D. Murphree, R. Paolino, D. A. Rahmlow, M. G. Kozlov, and D. DeMille, Phys. Rev. Lett. **112**, 163002 (2014).

[125] T. A. Isaev, S. Hoekstra, and R. Berger, Phys. Rev. A **82**, 052521 (2010).

[126] A. Borschevsky, M. Ilia$s$, V. A. Dzuba, K. Beloy, V. V. Flambaum, and P. Schwerdtfeger, Phys. Rev. A **86**, 050501 (2012).

[127] M. K. Nayak and B. P. Das, Phys. Rev. A **79**, 060502 (2009).

[128] D. DeMille, S. B. Cahn, D. Murphree, D. A. Rahmlow, and M. G. Kozlov, Phys. Rev. Lett. **100**, 023003 (2008).

[129] Y. Y. Dmitriev, Y. G. Khait, M. G. Kozlov, L. N. Labzowsky, A. O. Mitrushenkov, A. V. Shtoff, and A. V. Titov, Phys. Lett. A **167**, 280 (1992).

[130] L. D. Carr, D. DeMille, R. V. Krems, and J. Ye, New J. Phys. **11**, 055049 (2009).

[131] E. S. Shuman, J. F. Barry, and D. DeMille, Nature **467**, 820 (2010).

[132] J. F. Barry, D. J. McCarron, E. B. Norrgard, M. H. Steinecker, and D. DeMille, Nature **512**, 286 (2014).

[133] M. Zeppenfeld *et al.*, Nature **491**, 570 (2012).

[134] J. H. Christenson, J. W. Cronin, V. L. Fitch, and R. Turlay, Phys. Rev. Lett. **13**, 138 (1964).

[135] M. Pospelov and A. Ritz, Ann. Phys. (N. Y). **318**, 119 (2005).

[136] J. Engel, M. J. Ramsey-Musolf, and U. van Kolck, Prog. Part. Nucl. Phys. **71**, 21 (2013).

[137] T. E. Chupp and M. J. Ramsey-Musolf, arXiv:1407.1064.

[138] P. G. H. Sandars, Phys. Lett. **14**, 194 (1965).

[139] P. G. H. Sandars, Phys. Rev. Lett. **19**, 1396 (1967).

[140] L. I. Schiff, Phys. Rev. **132**, 2194 (1963).

[141] V. V. Flambaum and A. Kozlov, Phys. Rev. A **85**, 022505 (2012).

[142] E. S. Ensberg, Phys. Rev. **153**, 36 (1967).

[143] M. A. Player and P. G. H. Sandars, J. Phys. B **3**, 1620 (1970).

[144] J. J. Hudson, D. M. Kara, I. J. Smallman, B. E. Sauer, M. R. Tarbutt, and E. A. Hinds, Nature **473**, 493 (2011).

[145] S. Eckel, P. Hamilton, E. Kirilov, H. W. Smith, and D. DeMille, Phys. Rev. A **87**, 052130 (2013).

[146] The ACME Collaboration, Science **343**, 269 (2014).

[147] W. C. Griffith, M. D. Swallows, T. H. Loftus, M. V. Romalis, B. R. Heckel, and E. N. Fortson, Phys. Rev. Lett. **102**, 101601 (2009).

[148] M. D. Swallows, T. H. Loftus, W. C. Griffith, B. R. Heckel, E. N. Fortson, and M. V. Romalis, Phys. Rev. A **87**, 012102 (2013).

[149] S. A. Murthy, D. Krause, Z. L. Li, and L. R. Hunter, Phys. Rev. Lett. **63**, 965 (1989).

[150] B. C. Regan, E. D. Commins, C. J. Schmidt, and D. DeMille, Phys. Rev. Lett. **88**, 071805 (2002).

[151] R. H. Parker, M. R. Dietrich, M. R. Kalita, N. D. Lemke, K. G. Bailey, M. Bishof, J. Greene, R. J. Holt, W. Korsch, Z.-T. Lu, P. Mueller, T. P. O'Connor, and J. T. Singh, arXiv:1504.07477.

[152] M. A. Rosenberry and T. E. Chupp, Phys. Rev. Lett. **86**, 22 (2001).

[153] D. Cho, K. Sangster, and E. A. Hinds, Phys. Rev. A **44**, 2783 (1991).

[154] M. V. Romalis and M. P. Ledbetter, Phys. Rev. Lett. **87**, 067601 (2001).

[155] D. M. Kara, I. J. Smallman, J. J. Hudson, B. E. Sauer, M. R. Tarbutt, and E. A. Hinds, New J. Phys. **14**, 103051 (2012).

[156] M. R. Tarbutt, B. E. Sauer, J. J. Hudson, and E. A. Hinds, New J. Phys. **15**, 053034 (2013).

[157] L. R. Hunter, S. K. Peck, A. S. Greenspon, S. S. Alam, and D. DeMille, Phys. Rev. A **85**, 012511 (2012).

[158] A. N. Petrov, L. V. Skripnikov, A. V. Titov, N. R. Hutzler, P. W. Hess, B. R. O'Leary, B. Spaun, D. DeMille, G. Gabrielse, and J. M. Doyle, Phys. Rev. A **89**, 062505 (2014).

[159] H. Loh, K. C. Cossel, M. C. Grau, K.-K. Ni, E. R. Meyer, J. L. Bohn, J. Ye, and E. A. Cornell, Science **342**, 1220 (2013).

[160] E. Kirilov, W. C. Campbell, J. M. Doyle, G. Gabrielse, Y. V. Gurevich, P. W. Hess, N. R. Hutzler, B. R. OLeary, E. Petrik, B. Spaun, A. C. Vutha, and D. DeMille, Phys. Rev. A **88**, 013844 (2013).

[161] A. C. Vutha, B. Spaun, Y. V. Gurevich, N. R. Hutzler, E. Kirilov, J. M. Doyle, G. Gabrielse, and D. DeMille, Phys. Rev. A **84**, 034502 (2011).

[162] K. Asahi *et al.*, Phys. Part. Nucl. **45**, 199 (2014).

[163] T. Inoue *et al.*, Hyperfine Interact. **231**, 157 (2015).

[164] E. R. Tardiff *et al.*, Hyperfine Interact. **225**, 197 (2013).

[165] L. P. Gaffney *et al.*, Nature **497**, 199 (2013).

[166] R. H. Parker *et al.*, Phys. Rev. C **86**, 065503 (2012).

[167] R. J. Holt *et al.*, Nucl. Phys. A **844**, 53c (2010).

[168] B. Santra, U. Dammalapati, A. Groot, K. Jungmann, and L. Willmann, Phys. Rev. A **90**, 040501 (2014).

[169] K. Jungmann, Hyperfine Interact. **227**, 5 (2014).

[170] B. J. Wundt, C. T. Munger, and U. D. Jentschura, Phys. Rev. X **2**, 041009 (2012).

[171] J. A. Ludlow and O. P. Sushkov, J. Phys. B **46**, 085001 (2013).

[172] D. Budker, Nat. Mater. **9**, 608 (2010).

[173] D. Budker, S. K. Lamoreaux, A. O. Sushkov, and O. P. Sushkov, Phys. Rev. A **73**, 022107 (2006).

[174] S. Eckel, A. O. Sushkov, and S. K. Lamoreaux, Phys. Rev. Lett. **109**, 193003 (2012).

[175] P. G. H. Sandars, Phys. Lett. **22**, 290 (1966).

[176] V. V. Flambaum, Sov. J. Nucl. Phys. **24**, 199 (1976).

[177] L. V. Skripnikov, A. N. Petrov, and A. V. Titov, J. Chem. Phys. **139**, 221103 (2013).

[178] T. Fleig and M. K. Nayak, J. Mol. Spectrosc. **300**, 16 (2014).

[179] Z. W. Liu and H. P. Kelly, Phys. Rev. A **45**, 4210 (1992).

[180] V. A. Dzuba and V. V. Flambaum, Phys. Rev. A **80**, 062509 (2009).

[181] S. G. Porsev, M. S. Safronova, and M. G. Kozlov, Phys. Rev. Lett. **108**, 173001 (2012).

[182] H. S. Nataraj, B. K. Sahoo, B. P. Das, and D. Mukherjee, Phys. Rev. Lett. **106**, 200403 (2011).

[183] S. A. Blundell, J. Sapirstein, and W. R. Johnson, Phys. Rev. D **45**, 1602 (1992).

[184] M. S. Safronova, 45th Annual Meeting of the APS Division of Atomic, Molecular and Optical Physics **[online]**, meetings.aps.org/Meeting/DAMOP14/Event/220745 (2014).

[185] A. Derevianko, APS April Meeting 2015 **[online]**, http://meetings.aps.org/Meeting/APR15/Event/244003 (2015).

[186] N. V. Novikov, O. P. Sushkov, V. V. Flambaum, and I. B. Khriplovich, Sov. Phys. JETP **46**, 420 (1977).

[187] C. J. Campbell, A. V. Steele, L. R. Churchill, M. V. Depalatis, D. E. Naylor, D. N. Matsukevich, A. Kuzmich, and M. S. Chapman, Phys. Rev. Lett. **102**, 233004 (2009).

[188] A. Kramida, Y. Ralchenko, J. Reader, and The NIST ASD Team (2013), NIST Atomic Spectra Database (ver. 5.1) **[Online]**, http://physics.nist.gov/asd (2015).

[189] J. Blaise and J.-F. Wyart, Energy levels and atomic spectra of actinides, International Tables of Selected Constants 20 **[online]**, http://web2.lac.u-psud.fr/lac/Database/Conten (1992).

[190] V. A. Dzuba, Phys. Rev. A **78**, 042502 (2008).

[191] B. M. Roberts, V. A. Dzuba, and V. V. Flambaum, Phys. Rev. A **88**, 012510 (2013).

[192] R. J. Rafac, C. E. Tanner, A. E. Livingston, and H. G. Berry, Phys. Rev. A **60**, 3648 (1999).

[193] L. Young, W. T. Hill, S. J. Sibener, S. D. Price, C. E. Tanner, C. E. Wieman, and S. R. Leone, Phys. Rev. A **50**, 2174 (1994).

[194] A. A. Vasilyev, I. M. Savukov, M. S. Safronova, and H. G. Berry, Phys. Rev. A **66**, 020101 (2002).

[195] L. N. Shabanova, Y. N. Monakov, and A. N. Khlyustalov, Opt. Spektrosk. **47**, 3 (1979).

[196] D. DiBerardino, C. E. Tanner, and A. Sieradzan, Phys. Rev. A **57**, 4204 (1998).

[197] V. M. Shabaev, I. I. Tupitsyn, K. Pachucki, G. Plunien, and V. A. Yerokhin, Phys. Rev. A **72**, 062105 (2005).

[198] B. K. Sahoo, B. P. Das, R. K. Chaudhuri, and D. Mukherjee, Phys. Rev. A **75**, 032507 (2007).

[199] V. A. Dzuba, V. V. Flambaum, A. Y. Kraftmakher, and O. P. Sushkov, Phys.

Lett. A **142**, 373 (1989).

[200] U. I. Safronova, W. R. Johnson, and M. S. Safronova, Phys. Rev. A **74**, 042511 (2006).

[201] M. S. Safronova and U. I. Safronova, Phys. Rev. A **87**, 062509 (2013).

[202] B. M. Roberts, V. A. Dzuba, and V. V. Flambaum, Phys. Rev. A **89**, 012502 (2014).

[203] D. S. Elliot, *private communication* (2013).

[204] K. P. Geetha, A. D. Singh, B. P. Das, and C. S. Unnikrishnan, Phys. Rev. A **58**, R16 (1998).

[205] B. K. Sahoo, P. Mandal, and D. Mukherjee, Phys. Rev. A **83**, 030502 (2011).

[206] W. R. Johnson and J. Sapirstein, Phys. Rev. Lett. **57**, 1126 (1986).

[207] M. D. Davidson, L. C. Snoek, H. Volten, and A. Doenszelmann, Astron. Astrophys. **255**, 457 (1992).

[208] S. Olmschenk, K. C. Younge, D. L. Moehring, D. N. Matsukevich, P. Maunz, and C. Monroe, Phys. Rev. A **76**, 052314 (2007).

[209] S. Olmschenk, D. Hayes, D. N. Matsukevich, P. Maunz, D. L. Moehring, K. C. Younge, and C. Monroe, Phys. Rev. A **80**, 022502 (2009).

[210] E. H. Pinnington, G. Rieger, and J. A. Kernahan, Phys. Rev. A **56**, 2421 (1997).

[211] A. Kastberg, P. Villemoes, and A. Arnesen, J. Opt. Soc. Am. B **10**, 1330 (1993).

[212] J. Sherman, A. Andalkar, W. Nagourney, and E. N. Fortson, Phys. Rev. A **78**, 052514 (2008).

[213] V. A. Dzuba and V. V. Flambaum, Phys. Rev. A **83**, 052513 (2011).

[214] E. Arimondo, M. Inguscio, and P. Violino, Rev. Mod. Phys. **49**, 31 (1977).

[215] K. Wendt, S. A. Ahmad, F. Buchinger, A. C. Mueller, R. Neugart, and E.-W. Otten, Z. Phys. A **318**, 125 (1984).

[216] A.-M. Mårtensson-Pendrill, D. S. Gough, and P. Hannaford, Phys. Rev. A **49**, 3351 (1994).

[217] R. J. Rafac and C. E. Tanner, Phys. Rev. A **56**, 1027 (1997).

[218] P. Villemoes, A. Arnesen, F. Heijkenskjold, and A. Wannstrom, J. Phys. B **26**, 4289 (1993).

[219] V. A. Dzuba, V. V. Flambaum, and O. P. Sushkov, Phys. Lett. A **140**, 493 (1989).

[220] B. K. Sahoo, M. R. Islam, B. P. Das, R. K. Chaudhuri, and D. Mukherjee, Phys. Rev. A **74**, 062504 (2006).

[221] N. Auerbach, V. V. Flambaum, and V. Spevak, Phys. Rev. Lett. **76**, 4316 (1996).

[222] V. Spevak, N. Auerbach, and V. V. Flambaum, Phys. Rev. C **56**, 1357 (1997).

[223] V. V. Flambaum, D. W. Murray, and S. Orton, Phys. Rev. C **56**, 2820 (1997).

[224] W. C. Haxton and E. M. Henley, Phys. Rev. Lett. **51**, 1937 (1983).

[225] V. A. Dzuba, V. V. Flambaum, and M. G. Kozlov, Phys. Rev. A **54**, 3948 (1996).

[226] A. Dalgarno and J. T. Lewis, Proc. R. Soc. A **233**, 70 (1955).

[227] S. G. Porsev, Y. G. Rakhlina, and M. G. Kozlov, JETP Lett. **61**, 459 (1995).

[228] B. P. Das, Phys. Rev. A **56**, 1635 (1997).

[229] A. D. Singh and B. P. Das, J. Phys. B **32**, 4905 (1999).

[230] M. Gustavsson, G. Olsson, and A. Rosén, Z. Phys. A **290**, 231 (1979).

[231] G. zu Putlitz, Ann. Phys. **466**, 248 (1963).

[232] V. A. Dzuba and J. S. M. Ginges, Phys. Rev. A **73**, 032503 (2006).

[233] V. A. Dzuba and V. V. Flambaum, J. Phys. B **40**, 227 (2007).

[234] I. Ahmad, J. E. Gindler, R. R. Betts, R. R. Chasman, and A. M. Friedman, Phys. Rev. Lett. **49**, 1758 (1982).

[235] V. Grafen, B. Ackermann, H. Baltzer, and T. Bihn, Phys. Rev. C **44**, R1728 (1991).

[236] E. Traykov *et al.*, Nucl. Instr. and Meth. B **266**, 4532 (2008).

[237] P. D. Shidling *et a.*, Nucl. Instr. and Meth. A **606**, 305 (2009).

[238] M. A. Hohensee, N. Leefer, D. Budker, C. Harabati, V. A. Dzuba, and V. V. Flambaum, Phys. Rev. Lett. **111**, 050401 (2013).

[239] C. T. M. Weber, N. Leefer, and D. Budker, Phys. Rev. A **88**, 062503 (2013).

[240] H. Kawamura *et al.*, Hyperfine Interact. (2015), 10.1007/s10751-015-1193-1.

[241] H. Kawamura *et al.*, Nucl. Instr. and Meth. B **317**, 582 (2013).

[242] H. Arikawa *et al.*, Rev. Sci. Instrum. **85**, 02A732 (2014).

[243] V. A. Dzuba, V. V. Flambaum, and O. P. Sushkov, J. Phys. B **17**, 1953 (1984).

[244] V. A. Dzuba, V. V. Flambaum, P. G. Silvestrov, and O. P. Sushkov, J. Phys. B **20**, 1399 (1987).

[245] V. A. Dzuba, V. V. Flambaum, P. G. Silvestrov, and O. P. Sushkov, Phys. Lett. A **131**, 461 (1988).

[246] H. S. Nataraj, B. K. Sahoo, B. P. Das, and D. Mukherjee, Phys. Rev. Lett. **101**, 033002 (2008).

[247] A. Shukla, B. P. Das, and J. Andriessen, Phys. Rev. A **50**, 1155 (1994).

[248] W. R. Johnson, D. S. Guo, M. Idrees, and J. Sapirstein, Phys. Rev. A **34**, 1043 (1986).

[249] D. Mukherjee, B. K. Sahoo, H. S. Nataraj, and B. P. Das, J. Phys. Chem. A **113**, 12549 (2009).

[250] T. Byrnes, V. A. Dzuba, V. V. Flambaum, and D. W. Murray, Phys. Rev. A **59**, 3082 (1999).

[251] B. M. Roberts, Y. V. Stadnik, V. A. Dzuba, V. V. Flambaum, N. Leefer, and D. Budker, Phys. Rev. Lett. **113**, 081601 (2014).

[252] B. M. Roberts, Y. V. Stadnik, V. A. Dzuba, V. V. Flambaum, N. Leefer, and D. Budker, Phys. Rev. D **90**, 096005 (2014).

[253] Y. V. Stadnik, B. M. Roberts, and V. V. Flambaum, Phys. Rev. D **90**, 045035 (2014).

[254] D. Colladay and V. A. Kostelecký, Phys. Rev. D **55**, 6760 (1997).

[255] D. Colladay and V. A. Kostelecký, Phys. Rev. D **58**, 116002 (1998).

[256] V. A. Kostelecký and C. D. Lane, Phys. Rev. D **60**, 116010 (1999).

[257] F. T. Avignone III, R. Brodzinski, S. Dimopoulos, G. D. Starkman, A. K. Drukier, D. N. Spergel, G. Gelmini, and B. W. Lynn, Phys. Rev. D **35**, 2752 (1987).

[258] M. Pospelov, A. Ritz, and M. Voloshin, Phys. Rev. D **78**, 115012 (2008).

[259] F. T. Avignone III, R. J. Creswick, and S. Nussinov, Phys. Lett. B **681**, 122 (2009).

[260] F. T. Avignone III, J. Phys. Conf. Ser. **173**, 012015 (2009).

[261] A. Derevianko, V. A. Dzuba, V. V. Flambaum, and M. Pospelov, Phys. Rev. D **82**, 065006 (2010).

[262] V. A. Dzuba, V. V. Flambaum, and M. Pospelov, Phys. Rev. D **81**, 103520 (2010).

[263] A. V. Derbin, I. S. Dratchnev, A. S. Kayunov, and V. N. Muratova, JETP Lett. **95**, 339 (2012).

[264] A. V. Derbin, S. V. Bakhlanov, I. S. Dratchnev, A. S. Kayunov, and V. N. Muratova, Eur. Phys. J. C **73**, 2490 (2013).

[265] D. F. J. Kimball, I. Lacey, J. Valdez, J. Swiatlowski, C. Rios, R. Peregrina-Ramirez, C. Montcrieffe, J. Kremer, J. Dudley, and C. Sanchez, Ann. Phys. **525**, 514 (2013).

[266] B. J. Venema, P. K. Majumder, S. K. Lamoreaux, B. R. Heckel, and E. N. Fortson, Phys. Rev. Lett. **68**, 135 (1992).

[267] Y. V. Stadnik and V. V. Flambaum, Phys. Rev. D **89**, 043522 (2014).

[268] P. W. Graham and S. Rajendran, Phys. Rev. D **88**, 035023 (2013).

[269] G. Bertone, D. Hooper, and J. Silk, Phys. Rep. **405**, 279 (2005).

[270] V. A. Kostelecký and C. D. Lane, J. Math. Phys. **40**, 6245 (1999).

[271] P. A. Bolokhov, S. Groot Nibbelink, and M. Pospelov, Phys. Rev. D **72**, 015013 (2005).

[272] P. A. Bolokhov, M. Pospelov, and M. V. Romalis, Phys. Rev. D **78**, 057702 (2008).

[273] B. R. Heckel, C. E. Cramer, T. S. Cook, S. Schlamminger, E. G. Adelberger, and U. Schmidt, Phys. Rev. Lett. **97**, 021603 (2006).

[274] B. R. Heckel, E. G. Adelberger, C. E. Cramer, T. S. Cook, S. Schlamminger, and U. Schmidt, Phys. Rev. D **78**, 092006 (2008).

[275] Y. V. Stadnik and V. V. Flambaum, Eur. Phys. J. C **75**, 110 (2015).

[276] F. Allmendinger, W. Heil, S. Karpuk, W. Kilian, A. Scharth, U. Schmidt, A. Schnabel, Y. Sobolev, and K. Tullney, Phys. Rev. Lett. **112**, 110801 (2014).

[277] C. J. Berglund, L. R. Hunter, D. Krause, Jr., E. O. Prigge, M. S. Ronfeldt, and S. K. Lamoreaux, Phys. Rev. Lett. **75**, 1879 (1995).

[278] L.-S. Hou, W.-T. Ni, and Y.-C. M. Li, Phys. Rev. Lett. **90**, 201101 (2003).

[279] F. Canè, D. Bear, D. F. Phillips, M. S. Rosen, C. L. Smallwood, R. E. Stoner, R. L. Walsworth, and V. A. Kostelecký, Phys. Rev. Lett. **93**, 230801 (2004).

[280] I. Altarev *et al.*, Phys. Rev. Lett. **103**, 081602 (2009).

[281] J. M. Brown, S. J. Smullin, T. W. Kornack, and M. V. Romalis, Phys. Rev. Lett. **105**, 151604 (2010).

[282] C. Gemmel *et al.*, Phys. Rev. D **82**, 111901 (2010).

[283] S. K. Peck, D. K. Kim, D. Stein, D. Orbaker, A. Foss, M. T. Hummon, and L. R. Hunter, Phys. Rev. A **86**, 012109 (2012).

[284] V. A. Kostelecký and N. Russell, Rev. Mod. Phys. **83**, 11 (2011), [for an up-to-date version, see arXiv:0801.0287].

[285] N. Leefer and M. A. Hohensee, arXiv:1307.6762.

[286] P. W. Graham and S. Rajendran, Phys. Rev. D **84**, 055013 (2011).

[287] D. A. Varshalovich, A. N. Moskalev, and V. K. Khersonskii, *Quantum Theory of Angular Momentum* (World Scientific, Singapore, 1988).

[288] V. A. Dzuba and V. V. Flambaum, Phys. Rev. A **77**, 012514 (2008).

[289] V. A. Dzuba, Phys. Rev. A **71**, 032512 (2005).

[290] P. Schwerdtfeger and G. A. Bowmaker, J. Chem. Phys. **100**, 4487 (1994).

[291] P. Neogrády, V. Kellö, M. Urban, and A. J. Sadlej, Int. J. Quantum Chem. **63**, 557 (1997).

[292] B. O. Roos, R. Lindh, P.-A. Malmqvist, V. Veryazov, and P.-O. Widmark, J. Phys. Chem. A **109**, 6575 (2005).

[293] P. Schwerdtfeger, Table of experimental and calculated static dipole polarizabilities [**online**], http://ctcp.massey.ac.nz/dipole-polarizabilities (2015).

[294] D. Budker, D. F. J. Kimball, and D. DeMille, *Atomic Physics*, 2nd ed. (Oxford University Press, Oxford, 2008).

[295] D. Budker, P. W. Graham, M. P. Ledbetter, S. Rajendran, and A. O. Sushkov, Phys. Rev. X **4**, 021030 (2014).

[296] C. Beck, Phys. Rev. Lett. **111**, 231801 (2013).

[297] Y. V. Stadnik and V. V. Flambaum, Phys. Rev. Lett. **113**, 151301 (2014).

[298] S. Pustelny, D. F. J. Kimball, C. Pankow, M. P. Ledbetter, P. Wlodarczyk, P. Wcislo, M. Pospelov, J. R. Smith, J. Read, W. Gawlik, and D. Budker, Ann. Phys. **525**, 659 (2013).

[299] A. Derevianko and M. Pospelov, Nat. Phys. **10**, 933 (2014).

[300] B. M. Roberts, Y. V. Stadnik, V. V. Flambaum, and V. A. Dzuba, arXiv:1511.04098.

[301] Y. V. Stadnik, B. M. Roberts, V. V. Flambaum, and V. A. Dzuba, arXiv:1511.04100.

[302] B. M. Roberts, Y. V. Stadnik, V. A. Dzuba, V. V. Flambaum, N. Leefer, and D. Budker, J. Phys. Conf. Ser. **635**, 022033 (2015).

[303] S. Weinberg, Phys. Rev. Lett. **37**, 657 (1976).

[304] S. Weinberg, Phys. Rev. Lett. **40**, 223 (1978).

[305] R. D. Peccei and H. R. Quinn, Phys. Rev. Lett. **38**, 1440 (1977).

[306] R. D. Peccei and H. R. Quinn, Phys. Rev. D **16**, 1791 (1977).

[307] F. Wilczek, Phys. Rev. Lett. **40**, 279 (1978).

[308] J. E. Moody and F. Wilczek, Phys. Rev. D **30**, 130 (1984).

[309] J. E. Kim, Phys. Rev. Lett. **43**, 103 (1979).

[310] M. A. Shifman, A. I. Vainshtein, and V. I. Zakharov, Nucl. Phys. B **166**, 493 (1980).

[311] A. R. Zhitnitsky, Sov. J. Nucl. Phys. **31**, 529 (1980).

[312] M. Dine, W. Fischler, and M. Srednicki, Phys. Lett. B **104**, 199 (1981).

[313] J. E. Kim and G. Carosi, Rev. Mod. Phys. **82**, 557 (2010).

[314] N. Brambilla *et al.*, arXiv:1404.3723.

[315] The CDMS Collaboration, Phys. Rev. Lett. **111**, 251301 (2013).

[316] D. N. Spergel *et al.*, Astrophys. J. Suppl. Ser. **170**, 377 (2007).

[317] A. G. Riess *et al.*, Astron. J. **116**, 1009 (1998).

[318] S. Perlmutter *et al.* (The Supernova Cosmology Project), Astrophys. J. **517**, 565 (1999).

[319] J. Preskill, M. B. Wise, and F. Wilczek, Phys. Lett. B **120**, 127 (1983).

[320] P. Sikivie, Int. J. Mod. Phys. A **25**, 554 (2010).

[321] P. W. Graham, I. G. Irastorza, S. K. Lamoreaux, A. Lindner, and K. A. van Bibber, Annu. Rev. Nucl. Part. Sci. **65**, 485 (2015).

[322] L. J. Rosenberg and K. A. van Bibber, Phys. Rep. **325**, 1 (2000).

[323] M. Kawasaki and K. Nakayama, Annu. Rev. Nucl. Part. Sci. **63**, 69 (2013).

[324] H. Baer, K.-Y. Choi, J. E. Kim, and L. Roszkowski, arXiv:1407.0017.

[325] P. Sikivie, Phys. Rev. Lett. **51**, 1415 (1983).

[326] P. Sikivie, Phys. Rev. D **32**, 2988 (1985).

[327] The ADMX Collaboration, Phys. Rev. Lett. **104**, 041301 (2010).

[328] K. Ehret *et al.* (ALPS Collaboration), Nucl. Instr. and Meth. A **612**, 83 (2009).

[329] The CAST Collaboration, Phys. Rev. D **92**, 021101 (2015).

[330] The IAXO Collaboration, Phys. Procedia **61**, 193 (2015).

[331] S. G. Karshenboim and V. V. Flambaum, Phys. Rev. A **84**, 064502 (2011).

[332] M. Pospelov, S. Pustelny, M. P. Ledbetter, D. F. J. Kimball, W. Gawlik, and D. Budker, Phys. Rev. Lett. **110**, 021803 (2013).

[333] K. Van Tilburg, N. Leefer, L. Bougas, and D. Budker, Phys. Rev. Lett. **115**, 011802 (2015).

[334] D. Cadamuro, S. Hannestad, G. G. Raffelt, and J. Redondo, J. Cosmol. Astropart. Phys. **2011**, 003 (2011).

[335] P. Sikivie, Phys. Rev. Lett. **113**, 201301 (2014).

[336] G. G. Raffelt, in *Axions*, Lecture Notes in Physics, Vol. 741, edited by M. Kuster, G. Raffelt, and B. Beltrán (Springer, Berlin, 2008) Chap. 3, pp. 51–71.

[337] B. A. Dobrescu and I. Mocioiu, J. High Energy Phys. **2006**, 005 (2006).

[338] T. Topcu and A. Derevianko, Phys. Rev. A **88**, 042510 (2013).

[339] N. Leefer, C. T. M. Weber, A. Cingöz, J. R. Torgerson, and D. Budker, Phys.

Rev. Lett. **111**, 060801 (2013).

[340] A. Cingöz, N. Leefer, S. J. Ferrell, A. Lapierre, A. T. Nguyen, V. V. Yashchuk, D. Budker, S. K. Lamoreaux, and J. R. Torgerson, Eur. Phys. J. Spec. Top. **163**, 71 (2008).

[341] L. Bougas, G. E. Katsoprinakis, D. Sofikitis, T. P. Rakitzis, P. C. Samartzis, T. N. Kitsopoulos, J. Sapirstein, D. Budker, V. A. Dzuba, V. V. Flambaum, and M. G. Kozlov, Phys. Rev. A **89**, 042513 (2014).

[342] V. V. Flambaum, I. B. Khriplovich, and O. P. Sushkov, Nucl. Phys. A **449**, 750 (1986).

[343] M. Pospelov and A. Ritz, Phys. Rev. Lett. **83**, 2526 (1999).

[344] R. J. Crewther, P. Di Vecchia, G. Veneziano, and E. Witten, Phys. Lett. B **88**, 123 (1979).

[345] V. V. Flambaum, D. DeMille, and M. G. Kozlov, Phys. Rev. Lett. **113**, 103003 (2014).

[346] The LIGO Collaboration, Reports Prog. Phys. **72**, 076901 (2009).

[347] M. Dine and W. Fischler, Phys. Lett. B **120**, 137 (1983).

[348] M. G. Kozlov and V. F. Ezhov, Phys. Rev. A **49**, 4502 (1994).

[349] L. V. Skripnikov, A. N. Petrov, N. S. Mosyagin, A. V. Titov, and V. V. Flambaum, Phys. Rev. A **92**, 012521 (2015).

[350] L. V. Skripnikov, A. N. Petrov, A. V. Titov, and V. V. Flambaum, Phys. Rev. Lett. **113**, 263006 (2014).

[351] C. T. Hill, Phys. Rev. D **91**, 111702 (2015).

[352] V. V. Flambaum, B. M. Roberts, and Y. V. Stadnik, arXiv:1507.05265.

[353] B. M. Roberts, V. V. Flambaum, and G. F. Gribakin, Phys. Rev. Lett. **116**, 023201 (2016).

[354] B. M. Roberts, Y. V. Stadnik, V. A. Dzuba, V. V. Flambaum, and M. Pospelov, *in preparation* (2015).

[355] V. V. Flambaum, V. A. Dzuba, M. Pospelov, A. Derevianko, and B. M. Roberts, J. Phys. Conf. Ser. **635**, 022012 (2015).

[356] R. Bernabei *et al.*, Eur. Phys. J. C **73**, 2648 (2013).

[357] R. Bernabei *et al.*, Nucl. Part. Phys. Proc. **263-264**, 87 (2015).

[358] R. Bernabei *et al.*, Eur. Phys. J. C **56**, 333 (2008).

[359] R. Bernabei *et al.*, Eur. Phys. J. C **67**, 39 (2010).

[360] K. Freese, M. Lisanti, and C. Savage, Rev. Mod. Phys. **85**, 1561 (2013).

[361] S. K. Lee, M. Lisanti, S. Mishra-Sharma, and B. R. Safdi, Phys. Rev. D **92**, 083517 (2015).

[362] The XENON100 Collaboration, Phys. Rev. Lett. **109**, 181301 (2012).

[363] The LUX Collaboration, Phys. Rev. Lett. **112**, 091303 (2014).

[364] The LUX Collaboration, Astropart. Phys. **62**, 33 (2015).

[365] The SuperCDMS Collaboration, Phys. Rev. Lett. **112**, 241302 (2014).

[366] M. Farina, D. Pappadopulo, A. Strumia, and T. Volansky, J. Cosmol. Astropart. Phys. **2011**, 30 (2011).

[367] C. Savage, G. B. Gelmini, P. Gondolo, and K. Freese, J. Cosmol. Astropart. Phys. **2009**, 010 (2009).

[368] P. Gondolo and G. B. Gelmini, Phys. Rev. D **71**, 123520 (2005).

[369] R. Bernabei *et al.*, Phys. Rev. D **77**, 023506 (2008).

[370] J. Kopp, V. Niro, T. Schwetz, and J. Zupan, Phys. Rev. D **80**, 083502 (2009).

[371] B. Feldstein, P. W. Graham, and S. Rajendran, Phys. Rev. D **82**, 075019 (2010).

[372] A. Dedes, I. Giomataris, K. Suxho, and J. D. Vergados, Nucl. Phys. B **826**, 148 (2010).

[373] R. Foot, Phys. Rev. D **90**, 121302 (2014).

[374] P. J. Fox and E. Poppitz, Phys. Rev. D **79**, 083528 (2009).

[375] M. Aguilar *et al.* (AMS Collaboration), Phys. Rev. Lett. **110**, 141102 (2013).

[376] J. Chang *et al.*, Nature **456**, 362 (2008).

[377] M. Ackermann *et al.* (Fermi LAT Collaboration), Phys. Rev. Lett. **108**, 011103 (2012).

[378] O. Adriani *et al.*, Nature **458**, 607 (2009).

[379] O. Adriani *et al.*, Phys. Rev. Lett. **111**, 081102 (2013).

[380] Q.-H. Cao, E. Ma, and G. Shaughnessy, Phys. Lett. B **673**, 152 (2009).

[381] A. Ibarra, A. Ringwald, D. Tran, and C. Weniger, J. Cosmol. Astropart. Phys. **2009**, 017 (2009).

[382] N. F. Bell, Y. Cai, R. K. Leane, and A. D. Medina, Phys. Rev. D **90**, 035027 (2014).

[383] The XENON Collaboration, Science **349**, 851 (2015).

[384] The XENON Collaboration, Phys. Rev. Lett. **115**, 091302 (2015).

[385] R. Foot, arXiv:1508.07402.

[386] J. Amaré *et al.*, arXiv:1508.06152.

[387] J. Amaré *et al.*, arXiv:1508.07213.

[388] J. Amaré *et al.*, arXiv:1508.07907.

[389] J. Xu, F. Calaprice, F. Froborg, E. Shields, and B. Suerfu, AIP Conf. Proc. **1672**, 040001 (2015).

[390] The XMASS Collaboration, arXiv:1511.04807.

[391] The XENON100 Collaboration, Phys. Rev. D **90**, 062009 (2014).

[392] A. M. Green, Phys. Rev. D **63**, 043005 (2001).

[393] A. M. Green, Mod. Phys. Lett. A **27**, 1230004 (2012).

[394] L. D. Landau and E. M. Lifshitz, *Quantum Mechanics: Non-relativistic Theory* (Pergamon, Oxford, 1977).

[395] H. S. W. Massey, Reports Prog. Phys. **12**, 248 (1949).

[396] A. Dalgarno and H. R. Sadeghpour, Phys. Rev. A **46**, R3591 (1992).

[397] R. C. Forrey, H. R. Sadeghpour, J. D. Baker, J. D. Morgan, and A. Dalgarno, Phys. Rev. A **51**, 2112 (1995).

[398] V. B. Berestetskii, E. M. Lifshitz, and L. P. Pitaevskii, *Quantum Electrodynamics* (Pergamon, Oxford, 1982).

[399] R. Essig, J. Mardon, and T. Volansky, Phys. Rev. D **85**, 076007 (2012).

[400] R. Essig, M. Fernandez-Serra, J. Mardon, A. Soto, T. Volansky, and T.-T. Yu, arXiv:1509.01598.

[401] R. Bernabei *et al.*, Nucl. Instr. and Meth. A **592**, 297 (2008).

[402] The CoGeNT Collaboration, arXiv:1401.3295.

[403] The BABAR Collaboration, Phys. Rev. Lett. **113**, 201801 (2014).

[404] H. An, M. Pospelov, and J. Pradler, Phys. Lett. B **725**, 190 (2013).

[405] The XENON100 Collaboration, Phys. Rev. D **83**, 082001 (2011).

[406] The XENON100 Collaboration, Phys. Rev. D **86**, 112004 (2012).

[407] The XENON100 Collaboration, Astropart. Phys. **54**, 11 (2014).

[408] M. Szydagis *et al.*, J. Instrum. **6**, P10002 (2011).

[409] J. I. Collar, arXiv:1106.0653.

[410] The XENON10 Collaboration, Phys. Rev. Lett. **107**, 051301 (2011).

[411] R. Essig, A. Manalaysay, J. Mardon, P. Sorensen, and T. Volansky, Phys. Rev. Lett. **109**, 021301 (2012).

[412] The CoGeNT Collaboration, Phys. Rev. D **88**, 012002 (2013).

[413] The CoGeNT Collaboration, Phys. Rev. Lett. **107**, 141301 (2011).

[414] P. J. Fox, J. Kopp, M. Lisanti, and N. Weiner, Phys. Rev. D **85**, 036008 (2012).

[415] C. McCabe, Phys. Rev. D **84**, 043525 (2011).

[416] C. Kelso, D. Hooper, and M. R. Buckley, Phys. Rev. D **85**, 043515 (2012).

[417] W. R. Johnson, *Atomic Structure Theory* (Springer, New York, 2007).

[418] G. Fricke *et al.*, At. Data Nucl. Data Tables **60**, 177 (1995).

[419] V. A. Dzuba, V. V. Flambaum, and O. P. Sushkov, J. Phys. B **16**, 715 (1983).

[420] V. A. Dzuba, V. V. Flambaum, P. G. Silvestrov, and O. P. Sushkov, J. Phys. B **18**, 597 (1985).

[421] M. S. Safronova and W. R. Johnson, Adv. At. Mol. Opt. Phys. **55**, 191 (2008).

[422] S. A. Blundell, W. R. Johnson, Z. W. Liu, and J. Sapirstein, Phys. Rev. A **40**, 2233 (1989).

[423] I. Lindgren and J. Morrison, *Atomic many-body theory*, 2nd ed. (Springer-Verlag, New York, 1986).

[424] S. G. Porsev and A. Derevianko, Phys. Rev. A **73**, 012501 (2006).

[425] A. Derevianko, S. G. Porsev, and K. Beloy, Phys. Rev. A **78**, 010503 (2008).

[426] V. A. Dzuba, Phys. Rev. A **90**, 012517 (2014).

[427] M. S. Safronova, M. G. Kozlov, W. R. Johnson, and D. Jiang, Phys. Rev. A **80**, 012516 (2009).

[428] W. R. Johnson, Adv. At. Mol. Opt. Phys. **25**, 375 (1989).

[429] V. A. Dzuba, V. V. Flambaum, P. G. Silvestrov, and O. P. Sushkov, Phys. Lett. A **118**, 177 (1986).

[430] V. A. Dzuba and W. R. Johnson, Phys. Rev. A **57**, 2459 (1998).